New NMR Methods and their Applications in Mechanistic Studies

A thesis submitted to the University of Edinburgh for the degree of Doctor of Philosophy in the College of Science and Engineering

Ran Wei

UNN: S1779178

Supervisor: Professor Guy C. Lloyd-Jones FRS

2022

School of Chemistry

The University of Edinburgh

Declaration

I declare that the work presented in this thesis was completed by myself, under the supervision of Prof. Guy C. Lloyd-Jones. The work reported herein is original except where explicitly stated otherwise in the text, and that this work has not been submitted for any other degree or professional qualification.

Parts of this work have been published in publications below.

1) *Eur. J. Org. Chem.*, 17, 2331-2342, **2021**.

2) *J. Org. Chem.*, 86, 9023–9029, **2021**.

3) *Prog. Nucl. Magn. Reson. Spectrosc.*, 129, 28–106, **2022**.

Lay Summary

Nuclear Magnetic Resonance spectroscopy, commonly referred to as NMR, is a widely-used analytical technique in chemistry. The distinctive NMR signals provide rich chemical structural information, means, we can identify molecules based on their NMR signals. In addition, NMR experiments can be quantitative under appropriate conditions. After acquiring an NMR spectrum, the area under different signals can be measured to reflect the relative number of atoms responsible for these signals. This feature allows us to continuously measure the signals of a chemical reaction, and to distinguish different reaction components such as reactants, products, and intermediates. Measuring the integrals of these components further allows us to construct concentration profiles as a function of time throughout the evolving chemical reaction, for example, the growth of products and the decay of reactants. Therefore, NMR offers a suitable tool for chemical reaction monitoring. However, traditional NMR experiments require preparation procedures such as loading the sample into an NMR tube, then inserting the tube into the spectrometer, *etc*. These preparation procedures take some time. If the reaction evolves too fast and is irreversible, it becomes challenging as during the preparation time the reaction might be completed. Valuable information may have disappeared even before the measurement takes place. To overcome this problem, specialised equipment needs to be employed to cooperate with NMR spectroscopy, allowing data measurements within a shorter timeframe. This work describes a stopped-flow NMR technique that was able to monitor irreversible chemical reactions completed within half a second, an achievement not possible by traditional NMR experiments.

In addition to the studies of chemical reactions, as stated earlier, NMR experiments can give information on the quantity of species, e.g., reactants, intermediates, and products involved in a reaction under appropriate conditions. Failure to satisfy these conditions will lead to incorrect quantification. One of such conditions involves an important parameter called the longitudinal relaxation time constant, T_1. When nuclear spins are excited by radiofrequency pulses for detection, T_1 determines the time needed for them to return to equilibrium before next excitation. This value therefore determines the parameter set-up that one should use in a quantitative NMR experiment. It is important to have a prior knowledge of the T_1 constant of studied species before acquiring an NMR spectrum. The second part of this work introduces a collection of T_1 measurement methods that are faster than traditional methods. They are expected to save the spectrometer time needed for these routine T_1 measurements.

Abstract

Tracing the fate of *fast* irreversible chemical reactions remains a challenging and intriguing task in chemistry. While *slow* reactions can be monitored by routine NMR techniques at ease, real-time monitoring of *fast* reactions that are initiated by mixing, however, poses challenges to traditional NMR experiments and therefore requires specialised techniques. A state-of-the-art stopped-flow piece of equipment was utilised in conjunction with a high-resolution NMR spectrometer, to enable the data collection of rapid reactions including identification of intermediates, side-products, and catalysts, and quantification of selectivity. This work consists of three main aspects regarding the stopped-flow technique: i) evaluating the physical parameters and functionalities of the stopped-flow instrument; ii) monitoring rapid irreversible reactions with half-lives shorter than seconds; and iii) exploiting the non-pre-magnetised input channel of the stopped-flow instrument for magnetisation transfer studies. Thus far, effective kinetic data collection for irreversible chemical reactions of half-lives in the order of milliseconds was achieved, with the aid of interleaved stopped-flow experiments. This was demonstrated by the base-catalysed protodeboronation of pentafluorophenyl boronic acid, of $t_{1/2} = 45$ milliseconds at 313 K. The functionality of the non-pre-magnetised stopped-flow input channel was experimentally validated by the chemical exchange studies without the necessity of isotopic labelling. In addition to the stopped-flow technique, a closely-related yet independent work on the measurements of longitudinal relaxation time constant (T_1) was conducted. T_1 is an important NMR parameter essential for quantitative NMR experiments and molecular dynamic studies. Therefore, prior to kinetic analysis, it is necessary to measure the T_1 of spins in the system. Comparing to the most conventional approaches such as the 'Inversion Recovery' experiments, the methodologies developed in this work showed significant improvements in time efficiency and achieved sufficiently accurate T_1 measurements. Furthermore, it was proved that continuous heteronuclear decoupling could be applied in T_1 measurements, affording sensitivity enhancements from the removal of *J*-couplings and the Nuclear Overhauser Effects. This application is particularly beneficial for insensitive nuclei, which intrinsically require longer experimental time. Throughout the developments of T_1 methods with heteronuclear decoupling, a range of decoupling schemes were evaluated to highlight the appropriate choice for different spin systems.

Acknowledgements

I appreciate this chance to say thank you and farewell properly to the people and things that have lightened up my experience here as a doctoral student.

My gratitude firstly goes to the Scottish Munros and hills, for many pleasant walks in the sunshine and in the rain. To Edinburgh, for being a wonderful city, and particularly to the Usher Hall, for countless beautiful concerts at considerate student price. If life is a jar of memories, the three years in Edinburgh will no doubt be one of my favourite collections.

I would like to thank the Lloyd-Jones group members, without whom my PhD would not have been so enjoyable. Not only were they kind, patient, and helpful when I struggled in the lab, but they have been valuable friends off work. It is wonderful to see people being excellent in different ways, and I feel fortunate to have worked with such a vibrant group. It saddens me to say goodbye, if our life pathways will not cross again, I wish every one of you thrive and shine.

Supervised by two inspirational and supportive professors was beyond my expectation when I set out for my PhD studies. I feel truly grateful and honoured. I would like to first thank my assistant supervisor, Prof. Dušan Uhrín. It has always been delightful when I was given generous advice, and exciting ideas on NMR experiments from Dušan. His knowledge and expertise have absolutely enriched my studies.

Surely, I cannot overstate my gratitude towards my supervisor Prof. Guy Lloyd-Jones, for allowing me the opportunity to join the group. My PhD life is a fruitful and fun process of learning. Guy has undoubtedly played the most significant part in it. He has been caring and supportive throughout my work. Many times, when I doubted myself, he believed in me more than I did in myself. Guy has set a great example that being a respectful scientist not only requires outstanding intelligence, but also true dedication and hard work. It is fortunate to have someone to look up to in my career, and Guy has been a source of motivation and inspiration.

Upon completion of this thesis, I want to thank my parents, for being the best parents and my best friends. I used to tease mom for loving me blindly, irrationally, and passionately, and would always get an adorable grin in return. Later I have come to realise, all my courage and joy stems from that unconditional love. Thank you for being honest with my imperfections and flaws, yet accepting me as I am. You have taught me to seek for the silver linings in dark clouds, to face challenges not fearing of defeats. My greatest luck is being your daughter, and there is not a day goes by that I am not grateful for that.

Table of Contents

Table of Figures

Table of Tables

Abbreviations

1D	one dimensional
2D	two dimensional
B_0	external static magnetic field
B_1	radiofrequency magnetic field
B_2	decoupling magnetic field
BEBOP	Broadband Excitation By Optimised Pulses
CHORUS	CHirped ORdered pulses for Ultra-broadband Spectroscopy
CIDNP	Chemically Induced Dynamic Nuclear Polarisation
CPD	Composite Pulse Decoupling
CPMG	Carr-Purcell-Meiboom-Gill
CW	Continuous Wave
DEPT	Distortionless Enhancement by Polarisation Transfer
DESIRE	DEcoupling SIdeband REsolved spectroscopy
DESPOT	Driven-Equilibrium Single-Pulse Observation
DIPSI	Decoupling In the Presence of Scalar Interactions
DISPEL	Destruction of Interfering Satellite by Perfect Echo Low-pass filtration
EPR	Electron Paramagnetic Resonance
ERETIC	Electronic REference To access In vivo Concentrations
EXSY	EXchange SpectroscopY
FLIPS	Faster Longitudinal relaxation Investigated by Progressive Saturation
FLOPS	Faster Longitudinal relaxation by Ordered Progressive Saturation
FLAPS	Faster Longitudinal relaxation by Amplified Progressive Saturation
FID	Free Induction Decay
FT	Fourier Transform
GARP	Globally-optimised, Alternating-phase, Rectangular Pulses
HMBC	Heteronuclear Multiple-Bond Correlation
HSQC	Heteronuclear Single Quantum Correlation
INEPT	Insensitive Nuclei Enhanced by Polarisation Transfer
IS	Internal Standard
mL	millilitre
MOLLI	MOdified Look-Locker Inversion recovery
MRI	Magnetic Resonance Imaging

ms	millisecond
NMR	Nuclear Magnetic Resonance
NOEs	Nuclear Overhauser Effects
NOESY	Nuclear Overhauser Effect SpectroscopY
PFGs	Pulsed Field Gradients
ppm	parts per million
qNMR	quantitative Nuclear Magnetic Resonance
RF	Radio Frequency
RINMR	Rapid Injection NMR
SM	Starting Material
S/N	Signal-to-Noise ratio
SHARPER	Sensitive, Homogenous, And Resolved PEaks in Real-time
SSFT	Steady-State Fourier Transform
T_1	Longitudinal Relaxation Time constant
T_2	Transverse Relaxation Time constant
µL	microliter
UV-vis	Ultraviolet-visible
WET	Water suppression Enhanced through T_1 effects
WURST	Wideband, Uniform-Rate Smooth Truncation

Chapter 1 Introduction

1.1 NMR Spectroscopy in Chemical Reactions

Solution-state NMR has remained a powerful and versatile analytical tool in physics, chemistry and biochemistry, owing to its distinguished capabilities in providing rich structural information. The comprehensive information derived from chemical shifts, multiplet structures, signal lineshapes, as well as the quantitative nature of NMR spectra, have in conjunction promoted NMR to be one of the most popular analytical techniques. Indeed, NMR spectroscopy offers such a wealth of information that it is rare to find a modern chemistry department today without high resolution NMR spectrometers. The interrogation of chemical reaction mechanisms[1], on the other hand, presents an intriguing yet important task. Tracing the components of a reaction, including the decay of reactants, growth of products, identification of short-lived intermediates or side-products, catalytic activity and selectivity, offers invaluable insights. This generated knowledge-base, in turn, could be employed to feedback the optimisation of known processes, and the design of new ones.

A broad range of spectroscopic tools are available for structural analysis and the investigation of reaction kinetics, such as infrared spectroscopy, Raman spectroscopy, ultraviolet-visible (UV-vis), X-Ray, Electron Paramagnetic Resonance (EPR) spectroscopy, Mass spectrometry *etc*. These techniques vary significantly in complexity and cost, as well as their suitability in meeting particular challenges. While these alternatives offer other advantages and should always be implemented when beneficial, ideal techniques for mechanistic studies should a) provide structural information for identification of chemical species evolving throughout the reaction; b) allow straightforward quantitation of concentrations; and c) be applicable under the conditions under which the reaction of interest is usually employed (concentration, solvent, temperature, etc.). As such, *in-situ* NMR spectroscopy fulfils all of the requirements outlined above and is applicable to a broad range of nuclei common in organic chemistry. It therefore enjoys arguably unmatched superiority and remains one of the most widely utilised techniques for kinetic analysis of organic reactions.

Chemical reaction studies by NMR can be categorised into two classes, systems at equilibrium and systems that are irreversible upon initiation, Figure 1. The analysis of reversible reactions by NMR spectroscopy has been well-established and will be discussed in a succeeding section. In contrast, studies of irreversible processes are limited by the lifetime of the reactions. Monitoring reactions that proceed '*slowly*', for example, over a period of minutes to hours, can be conducted by static NMR (section 1.1.2.1) or flow NMR (section 1.1.2.2) experiments. However, monitoring '*fast*' irreversible reactions that are initiated by mixing, typically at a timescale of seconds to milliseconds, poses a considerably different challenge. *In-situ* monitoring of such rapid reactions normally requires specialised techniques such as rapid injection NMR (section 1.1.2.3) and stopped-flow NMR (section 1.1.2.4) methods. Alternatively, an *ex-situ* quenched-flow method can be utilised to accurately control the quench timing and build up the reaction temporal profile. The following discussion will mainly focus on *in-situ* reaction monitoring methods.

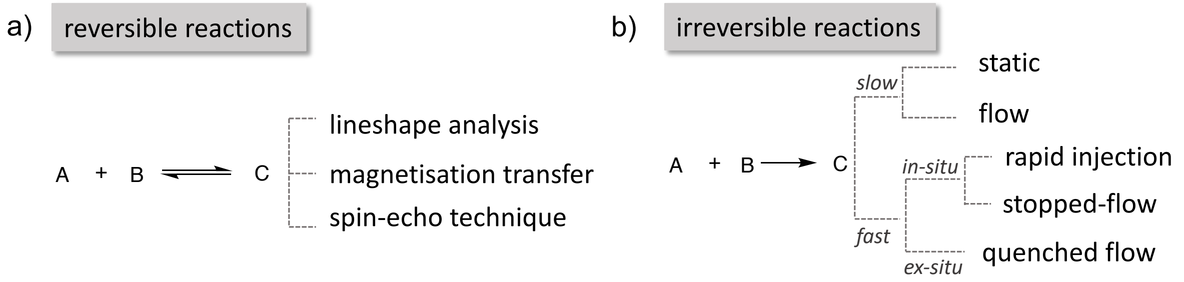

Figure 1. Generic NMR analysis techniques for the kinetics of a) reversible, and b) irreversible, rapid reactions A + B = C. Herein '*fast*' refers to reactions with (pseudo) first-order half-lives, $t_{1/2}$, on the order of seconds or lower.

1.1.1 Reversible Chemical Reaction Studies by NMR

The studies of chemical reactions at equilibrium in real-time date back to the earliest stages of NMR. When nuclei spin species are reversibly transferred between non-equivalent chemical sites, kinetic information can be obtained by signal lineshape analysis[2–4], magnetisation transfer experiments[5], and spin-echo techniques[6–8] under dynamic chemical equilibrium. Gutowsky[2] and McConnell[3] initially reported the pioneer discovery of the relationship between the absorption lineshape, chemical shift difference and chemical exchange phenomena based on modified Bloch equations[9]. It was found that fast exchange rates could be derived from line broadening and distortion effects, and activation parameters derived from the temperature dependence of rates, Figure 2a. This strategy is limited to *fast* exchanging systems where the exchange rates exceed the chemical shift difference (in s^{-1}). The terms *fast* and *slow* here are based on the chemical shift timescale. When the exchange is very slow ($k \ll \Delta\nu_{AB}$, k is the reaction rate, and $\Delta\nu_{AB}$ is the chemical shift difference) the dynamic exchange has negligible influence on the appearance of signals (Figure 2a, i), in this slow exchange regime the exchange can be studied via magnetisation transfer experiments. As exchange rate increases, signals broaden and reduce in peak height (Figure 2a, ii-iv). With the exchange rate further increases, the two signals merge into one and reach the coalescence point (Figure 2a, v). At exchange rates beyond the coalescence point, one signal appears at the midpoint of the previous two signals and continues to narrow down in linewidth whilst increaseing in peak height (Figure 2a, vi-vii). In the very fast exchange regime ($k \gg \Delta\nu_{AB}$), the linewidth restores and a sharp resonance is observed (Figure 2a, viii). In practice, since the observed linewidth of resonances is governed by both the transverse relaxation time T_2 and instrumental imperfections, it can sometimes be challenging to distinguish the effects of exchange from relaxation and from B_0 inhomogeneity. More recently, SHARPER[10] (Sensitive, Homogeneous And Resolved PEaks in Real time) presents a complementary tool to the lineshape analysis methods. It is more tolerant towards B_0 inhomogeneity, and is able to derive activation parameters from temperature-dependent line-broadening effects. Additionally, SHARPER removes heteronuclear coupling, or in the case of sel-SHARPER (selective SHARPER), both heteronuclear and homonuclear couplings are removed, yielding a clean and sharp signal. The SHARPER family was joined by an updated experiment termed MR-SHARPER[11] (multiple resonance SHARPER) which allows simultaneous monitoring of multiple signals by using precise timing of acquisition intervals.

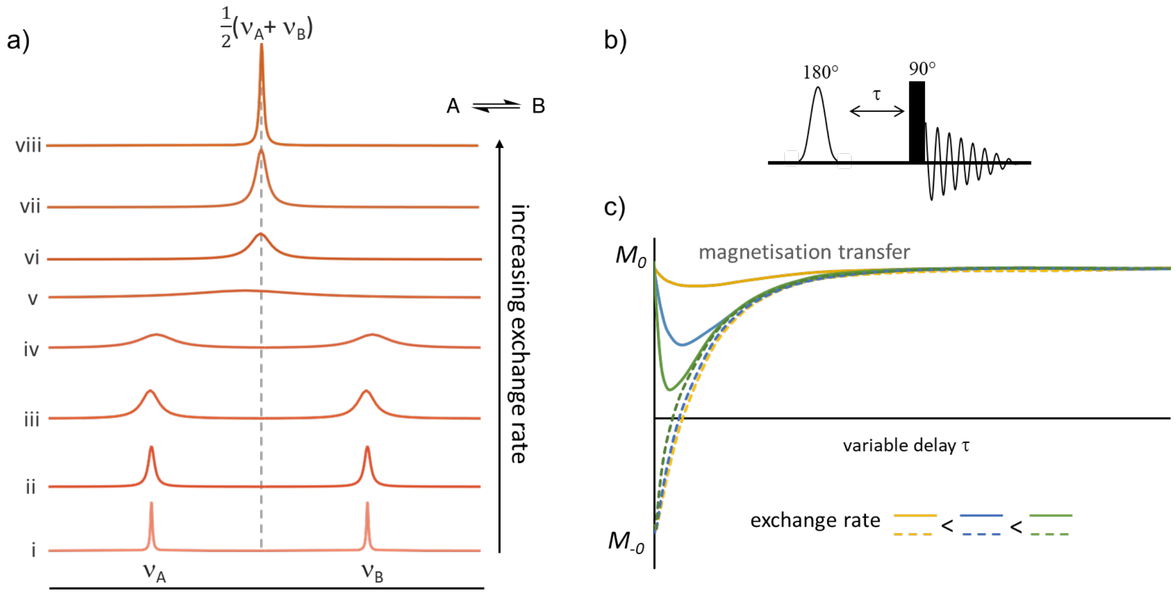

Figure 2. a) Lineshape analysis between two equally populated exchanging spins A and B at chemical shifts ν_A and ν_B, respectively. From bottom to top: (i) no or slow exchange; (ii-iv) signal dynamic broadening in slow-intermediate regime; (v) coalescence point; (vi-vii) signal dynamic narrowing in the intermediate-fast regime; (viii) signal averaging in the very fast exchange regime. b) Pulse sequence of selective inversion recovery experiment for magnetisation transfer studies. c) The effect of magnetisation transfer on signal integrals. The dashed lines represent the integral of spins inverted by the selective 180º pulse, the solid lines represent the signal integral of spins unaffected by the selective 180º pulse.

Magnetisation transfer methods, alternatively, study the evolution of signal intensities based on the theory that signal intensities are governed by both the longitudinal relaxation time constant T_1 and the lifetime of the spin at an exchanging site, under the condition that residual transverse magnetisation is negligible after detection. For example, between two chemically-exchanging sites, the evolution of a spin at one site is affected upon an instantaneous selective disturb of the counter-site. By following the return of spins back to its magnetic equilibrium as a function of time, it is possible to generate the exchange rate and the specific longitudinal relaxation time constant at this site simultaneously in one experiment. Figure 2b shows the pulse sequence for selective inversion recovery experiments. An initial soft 180° pulse selectively inverts one signal, after a delay time τ, a hard 90° pulse is applied followed by immediate FID acquisition. This cycle is repeated with incremented variable delays, and signals are recorded as a function of the variable delay τ. Figure 2c shows a simple example of a two-site system. If the two sites undergo chemical exchange, the selectively inverted spins will experience recovery faster than its intrinsic longitudinal relaxation, owing to the magnetisation contribution from the counter-site. On the contrary, the counter spins will experience a reduction in magnetisation before recovery to the dynamic equilibrium, displaying a 'V-shape' (Figure 2c). The faster the chemical exchange, the deeper the 'V-shape' will be. This observation is a straightforward indicator of chemical exchange, and the quantitative information can be fitted to kinetic models to determine exchange rate constants quantitatively. If the selective inversion is replaced with selective saturation pulse, a saturation recovery experiment with similar principles can be utilised for magnetisation transfer studies. Interestingly, this technique also found usefulness in detecting saturation transfer through NOEs (Nuclear Overhauser Effects)[12], a cross-relaxation phenomenon through space rather than through chemical bonds. This characteristic provided the foundation for NOESY experiment[13], a technique informative in intramolecular distance and spatial structural analysis.

Spin-echo techniques, or CPMG (Carr-Purcell-Meiboom-Gill) relaxation dispersion, built their pulse scheme upon the spin-echo block, which comprises a 90° excitation pulse and a 180° refocusing pulse '90°-τ-180°-τ', and further extended the sequence with an additional train of 180° pulses '90°-τ-180°-τ, -τ-180°-τ, …' spaced by interval time τ. In the absence of chemical exchange, the magnetisation at a frequency-specific site is refocused at the end of first τ after each 180° pulse. Hence an exponential decay in signal amplitude corresponding to the transverse relaxation time constant T_2 should be expected. In the presence of exchange, however, the refocusing would be perturbed and an artificial enhancement in relaxation is observed, dependent on the exchange rate and interval time between consecutive 180° pulses.

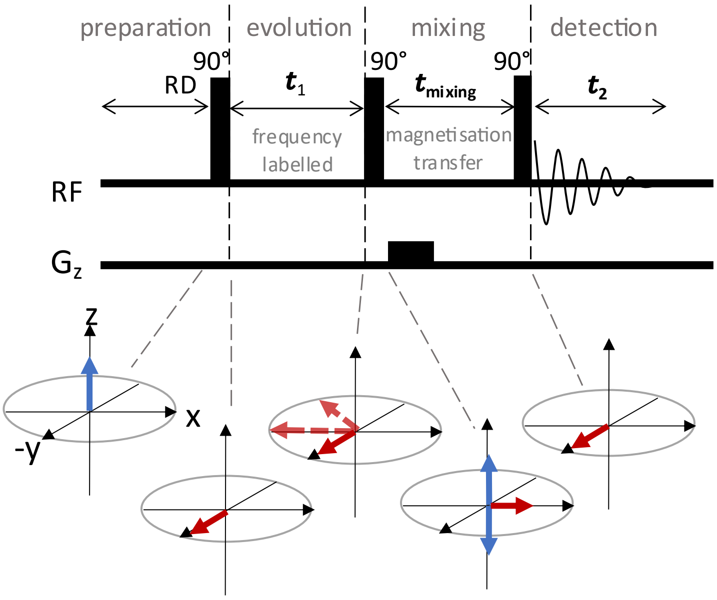

Figure 3. Pulse scheme of the 2D EXSY experiment, subdivided into four time periods. t_{mixing} denotes the time duration for magnetisation exchange, RD denotes the relaxation delay, RF represents the radiofrequency channel, and G_z is the pulsed field gradient. An array of 1D experiments of equally incremented t_1 are acquired as a function of t_2 to yield a 2D spectrum. Magnetisation evolution under the sequence, blue arrows represent longitudinal magnetisation, maroon arrows represent transverse magnetisation.

These above studies have established the potential of NMR experiments in probing inter- and intramolecular dynamic behaviours. With the blooming of 2D NMR spectroscopy from the 1970s, another influential and extensively utilised method that will be discussed here, is the 2D EXSY[14] (EXchange SpectroscopY) experiment (Figure 3). EXSY, initially proposed in 1979, is an extension of the saturation transfer experiment. It adopts a triple 90° pulse scheme, separated by four time periods, preparation, evolution, mixing/exchanging and detection. Transverse magnetisation after the initial 90° pulse becomes frequency-labelled during the evolution period of t_1, the length of which is limited by the transverse relaxation time constant T_2, in a way that transverse magnetisation cannot be fully decayed. A second 90° pulse tilts the magnetisation back to the z-orientation where they experience magnetisation transfer from chemical exchange, dipolar couplings as well as longitudinal recovery. The fixed mixing time therefore needs to be carefully adjusted so that it is considerably long for peak amplitude enhancement but sufficiently shorter than T_1 to achieve quantitative results. As a result, this feature determines that EXSY is particularly informative for *slow* exchanging systems, as for faster exchange, e.g. $k \gg 1/T_1$, the quantitative capability would be lost. The following field gradients help to scramble any residual transverse magnetisation and eventually the exchanged magnetisations are recorded over a time t_2. An intuitive 2D EXSY spectrum is yielded from a set of repeated experiments with equally incremented t_1, where cross peaks manifest the occurrence of magnetisation transfer at corresponding frequencies. Devoid of chemical exchange, this same experiment is commonly referred to as 2D NOESY experiment[13], focusing on the homo- and heteronuclear cross relaxation in solution and solid-state NMR. Analogously, when dipolar coupling is obscuring the study of chemical exchange, a modified clean-EXSY[15] sequence could be implemented to remove the undesired NOE effects.

1.1.2 Irreversible Chemical Reaction Studies by NMR

While NMR experiments have demonstrated their capabilities in studying reactions at equilibrium, the nonstationary analysis of irreversible chemical processes has had a race against time. To date, considerable amounts of work have been conducted to analyse irreversible reactions by *in-situ* and *ex-situ* methods. *Ex-situ* methods refer to reactions that are conducted under standard laboratory conditions outside the NMR tube, then transferred into the tube for measurements. *In-situ* methods indicate reactions are conducted entirely within the NMR tube. *Ex-situ* monitoring enjoys a few advantages, such as minimum spectrometer time; the analytes in the NMR tube completely represent those obtained in laboratory; compatible with a wide range of reactions; and the quenched analytes can be further studied by other complementary techniques. However, *ex-situ* method also suffers from disadvantages, such as the requirement for a large amount of sample volume or aliquots to generate one kinetic profile. It is more labour-intensive, and more prone to random errors from the researchers and instruments. The quenching procedure could cause the loss of valuable transient intermediate information. In this work, the discussion is mainly focused on *in-situ* reaction monitoring NMR methods. The main approaches, based on the lifetimes of the experiments and the coupled techniques to traditional NMR spectrometers, could be divided into the following categories: static monitoring (interrupted *in-situ* and continuous *in-situ*), continuous flow experiments[16,17], rapid injection[18–20], and stopped-flow[21–24] NMR experiments, Figure 4. Each of these approaches hold their individual features, advantages, and limitations, therefore they should be appropriately employed to meet particular requirements.

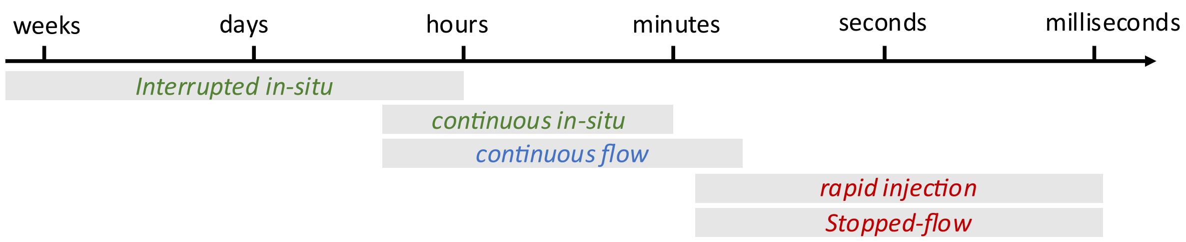

Figure 4. Schematic representation of the *in-situ* reaction monitoring NMR processes based on the lifetimes of chemical reactions.

1.1.2.1 Static NMR Experiments

Firstly, static monitoring in standard NMR tubes is perhaps the most accessible and extensively used approach, as it does not require specialised equipment and can be conveniently practiced following the routine procedures of normal NMR experiments. The term 'static' here refers to the fact that the analytes are transferred to the NMR tube for detection without specialised equipment setup. This method is applicable for *in-situ* assessment of slow reactions from hours to days, providing sufficient access to NMR spectrometers is allowed. It can be conducted in deuterated solvents owing to the small volume of sample required, which could be a challenge for the methods discussed in succeeding sections. Based on the reaction lifetimes, static experiments can be further categorised into interrupted and continuous *in-situ* monitoring. The former typically has a longer reaction time window and measurements can be conducted in an automated manner. The tube with reaction components is loaded onto the auto-sampler system, the spectrometer is then commanded to take a series of spectra at pre-set time intervals. Providing sufficient data density can be acquired, the benefit of this method is that other experiments can be efficiently performed on the same spectrometer during the intervals. Noteworthily, as the tube continuously moves in and out of the magnet, temperature change needs to be considered. If a consistent temperature needs to be maintained, the tube can be manually transferred to a thermostat setup during the intervals. If the detection temperature is significantly different from the commonly utilised spectrometer temperature, a long delay time can be set up to allow for temperature equilibration. For reaction monitoring over a period of minutes to hours, if exclusive access to spectrometer is permitted, continuous *in-situ* monitoring provides good control over the reaction temperature with undisturbed data acquisition. When the reaction lifetimes are in the range of minutes, it might be necessary to maximise the data density before the reactions complete. To achieve this, the pre-acquisition procedures such as tuning, matching, and shimming can be performed on a dummy sample which is as identical as possible to the reaction mixture. Alternatively, if most of the reaction components can be mixed into the NMR tube, without initiating the reaction, the pre-acquisition processes can be performed on this tube. Then it is removed from the spectrometer and the final reagent that initiates the reaction added, the tube is immediately reinserted into the spectrometer for measurements.

Although static NMR experiments are conducted extensively and should be familiar to most users, it is still worth a brief discussion of some considerations before one set out the experiments. The choice of NMR tubes, for example, is an important first consideration. Apart from the most common 5 mm borosilicate glass tubes, other tubes of different diameters from 1-10 mm, or even of volume in the order of microliters, can be purchased, providing the probe can accommodate specialised tubes. Different materials of the tube including quartz and sapphire are also available to accommodate analytes that may react with the glass surface, notwithstanding at a higher price. Specialised tubes such as J-Young NMR tubes house a valve to fit a Teflon cap and for easy attachment to Schlenk line, when air- or moisture-sensitive samples are used. For sensitive reactions, reagents can also be injected via septum cap rather than using conventional NMR caps. Shigemi tubes with a flat bottom are sample-saving, as ineffective sample volume outside the detection region is replaced by solid glass at the bottom of the tube. A diverse range of tubes are commercially available today, it is strongly recommended to ensure the compatibility of the tube with the spectrometer probe prior to any measurements.

Another criterion concerning qualitive and quantitative NMR analysis is the choice of internal standard (IS). There often exists a confusion between internal standard and internal reference, whereas the latter is exclusively used to normalise the relevant chemical shifts of peaks in a spectrum, the former additionally offers a constant concentration guidance for quantitative monitoring of the evolving species. The quantitative nature of NMR experiments is one of the main reasons for its popularity. Internal standards are a common practice to remove any instrumental variations in absolute integrals when accurate quantification is required. A qualified internal standard should be equipped with a few characteristics, i) well-resolved and distinctive chemical shift within the spectrum, ii) stable and inert to the reaction conditions, iii) non-volatile over the course of the reaction, and iv) ideally, has a similar T_1 as the analytes. Alternatively, external standard methodologies are available. For example, ERETIC[25] (Electronic REference To access In vivo Concentrations) represents such a method that has the advantages of simpler sample preparation and free of sample contamination. Although this method requires special NMR tubes and extra precautions thereby remaining rare in practical laboratory work, it yet offers an alternative option for potential users.

1.1.2.2 Flow NMR Experiments

Prior to the introduction of flow NMR, flow chemistry received interest for its automated and continuous manner so as to be inherently time- and labour-saving for operators[26]. It has been widely applicable in industrial scale and laboratory scale, offering improved mixing, heat and mass transfer, and productivity compared to traditional batch processes. Flow platforms are also easy to couple with various spectroscopic tools[27,28]. The first cooperation of flow method and NMR spectrometer was proposed by Suryan[29] in 1951, and thereafter enjoyed development along with the growing popularity of NMR spectroscopy especially after the revolutionary mathematic Fourier Transform[30] in 1966.

The adaptation of flow method to NMR spectrometer was greatly facilitated by tailored probes[31,32], flow cells[33,34], and coils[35] of different geometries, which could be integrated into high-field[36–38] and low-field[39–42] spectrometers for reaction monitoring. For biological reaction monitoring with limited sample availability, microfluidic flow probes[37,38] have been developed to allow for smaller reaction volumes. It is worth mentioning that low-field benchtop NMR has enjoyed particular popularity in this field, owing to its combined benefits of low cost and maintenance, as well as its flexibility of the small-sized spectrometer which can easily be coupled to a reaction system even in a fume hood. Furthermore, benchtop NMR instruments adopt shorter distance from the reaction vessel to the magnet, hence further reducing sample volume requirements and the dead time between reaction and detection. In the case of high-resolution flow experiments, the necessity of probe modification was circumvented by innovative design of flow tubes, allowing the continuous-flow system to conveniently couple to standard NMR spectrometers, Figure 5a.[43] One main advantage of flow monitoring is the reaction takes place in a reaction vessel, therefore compatible with different types of reaction conditions. The analytes flow through spectrometer for measurement and represent the '*real*' reaction mixture as those in the vessel. The addition of reagents is possible during data acquisition. Another advantage of flow experiments is that the reaction solution can be simultaneously analysed by complementary techniques such as UV-Vis and IR[44,45].

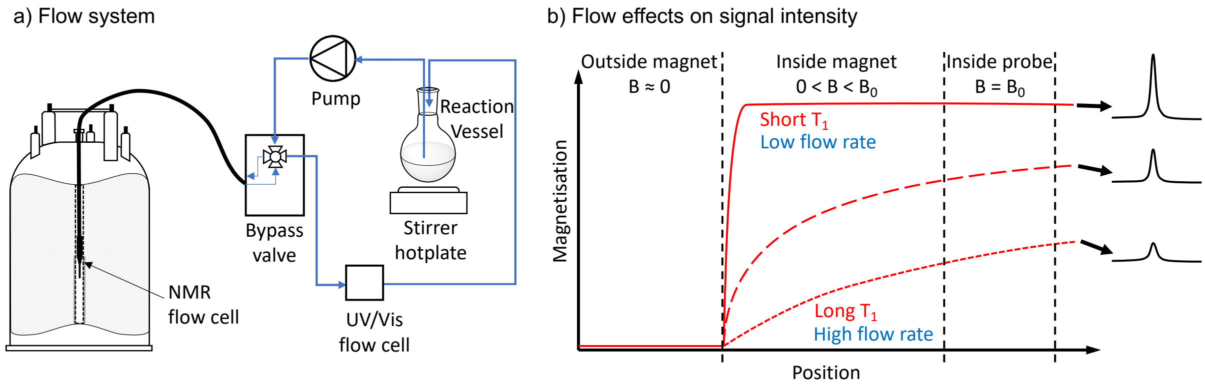

Figure 5. a) A closed-loop recirculating flow system. b) Flow effects on the pre-magnetisation of analytes. Solid line displays a scenario where the analyte has a short T_1 and the flow rate is low (long residence time), i.e., the analyte is fully polarised; dashed lines represent analytes with long T_1 and high flow rate, the partial polarisation leads to attenuated signal intensity.[1,43]

Different from static measurements discussed above, deuterated solvent is generally not recommended in flow experiments due to the larger quantity of materials required. Usually, NMR spectrometers use deuterium solvents to stabilise the magnetic field strength (locking). This is achieved by matching the deuterium absorption of the solvent with the lock frequency of the spectrometers. However, NMR acquisition under unlock mode is feasible, as for modern high-field spectrometers the drift in magnetic field strength is small in a short timeframe thus having negligible effects on the resultant spectra. Unwanted strong solvent signals could be effectively bypassed via the application of selective-saturation solvent suppression methods such as WET[46] (Water suppression Enhanced through T_1 effects). When reproducible and quantitative results are desired, the effects of flow, including intrinsic-flow effects and out-flow effects,[47] need to be considered. These in- and out-flow effects are dependent on a range of factors, including the characteristic flow regime, flow rate, the longitudinal relaxation time constants (T_1) and residence time of analytes in the pre-magnetisation region. Generally, turbulent flow must be avoided at the detection region, and flow can be considered laminar when Reynold number is relatively small. Flow rate, on the other hand, has an influence on the lag/dead time before data acquisition. It is recommended to measure the T_1 of all analytes under static conditions prior to reaction monitoring under flow conditions. Without pre-magnetisation reservoirs, the T_1 and residence time determines the extents of polarisation, reflected in the signal intensities, Figure 5b. These variations in signal intensity will translate into incorrect quantitation. The flow profile and the pre-magnetisation extent of nuclei should therefore be adjusted and optimised carefully. Another undesired consequence of the continuous flow is that the sample volume experiencing the radiofrequency (RD) will be partially purged outside the detection volume, leading to a faster FID decay and broadened resonances. This artificially enhanced effective relaxation[40] in continuous-flow and a correction factor[43] were reported to alleviate the quantitative distortion caused by in- and out-flow effects. Overall, it is beneficial to evaluate the above-mentioned effects of a given continuous flow system and analytes prior to conducting reaction monitoring. Owing to the circulatory feature, flow NMR experiments, in principle, could achieve signal averaging, i.e., improved signal-to-noise ratio (S/N) from multiple acquisitions under identical experiment conditions, which is a potential constraint for rapid injection and stopped-flow methods to be introduced in the succeeding text.

1.1.2.3 Rapid Injection NMR

The demand to follow faster nonequilibrium reactions encouraged the mechanical incorporation of rapid-injection[18–20] and stopped-flow[21–24] techniques to NMR setups. These specialised techniques accelerate the reaction monitoring towards a significantly shorter timescale from minutes to even milliseconds. The rapid-injection NMR relies on one solution injected rapidly to another already in the tube, using the NMR tube itself as the mixing chamber. The rapid and efficient mixing is achieved by high-speed fluidic turbulence. Rapid-injection NMR was initially proposed by McGarrity and co-workers[18]. The original prototype of McGarrity's injection apparatus compromises a gastight syringe, driven by a pneumatic piston whose movement triggers the acquisition pulse sequence. The syringe is mounted above the spectrometer and coupled to a long Teflon needle for solvent delivery. This device was successfully implemented for kinetic study and observation of reactive intermediates[48–51] in spite of its main drawbacks of (a) line broadening resulted from the injector and capillary inhabited inside the NMR tubes which disturbs the magnetic field homogeneity, and (b) diffusion of injectant from the capillary into the reaction solution throughout the experiment. After this, a range of inventive instruments[52–55] were developed by interested research groups to tackle the limitations of the original apparatus and pave the way for improved performance or for their specific applications.

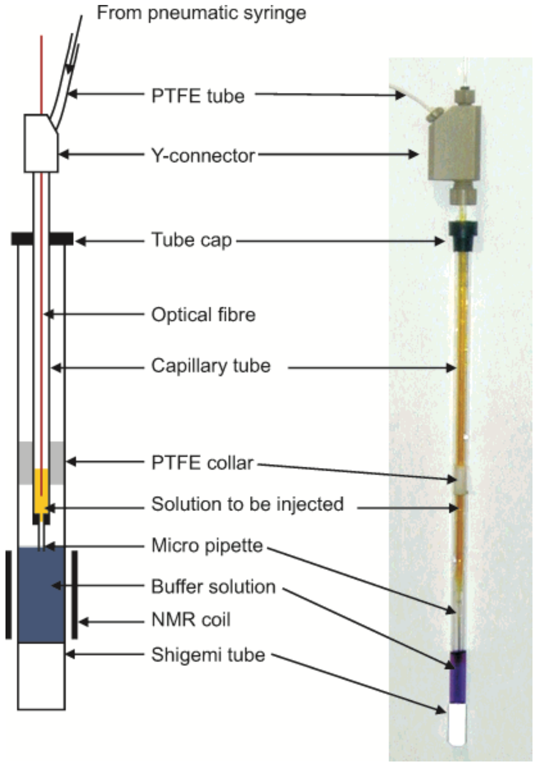

Figure 6. An example of rapid injection apparatus designed by Hore *et al.*, this figure was reproduced directly from their publication in 2003.[52]

Hore and co-worker's rapid injection device[52] allows efficient and homogeneous sample-mixing in tens of milliseconds, with an additional potential to include an optical fibre for photo-CIDNP (Chemically Induced Dynamic Nuclear Polarisation) experiments. Their apparatus compromises two main parts, as shown in Figure 6, a coaxial glass capillary tubing fitted inside the NMR tube, and a glass syringe pneumatic injector outside the magnet. The diffusion of injectant into the tube prior to injection is obviated by the introduction of a small bubble at the end tip of the injector. Rapid mixing is achieved by a high-speed collimated jet of solution held inside the capillary into the other in the NMR tube. Shigemi tubes were utilised over conventional tubes here, for the more vigorous turbulence from flat-bottomed tubes than round-bottomed tubes, hence more efficient mixing, and an apparent bonus of smaller sample volume requirement. Based on this work, Franco *et al.*[53] reported a moderately optimised device that removes the injector from the detection region after mixing, to obtain minimal perturbation of the magnetic field homogeneity. The removal of injector is delicately governed by an air injection using a pneumatic air syringe. Another dual-syringe apparatus assembly was introduced by Reich and co-works[54], allowing for simultaneous injection of two solutions in a single experiment. One unique characteristic of this device lies in the incorporation of a mechanical stirrer, alleviating the inefficient mixing from sample solubility or temperature at solvent freezing point. Although the authors claimed their preference to operate with 10 mm tubes for better sensitivity in multinuclear experiments, and Denmark[55] suggested in another publication that 10 mm tubes require less time to achieve homogeneous sample mixing than 5 mm tubes, it should still remain prudent when precious reagents are involved. Denmark and co-workers[55] later on optimised on their work and designed a system that fulfils the requirements of accurate metering, rapid mixing and high chemical resistance in measurements. Accurate metering of inject volumes and inject rates was achieved by a hydraulics system, which consists of an injector tip, two pneumatic actuators to drive and retreat the injector tip respectively, and three electronically controlled optical sensors. Efficient and homogenous mixing was aided by an extra s-shaped paddle at the bottom of the injector to resolve the concentration gradient formed from reagent delivery. A gas inlet was added to the reservoir to enable air- and moisture-sensitive reagents to be used. This rapid-injection NMR system, proved robust and reproducible in three case studies for kinetic analysis, was reported to adopt a ca. 2 second delay time between injection and data acquisition. While the development of more sophisticated apparatuses aims for faster mixing, the main drawback of rapid injection methods, however, is perhaps the constant necessity to remove and clean after each measurement and reinsert the tube for new measurement. To sample a kinetic profile with satisfactory data density, this practice can be cumbersome, and pose limitations on sample volume.

1.1.2.4 Stopped-flow NMR

The first stopped-flow experiment[56] was reported in 1940, long before the first ever recorded high resolution NMR spectrum of ethanol[57]. Similar to flow and rapid-injection techniques, the stopped-flow apparatus also found its application to a range of spectroscopic tools[58–63], among which its initial incorporation with NMR spectrometers occurred in the 1970s[21–23]. Thereafter the stopped-flow instrumentation has undergone continuous optimisations to achieve rapid mixing and minimal phenomenological dead time, probing the limit of very fast reaction monitoring. The primary difference between the rapid-injection technique discussed above and the stopped-flow technique lies in the way they mix the analytes. Instead of storing one solution in the NMR tube which is located at the magnet bore and introducing the other from outside the tube (Figure 7a), in the stopped-flow technique the reactants are introduced from separate syringes to a mixing device and the nascent reaction mixture delivered to an NMR flow cell for detection, (Figure 7b and 7c). The main components of a conventional stopped-flow apparatus generally include driving syringes, a mixing cell, and a stopping syringe at the observation region. The driving syringes push analytes into the mixing cell, where they become rapidly and sufficiently mixed, then the flow mixture enters the stopping syringe and gets trapped. The stopping movement is sensed and triggers acquisition. While the principles of stopped-flow apparatus are easy to comprehend, the sought-after desires focus primarily on the minimum deadtime. Deadtime of a stopped-flow experiment comprises three main parts, i) the mixing time of analytes in the mixer, ii) the transport time from the mixer to the tube, and iii) the waiting time for the flow to stop and the liquid oscillation to cease for measurements.

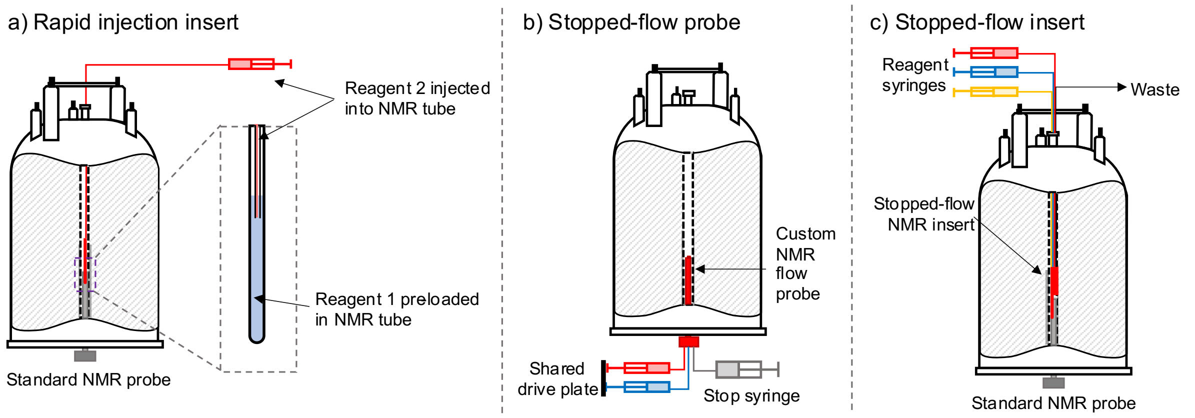

Figure 7. Schematic representations of a) rapid injection apparatus designed to insert into a standard NMR probe, b) a classic stopped-flow setup with a customized stopped-flow probe, and c) a variable ratio stopped-flow apparatus designed to insert into standard NMR probes.[64]

Sykes *et al.*[21] constructed a preliminary rapid mixing cell capable of studying reactions with half-life times in the range of 10 ms, although it was highlighted that the longitudinal relaxation time constant (T_1) of studied nuclei must be substantially smaller than the half-life time of the studied reaction, otherwise, the relaxation mechanism of the nuclei spin system overshadowed the concentration changes of the reactions. This limitation was later on bypassed by their own modified eight-jet mixing cell[65] owing to an inclusion of a pre-magnetisation reservoir. Ernst and co-workers[22] continued optimising their apparatus and achieved an impressive deadtime of only 2 ms. They also underlined the sensitivity of stopped-flow experiments to lineshape distortions due to the stopping motions. Despite the mechanical limitations at that time, for example, the drive and stop syringes were manually operated by means of three-way stopcocks, the principles of their work remained influential to the following stopped-flow developments. A high pressure stopped-flow probe was introduced by Tanaka *et al.*[24], tolerant of pressures up to 200 MPa with a deadtime of several hundred milliseconds. They introduced inlet pathways for nitrogen gas and pressure transmitting fluid, expanding the applications of stopped-flow NMR to monitor fast reactions under high pressure as well as to study the effects of pressure on fast reactions. More recently, customised probes[66,67] were constructed for greater reagent polarisation and temperature control. Landis *et al.*[68] simulated the effects of fast reaction evolution on the FIDs using numeric methods. The appearance of resonances such as linewidth, phase shift, and intensity are only significantly affected when the reaction half-life is ≤ 0.01 s, which is faster than the deadtime of currently available stopped-flow systems.

The conventional stopped-flow setup has some practical limitations. The first is that it often requires a custom NMR probe, rendering the use of cryoprobe impossible. Secondly the delivery volume is restricted by the volume of the stopping syringe. Furthermore, the delivery volume from solution syringes is in a fixed volumetric ratio due to the single shared drive plate (Figure 7b). Very recently, a programme-controlled three-syringe stopped-flow system was introduced to address these limitations. This state-of-the-art instrument in the Lloyd-Jones group was employed throughout this project, for the interrogation of very fast irreversible chemical reactions.

1.1.3 Temporal Resolution Enhancement by Interleaved Experiments

As introduced previously, to generate a satisfactory kinetic profile, sufficient time points need to be acquired before the reaction finishes. In practice, one straightforward method is to reduce the excitation pulse angle, trading sensitivity for temporal resolution. For example, Figure 8a shows that 30° pulses effectively shorten the required repetition time between two transients to 2.95* T_1 for a 99.3% relaxation recovery, at the price of 50% sensitivity loss comparing to a 90° pulse. 10° pulses are able to enhance the temporal resolution by shortening the repetition time to just 0.77* T_1, with 17% sensitivity retained. The sensitivity loss needs to be carefully considered for fast reaction monitoring, as signal averaging, a process that is commonly used in traditional NMR experiments for sensitivity enhancement, is not possible for rapidly evolving reactions. Therefore, in practice, researchers should adjust these acquisition parameters in an NMR experiment reasonably, aware of the demands and limitations. Alternatively, for very fast reactions that evolve too fast to afford sufficient data points even with reduced pulse angle, an approach to allow more data acquisition in a given timescale relies on an interleaved manner.[64] Interleaved method is practically a pseudo real-time approach. By repeating a chain of experiments under the same conditions except changing the time gap between the reaction initiation and data acquisition, the data points obtained from separate experiments with different timing offsets can then be reconstructed to give a reaction profile with manually enhanced temporal resolution, Figure 8b. This interleaved approach can easily integrate with the stopped-flow technique introduced in this work, as the latter enjoys programme-controlled experimental conditions and easy refreshment of analytes, allowing repeated measurements to be conveniently conducted. This method was practically employed in this project for fast reactions with half-life time in the order of milliseconds (section 2.2).

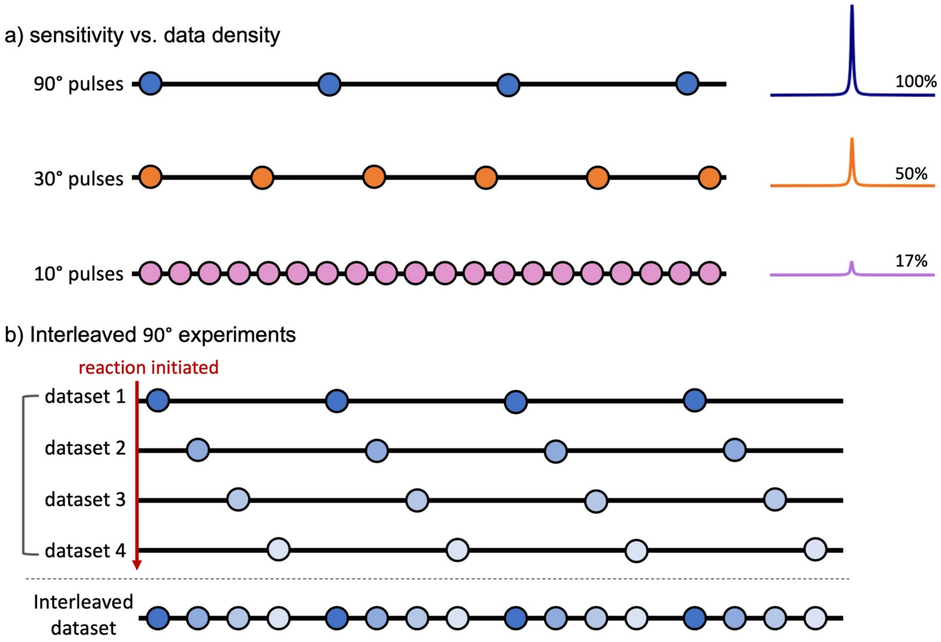

Figure 8. a) Graphical representations of the relationship between sensitivity and data density achievable in a time window. b) Manually enhance data sensitivity by four interleaved data sets using 90º pulses, maximum sensitivity retained.

1.2 Longitudinal Relaxation and Impact

Another focus of this work is the longitudinal relaxation time measurements. Relaxation mechanisms[69], briefly touched upon in preceding text, play an important role in the resultant signals in a NMR spectrum. These two relaxation phenomena, including longitudinal relaxation and transverse relaxation, vary in their different pathway for energy release. In an applied static magnetic field, NMR-active nuclei are distributed in their higher energy level and lower energy level following the Boltzmann distribution

$$N_\beta / N_\alpha = exp\left(\frac{-\Delta E}{kT}\right) \qquad \textbf{Equation 1}$$

N_β and N_α are the population of nuclei in higher energy state and lower energy state respectively, ΔE is the energy difference between two levels, k is the Boltzmann constant and T is the temperature. When nuclei are excited by the transmitter radiofrequency (RF) pulse in a perpendicular direction to the external magnetic field B_0, an absorption of energy occurs and a migration of nuclei from their lower energy state to higher energy state is triggered which breaks the Boltzmann distribution. These excited nuclei will then release the energy to return to their lower energy state by a phenomenon called relaxation. By different pathways for energy release, relaxation is categorised into longitudinal (spin-lattice) relaxation and transverse (spin-spin) relaxation, the former represents energy transferred to surrounding lattice and in the direction of the external magnetic field, whist the latter represents energy transferred to neighbouring nuclei and in the direction perpendicular to the magnetic field, respectively. The relaxation of nuclei offers valuable insights into the study of nuclei dynamics[70,71]. For example, T_2 has an effect on the spectral resolution as natural linewidth at half height $\Delta_{1/2} = 1/\pi T_2$. In other words, the slower the transverse magnetisation decays away, the narrower the signals are. On the other hand, T_1 is crucial when deciding the relaxation delay between acquisition cycles, for a multiple-spin system, delay normally needs to be 5 times the longest T_1 value so that 99.3% spins are returned to equilibrium. Otherwise, partially relaxed spins and fully relaxed spins will lead to errors in both relative quantitation and absolute quantitation. In the context of qualitative NMR, T_1 also plays a role in determining the Ernst angle[30] for optimal sensitivity within a given spectrometer time. Regarding the stopped-flow experiments, where spins are not fully magnetised upon entering the flow cell, T_1 constants are correlated with the pre-magnetisation level of different analytes in the same experiment. Therefore, it is highly advised to estimate or measure the T_1 values of spins before performing kinetic studies. Considering the significance of longitudinal relaxation on quantitative analysis, the methodologies for T_1 determination will be discussed here.

1.2.1 Longitudinal Relaxation Time Measurements

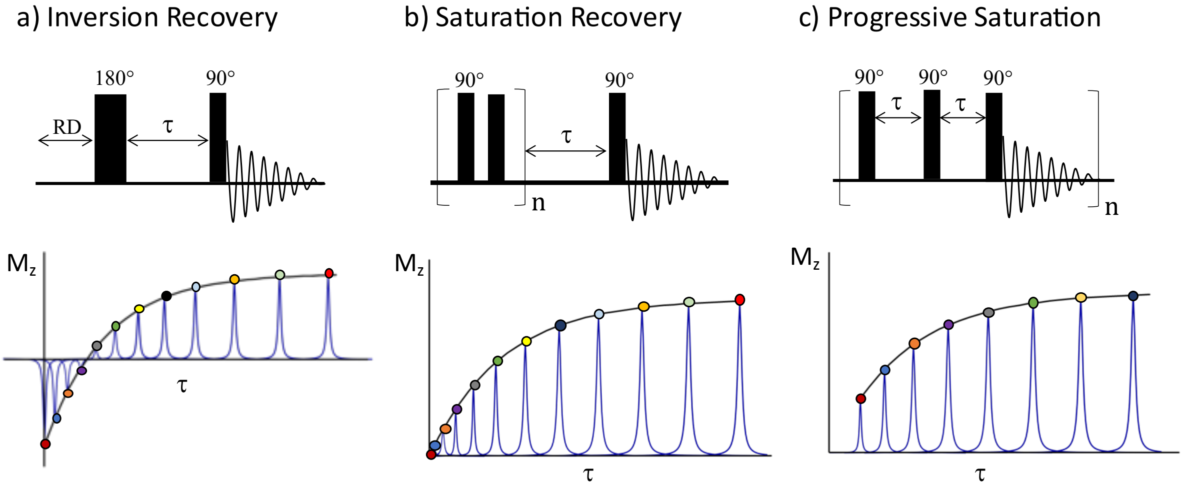

Figure 9. Pule sequences for a) inversion recovery, experiment is repeated with variable delay time τ; b) saturation recovery, n denotes the number of 90° pulses applied to saturate the z-magnetisation, experiment is also repeated with variable delay time τ; and c) progressive saturation, identical 90° pulses are equally spaced by repetition time τ. The fitted data to derive T_1 constants are shown below each sequence respectively. Differently coloured data points indicate that they are acquired stepwise in each repeated cycle.

There are a wide variety of methods for T_1 measurement, and comprehensive reviews[72] are also available. Among the T_1 measurement experiments such as inversion recovery[69,73,74], saturation recovery[75,76], null approximation, and progressive saturation[77] (Figure 9), the most widely used method, available that can be performed in automation on nearly all spectrometers, is the inversion recovery experiment (Figure 9a). It investigates the longitudinal relaxation by employing an initial 180° pulse, which inverts the equilibrium magnetisation to -z-axis, then waiting for a delay time τ. During this τ period the inverted magnetisation relaxes towards the equilibrium state. A followed 90° pulse then rotates the magnetisation to transverse plane for detection, the signal intensity reflects how much the magnetisation has relaxed. By repeating this cycle with a series of incremented variable delay time τ (a minimum of 10 values and the largest variable delay at least 5*T_1 is recommended,), the longitudinal relaxation recovery curve can be sampled. An exponential function between the integral M_t against τ is obtained following the relationship:

$$M_t = M_0 \cdot (1 - 2 \cdot e^{-\tau/T_1})$$ **Equation 2**

M_0 is the thermal equilibrium, T_1 is the longitudinal relaxation time constant. The null approximation, in practice, is used for a faster estimation of T_1 value. It employs the same pulse sequence as the inversion recovery experiment and simply utilises the fact that signal integral reaches zero when the recovery time equals $T_1 \times \ln 2$. Therefore, by reducing the time for positive signal integral and conversely increasing the time for negative integral, an estimated T_1 is quickly derived. The closely related saturation recovery experiment[75,76], Figure 9b, consists of a loop of repetitive 90° pulses, to saturate the magnetisation rather than inverting it. The saturated magnetisation then starts to relax upon the extinction of the saturation pulses, back to equilibrium state during delay time τ. Similar to the Inversion Recovery experiment, the final 90° pulse monitors the integral determined by longitudinal relaxation rate and delay time. By repeating this cycle for a range of τ values again yields an exponential relationship between signal integral and time following Equation 3.

$$M_t = M_0 \cdot (1 - e^{-\tau/T_1})$$ **Equation 3**

Progressive saturation experiment[77] (Figure 9c), proposed by Freeman *et al.*, adopts an equally spaced 90° pulse train to drive the magnetisation to a steady state, and by varying the delay time τ, a recovery curve is sampled. The saturation recovery and progressive saturation methods bypass the relaxation delay (RD) required before each cycle in inversion recovery, allowing a reduced overall experimental time. This advantage is more substantial for samples of low concentration or insensitive nuclei as signal averaging is usually necessary for sensitivity. In the progressive saturation experiment, the recovery of magnetisation occurs during the interval delay time between equally spaced 90° pulses. The first 90° pulse reads out the thermal equilibrium integral M_0, and the following train of 90° pulses establishes a steady-state where relaxation and excitation reach a dynamic balance. It was reported that a reasonable steady-state is attained after three consecutive 90° pulses. Under the condition that the transverse magnetisation is eliminated prior to the next excitation pulse, this dynamic balance would be determined by longitudinal relaxation only, following Equation 4.

$$T_1 = -\tau / ln\left(1 - \frac{M_n}{M_0}\right)$$ **Equation 4**

In Equation 4, M_n is the signal integral measured when steady-state is established, τ is the repetition time between pulses. The choice of τ needs to be careful, since the signal intensity detected at the steady-state is directly proportional to the time and longitudinal relaxation rate.

Too short of a repetition time will lead to low signal-to-noise ratio (S/N), or in the worst case, loss of signal, while too long of a repetition time will allow the spins to fully relax back to equilibrium. The following procedure is similar to the previous two methods, a series of incremented repetition time τ is used to sample the recovery curve. As can been seen from Figure 9, both saturation recovery and progressive saturation methods only sample part of the inversion recovery curve. In the original publication of progressive saturation experiment, the author emphasised that the pulse angles must be 90° to ensure a complete rotation of z-magnetisation onto the transverse plane. This steady-state theory, also investigated by Kaptein termed SSFT[78] (Steady-State Fourier Transform), used a $[180°\text{-}(\theta(\text{FID})\text{-}\tau)_n]$ sequence. In contrast, it stated the pulse angle adopted here must be $\theta<90°$ (typically 30°). Such small flip angle steady-state experiments have been applied in MRI[79,80] and hyperpolarised heteronuclei[81] T_1 measurements, but have not been widely adopted in routine solution phase NMR spectroscopy. In this work, it was proved that variable angles ($0°<\theta\leq90°$) can be implemented for the T_1 determination, alleviating the sensitivity challenge in systems with long T_1 values and short repetition time.

Apart from the above T_1 measurement methods, other approaches such as Fast Inversion Recovery[82], and Modified Fast Inversion Recovery[83] edit the waiting time in the original Inversion Recovery pulse sequence to moderately alleviate the long experimental time. An early single-scan method[84,85] samples the recovery curve by repeating a 90°-180°-90° sequence after an inversion pulse, therefore non-destructively observing the relaxation back to equilibrium, but the method is too limited for general application. A spatially-selective single-scan method[86] has circumvented some of these limitations by detecting magnetisation in different slices of the sample. However, this comes at a penalty of reduced sensitivity. The original 'Look-Locker' technique[87,88] described the steady-state driven by low-flip angle pulses from an initial state that could be inversion, saturation or equilibrium. The MOdified Look-Locker Inversion recovery (MOLLI) sequence[89] is now widely employed for T_1 mapping in (MRI) (Magnetic Resonance Imaging). The Variable Nutation, or Driven-Equilibrium Single-Pulse Observation of T_1 relaxation (DESPOT) technique, is similar to Progressive Saturation, but varies the pulse angle, θ, instead of τ. Indirect T_1 measurements utilise polarisation transfer such as INEPT[90,91] (Insensitive Nuclei Enhanced by Polarisation Transfer), or DEPT[92] (Distortionless Enhancement by Polarisation Transfer) to measure the T_1 constants of low gyromagnetic ratio nuclei, or high gyromagnetic ratio nuclei with overlapped signals. All these outlined methods offer an extensive range of options for T_1 estimation, all based on analysis of the exponential function of longitudinal relaxation recovery against time following the relationship below, in which α is determined by the starting point of the recovery curve.

$$M_t = M_0 \cdot (1 - \alpha \times e^{-\tau/T_1}) \qquad \textbf{Equation 5}$$

1.3 Nuclear Overhauser Effects from Heteronuclear Decoupling

The Overhauser phenomenon was first proposed by Albert W. Overhauser[93]. It was found the nuclear signal intensity could be greatly enhanced by a factor of > 1000 from the saturation of unpaired electrons. This polarisation transfer between nuclei and electrons originates from the cross relaxation between them when the Boltzmann population distribution of electrons is disturbed. Interestingly, this novel theoretical prediction was not well received upon its first publication and encountered scepticism from a few notable Nobel laureates. Later in the same year, successful experimental validation[94] confirmed the proposal, and this Overhauser effect has thereafter become a pivotal topic in NMR spectroscopy. The original *nuclear-electron* Overhauser effect requires external microwave irradiation and the addition of free radicals to the sample as the polarisation source. This procedure constructs the concept of dynamic nuclear polarisation (DNP), a hyperpolarisation technique that has found widespread applications in solution-[95] and solid-state[96,97] NMR. The work herein will mainly discuss *nuclear-nuclear* Overhauser effect, with a particular focus on heteronuclear Overhauser effect.

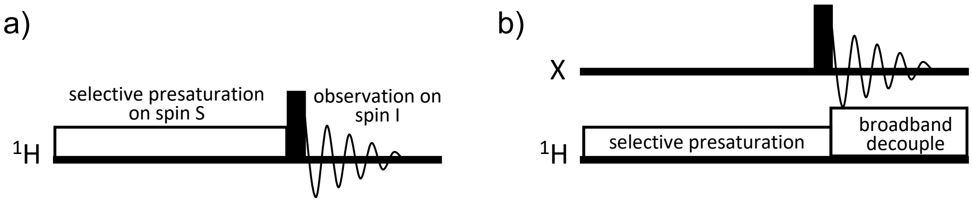

Figure 10. a) A scheme for measuring steady-state homonuclear NOEs. b) A scheme to measure steady-state heteronuclear NOEs.

Different from scalar couplings through chemical bonds, the NOEs arise from dipole-dipole cross relaxation between spins that share dipolar couplings through space. In solution-state NMR, the rapid random molecular tumbling usually averages the dipolar couplings to zero on the NMR timescale, thus do not produce resonance splitting in the way of scalar coupling. However, in solid-state NMR, the dipolar interactions contribute to the appearance of resonances due to rigid molecular movement. Since the magnitude of dipolar couplings is typically magnitudes larger than that of *J*-coupling, solid-state NMR signals display significantly broader linewidths. This signal broadening can be alleviated by a magic-angle spinning (MAS) technique, where the sample is rotated around an axis at a 54.7° with respect to the magnetic field B_0. Although the dipolar couplings do not normally affect the linewidth in solution NMR, their existence can be probed via the perturbation of one resonance and observing the intensity change of another. The perturbation usually involves saturation (equalising the spin population difference between different energy levels) or inversion (inverting the population difference) of the target resonance, Figure 10. Upon the perturbation of spin S, the magnitude of NOEs observed for spin I is expressed as the relative integral change:[98]

$$\eta_I\{S\} = {}^{(M - M_0)}/_{M_0} \times 100\% \qquad \textbf{Equation 6}$$

M is the signal integral of spin I in the presence of NOEs, and M_0 is the equilibrium integral in the absence of NOEs. Figure 11a shows example of the homonuclear and heteronuclear NOEs. The sign of NOE depends on the rate of molecular motions, which can be fast (small molecules in low-viscosity solvent) or slow (large molecules in high-viscosity solvent). The former displays positive enhancement while the latter gives negative enhancement. Figure 11b presents a simplified heteronuclear two-spin system (I = 1/2), with four energy levels and six possible transition probabilities represented by W_0, W_1, and W_2. The subscripts indicate the magnetic quantum number of the transitions. The four W_1 transition pathways involve a single-spin flip, e.g., $\alpha_A\alpha_X$ to $\alpha_A\beta_X$ represents a flip of spin X, contributing to observable NMR signals. The zero-quantum transition (W_0) and double-quantum transition (W_2) involve simultaneous flip of two spins, which cannot be directly observed due to the '*quantum mechanical selection rule'*. These two-spin flip transitions, however, are responsible for the NOEs and are referred to as cross-relaxation. When W_2 is dominant, the NOEs are positive; when W_0 is dominant, the NOEs are negative.

The sign of heteronuclear NOEs further depends on the gyromagnetic ratio of the cross-relaxing nuclei. For example, the NOEs from ^1H to ^{15}N or ^{29}Si, display negative enhancement. Depending on the NOEs magnitude, the $^{15}N\{^1H\}$ or $^{29}Si\{^1H\}$ signals can be attenuated, cancelled (disappearing from the spectrum) or negatively enhanced if full negative NOEs can be exploited. The magnitude of NOEs is sensitive to the internuclear distance r, being inversely proportional to the six powers of r (r^{-6}). It is this feature that empowers NOEs, more commonly proton-proton, a valuable tool for structural analysis of, for example, proteins and other molecules.

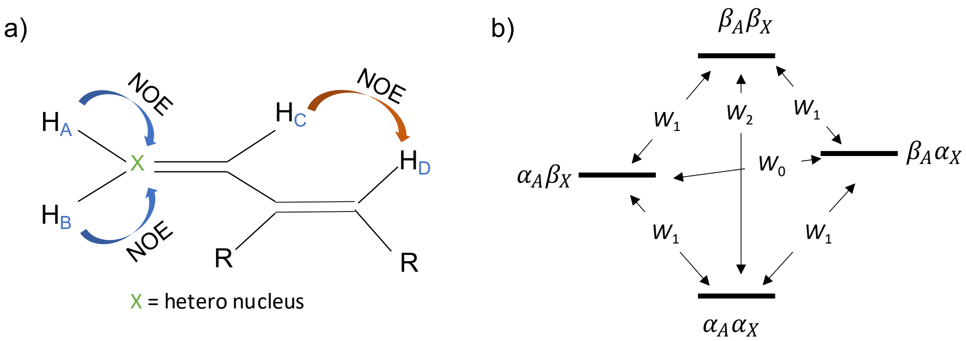

Figure 11. a) Schematic representation of homonuclear NOEs (orange arrow), and heteronuclear NOEs (blue arrows). b) Energy-level diagram for a heteronuclear two-spin system with $\gamma_A > \gamma_X$, showing the possible relaxation pathways.

The heteronuclear NOEs are occasionally employed to provide structural information.[99] Note the scheme for heteronuclear steady-state NOE measurement in Figure 10b, if broadband ^1H decoupling is applied during FID acquisition of spin X, then a sufficiently long delay must be adopted during transients to allow the site-specific NOEs to dissipate. Nowadays, heteronuclear NOEs are more routinely used as a means of sensitivity enhancements, by polarisation transfer from sensitive nuclei to insensitive nuclei, such as $^{13}C\{^1H\}$ spectra. There are a range of experiments that utilise the decoupler in different ways (Figure 12), they vary in the resultant spectra in terms of the existence of NOEs, removal of *J*-couplings, and whether reliable quantitation is achieved. It is necessary to distinguish them and confirm the desired outcome before one sets out to conduct an experiment. For instance, only inverse-gated $^{13}C\{^1H\}$ experiments[100] produce quantitative spectra providing the relaxation delay (RD) is sufficiently long to dissipate NOEs. Gated-decoupling method aims to utilise the NOEs and preserve the multiplicity information. Continuous decoupling and power-gated decoupling both display the NOEs and remove *J*-couplings and are not quantitative. The difference between them is that, power-gated decoupling applies a lower-power during the RD to alleviate the power output from the probe as well as to minimise the effect of sample heating.

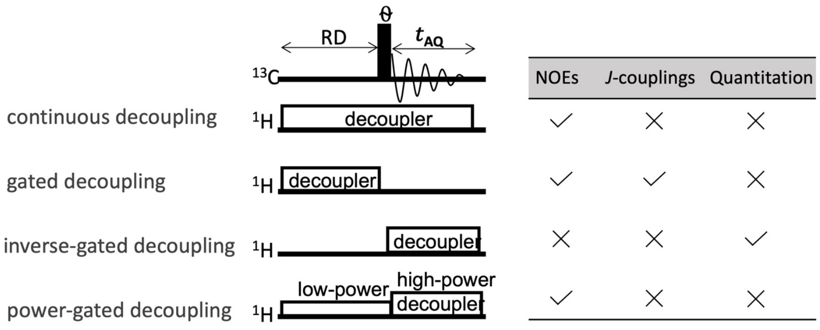

	NOEs	*J*-couplings	Quantitation
continuous decoupling	✓	✕	✕
gated decoupling	✓	✓	✕
inverse-gated decoupling	✕	✕	✓
power-gated decoupling	✓	✕	✕

Figure 12. Different decoupling manners for $^{13}C\{^1H\}$ experiments. The obtained spectra with respect to the enhancements from NOEs, multiplicity from *J*-couplings, and quantitation are listed on the right.

1.3.1 Theoretical Heteronuclear NOEs

In practice, to efficiently take advantage of the NOEs for sensitivity enhancement, ^{1}H is usually the optimal choice for the decoupled nucleus, owing to its ubiquity in molecules, high gyromagnetic ratio, and high natural abundance. The maximum enhancement factors are determined by $\eta = {\gamma_I}/{2\gamma_S}$, where γ_I and γ_S are the gyromagnetic ratios of the decoupled nucleus and the detected nucleus respectively. Table 1 presents the theoretical maximum NOE factors achievable by {^{1}H}-X experiments, X is the heteronucleus detected.

Table 1. The gyromagnetic ratio and natural isotopic abundance of some spin-half (I = 1/2) nuclei, and the maximum NOE factors achievable by ^{1}H-decoupling.

Nucleus	^{1}H	^{13}C	^{15}N	^{19}F	^{29}Si	^{31}P
γ / ×10^{7} rad·s^{-1}·T^{-1}	26.7	6.7	−2.7	25.2	−5.3	10.8
Natural abundance / %	99.99	1.11	0.37	100	4.67	100
η_{max} ({^{1}H})	--	2.0	−4.9	0.5	−2.5	1.2

In other situations, for example, {^{31}P}^{1}H experiments, the maximum NOEs factor is

$$\eta = {\gamma_{31_P}}\Big/{2\gamma_{1_H}} = 0.20$$

For {^{13}C}^{1}H experiments, the maximum NOEs factor is

$$\eta = {\gamma_{13_C}}\Big/{2\gamma_{1_H}} = 0.125$$

If the sample has natural abundance ^{13}C, the enhancement will further reduce to

$$\eta = 0.125 \times 1.11\% = 0.0014$$

This enhancement is normally negligible. Therefore, the major advantage of heteronuclear decoupling here would be to remove the ^{13}C couplings for a cleaner spectrum, or to reveal small peaks that are overlapped with ^{13}C satellites. To generate ^{13}C satellite-free ^{1}H spectra, an alternative method termed DISPEL[101] (Destruction of Interfering Satellite by Perfect Echo Low-pass filtration) is available to supress one bond ^{13}C satellites without the need of broadband heteronuclear decoupling.

1.3.2 Decoupling Schemes for Heteronuclear Decoupling

The significance of spin decoupling for NMR spectroscopy cannot be overvalued. It affords two benefits that are always sought-after in NMR experiments, the resolution, and the sensitivity. The development of decoupling is closely associated with the history of NMR spectroscopy. Before the introduction of Fourier Transform (FT) NMR[30], the theory of continuous wave (CW) decoupling was developed[102] (Figure 13a). It introduced the idea of collapsing *J*-couplings by irradiating a scalar-coupled spin species with a strong CW radio frequency. The intensities of a multiplet are coalesced into a narrow singlet, leading to better sensitivity which could be further enhanced by NOEs. This CW decoupling approach, however, normally requires excessive radio frequency power level which renders it impractical. A more effective scheme for heteronuclear decoupling, commonly on proton frequencies, was proposed by Richard Ernst[103]. Noise decoupling (Figure 13b) utilised a random-phase decoupler that serves to scramble the α and β states of the decoupled spins. It remained the primary decoupling method for over a decade until the introduction of spin flip decoupling[104,105] (Figure 13c). Spin flip decoupling established on the theory that, for a scalar-coupled spin IS system, if spins I are continuously inverted at a rate fast compared with the coupling constant J_{IS}, then the heteronuclear couplings are refocused and do not split spins S. Simple 180° inversion pulses are sensitive to off-resonance effects and pulse imperfections, the accumulative errors from periodically applied 180° pulses could be significant. Therefore, by replacing the single inversion pulses with composite pulse clusters led to improved composite pulse decoupling[106] (CPD), a technique that has been widely employed up till today (Figure 13d and 13e). The inversion imperfections could further be improved by the introduction of supercycles[107]. This produced a family of supercycle CPD sequence such as MLEV16[108], named after the author, and WALTZ16[109], providing minimum residual splitting hence regularly used for ^{1}H decoupling. When decoupling nuclei with larger chemical shift range, for example ^{13}C or ^{15}N, it is more suitable to use computational optimisation schemes such as GARP[110] (Globally-optimised, Alternating-phase, Rectangular Pulses). There are numerous CPD sequences available today, some commonly applied schemes and their effective decoupling bandwidths, general applications are listed in Table 2.

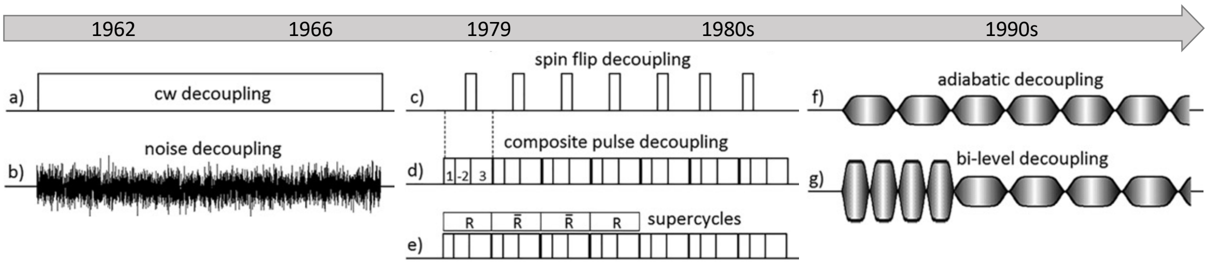

Figure 13. Schematic representation of the development of broadband decoupling in NMR spectroscopy. This figure is reconstructed from the publication by Ēriks Kupče.[111]

Table 2. Selective examples of composite pulse decoupling schemes for broadband decoupling.[112]

Scheme	Bandwidth ($\gamma B_2/2\pi$)	Applications
continuous wave[102]	<0.1	selective decoupling only
MLEV16[108]	1.5	^{1}H
WALTZ16[109]	2(1.8)	high-resolution ^{1}H
DIPSI2[113]	1.2	very high-resolution ^{1}H*
GARP[110]	4.8	X-nucleus
Adiabatic	>20	broadband uniform decoupling

*DIPSI can also be used as a mixing sequence, typically in TOCSY experiment.

The demand for increasing decoupling bandwidths arose, particularly with the advent of inverse detection 2D NMR experiments. The 1980s witnessed a booming growth of 2D NMR, Figure 14. Proton-detected heteronuclear shift correlation experiments such as HSQC (Heteronuclear Single Quantum Correlation) and HMBC (Heteronuclear Multiple-Bond Correlation), usually entail decoupling of ^{13}C. At the same time, spectrometers of higher and higher magnetic field strength became available, leading to increasing chemical shift dispersion. These advancements posed a challenge, that the radiofrequency power to reach required decoupling became much higher than the conventional proton decoupling. Excessive power could lead to sample heating that causes temperature fluctuations within the sample and deteriorates the spectral quality, or even worse, damages the cryogenic probes. Adiabatic broadband decoupling[114–116] proved to use the RF power more effectively (Figure 13f, Table 2) and minimise the RF power leakage. It replaced the composite inversion pulses employed in CPD schemes with adiabatic pulses. Supercycles were also used to compensate for inversion imperfections, as for the CPD. Intriguingly, the first application of adiabatic decoupling[117] was reported in 1979, the same year as the proposal of spin-flip decoupling. However, unlike the continuous developments of CPD schemes, the widespread experimental implementation of adiabatic decoupling was realised until 1995 and has become an indispensable tool afterwards[111]. A range of adiabatic pulses are available, such as WURST[118] (Wideband, Uniform-Rate Smooth Truncation) and Chirp[119] pulses. One advantage of adiabatic decoupling is that the decoupling bandwidth, the adiabatic pulse duration, and adiabatic factor can all be tailored for specific requirements. One disadvantage, however, is the accompanied cycling sidebands. A modification in the decoupling scheme, called bi-level adiabatic decoupling[120] (Figure 13g), could alleviate this unwelcome phenomenon. This is achieved by introducing a brief high-power level before the scheme. As a result, adiabatic decoupling became particularly important for the decoupling of X-nuclei at higher magnetic fields. They have also been used for accurate quantification of $^{13}C\{^{1}H\}$ spectra[121] and $^{1}H\{^{13}C\}$ spectra[122].

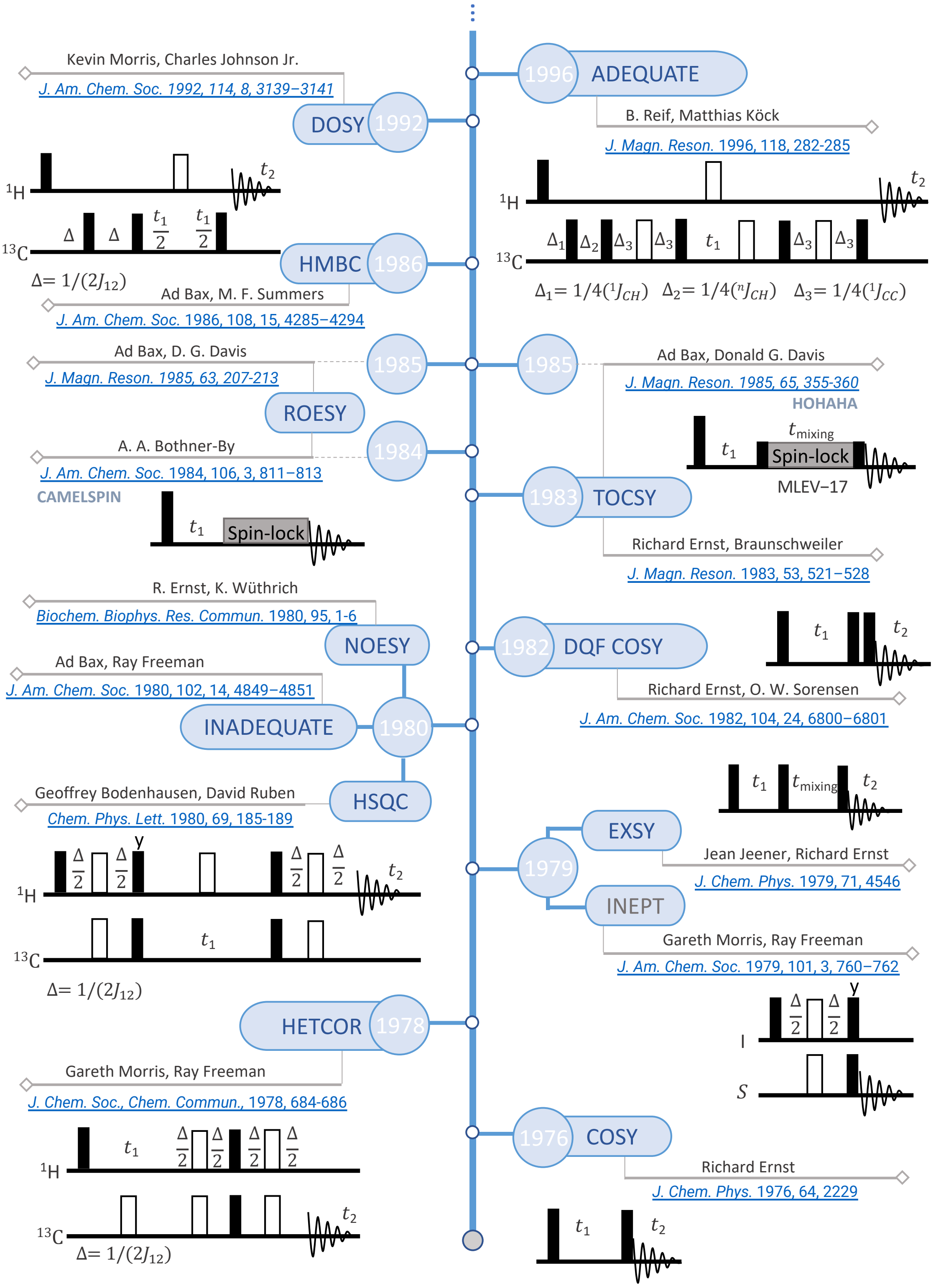

Figure 14. The history of 2D NMR, with some examples shown chronologically from bottom to top. The thriving of 2D NMR has stimulated the development of adiabatic pulses. Note INEPT[123] is not a multi-dimensional experiment. However, considering its importance as a building block for many other heteronuclear shift correlation experiments, it was included here.

1.4 ^{19}F NMR

1.4.1 Fluorine in Organic Chemistry

Before discussing in detail the NMR studies of ^{19}F, it is reasonable to briefly introduce the evolvement of fluorine in organic chemistry. The role that fluorine plays in chemistry has tremendously progressed. Among multiple reasons for its prosperity, one is the combination of its intrinsic properties including the relatively small size, high electronegativity, strong covalent bonding, and single valency[124]. The presence of fluorine has proved to have a profound influence on the physical properties and chemical reactivities of molecules comparing to their nonfluorinated analogues. For instance, the electron-withdrawing nature of fluorine attenuates the pK_a value of neighbouring functional groups[125], thus the acidity of a wide range of organic compounds can be effectively tuned by substituent fluorine atoms, with an additive effect from multiple fluorine substitutions. Modulation in pK_a values further exerts influences on physicochemical properties such as binding affinity, increased membrane penetration[126] and lipophilicity[127], which are advantageous to drug design. As a consequence, fluorine reaches beyond organic synthesis and also prevails in pharmaceuticals[128–130] and agrochemicals[131,132]. As a matter of fact, it was estimated that in 2010 up to 20% of administered drugs were fluorine-containing and the proportion has increased to approximately 30% in recent years[133], marking a pivotal contribution to health care. The proportion of fluorinated agrochemicals was even larger, taking >50% of all active agrochemicals[134]. These demands promoted fluorine chemistry one of the most active fields of organic chemistry.

Despite the longstanding interest and the fact that fluorine ranks the 13th most abundant element on Earth's crust, there are only very few natural products that contain fluorine, therefore the vast demand of fluorinated compounds largely relies on manual synthesis. Since the first reported fluoride replacement of halogens in 1863[135], and more recent breakthrough developments such as DAST[136] and Selectfluor[137], a broad array of fluorination methods have emerged and made various fluorinated compounds commercially available in the current market. Figure 15 displays some of these representative strategies that employ fluorine as electrophilic[138–141], nucleophilic[142–145], and chiral[146–150] reagents. Considering the many benefits and potentials from fluorine incorporation, it is fair to envision its enduring popularity and importance in organic chemistry, medicinal chemistry, and extended areas.

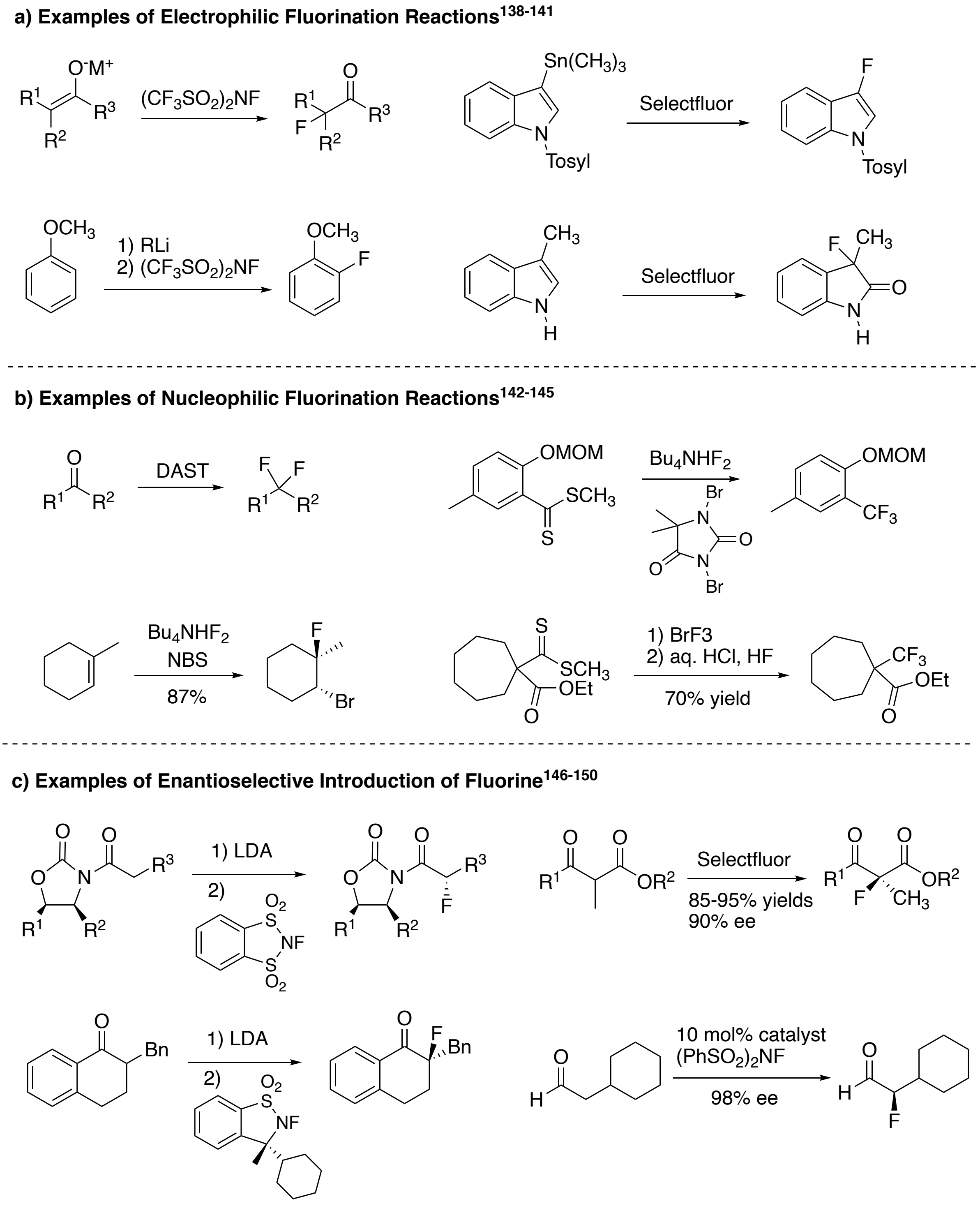

a) Examples of Electrophilic Fluorination Reactions[138-141]

b) Examples of Nucleophilic Fluorination Reactions[142-145]

c) Examples of Enantioselective Introduction of Fluorine[146-150]

Figure 15. Examples of fluorination reactions, utilising fluorinated compounds as a) electrophilic[138–141], b) nucleophilic[142–145], and c) chiral reagents respectively[146–150].

1.4.2 NMR Studies of Fluorine

Following its significance in synthesis, two main factors have contributed to the growing popularity of fluorine NMR. The first one is the advancements of modern spectrometers. Increasingly available low-field benchtop spectrometers[151] equipped with rare-earth permanent magnets have redrawn interests, owing to their low cost, easy maintenance and flexibility location-wise. The reduced sensitivity at low fields is sidestepped by the favourable nuclear properties of ^{19}F nucleus, thereby making ^{19}F NMR experiments preferably suitable for benchtop instruments. On the other side, developments in high-field cryoprobe spectrometers introduced probes that allow simultaneous tuning to ^{1}H, ^{19}F or/and X nuclei, where X could be any NMR-active nuclei. Switching between single-tune and dual-tune is no longer rare in commercially available high-resolution probes today. Battiste and Newmark[152] have comprehensively detailed the ^{19}F multidimensional experiments that can be performed on modern spectrometers. Another attractive technology is the advent of multiple receivers, this feature enables the direct and parallel detection of different nuclei species[153], or one nucleus being detected during the relaxation or decoupling of the other. Apart from the straightforward time-savings and increased throughput, these experiments are compatible with other fast NMR techniques for further enhancement in efficiency. Kovacs and Kupče[154] illustrated the versatility and productivity of this multi-receiver system, adapting to a broad range of routinely used 2D ^{1}H and ^{19}F experiments. Given the advantages of ^{19}F in organic chemistry as well as in NMR studies, this project will heavily focus on fluorine-involving reaction studies.

Fluorine as a nucleus for NMR has its favourable nuclear properties, including the 100% natural abundance, high gyromagnetic ratio at ~94% of that of proton, ½ spin, and significantly wide chemical shift dispersion. These properties translate into fluorine nucleus's intrinsically high sensitivity, similar coupling manner as that of proton and carbon, and strong dipolar interactions. The strong ^{19}F-^{19}F homonuclear and ^{19}F-^{1}H heteronuclear NOEs can be employed to aid structural studies[155] and CIDNP (Chemically Induced Dynamic Nuclear Polarisation) experiments[156], which was proved to create a 20- to 40-fold ^{19}F hyperpolarisation for sensitivity enhancement.[157] Fluorine nucleus is also exquisitely responsive to its surrounding local environment changes, leading to a wide chemical shift span up to 700 ppm (>350 ppm for organofluorine compounds), an almost 70-fold increase comparing to that of a proton nucleus. This wide signal dispersion, as mentioned earlier, makes fluorine NMR particularly attractive to low-field benchtop NMR spectrometers[158], for which low-resolution and low-sensitivity are commonly the major limitations. This large chemical shift dispersion of fluorine has been utilised for conformational and dynamic studies[159], where the extra motional timescales in lineshape and T_2 relaxation studies could effectively afford the detection of very subtle conformational changes. In contrast to the ubiquity of ^{1}H and ^{13}C in molecules, limited appearance of ^{19}F underlines that ^{19}F spectra are much less likely to suffer overlap troubles and provide an ideal tool for the studies of complex mixtures. Indirect utilisation of ^{19}F in mixture analysis was also possible using isotope-editing[160]. It simplifies overcrowded ^{1}H spectrum by showing only those protons that are coupled to fluorine of interest.

Moreover, in ^{19}F NMR experiments, non-deuterated solvents can be used without the concern of overwhelming solvent signals, owing to the absence of fluorine signals from non-fluorinated solvents. This could substantially reduce the running cost for kinetic studies using flow NMR and stopped-flow NMR, when large amount of sample is used. Figure 16 presents an example of the stopped-flow *in-situ* monitoring of the azole-catalysed acylation. In the ^{1}H spectrum, the methyl-proton of the product was overshadowed by the dominant solvent signal of CH_3CN (Figure 16a). Solvent suppression schemes were not viable as it would destroy the signal of interest, the use of deuterated solvent was not practical either considering the cost. Therefore, one strategy to this problem is to introduce ^{19}F-labelling, providing the label does not interfere with the reaction kinetics of interest. Normally *para*-F-C_6H_4 and *para*-CF_3-C_6H_4 groups can be used as ^{19}F labels, so that the label is not very close to the reaction centre. Owing to the large dispersion of fluorine chemical shift and its high sensitivity towards environment, resonances of different reaction components are less likely to overlap, therefore the reaction can be conveniently followed by ^{19}F NMR experiments (Figure 16b).

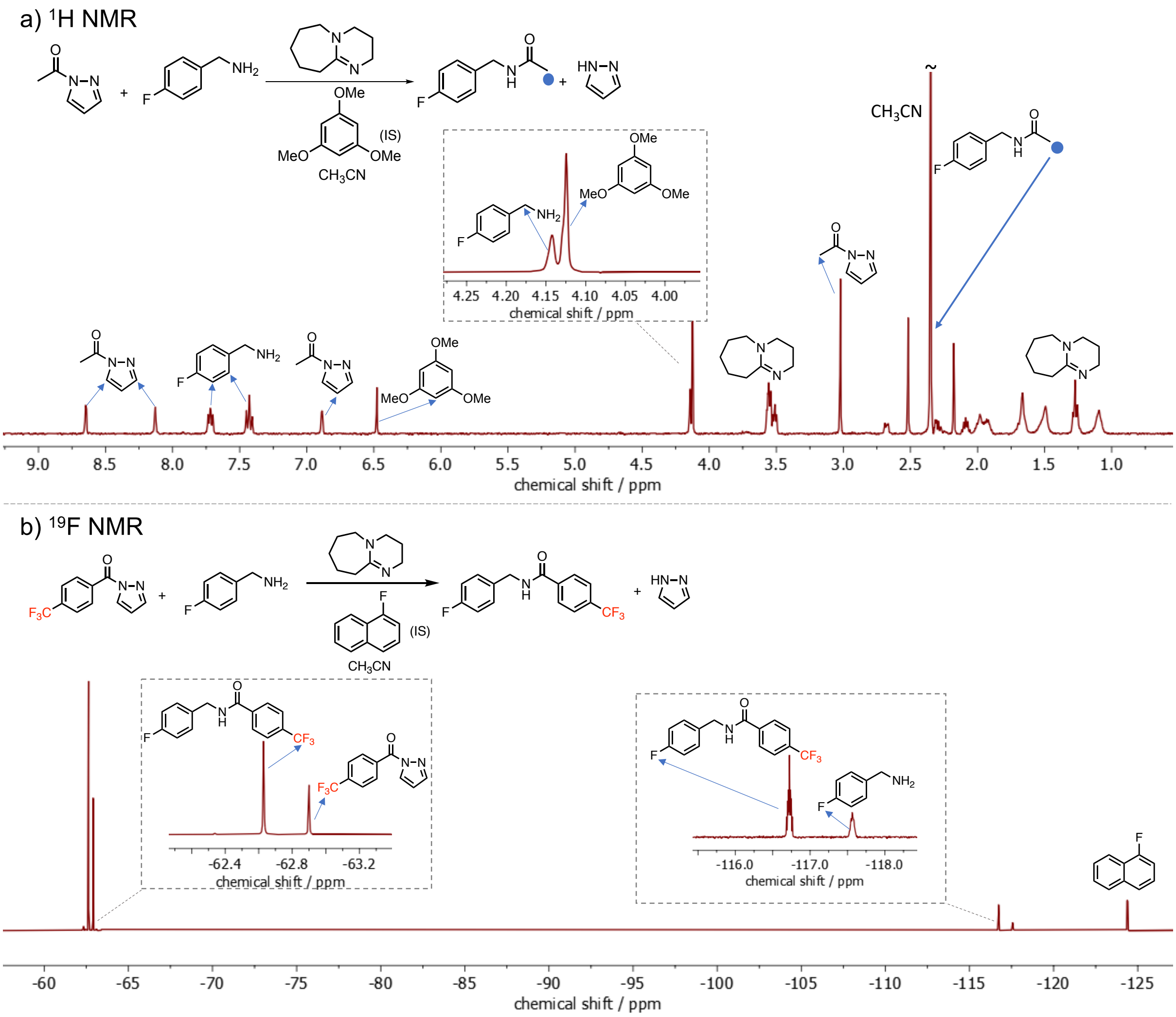

Figure 16. a) A transient ^{1}H NMR spectrum to monitor the azole-catalysed acylation, note the blue labelled methyl proton covered by the strong CH_3CN solvent signal, making it impossible to follow. b) A transient ^{19}F NMR spectrum to monitor the reaction by introducing ^{19}F labelling (p-CF_3-C_6H_4), all signals are well-resolved.

Besides the advantages brought about by the fluorine NMR, challenges also come along in the context of quantitative NMR (qNMR) measurements. The broad fluorine chemical shift range suggests that, in addition to the routine procedures for quantitative experiments[161,162], a higher requirement for uniform broadband excitation throughout the whole spectral width is needed. High-powered hard pulses, or amplitude-modulated pulses, are the most straightforward and frequently-used pulses in NMR experiments. However, they have limitations. For example, given the RF power limitations of the spectrometer hardware, a traditional 90° hard pulse can hardly afford the full coverage of a typical ^{19}F spectral window at >100 kHz, i.e. a 200 ppm range on a 500 MHz (^{1}H) spectrometer. Strictly speaking, a simple 90° hard pulse offers a relatively narrow bandwidth excitation of about 20 kHz, in the sense of accurate (±1-2%) quantification[163]. Figure 17a presents an example of non-uniform excitation delivered by conventional 90º pulse leading to signal amplitude losses at edges of the spectrum. This attenuation could cause serious off-resonance effects and inaccurate signal integrations. In addition, hard pulses are sensitive to B_1 inhomogeneities which could lead to variable flip angles across the active volume and cause phase errors.

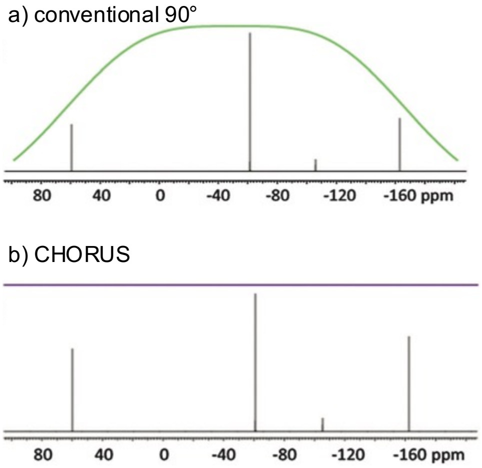

Figure 17. ^{19}F NMR spectra showing the inconsistent signal intensities acquired by (a) simple 90° pulse excitation and (b) CHORUS. Imposed green and purple lines represent simulated excitation profiles respectively. This figure was adapted from publication[163].

To circumvent the B_1 variations and off-resonance effects, a handful of measures can be employed experimentally. A convenient approach is when the resonances of interest are close enough to one another in the spectrum, the transmitter resonance can then be simply placed at the centre of the peaks. Second, when peaks are far apart, the wide spectral window can be divided into smaller regions, and multiple spectra are acquired with each acquisition covering a different region. However, this is cumbersome and poses potential instrumental and data processing errors. In practice, a smaller excitation pulse angle, or equivalently shorter pulse duration, is able to sweep a broader bandwidth uniformly without increasing the RF power amplitude, as for a given RF power the excitation bandwidth, $\Delta\omega$, is inversely proportional to its duration, τ_p. This method is useful and easy to operate when sensitivity is not a main constraint. Alternatively, specialised pulses can be employed in place of conventional hard pulses. As discussed in section for heteronuclear decoupling, one of the methods to improve excitation performance is also to use composite pulses which consist of a cluster of hard pulses with different flips angles and phases. Another approach which offers greater tolerance toward B_1 variations and off-resonance effects is to employ adiabatic pulses, also known as frequency-swept pulses.[164] For example, an adiabatic triple-pulse excitation scheme termed CHORUS (CHirped, ORdered pulses for Ultra-broadband Spectroscopy)[163,165] was developed to provide very broad excitation of more than 0.5 MHz, i.e. a 1000 ppm coverage on a 500 MHz spectrometer, with uniform amplitudes and phases (Figure 17b). Noteworthily, adiabatic pulses have one downside which is their longer pulse durations, typically from 0.5 milliseconds to 2 milliseconds, much longer than their hard pulse counterparts (a few microseconds). These long pulses are not suitable for systems with significant homonuclear scalar coupling or spins with rapid transverse relaxation. The *J*-modulation during the excitation pulse could lead to phase distortions and reduced integrations. An optimised sequence[165] attempted to mitigate this limitation by compressing the duration of the original CHORUS sequence, or more recently, by the combination of perfect echo and CHORUS[166], to allow this approach more robust in strong homonuclear coupling systems. Figure 18 has experimentally demonstrated the off-resonance effects from conventional hard pulses on quantification, while CHORUS was able to excite a wide frequency range uniformly. Despite the implementation of adiabatic pulses normally requires manual parameter adjustments, they have proved functional in challenging systems and promoted the continuous developments of NMR experiments on X-nucleus. Throughout this work, ^{19}F NMR was utilised for reaction monitoring on a 9.4 T spectrometer, and NMR experimental parameters such as the radiofrequency offset and spectral width were carefully considered to ensure accurate quantitation.

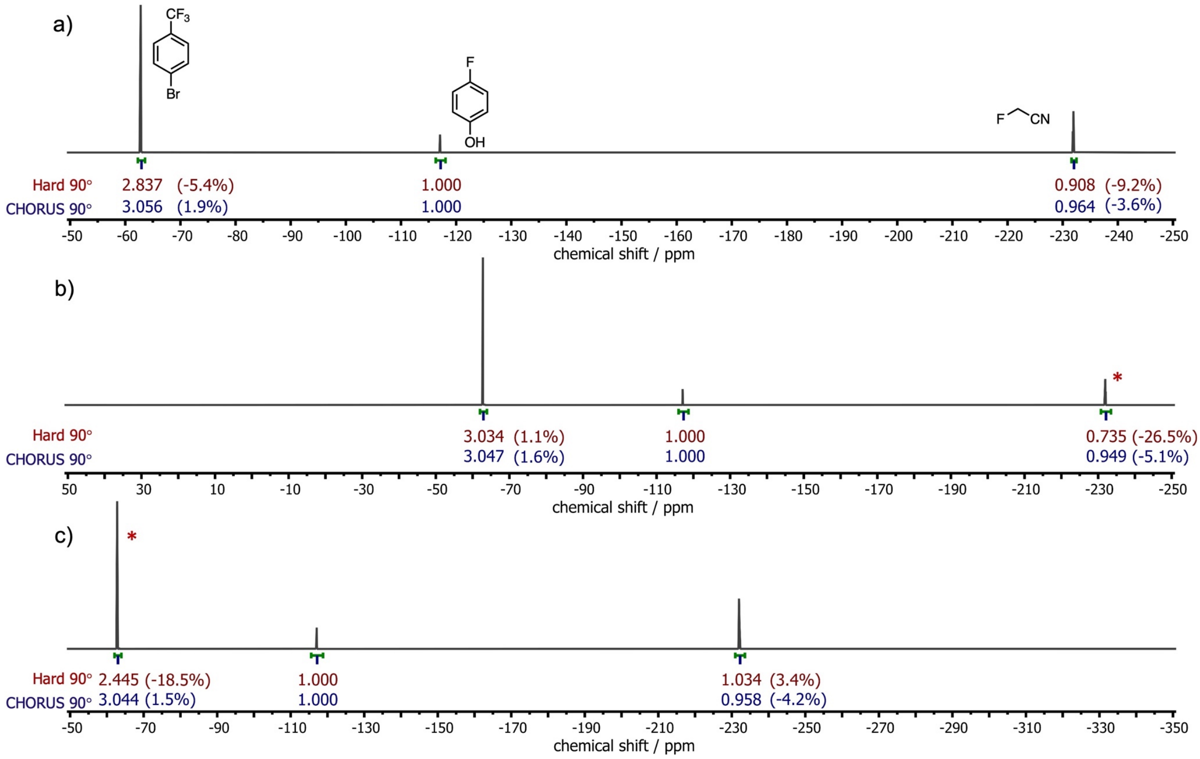

Figure 18. ^{19}F NMR spectra of a mixture sample of 4-bromobenzotrifluoride, 4-fluorophenol and fluoroacetonitrile in the ratio of 1:1:1 in $CDCl_3$. The transmitter offset (in ppm) was set to a) -150 ppm; b) -100 ppm; c) -200 ppm. Maroon integrals were measured by hard 90º pulses, navy integrals were measured by CHORUS 90º pulses. Note the asterisk-labelled signals that showed significantly attenuated integrals.

1.5 Aims and Objectives

This project aims to develop new stopped-flow technique, in collaboration with NMR spectroscopy, ultimately to facilitate the mechanistic elucidation of chemical reactions. Current investigations in very fast irreversible reactions rely mostly upon an ex-situ quenching manner, which requires repeated preparation of aliquots and a sufficient record of individual reactions with incremented reaction time. This traditional approach firstly is labour-intensive, secondly requires large amount of sample, which sometimes renders it unfeasible for valuable materials. Additionally, ex-situ monitoring suffers from the loss of short-living transients or intermediates information, the manually-repetitive feature also poses accumulative data interpretation errors. Therefore, the state-of-the-art stopped-flow NMR instrument studied in this project prospects to offer a unique tool to break through the speed-limit of in-situ reaction monitoring. It enables the investigation of very fast irreversible chemical reactions in the timescale of milliseconds, which are otherwise impossible by traditional NMR experiments. On the other hand, NMR has early established its capabilities in chemical exchange studies. However, these experiments are mostly exclusive for equilibrium systems, as described in section 1.1.1. An alternative approach to study chemical exchange is isotopic substitution, where the isotopically substituted labels can be tracked during the course of a reaction to give information on the underlying reaction mechanism. Nevertheless, the synthetic procedures for the installation of isotopic labels can be expensive and laborious. The stopped-flow instrument studied here has four dedicated input channels, three of which pre-magnetised and one not pre-magnetised. By utilising this feature, the spins can be '*magnetically-labelled*' rather than '*isotopically-labelled*', if inputted via the non-pre-magnetised channel. Tracking the evolution of this label in a reactant, intermediate or product is expected to allow deductions to be made about the reaction mechanism.

During the progress of the project, reaction monitoring constituted a considerable proportion of the work. The frequent requirement for T_1 measurements led to an unexpected route – the development of T_1 measurement experiments. As mentioned in section 1.2, T_1 plays an important role in quantitative NMR experiments. There is large motivation in accelerating the process of T_1 measurement compared to the currently used methods (section 1.2.1). Consequently, a sub-task of this project aims to develop rapid T_1 measurement experiments. These methods are anticipated to save spectrometer time in routine T_1 measurement, which in turn could be more productively used, for example, in attaining improved sensitivity in the experiment of interest. Therefore, a list of objectives is detailed as follow, to achieve the aims outlined above.

1. Assimilate the details and operating principles of the stopped-flow equipment.
2. Evaluate the parameters of the stopped-flow equipment, including the pre-magnetisation levels of the three input channels with pre-magnetisation coils and the one input channel without pre-magnetisation coil.
3. Determine the appropriate rapid reaction systems to test the capability of the stopped-flow NMR system.
4. Monitor fast irreversible reactions in the order of milliseconds; and exploit the potential of the stopped-flow NMR instrument by using interleaved approach for monitoring very fast irreversible reactions.
5. Utilise the non-pre-magnetised input channel for short-living chemical exchange studies which are otherwise challenging via traditional methods.
6. Develop new T_1 measurement experiments that are faster compared to the currently available T_1 measurement methods.
7. Optimise the new T_1 methods, particularly for the measurements of heteronuclei which are intrinsically insensitive and take long experimental time.

Chapter 2 Stopped-flow NMR

2.1 Stopped-flow Instrument Studies

2.1.1 General Design Characteristics

The use of an in-house built stopped-flow instrument was encouraged by previous studies in the Lloyd-Jones group[167,168]. A wide range of base-mediated protodeboronation of boronic acids have been investigated in detail. Some examples are shown in Figure 19.

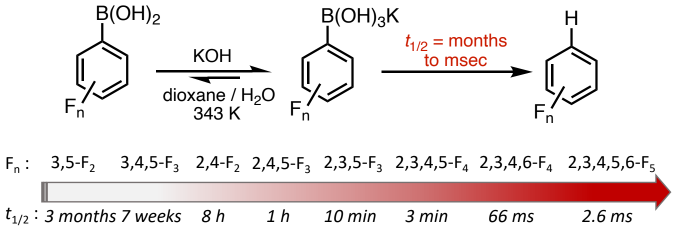

Figure 19. Examples of base-catalysed protodeboronation of polyfluorophenyl boronic acids, with half-lives ranging from months to milliseconds[168].

The half-lives, $t_{1/2}$, of these reactions span from 3 months (3,5-difluorophenylboronate) to 2.6 milliseconds (2,3,4,5,6-pentafluorophenylboronate) at 343 K and pH ≥ 13. Reactions that proceed *slowly*, for example, with $t_{1/2}$ on the order of minutes or more, can be analysed via routine static NMR experiments. However, reactions that proceed *fast* pose challenges to traditional NMR methods as valuable information would have been gone before measurements occur. These *fast* reactions therefore would require specialised technique, in this case, a custom-built stopped-flow insert (Figure 20). Over recent years, this stopped-flow instrument has been optimised to facilitate the studies on the mechanism of CF_3 transfer from $TMSCF_3$[169], CF_2 generation[170], and arene C–H silylation by $TMSCF_3$[171]. To fully exploit the potential of this technique for quantitative and accurate *in-situ* kinetic analysis of very *fast* chemical reactions, this work began with exploring the detailed physical and NMR parameters of this stopped-flow instrument.

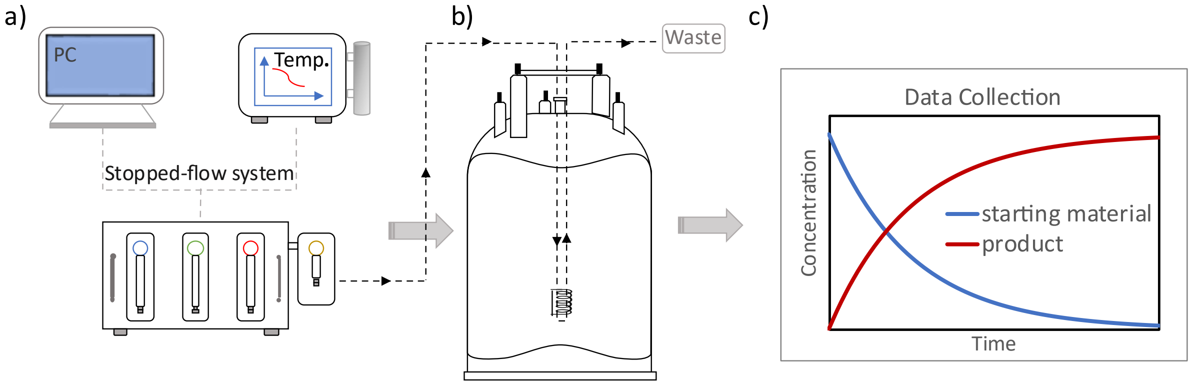

Figure 20. Graphic representation of the stopped-flow system. a) Pump station with four syringes (3 solution syringes and 1 solvent syringe) controlled by programmed computer and an external thermostatic re-circulator; b) standard NMR spectrometer that hosts the stopped-flow capillary cell for measurements; c) rapid data collection achieved.

There are a few distinct features between the stopped-flow technique discussed herein (Figure 21b) and the conventional design (Figure 21a). One major difference is, in contrast to custom-built stopped-flow NMR probes, the system here is inserted directly into a standard NMR probe head. The use of three independent drive solution syringes allows systematic variation in reagent concentrations, using a single set of stock solutions (*A*, *B*, *C*). The use of computer-controlled drives allows the flow to be stopped by the resistance present in the open-ended circuit ('waste' in Figure 21b) after arresting the movement of the drives. The trigger signal is programmed and sent to the NMR console from the syringe drive unit, rather than from a microswitch on a stop syringe. This configuration reduces the acute pressure and flow oscillations induced by the 'hard stop' of a classic stop-syringe (Figure 21a). The total delivery volume is not constrained by the volume of the stop-syringe either. Furthermore, the programmed trigger allows accurate control of the delay time between the shot and data acquisition, therefore facilitating interleaved stopped-flow experiments. This aspect will be further discussed in section 2.2.3. Thermostatting is achieved by two independent thermostatic systems. An auxiliary system is coupled to the stopped-flow umbilical, providing thermostatting to the pre-magnetisation, mixing, and sample transport stages. For the auxiliary system here an aqueous ethylene glycol heat transfer medium is used, and a Pt100 temperature probe located close to the mixer to pre-calibrate the auxiliary system to be within ± 0.5 K of the spectrometer thermostat. After delivery of the nascent reaction solutions to the NMR flow-cell, gas flow (dry air or N_2) from standard NMR spectrometers is used to stabilise the temperature of analyte solutions.

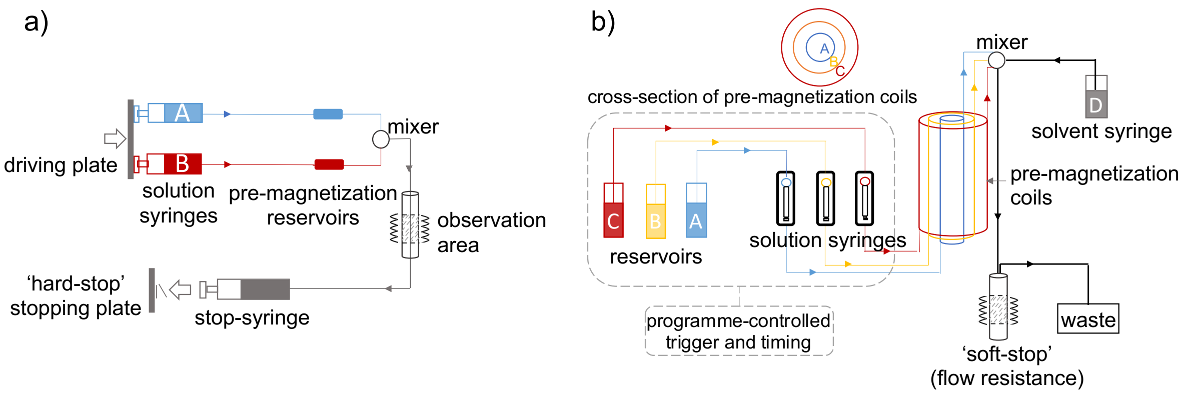

Figure 21. Schematic representations of a) classical dual-input 'hard-stop' stopped-flow apparatus, and b) variable-ratio triple input 'soft-stop' stopped-flow apparatus. Reagents from syringes A, B, and C travel through pre-magnetisation coils close to probe in an upward spiral manner; the analytes then reach a mixer before entering the glass capillary tube inserted inside an NMR probe. Syringe D denotes the solvent input, with no pre-magnetisation available.Reactant nuclei are polarised in pre-magnetisation reservoirs placed immediately before the mixer. Unlike custom-built stopped-flow probes, the stopped-flow insert cannot provide 100% pre-magnetisation. Rather, in general >90% pre-magnetisation can be achieved under certain delivered volumes. This phenomenon will be discussed in detail in the succeeding section. Upon injection, pre-magnetised reactants travel to the mixer, efficient mixing is achieved by a sufficiently high flow-rate to generate turbulence, which is required to initiate the reaction with a clearly defined starting point. Flow rates ranging from 0.2 mL/s to 2 mL/s are available, resulting in dead-times ranging from 0.75 to 0.075 seconds, respectively. Details on the mixing efficiency measurements and thermostat evaluation were conducted by collaborators and can be found in our recent publication[64]. The flow is also used to purge the previous contents from the sample cell and replace it with the nascent reaction mixture. It was determined that a total volume of ≥ 600 μL is necessary to fully displace the previous sample and refill the 3 mm outer-diameter 180 μL capacity glass flow-cell primed for NMR measurements. The capacity of the flow-cell in the detection region of the NMR receiver coil is approximately 93 μL. This results in advantages and disadvantages, the former being a reduced volume of precious samples, the latter being an approximately 3-fold lower S/N compared to a normal 5 mm NMR tube. Nevertheless, since the stopped-flow insert is compatible with standard NMR probes, the sensitivity loss can be compensated for by the use of highly-sensitive He or N_2 cryoprobes.

2.1.2 Pre-magnetisation Profiles

The use of pre-magnetisation reservoirs originates from the necessity to establish a Boltzmann distribution before NMR experiments. Radiofrequency (RF) pulses are applied at a direction perpendicular to the external magnetic field B_0 and disturb this distribution. The relaxation of the excited spins back to equilibrium gives rise to the NMR signals. In the absence of Boltzmann distribution, spins are NMR-*invisible*. In conventional NMR spectroscopy, this Boltzmann distribution of spin populations is developed in the analyte solution in the probe-head at the centre of the magnetic field (B_0) of the spectrometer. Whilst it takes significant time for the spins to develop their initial Boltzmann distribution (99.3% equilibration requires $5\times T_1$), in routine NMR spectroscopy this 'pre-magnetisation' process occurs during the pre-acquisition processes such as locking, shimming, and tuning, after the sample tube has been inserted into the spectrometer. In stopped-flow NMR, however, these pre-acquisition processes are performed on *'old'* reagents, and *'fresh'* reagents need to be injected each time for detection. Therefore, it is important to make sure the *'fresh'* reagents are pre-magnetised before measurements. Failure to achieve this will result in incorrect kinetic analysis. We explored this phenomenon to highlight the significance of pre-magnetisation prior to stopped-flow NMR experiments. Figure 22 rationalises this process using simulated first order processes ('reactant A' → 'product B').

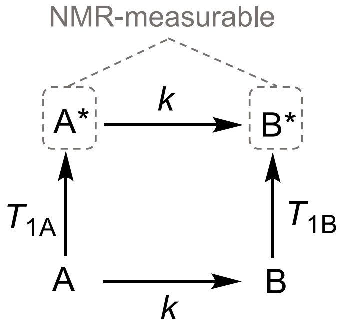

Figure 22. NMR experiments on a first order reaction A → B, without pre-magnetisation. Vertical arrows represent the magnetisation of studied spins by the magnet, horizontal arrows represent the reaction. T_{1A} and T_{1B} are the longitudinal relaxation time constants of reactant A and product B respectively, *k* is the reaction rate constant. A and B without asterisk represent spins not magnetised, i.e., not NMR-measurable. A* and B* represent magnetised spins and are NMR-measurable.

A*, B* represent samples that are fully magnetised before the applications of radiofrequency pulses. Therefore, the measured signals (A*, B*) directly reflect the reaction profiles (Figure 23, solid lines). On the contrary, without pre-magnetisation, the studied species go through two processes, one is the magnetisation, governed by the longitudinal relaxation time constant T_1;

the other is the reaction itself, governed by the reaction rate constant k. The concentrations of reactant A and product B at time t follow the equations:

$$[A]_t = [A]_0 \times e^{-kt} \qquad \textbf{Equation 7}$$

$$[B]_t = [A]_0 \times [1 - e^{-kt}] \qquad \textbf{Equation 8}$$

The magnetisation of A and B both follow the longitudinal relaxation recovery:

$$M_t = M_0 \times \left[1 - e^{-t/T_1}\right] \qquad \textbf{Equation 9}$$

Since only the magnetised spins are NMR-visible, the measured reactant concentration is calculated from:

$$[A^*]_t = [A]_0 \times e^{-kt} \times \left[1 - e^{-t/T_{1A}}\right] \qquad \textbf{Equation 10}$$

This is a multiplication of two first-order processes, the decay due to the reaction, and the rise due to the relaxation. Similarly, the measured product signal B* is attributed to two sources, one is the continuous magnetisation of the un-pre-magnetised product B, which is produced by the un-pre-magnetised reactant A. The other is produced from the pre-magnetised reactant A*. Therefore, the measured product concentration is calculated from:

$$[B^*]_t = [A]_0[1 - e^{-kt}] \times \left\{\left[1 - e^{-t/T_{1A}}\right] \times e^{-kt} + \left[1 - e^{-t/T_{1B}}\right]\right\} \qquad \textbf{Equation 11}$$

Following these equations, the reaction profiles can be simulated. The dashed lines in Figure 23 show the apparent concentrations that would be determined based on the NMR signal intensities when the reaction is initiated without pre-magnetisation of spins, indicative of an erroneous analysis. When the reaction rate substantially exceeds the relaxation rates of the studied spins (e.g., Figure 23b) the NMR signal for the reactant can hardly be detected as it is consumed more rapidly than it is magnetised (see inset). Moreover, the NMR signal for the product (Figure 23b, yellow dashed line) predominantly reflects the magnetisation process, rather than the change in concentrations due to the chemical reaction of interest.

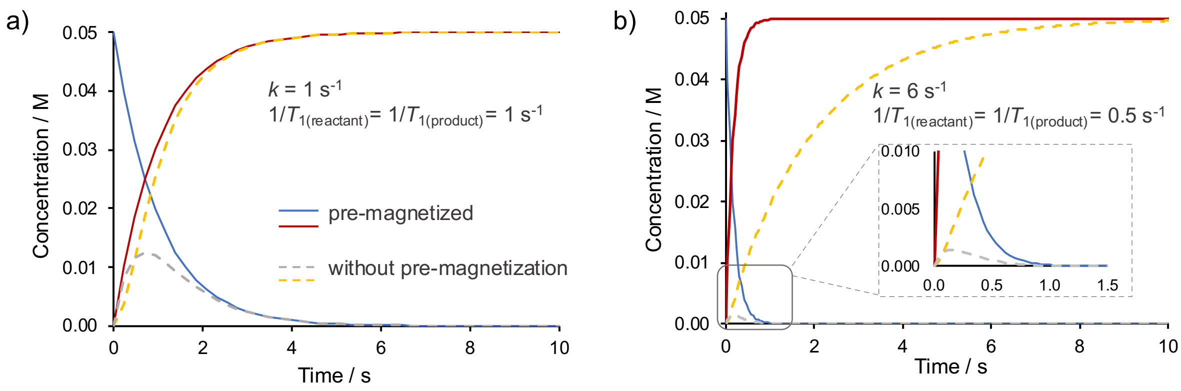

Figure 23. a) A simulated first-order reaction profile (reactant → product) showing the difference between the real concentrations (solid lines) versus those determined from the intensity of NMR signals arising from non-pre-magnetised reactants (dashed lines), when the reaction rate (k) is the same as the longitudinal relaxation rate ($1/T_1$). B) An analogous simulation where $k >> 1/T_1$. Inset: magnification of the first 1.5 seconds.

Therefore, for stopped-flow NMR analysis of reactions that proceed faster than the Boltzmann distributions of the various nuclei involved, attaining signal intensities that directly reflect concentrations requires that the reaction components are exposed to the magnetic field (B_0) for $>5\times T_1$ *before* the reaction is initiated by mixing. This requirement poses a technical challenge, as unlike the NMR spectrometers employed in the early stages of development of stopped-flow techniques, modern superconducting magnets have very little stray field. Thus, the reactants must be pre-magnetised in reservoirs located as close as possible to the field-centre, i.e., close to the probe head. This is achieved by a set of three pre-magnetisation reservoirs located just above the probe head, see Figure 25. It was noticed that the reservoirs afford high, but not complete, polarisation of the nuclei in the solutions before they are mixed and delivered to the flow-cell. Therefore, it is necessary to determine the pre-magnetisation profiles of the three independent syringes. To measure the pre-magnetisation levels, arbitrarily chosen stock solutions of 2- and 4-fluorophenyl boronic acid in 1:1 dioxane/H_2O were used. ^{19}F T_1 constants of the samples were measured by Inversion Recovery, at 1.65 ± 0.02 s and 2.06 ± 0.02 s respectively. After T_1 measurements, the pulse sequence (Figure 24a) was used to assess the pre-magnetisation effects. The setup parameters are shown below. Three spectra were collected in each experiment using 90° pulses. Theoretically, if the interscan delay t_R is longer than $5*T_1$, the second and third signals should experience a complete relaxation back to thermal equilibrium, i.e., 100% magnetisation. The first signal therefore reflects a partial pre-magnetisation level achieved under the delivered volume from a certain solution syringe.

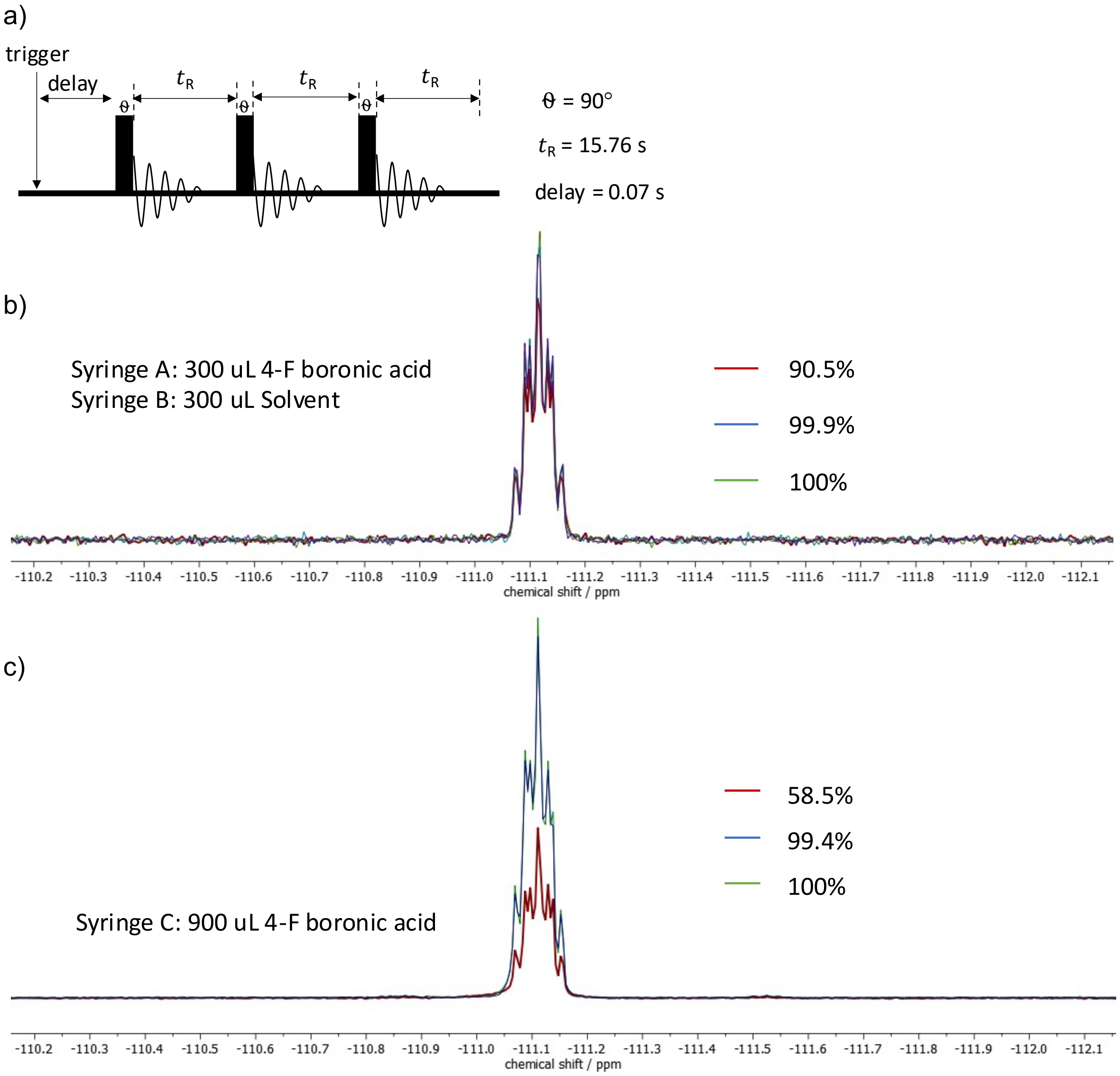

Figure 24. a) The pulse sequence used for ^{19}F stopped-flow experiments to measure pre-magnetisation profiles of three solution syringes. Two examples of different delivery volumes from b) solution syringe *A* (300 μL) and solution syringe *B* (300 μL), and c) solution syringe *C* (900 μL) to demonstrate how the pre-magnetisation level was calculated.

Two examples are presented in Figure 24. Figure 24b shows the delivery of 300 μL 4-fluorophenyl boronic acid from syringe *A*, and 300 μL solvent from syringe *B* as a total delivered volume (*A* + *B* + *C*) of ≥ 600 μL is required to fully purge the previous sample and refill the flow-cell. Integration of the signals shows that the first signal has a 90.5% integral comparing to the maximum integral of the last two signals. Similarly, Figure 24c shows 900 μL solution was delivered from syringe *C*. The first signal has only 58.5% integral of the third one. By repeating this experiment with different delivered volume from different solution syringes, the pre-magnetisation profiles were constructed in Figure 25a. This pre-magnetisation profiles provide a guideline in delivery volumes (*A*, *B*, *C*) to afford >90% pre-magnetisation. In this case, a flow rate of 1 mL/s was adopted for the investigation. It is reasonable to assume different flow rates would lead to moderate variations in the pre-magnetisation effects. Overall, the pre-magnetisation profiles of three syringes differs mainly based on the delivered volumes and the concentric arrangement of the coil-shaped reservoirs (Figure 25b). For instance, pre-magnetisation reservoir *A* (··•··) was placed at the innermost side, *B* (··•··) at in-between, and *C* (··•··) at the outermost respectively, therefore coil *A* houses the smallest capacity for pre-magnetisation whilst *C* affords the largest.

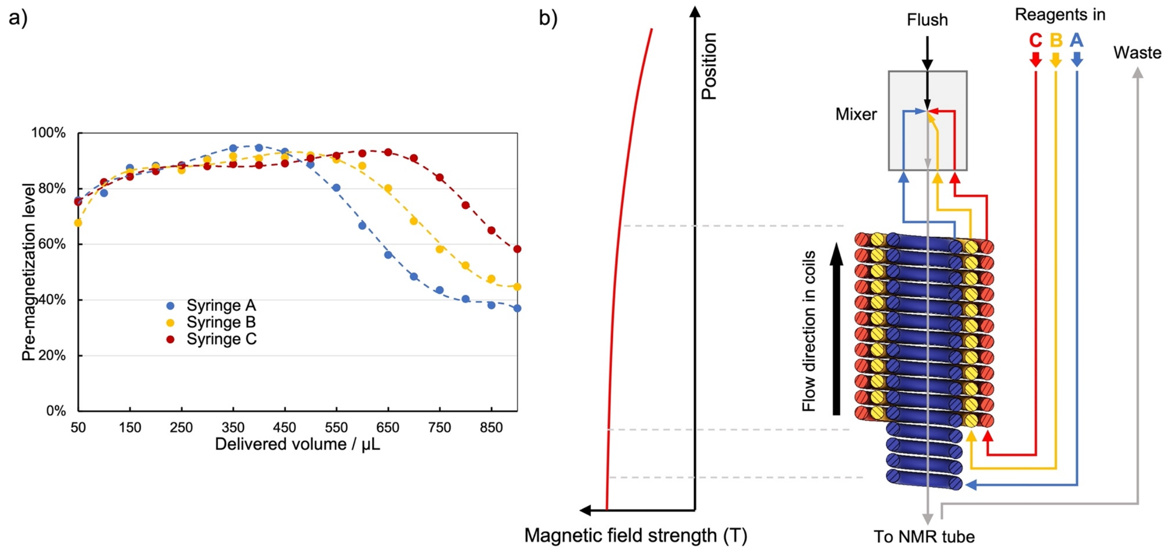

Figure 25. a) Pre-magnetisation profiles of solution syringes A, B, C. Delivery volumes ranging from 50 – 900 µL in increments of 50 µL were studied, the dashed lines through the datapoints are for visual guidance only. b) Vertical cross-section of the pre-magnetisation reservoirs. The reagents from solution syringes flow through the pre-magnetisation coils in an upward manner until they reach the mixer. The homogeneously mixed volume is then delivered back down to the flow-cell in the probe head at the magnetic field centre. The relative vertical position of the coils to NMR probe and the corresponding magnetic field strength experienced are illustrated in the left-hand section of the figure.

As indicated above, >90% pre-magnetisation of the solutions can be afforded by the pre-magnetisation coils, this contrasts with the 100% polarisation from the traditional static NMR experiments and some custom-built stopped-flow probes. Consequently, incomplete pre-magnetisation will result in spins continuing to be polarised inside the reaction-cell, in a T_1-dependent manner. This effect can be better comprehended from Figure 26, a simulation of spin polarisation in NMR probes. Following the relaxation recovery Equation 5, $M_t = M_0 \cdot (1 - x * e^{-\tau/T_1})$, where x in this case represents the pre-magnetisation extent. For example, magnetisation level starting from 0%, 50%, 90%, 95% correspond to x = 1, 0.5, 0.1, 0.05 respectively. Based on this equation, it can be calculated that from 90% to 99% magnetisation, it takes a time of 2.3*T_1, and from 0% to 99% magnetisation it takes 4.6*T_1. This calculation explained the general recommendation of 5*T_1 repetition time between consecutive scans upon 90° flip angles for sufficient relaxation, and the T_1-dependent continuing polarisation of incompletely polarised spins. Thus, in practice, precautions need to be taken prior to data collection. If the reactants or internal standards have substantially different T_1 constants, unequal magnetisation rates will compromise the accuracy of quantification of the data acquired within the reaction period.

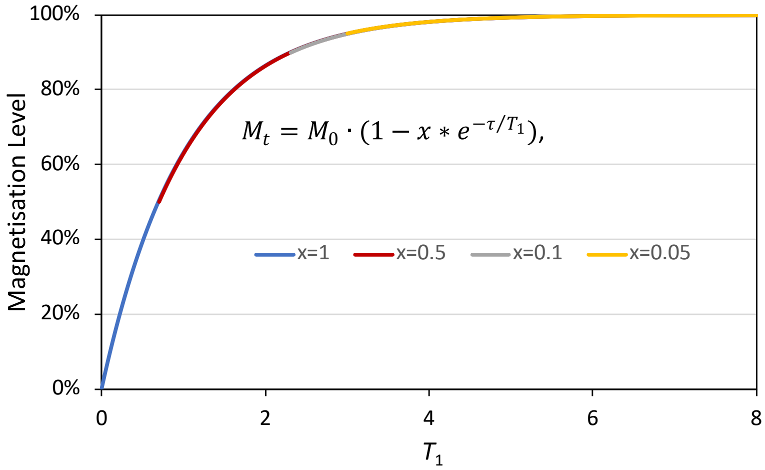

Figure 26. Graphical representation of unperturbed magnetisation growth of spins in a probe, x denotes the pre-magnetisation coefficient which determines the starting point of the recovery curve. Horizontal axis represents time in multiple of T_1. Four curves are overlapped, all reaching the final point of thermal equilibrium, i.e., 100% magnetisation.

To demonstrate this effect, a sample of Ph_3P and $Ph_3P{=}O$ mixture in 9:1 THF/H_2O was used to take advantage of their large difference in ^{31}P T_1 constants (Figure 27). The T_1 constants of Ph_3P and $Ph_3P{=}O$ were measured by Inversion Recovery experiments at 16.00 ± 0.01 s and 3.60 ± 0.01 s, respectively. Like the pre-magnetisation profile measurements, pulse sequence (Figure 24a) was utilised again. Three spectra were acquired in each experiment, and the interscan delay between acquisitions (>5×T_1) allows full relaxation to thermal equilibrium. Therefore, when normalising the integral of maximum peak as 100%, the first spectrum gives the pre-magnetisation level of the studied spins. 600 μL of the mixture of 0.5 M Ph_3P and 0.5 M $Ph_3P{=}O$ were injected in each experiment. A series of 26 interleaved experiments, as introduced in section 1.1.3, were repeated, with the only variation being the incremented trigger delay. The first spectrum of each experiment was extracted to reconstruct an interleaved dataset (Figure 27b). The faster relaxing ^{31}P in $Ph_3P{=}O$ reached 100% magnetisation earlier than the slower relaxing Ph_3P, showing a clear dependence of continued magnetisation on the T_1 constants (Figure 27a).

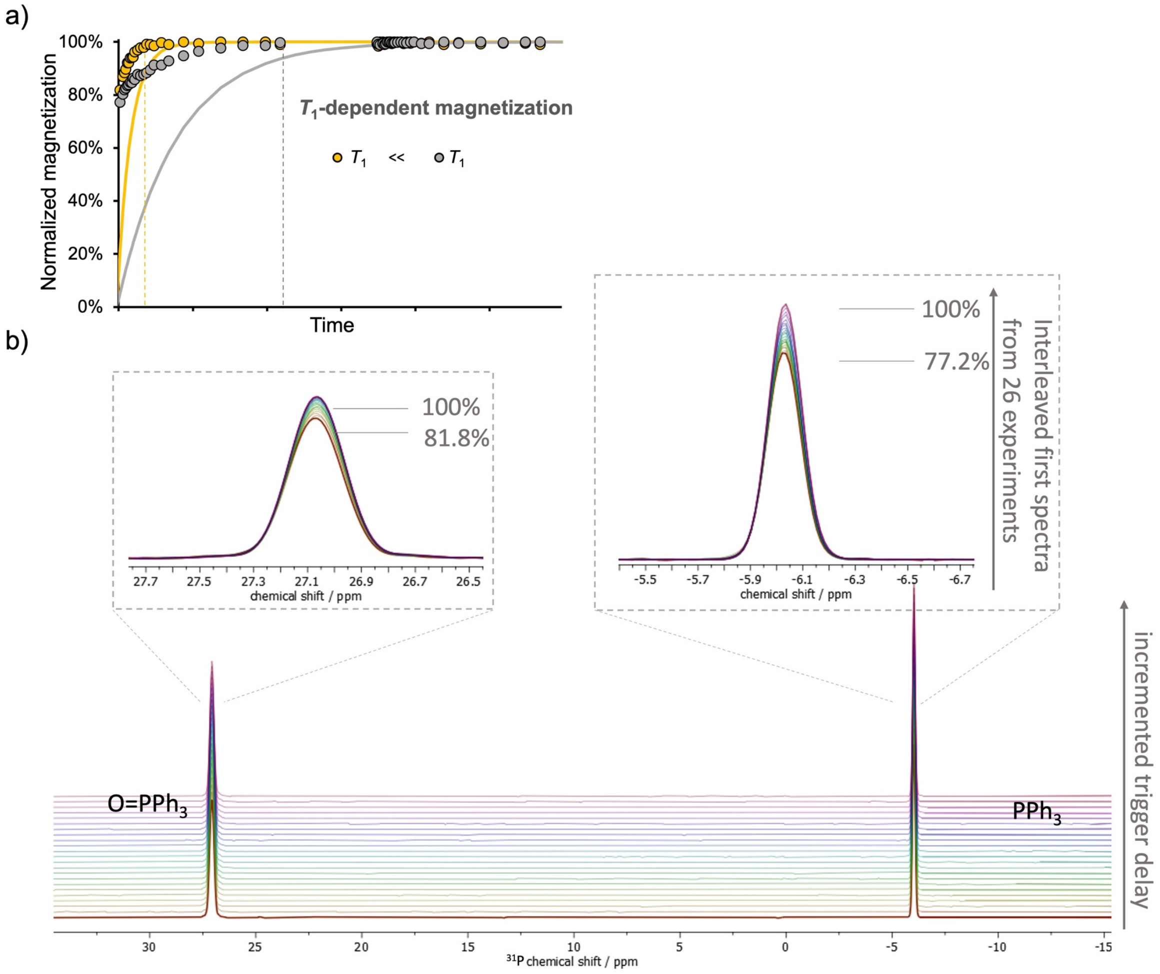

Figure 27. a) Continued polarisation of analytes in the flow tube (circles) after being 'shot' from the stopped-flow solution syringes, and simulated polarisation of analytes without pre-magnetisation (lines). Grey circles/line indicate the experimental data/simulation for Ph_3P, and yellow circles/line indicate the experimental data/simulation for $Ph_3P{=}O$, respectively. b) Interleaved ^{31}P stopped-flow experiments on Ph_3P and $Ph_3P{=}O$ to assess the continued magnetisation of analytes inside the flow tube after injection. Only the first spectrum of each separate experiment was shown, the 2nd and 3rd spectra were normalised to 100% integral.

2.1.3 Non-pre-magnetisation Channel

Apart from the three solution syringes, a solvent syringe was installed to facilitate the '*flush*' of the system (Figure 21b). This unique syringe was exploited here as a non-pre-magnetisation channel, or '*hypo-polarisation*' channel. In stark contrast to the three solution syringes (*A*, *B*, *C*), there is no polarisation reservoir for this channel (*D*), the spins therefore do not establish Boltzmann distribution if immediately measured when entering the flow tube. This effect, shown in Figure 23 as an undesirable outcome, could be turned into a valuable tool for magnetisation transfer studies. Applications of this will be discussed in succeeding sections. The first task, similar to the pre-magnetisation syringes, was to examine the pre-magnetisation levels of this solvent syringe. Albeit being named *'non-pre-magnetisation'* channel, the pre-magnetisation level was not exactly 0% upon measurements. This can be understood from the assembly in Figure 25b, the solution stored in this input experiences a subtle magnetic field strength depending on the proximity to the NMR probe. In addition, while transporting to the flow cell, the solution is polarised during the transport deadtime, in a T_1-dependent manner. This feature will pose a limitation to the study here. If the spins have a comparably short T_1 and complete relaxation is achieved during the transport deadtime, the spins will no longer be *'non-pre-magnetised'*. The investigation of the pre-magnetisation level of syringe *D* was conducted, using the pulse sequence and method from Figure 25a. Fresh stock solutions of 2- and 4-fluorophenyl boronic acid in 1:1 dioxane/H_2O were prepared, the ^{19}F T_1 constants were measured by Inversion Recovery experiments, at 1.55 ± 0.01 s and 1.96 ± 0.01 s respectively. 4-fluorophenyl boronic acid was inputted via syringe *D*, while 2-fluorophenyl boronic acid was inputted via syringe *B* to compensate for the total minimum volume of 600 μL when necessary. By incrementing the delivered volume from syringe *D* in 50 μL steps, the pre-magnetisation levels of 4-fluorophenyl boronic acid was calculated and reconstructed to plot Figure 28. Four different flow rates that lead to different transport dead times were measured. It can be seen at delivery volumes > 150 uL, the pre-magnetisation levels remain constant. As expected, the slowest flow rate at 0.5 mL/s (Figure 28, grey circles) needed the longest transport deadtime of 300 ms, therefore experiencing the highest pre-magnetisation level. The most frequently used flow rates at 1 mL/s (Figure 28, green circles) led to a transport deadtime of 150 ms, showing a slightly higher pre-magnetisation level than the other two. Flow rates at 1.5 mL/s and 2 mL/s led to transport deadtimes of 100 ms and 75 ms respectively, the pre-magnetisation levels did not show apparent difference for the studied spins here (T_1 = 1.96 ± 0.01 s). Nevertheless, it is noteworthy that the T_1 of the sample plays an important role in determining the pre-magnetisation levels prior to measurements. Throughout this work, although the pre-magnetisation level of channel-*D* was not strictly 0%, it is referred to as the 'non-pre-magnetisation channel' as a contrast to the traditional channels *ABC* which afford > 90% pre-magnetisation.

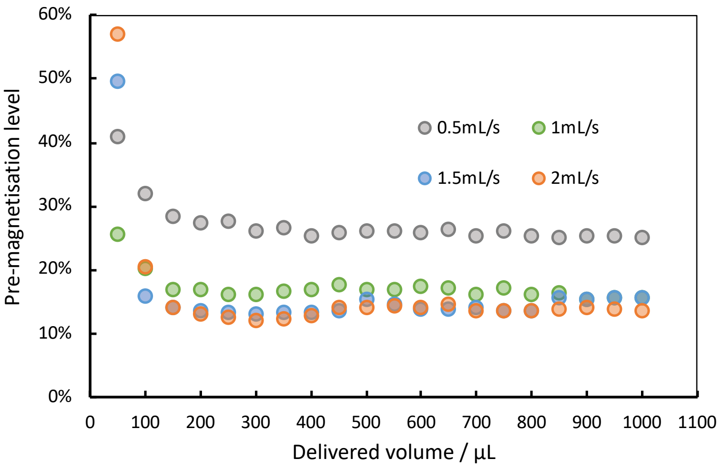

Figure 28. Pre-magnetisation extents of input solutions via solvent syringe D at variable flow rates. Volumes ranging from 50 – 1000 μL in increments of 50 μL were studied.

2.2 Rapid Irreversible Reaction Monitoring by Stopped-flow NMR

2.2.1 Protodeboronation of 2,3,4,6-tetrafluorophenyl Boronic Acid

As shown in Figure 19, the previous studies in the Lloyd-Jones group[168] have thoroughly explored the base-catalysed protodeboronation of up to 30 different arylboronic acids. These processes have a broad half-life spanning from milliseconds to months at 343 K, and the reaction rates can be conveniently tuned by varying the temperature. This greatly facilitates the selection of desired reaction rates. Therefore, setting out to probe the kinetics of rapid reactions using the stopped-flow technique, the research began with the protodeboronation of 2,3,4,6-tetrafluorophenyl boronic acid, which showed a half-life of 66 ms at 343 K measured by rapid quench-flow method. The reaction conditions in the publication[168] were maintained except for the temperature. The temperature was lowered to facilitate the operability of the experiments and was anticipated to slow down the reaction.

Prior to reaction monitoring, T_1 values of all ^{19}F atoms in the system were measured in the flow cell of the stopped-flow tube by Inversion Recovery experiments. Inversion Recovery experiments were acquired with a 56818 Hz spectral window, 0 dummy scans, 2 scans. The relaxation delay time was set to 15 s to ensure a complete relaxation back to equilibrium, and the acquisition time was 0.80 s. A variable delay list of 12 values/s {0.001, 0.1, 0.3, 0.5, 1, 2, 3, 4, 8, 10, 12, 15 s} was used. Internal standard TFA was measured in both the starting material and product, and the results could be found in Table 3. The measured T_1 values of TFA differed slightly in reactant and product, this was mainly due to the pH variation in two solutions.

Table 3. T_1 values of ^{19}F atoms in reactant 2,3,4,6-tetrafluorophenyl boronic acid, product 1,2,3,5-tetrafluorobenzene, and internal standard TFA in 1:1 dioxane/H_2O, measured by Inversion Recovery experiments.

T_1 measurements					
Reactant					
δ [ppm]	**TFA (IS)**	**2,3,4,6-tetrafluorophenyl boronic acid**			
	-76	-107.4	-127.4	-132.7	-168.5
T_1 [s]	2.123 ± 0.004	1.347 ± 0.009	0.865 ± 0.009	1.115 ± 0.014	1.043 ± 0.063
Product					
δ [ppm]	**TFA (IS)**	**1,2,3,5-tetrafluorobenzene**			
	-76	-114.5	-133.8	-168.0	--
T_1 [s]	2.209 ± 0.002	3.893 ± 0.002	2.541 ± 0.003	2.810 ± 0.005	--

To follow the reaction in stopped-flow system, a stock solution of 0.083 M 2,3,4,6-tetrafluorophenyl boronic acid and 0.020 M trifluoroacetic acid (IS), and a stock solution of 0.302 M (3 equivalent) of KOH were freshly prepared in 1:1 dioxane/H_2O in separate 25 mL volumetric flask. The stock solutions were transferred to stopped-flow reservoir bottles and connected to stopped-flow syringes, respectively. Both probe and thermostat system temperature were set at 300 K. The reaction was initiated by simultaneously inputting 300 μL of boronic acid and 300 μL of base solution from syringe *A* and syringe *B*, at a flow rate of 1 mL/s. The reactant 2,3,4,6-tetrafluorophenyl boronic acid (Figure 29) instantaneously converts to the intermediate boronate under excess base conditions. ^{19}F NMR spectra were then acquired with a minimum trigger delay of 0.039 s. As shown in Figure 31b, resonances from different ^{19}F sites were well separated and easy to distinguish. For example, signals at -76 ppm from TFA, at -109.2 ppm from the intermediate boronate, and at -168.0 ppm from the product were chosen to plot the reaction profiles. The reaction completed after ca. 50 s, a relatively '*slow*' reaction for the stopped-flow instrument. Pulse angles and interscan delays can be chosen flexibly as long as they provide sufficient relaxation and data density. In this case, 45° pulses were applied. The protodeboronation of 2,3,4,6-tetrafluorophenyl boronic acid was determined to have a $t_{1/2}$ of 10.43 s at 300 K.

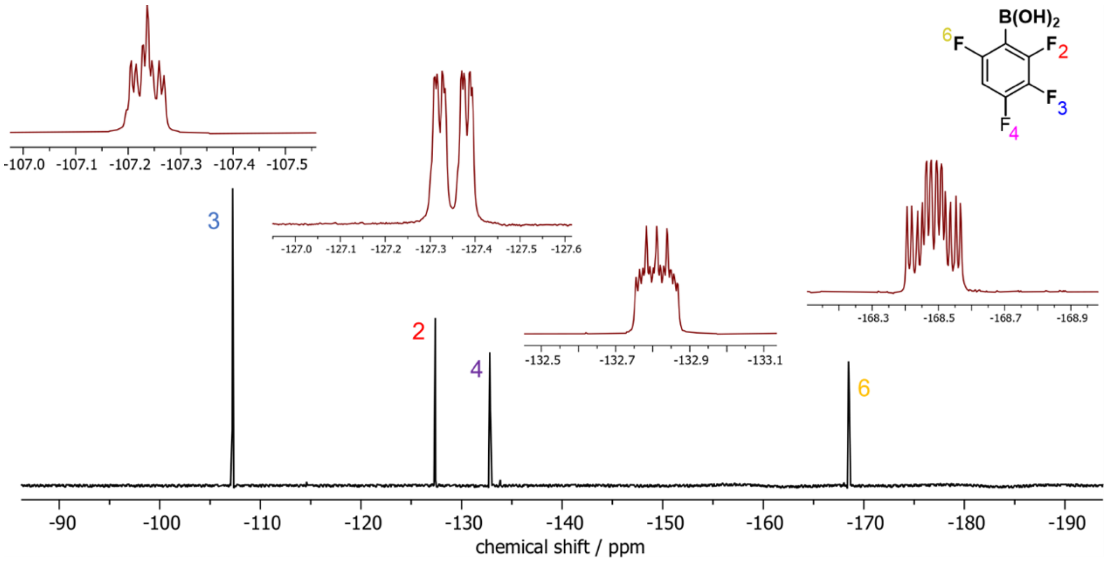

Figure 29. 1D ^{19}F NMR spectrum of the reactant 2,3,4,6-tetrafluorophenyl boronic acid and TFA (IS) in dioxane/H_2O at 300 K. The reactant instantaneously converts to the corresponding boronate under excess base conditions, followed by rapid protodeboronation.

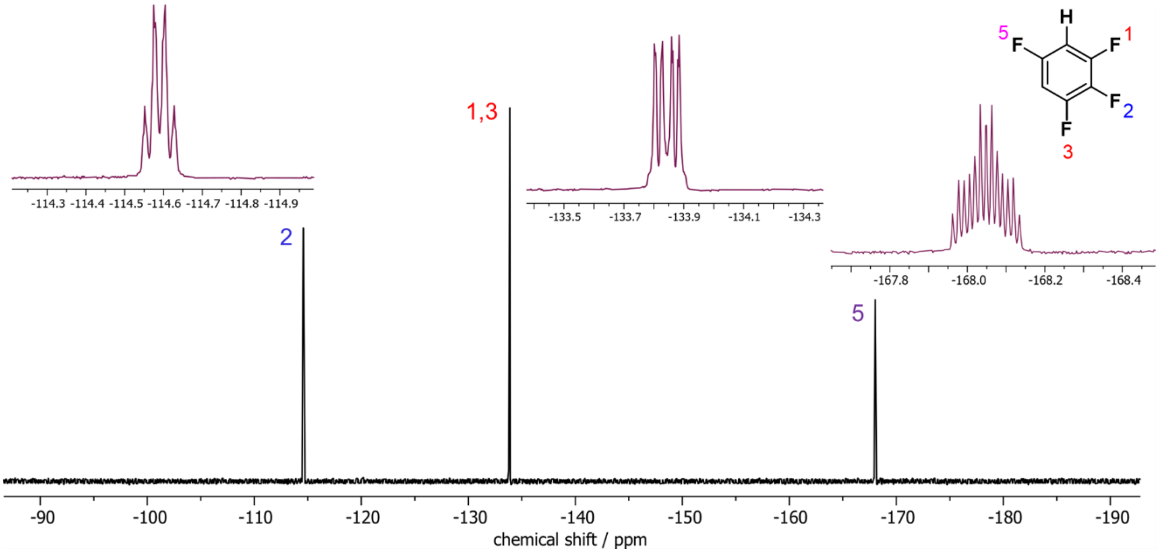

Figure 30. 1D ^{19}F NMR spectrum of the product 1,2,3,5-tetrafluorobenzene in dioxane/H_2O at 300 K.

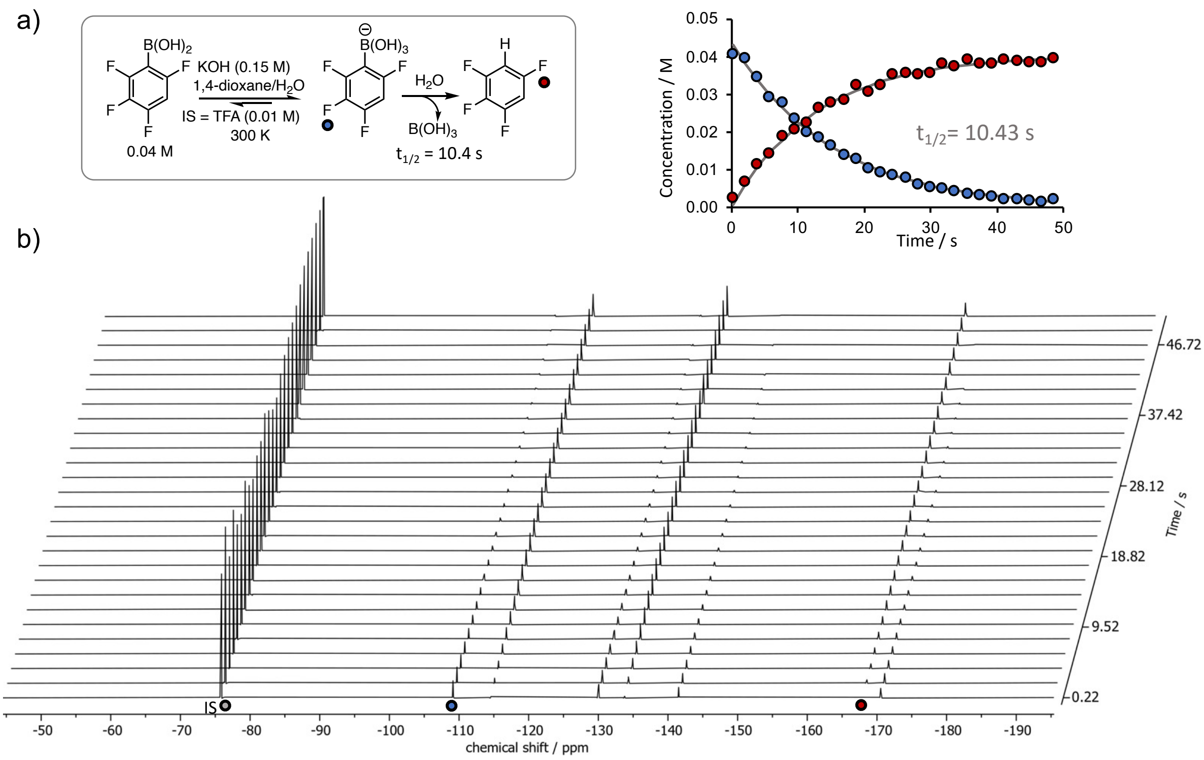

Figure 31. a) The protodeboronation of 2,3,4,6-tetrafluorophenyl boronic acid scheme at 300 K, and the reaction profile. b) Stacked ^{19}F stopped-flow spectra to monitor the reaction using 45° pulses. Intermediate boronate signal (blue circle), and product signal (maroon circle) were chosen to plot the reactions profile. Concentration was calculated based on the known concentration of internal standard TFA (grey circle).

2.2.2 Optimal Choice Between Sensitivity and Data Density

Following the successful monitoring of the protodeboronation of 2,3,4,6-tetrafluorophenyl boronic acid, the work continued to explore the optimal NMR acquisition parameters for real-time reaction monitoring. NMR spectroscopy is an intrinsically insensitive technique. To ensure accurate quantitation, NMR experiments requires a high signal-to-noise ratio (S/N). Approaches to improve sensitivity include for example, increasing the sample concentration or using high magnetic field strength with cryogenic probe. Alternatively, for given samples and instruments, NMR acquisition parameters such as pulse angle, interscan delay, acquisition time, receiver gain, and signal-averaging (number of FIDs) are important. In rapid irreversible reactions the analytes evolve too fast to allow signal averaging, constraining the number of FIDs to one per time point. Larger pulse angles afford higher sensitivity, but at a price of longer interscan delay t_R to ensure sufficient relaxation. The interscan delay t_R between consecutive pulses, on the other hand, determines the data density achievable in a fixed time window. Therefore, we explored the choice of pulse angles, θ, that are optimised for spectral sensitivity

(S/N) versus data density, for accurate kinetic analysis using the established example of the protodeboronation of 2,3,4,6-tetrafluorophenyl boronic acid from previous section.

The experiments were repeated using variable pulse angles, at 10°, 45° and 90° respectively. The interscan delay was 1.36 s (relaxation delay of 0.5 s and acquisition time of 0.8 s respectively) for 10° pulses, and 1.86 s (relaxation delay of 1 s and acquisition time of 0.8 s respectively) for 45° and 90° pulses. Reaction rates were derived from fitting the intermediate consumption using a first-order kinetic model, and intermediate concentrations were calculated based on the known concentration of internal standard TFA. As larger pulse angles afforded increased S/N, an improvement in the sensitivity can be visually seen by ^{19}F spectra acquired from 10° to 45° pulses (Figure 32). This improvement is also illustrated from the absolute integral of peaks against time (Figure 33). However, further increasing the pulse angle to 90° caused signal suppression, which can be seen from the absolute integrals of TFA in Figure 33c. Incomplete relaxation leads to incorrect quantitation, and in this case a 7% error in the estimated rate constant. This example demonstrated the significance of choosing the appropriate acquisition parameters such as the pulse angle θ, and the interscan delay t_R, with a prior knowledge of the T_1 constants of studied spin species.

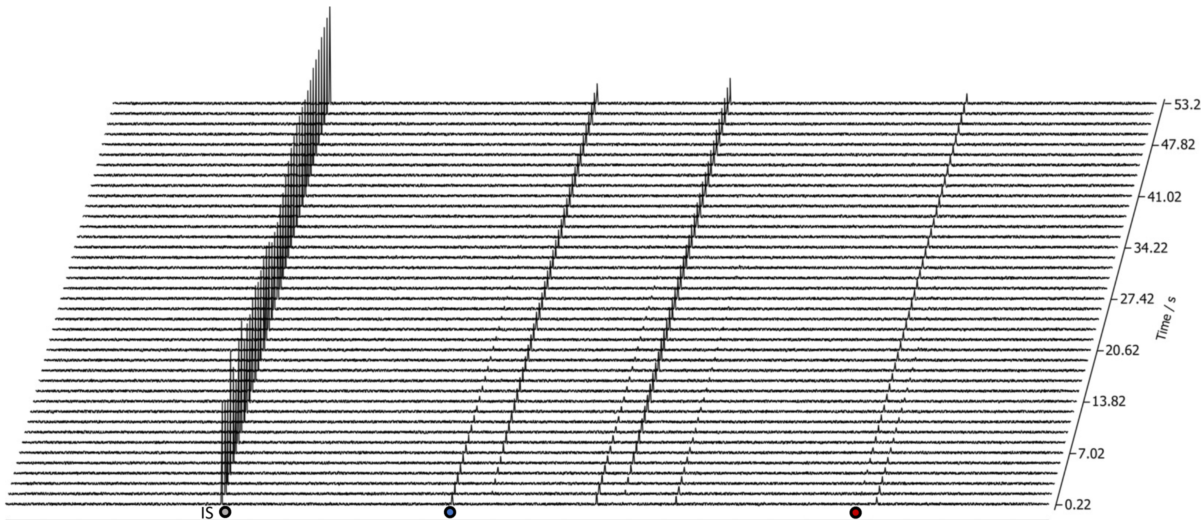

Figure 32. ^{19}F stopped-flow spectra to monitor the protodeboronation of 2,3,4,6-tetrafluorophenyl boronic acid using 10° pulses, showing a reduction in S/N comparing to the spectra obtained by 45° pulses.

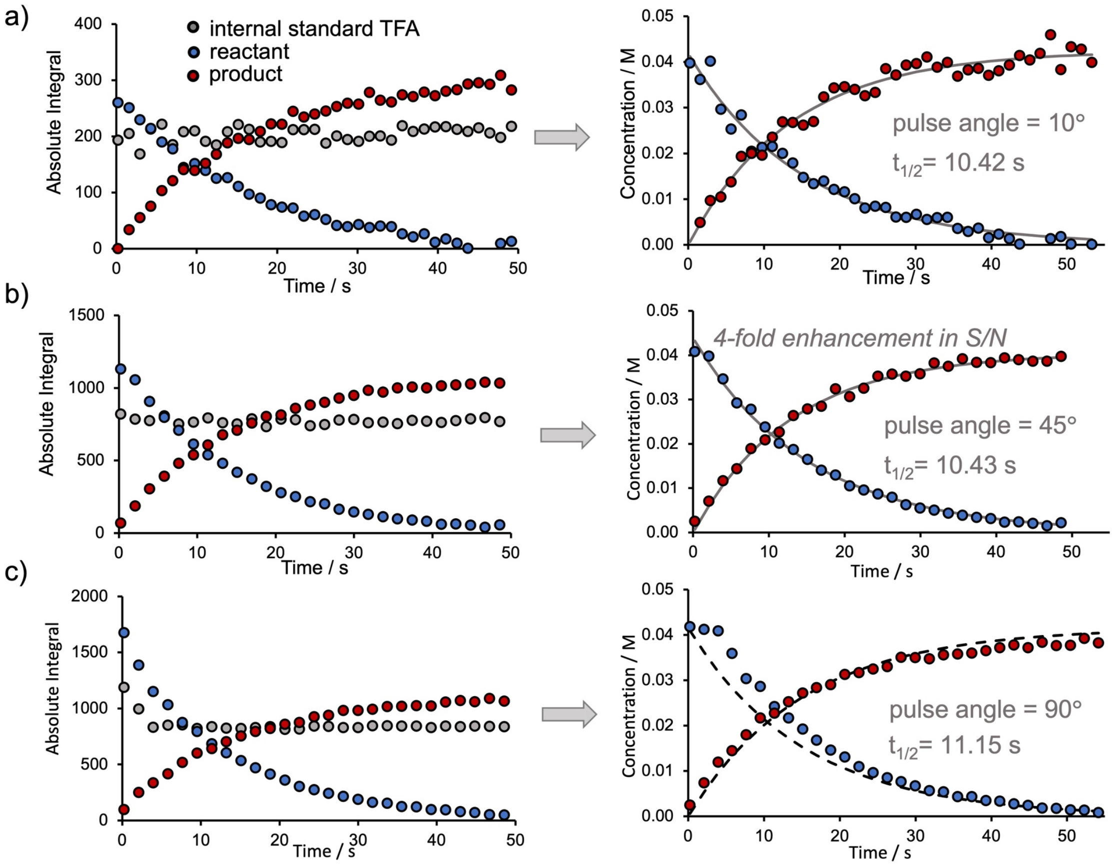

Figure 33. ^{19}F stopped-flow experiments to monitor the protodeboronation of 2,3,4,6-tetrafluorophenyl boronic acid using a) 10° pulses, b) 45° pulses, and c) 90° pulses. The left column shows the plots of absolute integral against time, and the right column shows the plots of concentration against time. Half-lives were calculated by non-linear regression of the first-order decay of intermediate boronate.

2.2.3 Reaction Monitoring via Interleaved Approach

As is evident from the discussion above, when larger pulse angles, $0° < \theta \leq 90°$, are employed to gain S/N, the interscan delay, t_R, must be extended to avoid saturation for a given longitudinal relaxation rate, $1/T_1$. This in turn inevitably leads to lower data density, particularly for *fast* reactions with limited time window for measurements. One approach to address this limitation is to manually enhance the data density through spectral 'interleaving'. The principle for this is straightforward; the reaction is performed multiple times, incrementing the delay between the trigger and the first excitation pulse for each experiment. Data points obtained from separate experiments can then be combined to produce an interleaved dataset. The process is illustrated schematically in Figure 34 for a reaction that is complete in about 4 seconds. To simulate the spectra, the T_1 constant of the measured species was set to 2 s, and the interscan delay t_R to 1.5 s, with the optimal pulse angle calculated as 60°. Three separate series (blue, red, yellow) were simulated with incremented trigger delays, and each series used to generate one data subset. These three data subsets were combined to generate the final dataset which contains three-fold higher data density. In practice, the trigger delays, interscan delay $\mathrm{t_R}$, and pulse angle can be adjusted based on the estimated reaction rate, known T_1 constants, and the required sensitivity and data density. The stopped-flow instrument, which is program-controlled, allows reactions to be conveniently and reproducibly initiated as a series of identical 'shots' from the same set of stock solutions. The interleaving experiment solely requires accurate timing of the trigger signal sent to the NMR spectrometer, so that the delay period can be reliably incremented.

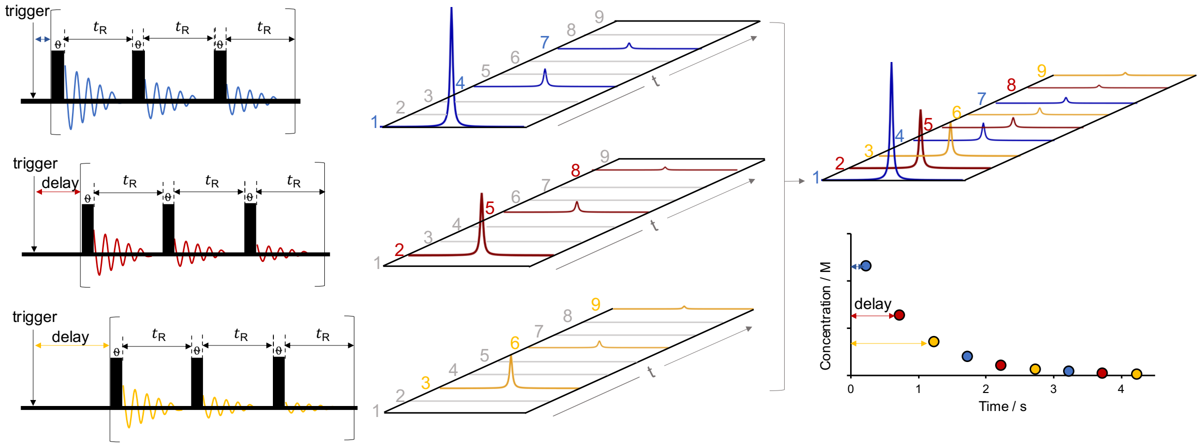

Figure 34. Schematic overview of the process of interleaving a series of spectra using an incremented trigger delay. The interleaved approach allows manually enhanced temporal resolution when studying reactions that are too fast to acquire enough data points within a single 'shot' of the stopped-flow system. The three different coloured subsets represent data obtained from identically initiated experiments; they are then combined to afford three-fold higher data density than the individual components.

With this interleaved stopped-flow method, we re-monitored the protodeboronation of 2,3,4,6-tetrafluorophenyl boronic acid, using 90° pulse angles with 5 interleaved experiments (Figure 35), 30° pulse angles with 2 interleaved experiments (Figure 36), and 10° pulse angles with one experiment (Figure 37). All the other acquisition and process parameters were kept identical for these experiments for back-to-back comparison. It is shown that as long as the interscan delay $\mathrm{t_R}$ allows sufficient relaxation of the spins, the kinetic analysis obtained from variable pulse angles agreed well with each other (Figure 38). As expected, 90° pulse angles afforded the highest S/N, albeit requiring more interleaved experiments for data density. The protodeboronation of 2,3,4,6-tetrafluorophenyl boronic acid was used here as an example to demonstrate the utility of this interleaving approach. In succeeding sections, this approach will be applied to faster reactions, highlighting that accurate kinetic data obtainable with maximum sensitivity and high data density by interleaved stopped-flow experiments.

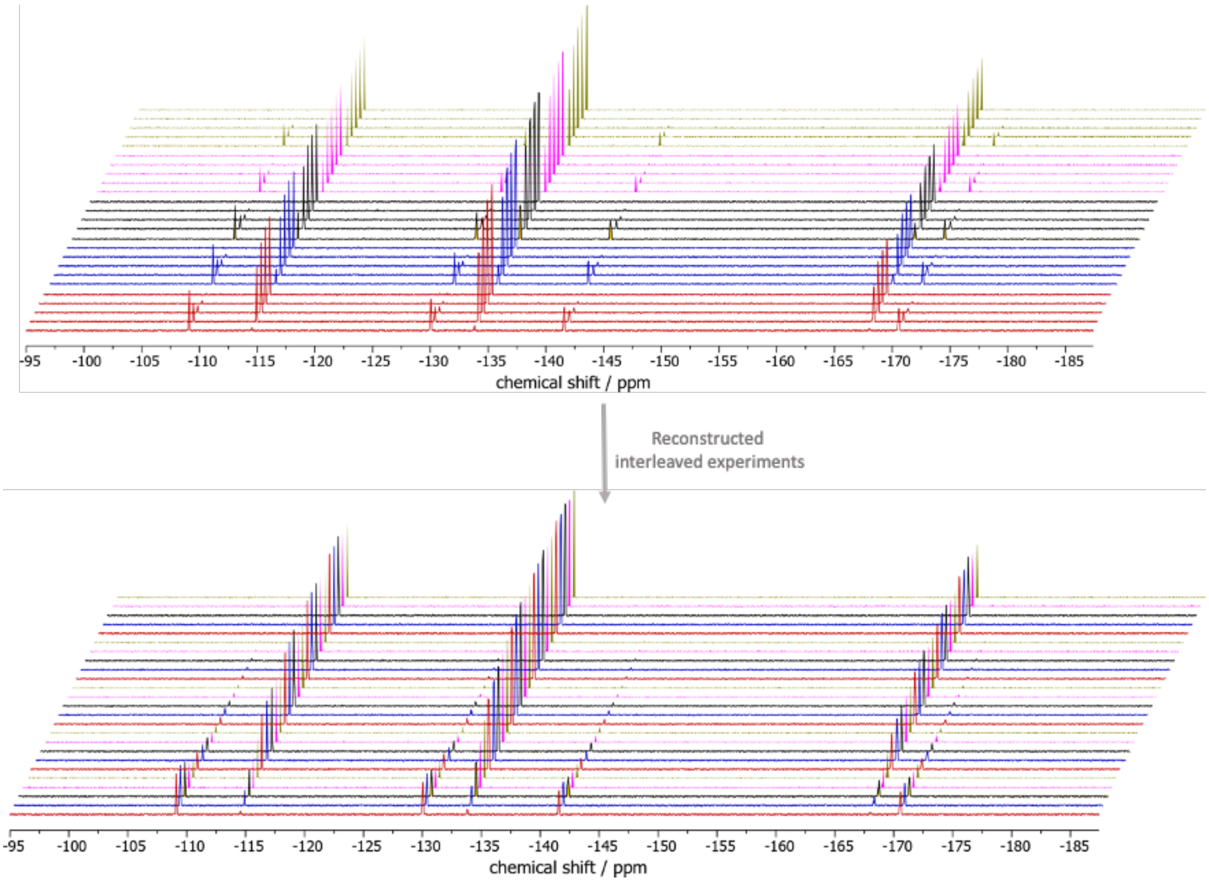

Figure 35. Reaction monitoring of the protodeboronation of 2,3,4,6-tetrafluorophenyl boronic acid using stopped-flow ^{19}F NMR spectroscopy. Five interleaved experiments were acquired with 90° pulses, repetition time t_R of 10.86 s, incremented delays {0.039 s, 2 s, 4 s, 6 s, 8s}. Each interleaved experiment is illustrated with a different colour.

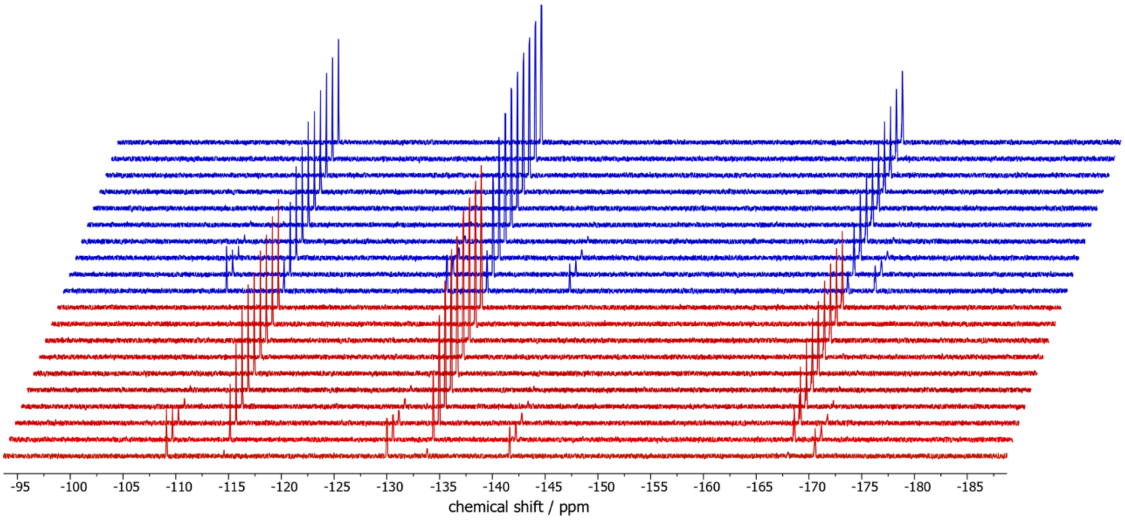

Figure 36. Reaction monitoring of the protodeboronation of 2,3,4,6-tetrafluorophenyl boronic acid using stopped-flow ^{19}F NMR spectroscopy. Two interleaved experiments were acquired with 30° pulses, repetition time t_R of 7.66 s, incremented delays {0.039 s, 3.5 s}.

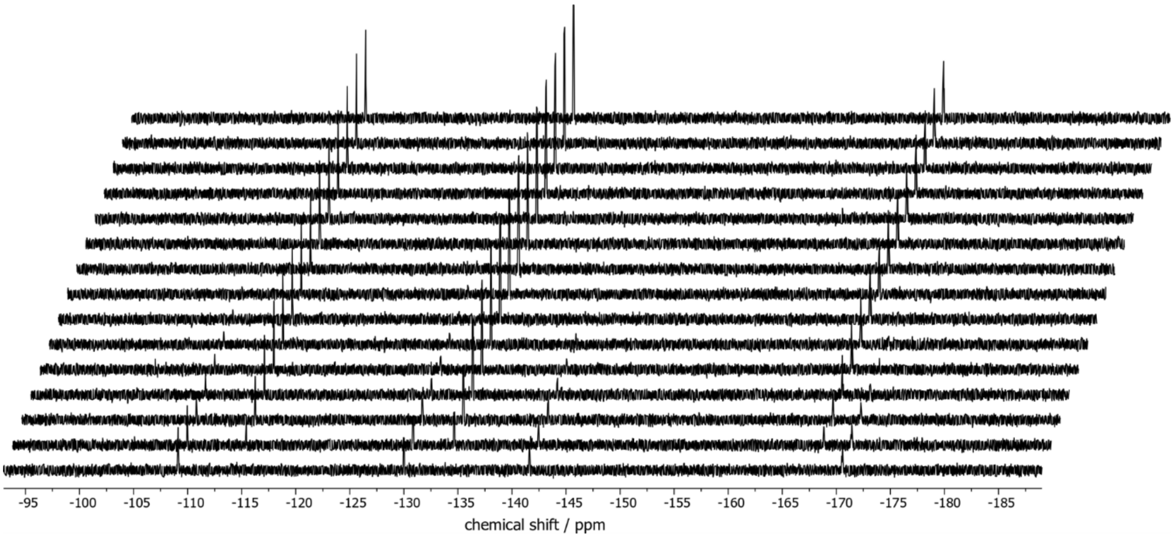

Figure 37. Reaction monitoring of the protodeboronation of 2,3,4,6-tetrafluorophenyl boronic acid using stopped-flow ^{19}F NMR spectroscopy. One experiment was acquired with 10° pulses, repetition time t_R of 3.66 s. Note the apparent signal-to-noise reduction comparing to the experiments acquired with 90° pulses.

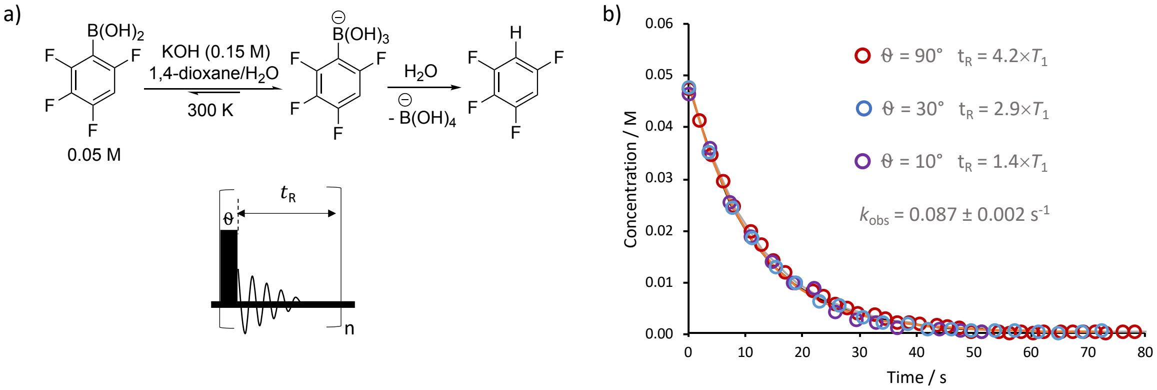

Figure 38. a) Scheme of the protodeboronation of 2,3,4,6-tetrafluorophenyl boronate monitored by stopped-flow ^{19}F NMR spectroscopy. Scheme of the NMR pulse sequence used for reaction monitoring. b) Kinetic analysis using variable pulse angle θ and repetition time t_R, based on the T_1 constants, allowing accurate quantitative analysis with an optimal balance of temporal resolution and spectral sensitivity.

2.2.4 Protodeboronation of 2,3,5,6-tetrafluorophenyl Boronic Acid

After establishing the sensitivity, data density, and interleaved stopped-flow approaches, the ambition was moved to monitor faster irreversible reactions. The protodeboronation of 2,3,5,6-tetrafluorophenyl boronic acid was expected to proceed more rapidly compared to 2,3,4,6-tetrafluorophenyl boronic. Similarly, prior to reaction monitoring, the T_1 values of all ^{19}F atoms in the system were measured in the flow cell of the stopped-flow tube (Table 4). Inversion Recovery experiments were acquired with an 89285 Hz spectral window, 0 dummy scan, 1 scan. Relaxation delay time was 40 s, acquisition time was 1.45 s. Variable delay list of 16 values/s {0.01, 0.1, 0.2, 0.3, 0.5, 0.7, 1, 1.2, 1.5, 2, 3, 5, 10, 15, 20, 40} was used for T_1 measurement.

Table 4. T_1 values of ^{19}F atoms in reactant 2,3,5,6-tetrafluorophenyl boronic acid, product 1,2,4,5-tetrafluorobenzene, and internal standard TFA in 1:1 dioxane/H_2O, measured by Inversion Recovery experiments.

T_1 measurements			
Reactant			
δ [ppm]	**TFA (IS)**	**2,3,5,6-tetrafluorophenyl boronic acid**	
	-76	-135	-141
T_1 [s]	1.906 ± 0.004	1.042 ± 0.009	1.110 ± 0.009
Product			
δ [ppm]	**TFA (IS)**	**1,2,4,5-tetrafluorobenzene**	
	-76	-140	--
T_1 [s]	2.091 ± 0.002	2.358 ± 0.002	--

A stock solution of 0.101 M 2,3,5,6-tetrafluorophenyl boronic acid and 0.024 M trifluoroacetic acid (IS) was freshly prepared in 1:1 dioxane/H_2O. A solution of 0.321 M (3 equivalent) of KOH in 1:1 dioxane/H_2O was prepared separately in 25 mL volumetric flask. The stock solutions were transferred to reservoir bottles and connected to stopped-flow syringes. The reaction was initiated by simultaneously inputting 300 μL of boronic acid and 300 μL of base solution from syringe *A* and syringe *B*, at a flow rate of 1 mL/s. The reactant 2,3,5,6-tetrafluorophenyl boronic acid (Figure 39) instantaneously converts to the corresponding boronate under excess base conditions. A transient ^{19}F stopped-flow spectrum of the rapid reaction with all the peaks from intermediate and product signals can be seen in Figure 40. Since the reaction completed within approximately 5 seconds, eight interleaved stopped-flow experiment with incremented trigger delays 0.039, 0.24, 0.44, 0.64, 0.84, 1.04, 1.24, and 1.44 s were performed (Figure 41b). The trigger delays can be easily programmed into the NMR pulse programme, to construct a satisfactory reaction profile with manually enhanced data density. 30° pulse angles were used, with interscan delays of 1.16 s. The integrals of the intermediate boronate and the TFA (IS) were measured. The concentrations of intermediate were then calculated based on the known concentration of TFA (IS). To evaluate the impact of kinetic analysis using different ^{19}F signals from the boronate, reaction plots from signals at -137 ppm and -143 ppm were both fitted to generate the reaction half-lives. The results showed excellent agreements, with a deviation of 0.6%.

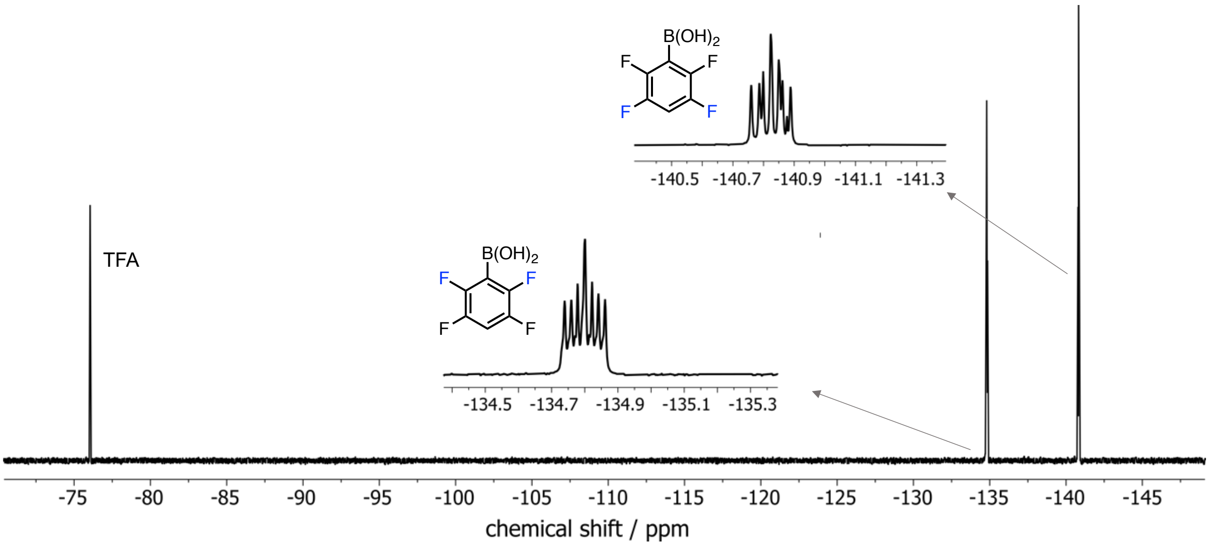

Figure 39. ^{19}F NMR spectrum of the reactant 2,3,5,6-tetrafluorophenyl boronic acid (blue-labelled ^{19}F) and TFA (IS) in dioxane/H_2O at 300K. The reactant instantaneously converts to the corresponding boronate under excess base conditions, followed by rapid protodeboronation.

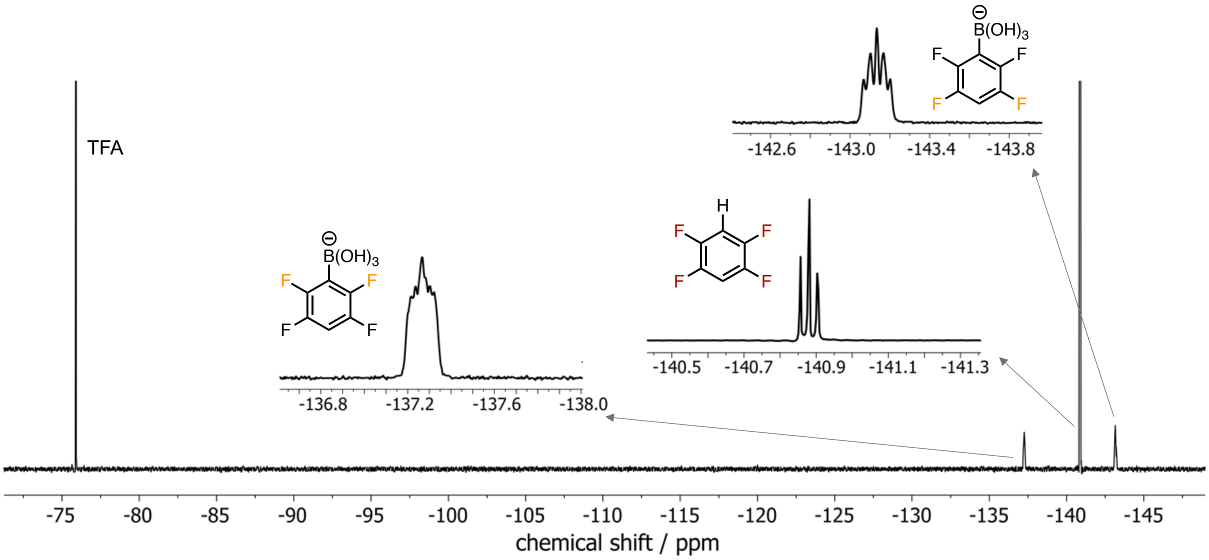

Figure 40. A transient ^{19}F stopped-flow NMR spectrum during the on-going reaction, showing the intermediate boronate (orange-labelled ^{19}F) and the product (maroon-labelled ^{19}F) signals.

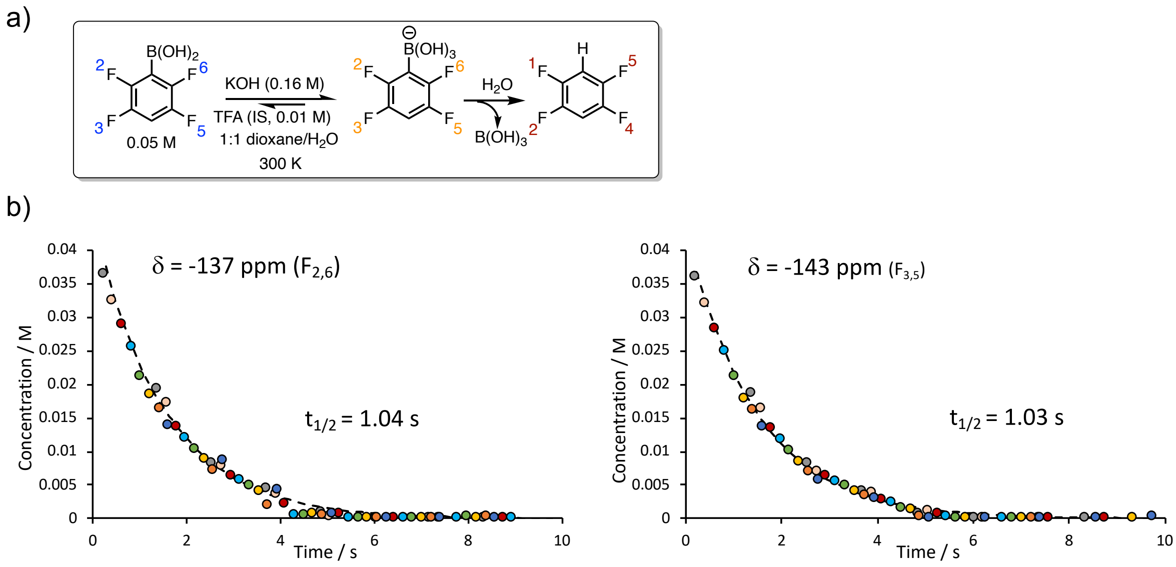

Figure 41. a) The protodeboronation of 2,3,5,6-tetrafluorophenyl boronic acid scheme at 300 K. b) Kinetic analysis by interleaved ^{19}F stopped-flow NMR experiments. Reaction profiles were plotted from the concentration of boronate, dotted line shows the first-order fitting to obtain half-lives. Concentrations were calculated based on the known concentration of internal standard TFA (-76 ppm). Circles of different colour represent data obtained from different interleaved experiments. (left) the concentration profile plotted from the ^{19}F signal at -137 ppm, and (right) from the ^{19}F signal at -143 ppm.

2.2.5 Protodeboronation of Pentafluorophenyl Boronic Acid at the Millisecond Timescale

The examples above have demonstrated the capability of stopped-flow NMR to monitor irreversible reactions completed within seconds. The following challenge therefore focused on probing the limit of the fastest reaction this technique can study. The protodeboronation of 2,3,4,5,6-pentafluorophenyl boronic acid was the fastest protodeboronation of any of the wide series of (hetero)arylboronates[168] that have been tested to date. The half-life time of this reaction was determined to be 2.6 milliseconds at 343 K by quenched-flow NMR methods. Prior to reaction monitoring, the ^{19}F T_1 constants of the reactant 2,3,4,5,6-pentafluorophenyl boronic acid, the internal standard trifluoroacetic acid (TFA), and the product 1,2,3,4,5-pentafluorobenzene were measured by Inversion Recovery experiments, shown in Table 5. Inversion Recovery experiments were acquired with a 56818 Hz spectral window, 0 dummy scans, 2 scans. The relaxation delay time was set to 15 s, and the acquisition time was 0.80 s. A variable delay list of 11 values/s {0.05, 0.1, 0.5, 1, 2, 3, 5, 8, 10, 12, 15 s} was used.

Table 5. T_1 constants of ^{19}F atoms in reactant 2,3,4,5,6-pentafluorophenyl boronic acid, product 1,2,3,4,5-pentafluorobenzene, and internal standard TFA in 1:1 dioxane/H_2O.

***T_1* measurements**				
Reactant				
δ [ppm]	**TFA (IS)**	**2,3,4,5,6-pentafluorophenyl boronic acid**		
	-76	-133.1	-153.8	-163.2
***T_1* [s]**	1.420 ± 0.004	1.249 ± 0.002	1.097 ± 0.016	1.190 ± 0.016
Product				
δ [ppm]	**TFA (IS)**	**1,2,3,4,5-pentafluorobenzene**		
	-76	-140.0	-156.2	-164.1
***T_1* [s]**	2.317 ± 0.003	2.896 ± 0.003	2.339 ± 0.014	2.753 ± 0.018

Based on the previous results, a stock solution of 0.0993 M 2,3,4,5,6-pentafluorophenyl boronic acid and 0.0261 M trifluoroacetic acid (IS) was freshly prepared in 1:1 dioxane/H_2O. A solution of KOH 0.3212 M (3 equivalent) in 1:1 dioxane/H_2O was prepared separately. The thermostats on the spectrometer and auxiliary system were both set to 300 K. The reaction was initiated by computer-controlled simultaneous delivery of 300 μL of the boronic acid solution, and 300 μL of base solution, at a flow rate of 1 mL/s. Interleaved ^{19}F NMR spectra were acquired with incremented trigger delays of 0.039, 0.08, 0.12, 0.16, 0.20, 0.25. 0.30, 0.35, 0.4, and 0.45 s. Figure 42 shows the ^{19}F spectrum of reactant, which instantaneously converts to boronate. A transient ^{19}F stopped-flow spectrum of the rapid reaction with all the peaks from intermediate and product signals can be seen in Figure 43. With the reaction completes within 0.6 seconds, effectively only a single data point can be obtained from each stopped-flow 'shot'. Consequently, θ can be set to 90° to maximise the sensitivity, and a series of 10 shots interleaved (Figure 44). Due to the phenomenological deadtime of 0.22 s at a flow rate of 1 mL/s, only the last 20% of conversion was able to be analysed. The half-life time of this process was determined as 117 ms.

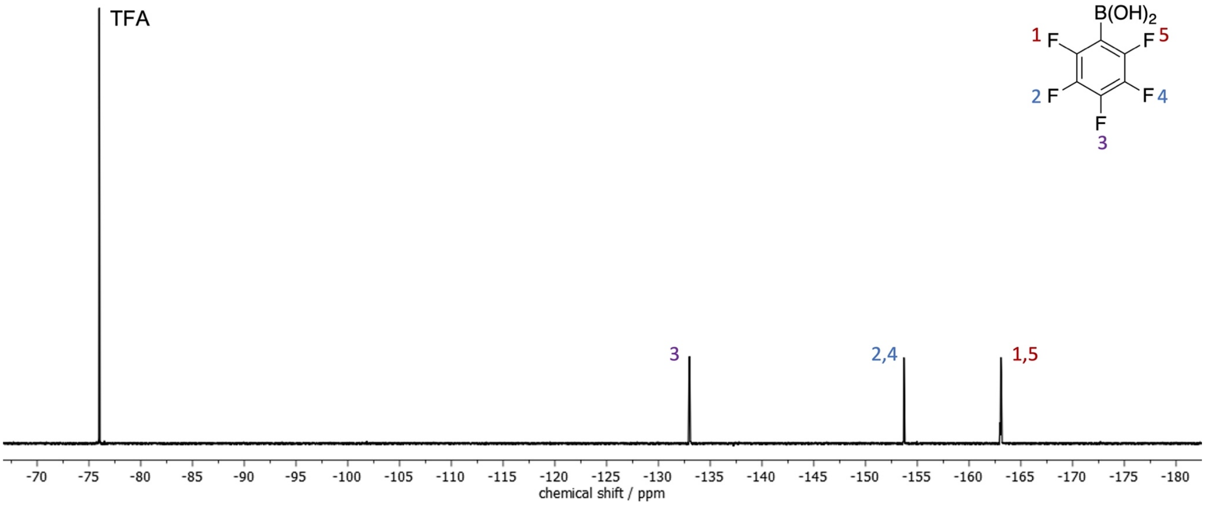

Figure 42. ^{19}F NMR spectrum of the reactant 2,3,4,5,6-pentafluorophenyl boronic acid and TFA (IS) in dioxane/H_2O at 300K. The reactant instantaneously converts to the corresponding boronate under excess base conditions, followed by rapid protodeboronation.

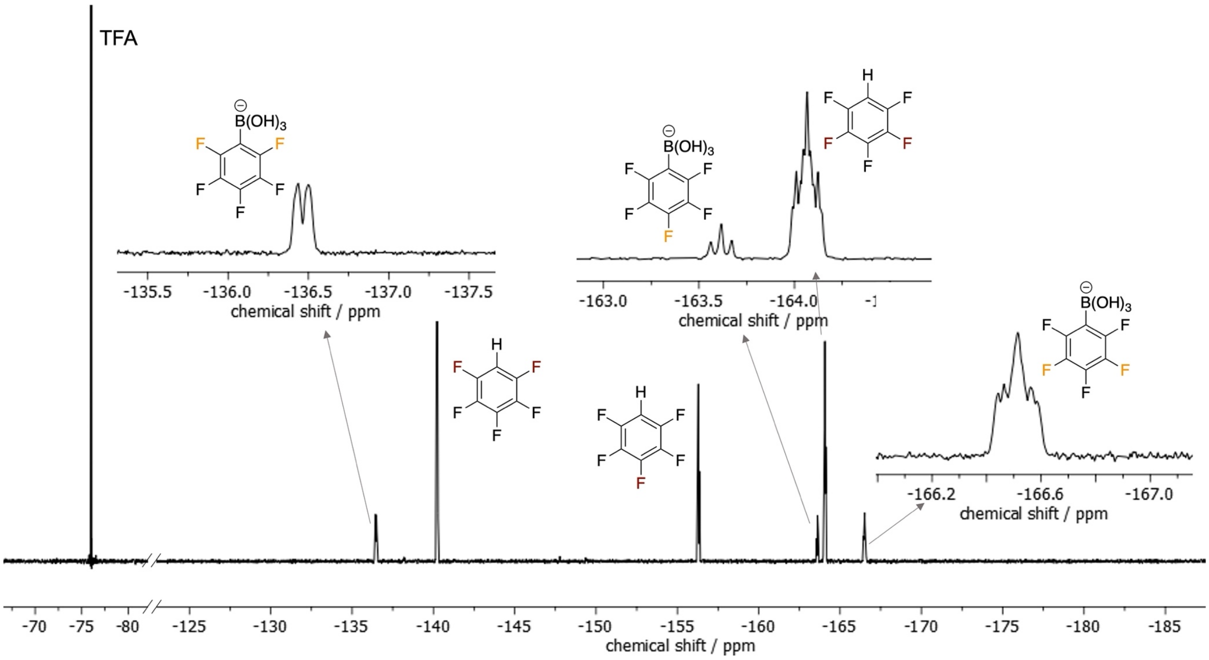

Figure 43. A transient ^{19}F stopped-flow NMR spectrum during the on-going reaction, showing the intermediate boronate (yellow-labelled ^{19}F) and the product (maroon-labelled ^{19}F) signals.

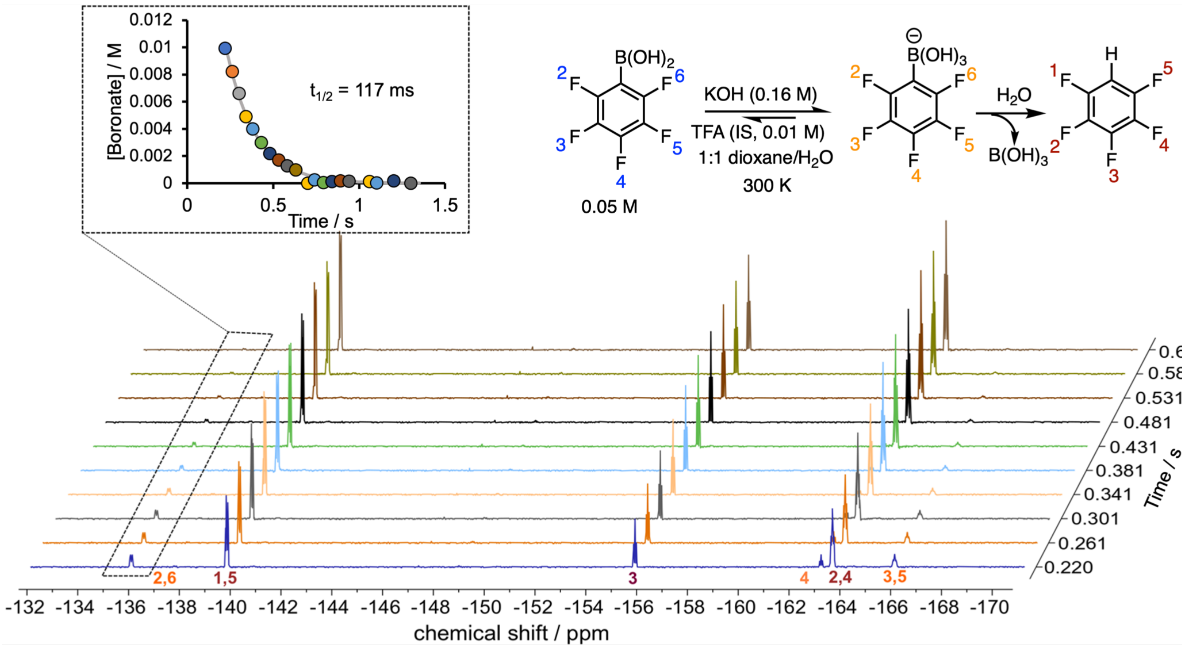

Figure 44. Interleaved ^{19}F stopped-flow spectra of the protodeboronation of pentafluorophenyl boronic acid mediated by KOH in 1: 1 dioxane/H_2O at 300 K. Top right: Reaction scheme for the base-catalysed protodeboronation of 2,3,4,5,6-pentafluorophenyl boronic acid at 300 K. Inset: first-order decay of the boronate intermediate, each differently-coloured data point is generated from an interleaved set of two spectra, with an incremented trigger delay (only the first ten spectra are shown); grey line: non-linear regression to obtain the first-order rate constant, k_{obs} = 5.9 s^{-1}; $t_{1/2}$ = 0.12 s.

By increasing the flow rate to 2 mL/s, a reduced phenomenological deadtime of 0.15 s was achieved, and the reaction at an elevated temperature at 313 K was able to be monitored *in-situ*. A solution of 0.103 M pentafluorophenyl boronic acid and 0.025 M TFA (IS) was freshly prepared in 1:1 dioxane/H_2O. A solution of KOH 0.299 M (3 equivalent) in 1:1 dioxane/H_2O was prepared separately. The thermostats on the spectrometer and auxiliary system were both set to 313 K. The reaction was initiated by simultaneous delivery of 300 μL of the boronic acid solution, and 300 μL of base solution, at a flow rate of 2 mL/s. Interleaved stopped-flow spectra were acquired with incremented trigger delays of 0.039, 0.06, 0.08, 0.10, 0.12, 0.14. 0.16, 0.18, 0.20, and 0.22 s. The interscan delay was 0.36 s, the pulse angle was 90°, only the first spectrum (data point) was used. The half-life of this reaction was determined to be 45 ms. Following this procedure, the half-lives at 283 K ($t_{1/2}$ = 608 ms), 300 K ($t_{1/2}$ = 117 ms), 305 K ($t_{1/2}$ = 78 ms), 313 K ($t_{1/2}$ = 45 ms), and 323 K ($t_{1/2}$ = 19 ms) were measured (Figure 45a). The activation parameters were able to be determined between 284 K to 323 K using the Eyring plot (Figure 45c), which correlate reasonably well with the previously determined rate by rapid quench flow method at 343 K[168]. The capability of the stopped-flow NMR to monitor very fast irreversible reactions in the millisecond timescale was proved, as artistically reflected in Figure 46.

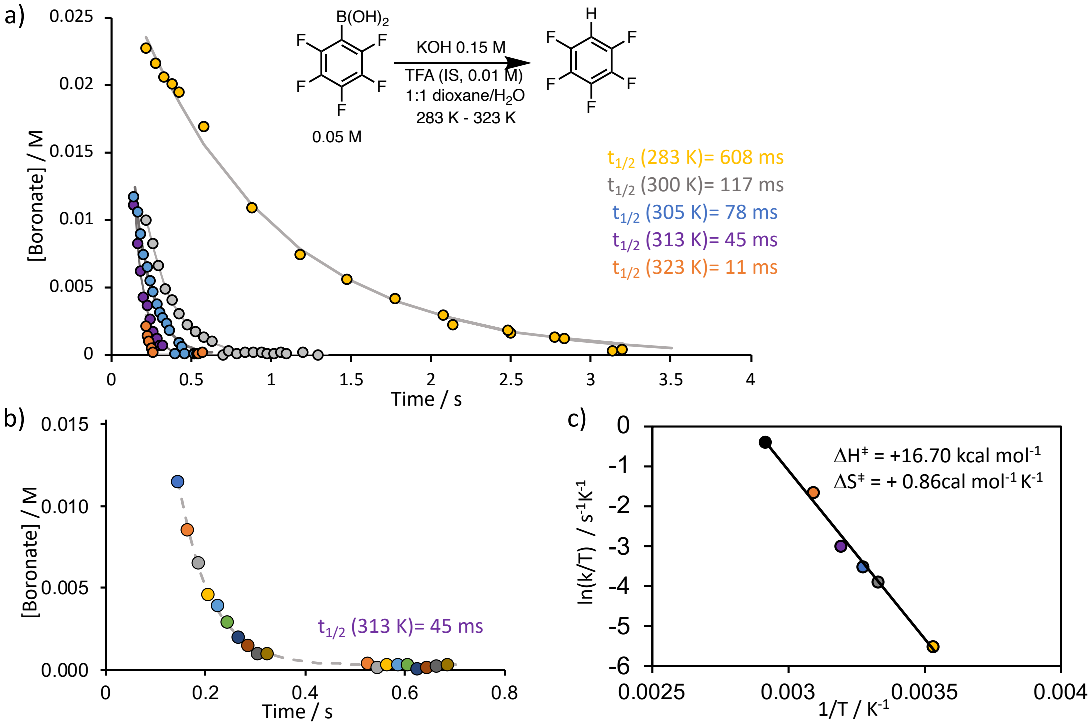

Figure 45. a) Base-catalysed protodeboronation of pentafluorophenyl boronic acid at variable temperature. b) A kinetic profile at 313 K showing interleaved ^{19}F stopped-flow NMR experiments. (c) Eyring analysis between 283 K and 343 K to derive the activation parameters; the datapoint coloured black is the value previously reported (343 K; t$_{1/2}$ = 0.003 s) as determined by rapid quench flow, then ^{19}F NMR analysis[168].

Figure 46. A cover art submitted to the European Journal of Organic Chemistry. It shows a young researcher looking into the vast starry sky, accompanied by an NMR spectrometer. The shooting stars represent the fleeting information embedded in rapid irreversible chemical reactions, for example, the base-catalysed protodeboronation of penta-fluorophenyl boronic acid which has a half-life of 0.12 s. With the aid of a stopped-flow NMR technique, the researcher is able to capture the information from the rapidly evolving reactions, to gain information that will shed light on the reaction mechanism.

2.2.6 Identification of Transient Intermediates

In addition to monitoring very fast irreversible chemical reactions, the stopped-flow technique is also useful in identifying short-living intermediates that are otherwise impossible with traditional NMR experiments. An example is illustrated in Figure 47. The rates of the protodeboronation of arylboronic esters were reported to be significantly different from that of arylboronic acids[172]. In the case of 2,4-dimethylpentane-2,4-diol 2,3,4,6-tetrafluorophenyl boronic ester, the base-catalysed protodeboronation reaction proceeds at least two orders of magnitude faster than that of boronic acid. The protonated products from two different reactants were identical, and the intermediate ester boronate was only present in the first 300 ms. Consequently, by traditional NMR experiment only the product signals and the trihydroxyboronate (within 60 s) were able to be detected. Stopped-flow NMR experiments, however, can achieve a phenomenological deadtime of 0.22 s at a flow rate of 1 mL/s. By increasing the flow rate to 2 mL/s, the deadtime can be further reduced to 0.15 s. Therefore, stopped-flow NMR was able to distinguish the transient intermediate originating from the arylboronic ester, Figure 47b.

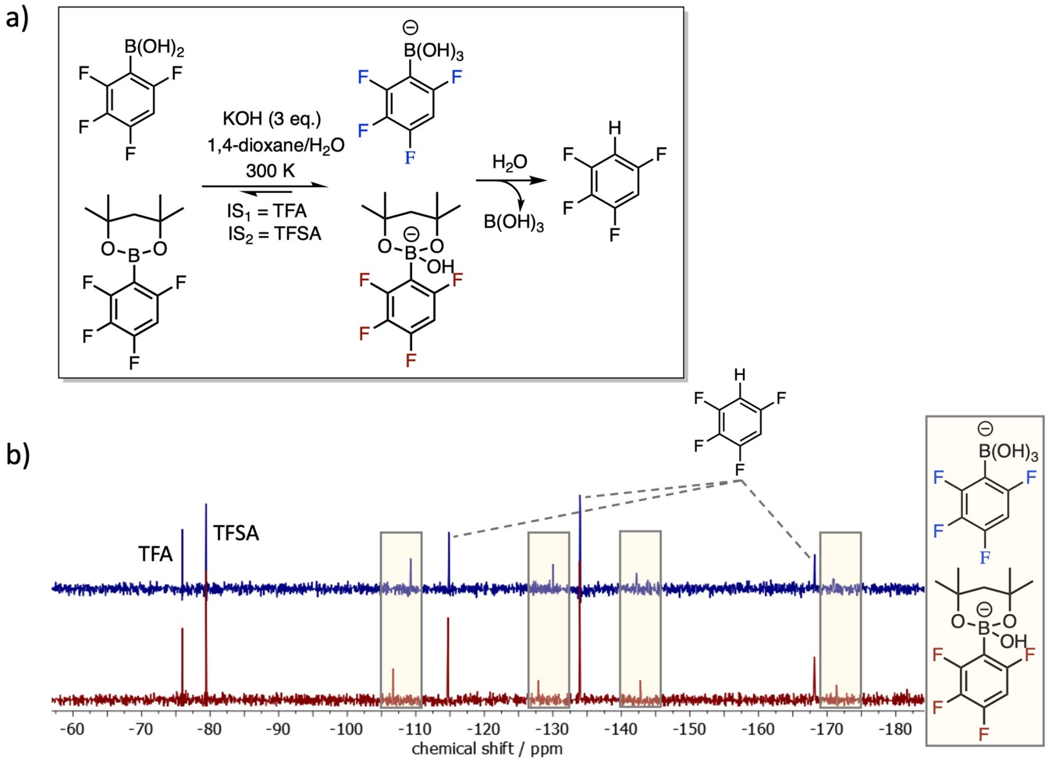

Figure 47. a) Reaction scheme of the protodeboronation of 2,3,4,6-tetrafluorophenyl boronic acid, and 2,4-dimethylpentane-2,4-diol 2,3,4,6-tetrafluorophenyl boronic ester. b) Stacked transient stopped-flow NMR spectra of the reactions, showing the intermediates, the product, and the IS signals. The product signals were identical from two reactants, the different intermediate signals were highlighted in light yellow boxes.

2.3 Chemical Exchange Studies Using a Non-pre-magnetised Channel

2.3.1 Choosing Appropriate Acquisition Parameters

The pre-magnetisation profile of channel-*D* has been previously evaluated in section 2.1.3. As explained earlier, if the solution is delivered via this non-pre-magnetised channel, the analytes will be 'NMR-*invisible*' as the spins do not establish the Boltzmann distribution. Instead, they will experience a T_1-dependent polarisation process. In the absence of other interferences such as chemical reactions, the analytes will simply display a longitudinal relaxation process, providing two requirements are carefully fulfilled, i) the pulse angle θ needs to be small to minimise the suppression of z-magnetisation by consecutive pulses; ii) the repetition time t_R needs to be short enough to afford sufficient data points to be collected for the fitting before reaching thermal equilibrium. An example of using this method to measure the ^{19}F T_1 value of 4-fluorophenal boronic acid in 1:1 dioxane/H_2O is illustrated in Figure 48b. A 0.0504 M 4-fluorophenyl boronic in 1:1 dioxane/H_2O solution was prepared. Sample was injected via the channel-D and measured immediately after a minimum trigger delay of 0.039 s in the stopped-flow cell. Spectra of 4-fluorophenyl boronic acid were acquired with 10° pulses, a 56818 Hz spectral window and a 1.086 s repetition time between pulses (0.786 s acquisition time and 0.3 s delay time). The gradient of slope equals to -0.505 s^{-1}, the T_1 value is therefore calculated to be (-1/-0.505) = 1.980 s, in good agreement with the T_1 value measured independently by Inversion Recovery experiment at 2.090 s.

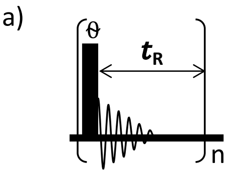

b) T_1-dependent polarisation via non-pre-magnetised channel

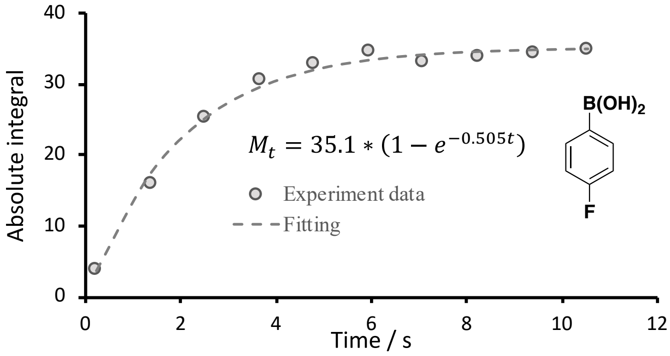

Figure 48. a) A basic pulse programme to monitor the absolute integral of analytes via the stopped-flow non-pre-magnetised channel. b) A graphical example of the fitting of signal integrals as an exponential function against time to calculate the T_1 value of ^{19}F in 4-fluorophenyl boronic acid.

To correctly reflect the T_1-dependent polarisation process, or in other words, to avoid signal suppression, as mentioned earlier, the pulse angle needs to be small in comparison to the repetition time between pulses. Insufficient relaxation during pulses will compromise correct quantification. This phenomenon was investigated using 4-fluorophenyl boronic acid as the test sample. The solution was delivered via channel-*D*, the experiments were acquired with identical parameters except for the variable pulse angles at 10°, 45°, and 90° respectively, repetition time between consecutive pulses was 1.56 s. Distinctive results from variable pulse angels were observed (Figure 49). The signals displayed an expected growth starting from slightly above zero, owing to the magnetisation during dead time. The latter part of the results appeared counter-intuitive, where the signals reached a plateau. By simulating the T_1-relaxation of the spins, it can be seen that only 10° pulses (Figure 49, grey circles) correctly represent the natural relaxation process, whereas 45° and 90° pulses both led to signal suppression as the repetition time of 1.56 s was too short for sufficient relaxation. These observations could be explained by the equations below.

$$M_{n+1} = \{[M_0 - (M_0 - M_n * cot\theta)e^{-\frac{t_R}{T_1}}] * \frac{[\Delta_1+\Delta_2+\cdots+\Delta_n]}{M_0} + x * M_0(e^{-\frac{t_n}{T_1}} - e^{-\frac{t_{n+1}}{T_1}})\} * sin\theta$$

$$M_0 = \frac{M_{n+1} - M_n * cos\,\theta * e^{-\frac{t_R}{T_1}}}{sin\theta * \left(1 - e^{-\frac{t_R}{T_1}}\right)}$$

Equation 12

M_0 is the thermal equilibrium, Δ_1, Δ_2, Δ_n represent the polarised spins during the 1st repetition time t_R, 2nd t_R, and nth t_R, therefore $[\Delta_1 + \Delta_2 + \cdots + \Delta_n]/_{M_0}$ denotes the proportion of magnetised spins in the system. $[M_0 - (M_0 - M_n * cot\theta)e^{-\frac{t_R}{T_1}}]$ denotes the sum of residual magnetisation from pervious pulse and recovered magnetisation during t_R. x is the pre-magnetisation coefficient, $x * M_0 * (e^{-t_n/T_1} - e^{-t_{n+1}/T_1})$ denotes the amount of magnetisation growth during t_R. Noteworthily, the thermal equilibrium M_0 was not directly measured here, instead it was calculated from the established steady-state, where M_{n+1} equates M_n, in the late period of the experiment. Equation 12 takes into consideration of two independent processes, one being the consecutive signal acquisition/suppression by pulses, the other being the partially magnetised spins continued being polarised inside the tube. The results iterated the significance of choosing appropriate pulse angle and repetition time, which again inevitably leads to the balance between sensitivity and data density. In practice, this could be determined with a prior knowledge of T_1 and the reaction lifetimes.

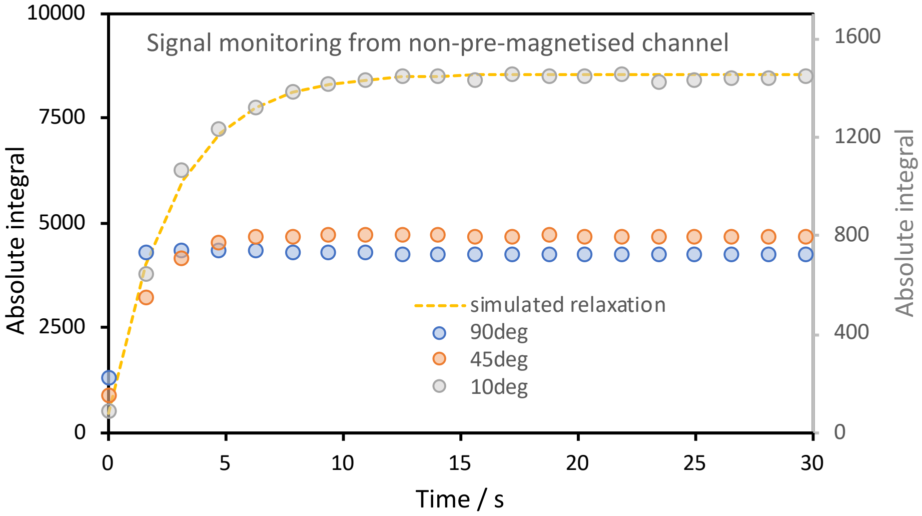

Figure 49. Signal monitoring from the non-pre-magnetised channel, using identical experimental parameters except for variable pulse angles 10°, 45°, and 90° respectively. Yellow dashed line shows the simulated longitudinal relaxation of T_1 = 2.7 s. Note the sensitivity reduction with decreased pulse angles, secondary axis was used for 10° pulses for visual guidance.

2.3.2 Effect of Pre-magnetisation on Reaction Profiles

In the presence of chemical reaction, the analytes delivered via the non-pre-magnetised channel will experience two processes, the T_1-dependent polarisation, and the chemical reaction. As mathematically predicted in section 2.1.2, the observed profiles of the analytes will be determined by the relaxation rate and the reaction rate. When these rates are comparable, for example, the base-catalysed protodeboronation of 2,3,5,6-tetrafluorophenyl boronic acid, which has a first order rate constant of 0.67 s^{-1} at 300 K, and a relaxation rate of ca. 0.9 s^{-1}, the reaction profile will deviate significantly from the '*real*' one when all substrates were delivered via pre-magnetised channels (see Figure 50 and Figure 41). The experiments were conducted under the same conditions as in traditional reaction monitoring experiments in section 2.2.4, the only difference being the reactant 2,3,5,6-tetrafluorophenyl boronic acid was delivered via channel-*D*. The reactant instantaneously converted to intermediate boronate, the boronate signals during the evolving reaction showed an initial rise followed by a decay (Figure 50, blue circles). The rise was due to that the polarisation of boronate exceeded the consumption of it in the first second. An internal standard TFA was prepared within the solution of the reactant hence no pre-magnetisation available, a second internal standard trifluoromethanesulfonic acid (TFSA) was delivered via pre-magnetisation channel to serve as a concentration reference. As expected, the absolute integrals of the TFA showed a longitudinal relaxation curve, starting with a 15% pre-magnetisation (Figure 50b, grey circles), while those of TFSA remained almost constant (Figure 50b, green circles). Figure 50c compares the conversion of the intermediate and product when the boronic acid was delivered via non-pre-magnetised and pre-magnetised channel respectively. In addition to the distinct shape of the boronate, the product also showed a difference. This was explained earlier in Figure 22, the product signals were contributed from two sources, one is from the polarised starting materials, the other is from the non-polarised starting material therefore continued to undergo a T_1-dependent polarisation and become 'NMR *visible*'. When the reaction rate is significantly greater than the relaxation rate, such as the protodeboronation of pentafluorophenyl boronic acid (Figure 51a), the consumption of boronate is too fast that only the '*tail*' of the decay was able to be captured. The product growth was essentially the T_1 polarisation of the product spins. As can be seen from Figure 51b, the concentration profiles (squares) were distinctly different from those that are pre-magnetised (solid lines). This distinction can provide a clear indicator to track the origin or destination of specific spins during the course a reaction.

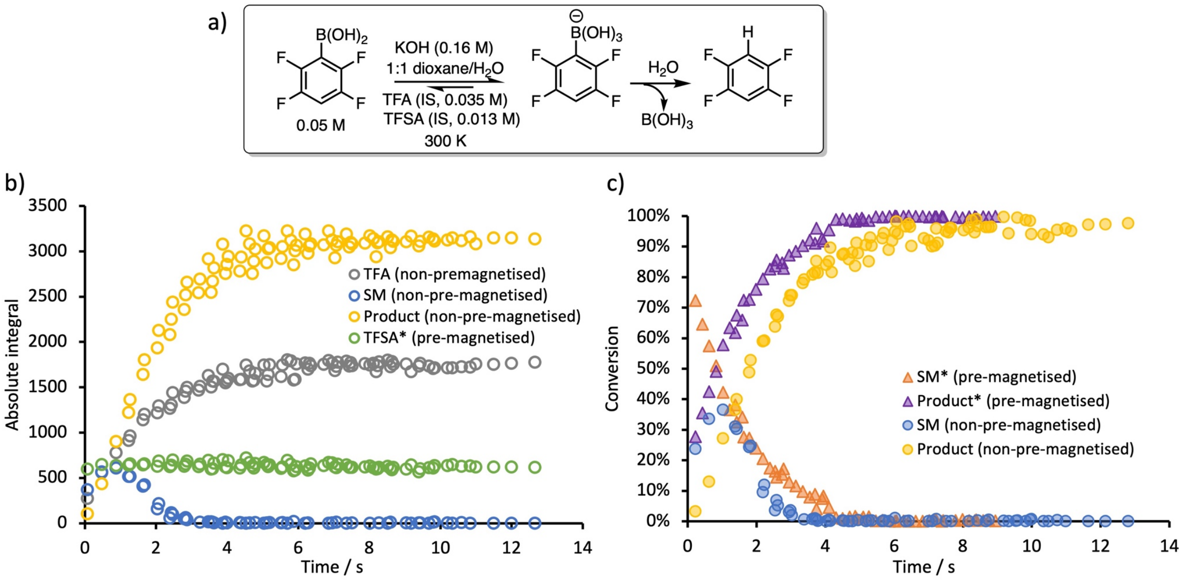

Figure 50. a) The scheme of the protodeboronation of 2,3,5,6-tetrafluorophenyl boronic acid. b) Monitoring the signal absolute integrals of the reaction. The boronic acid reactant and TFA (IS) was delivered via channel-*D* (non-pre-magnetised), KOH and TFSA (a second IS) was delivered via channel-*A* (pre-magnetised). c) A comparison of the reaction profiles, where reactants were delivered from different channels. Reaction profiles were reconstructed from 11 interleaved stopped-flow experiments, using 30° pulses, a repetition time of 1.16 s, and an incremented trigger delay list of {0.039, 0.44, 0.84, 1.24, 1.64, 2.04, 2.44, 2.84, 3.44, 3.84, 4.5 s}

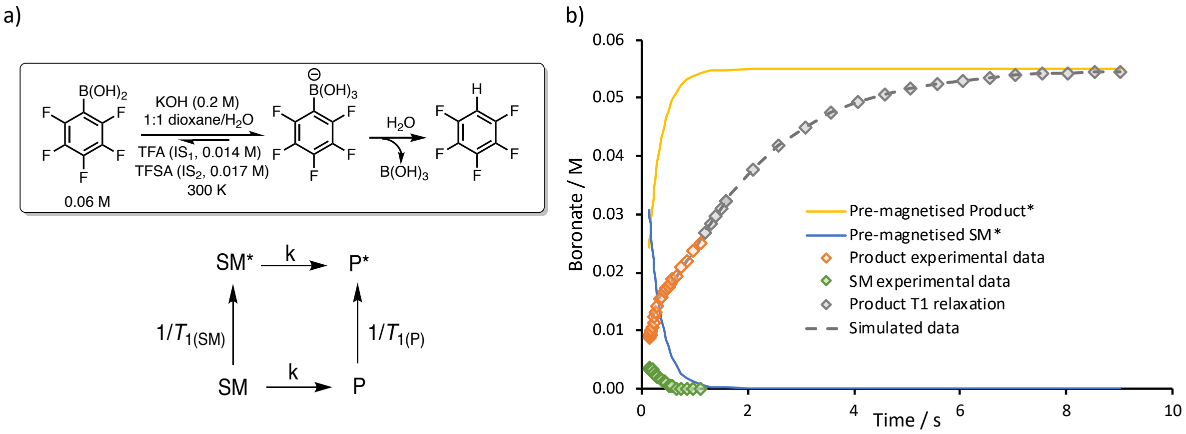

Figure 51. a) The scheme of the protodeboronation of 2,3,4,5,6-pentafluorophenyl boronic acid, and the processes when starting material (SM) / reactant was delivered via the non-pre-magnetised channel. b) The concentration profiles of the product signals (orange squares) and the SM signals (green squares). Yellow and blue solid lines represent the theoretical profiles for starting material and product under fully pre-magnetised conditions. Grey squares represent the continuous polarisation of product.

2.3.3 Probing Chemical Exchange Systems with Channel-D

After exploring the effects of non-pre-magnetisation on the reaction profiles, the work moved on to implement this method on challenging chemical reactions. The anion-initiated trifluoromethylation from the Ruppert–Prakash reagent[173], $TMSCF_3$, to carbon has gained great popularity as a synthetic method[174–178]. Earlier work in the Lloyd-Jones group has explored the mechanism of CF_3 transfer from R_3SiCF_3 (R = CH_3, or CH_3CH_2) to carbonyls (e.g., ketones and aldehydes)[169], providing a cornerstone for the investigation here. It was found the reaction turnover rates are dictated by the identity of the initiator cation, the concentration of the initiator counter-anion, the identity of the electrophiles, the identity of the reagent R_3SiCF_3, and the concentration ratio of electrophile/ R_3SiCF_3. Therefore, the overall reaction rates can be conveniently tuned from various factors. To design the reaction suitable for the stopped-flow system, the CF_3 transfer was conducted in THF at ambient temperature, TBAT ($[Bu_4N][Ph_3SiF_2]$) was chosen as the initiator, 4-fluorobenzaldehyde as the substrate, and $TMSCF_3$ and $TESCF_3$ as the competing reagents, Figure 52a. The ^{19}F nucleus on reagents, substrates and products allowed simultaneous analysis of all species involved in the reaction system, Figure 52b.

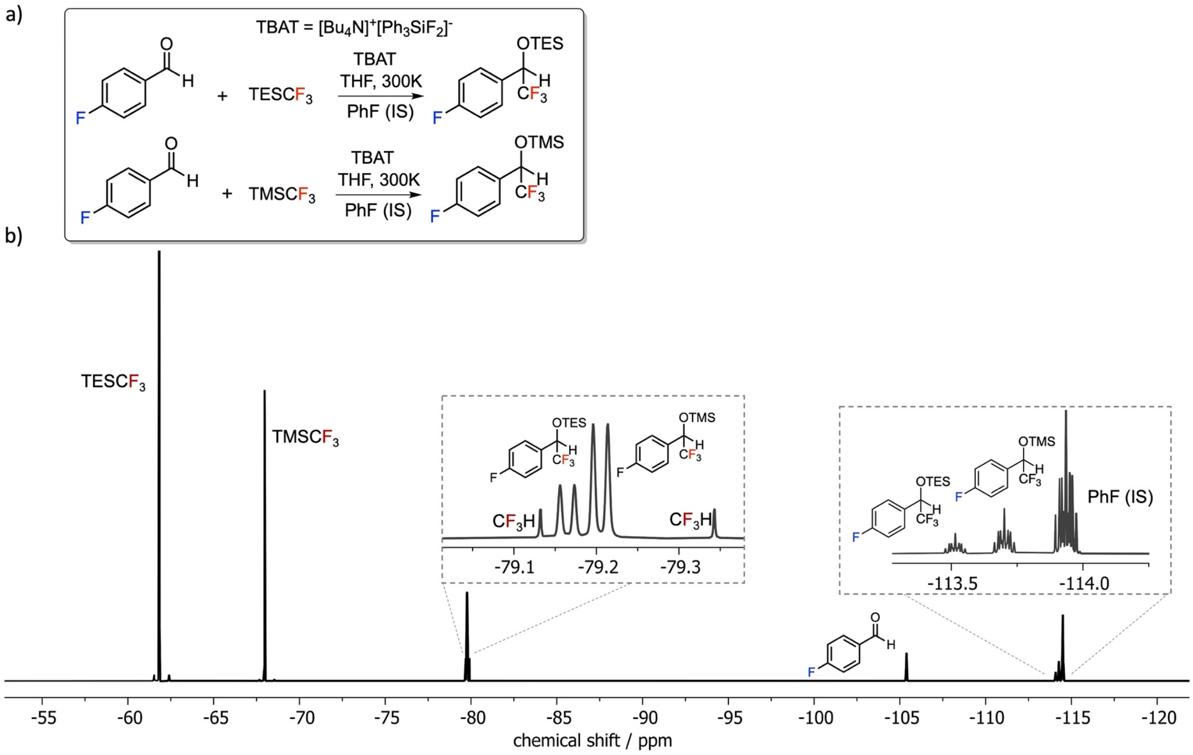

Figure 52. a) Trifluoromethylation of 4-fluorobenzaldehyde by $TESCF_3$ and $TMSCF_3$ as the CF_3 source respectively. b) A transient 1D ^{19}F spectrum of the reaction with all fluorinated species present.[169]

Preliminary studies began with testing the reaction rates of $TMSCF_3$ with aldehyde, in the presence of initiator. All stock solutions were prepared in the glovebox before connecting to N_2 filled stopped-flow system. 0.5 M 4-fluorobenzaldehyde, 0.5 M TMSCF3, and 0.5 M fluorobenzene (IS) were prepared in stock solution *A*, 3 mM TBAT was prepared in stock solution *B*. The $TMSCF_3$/aldehyde ratio was therefore constant at 1:1. The delivery volume of solution *A* remained at 300 uL, volume of *B* was incremented from 50 uL, 75 uL to 100 uL, and solvent from a third syringe was injected to compensate for the total volume of 600 uL. Consequently, by incrementing the [TBAT], the reaction proceeded faster as shown in Figure 53. In addition to the main product, an approximately 8% CF_3H was generated (Figure 53c), which was likely due to the traces of water vapor diffusing in from the thermostat liquid (50/50 water/ethylene glycol).

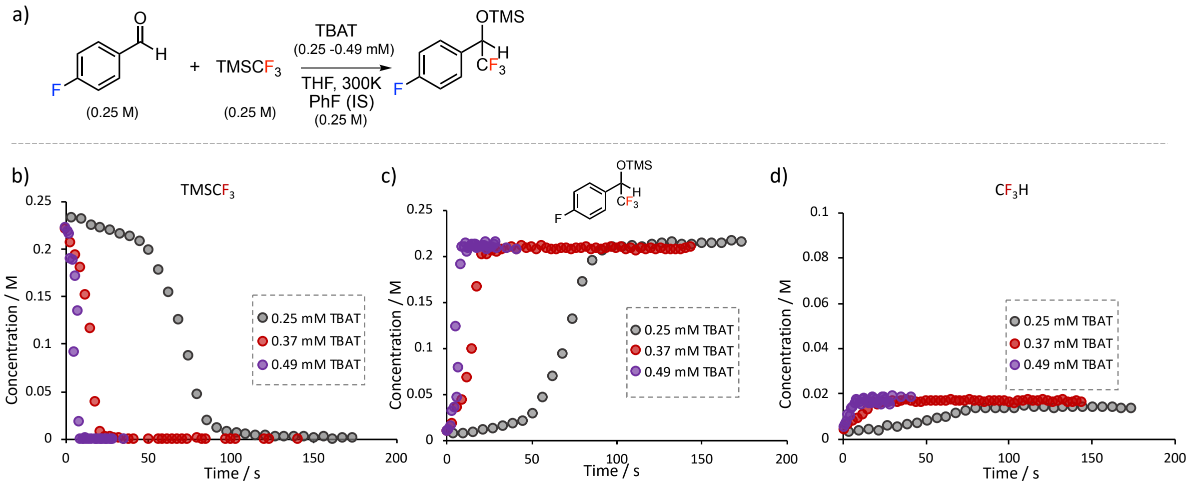

Figure 53. a) The trifluoromethylation of 4-fluorobenzaldehyde by $TMSCF_3$, only the initiator TBAT concentration was incremented. The temporal-concentration evolution of b) reagent $TMSCF_3$, c) product, and d) side-product CF_3H.

The initially confusing water interference was confirmed by increasing the residence time of TBAT within the stopped-flow system while keeping all other reaction conditions identical. Figure 54a shows a competing CF_3 transfer between $TMSCF_3$ and $TESCF_3$. The reaction conditions are 0.21 M aldehyde, 0.15 M $TMSCF_3$, 0.15 M $TESCF_3$ (from stock solution *A*), and 0.25 mM TBAT (from stock solution *B*), with an excessive amount of CF_3. The results showed the longer the TBAT is resident in the stopped-flow system (Figure 54d), the more CF_3H is generated. From Figure 54b and 54d, it can be seen the rapid generation of CF_3H is closely associated with the TBAT-catalysed reaction of $TMSCF_3$. Excessive $TESCF_3$ (Figure 54c) did not further produce CF_3H. Since $TMSCF_3$ was consumed to generate the *O*-silylated product (Figure 54g) and by-product CF_3H (Figure 54d), as a result, the $TESCF_3$/aldehyde concentration ratio varied based on the amount of water present. This led to a variation in the $TESCF_3$ reaction rates (Figure 54c). To minimise the impact of water, a ‘flush’ of TBAT was conducted, to purge the water-contaminated solution and refill with fresh TBAT prior to each stopped-flow measurement.

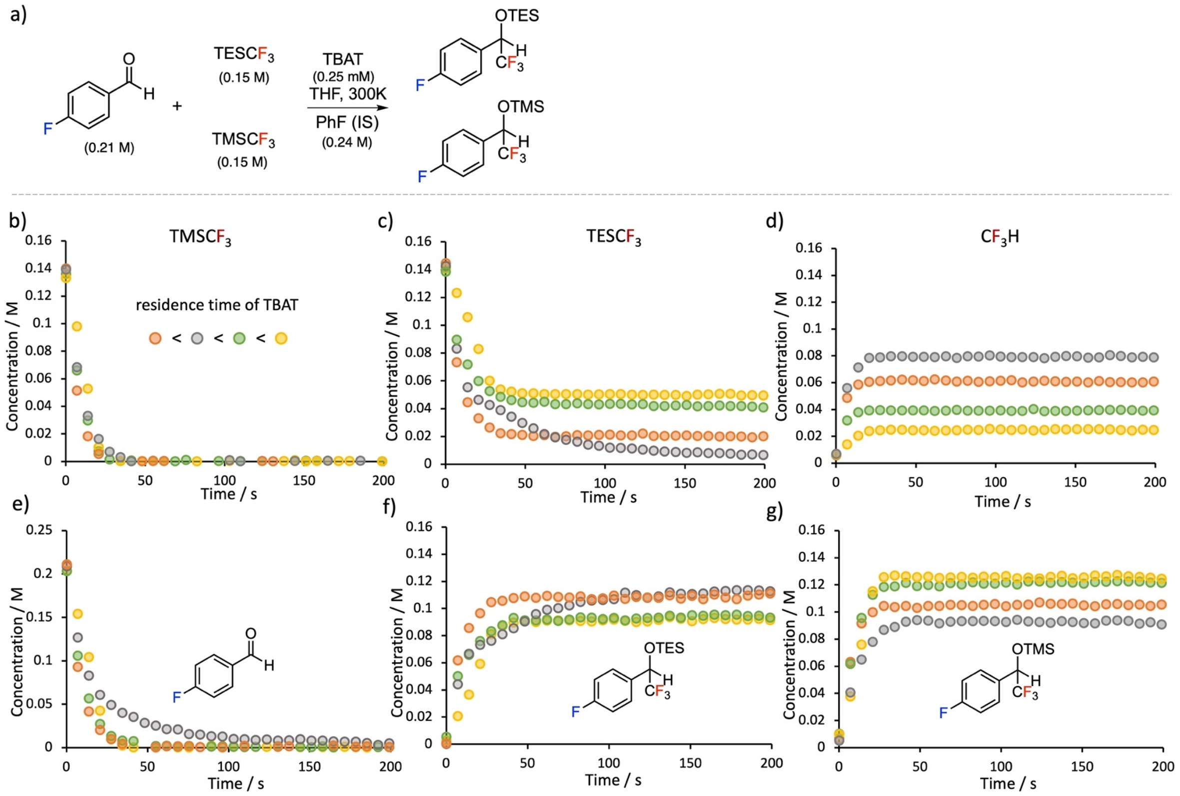

Figure 54. a) The trifluoromethylation of 4-fluorobenzaldehyde from competing $TMSCF_3$ and $TESCF_3$ reagents. The reaction conditions were kept identical, the only difference being the incremented residence time of TBAT within the stopped-flow system to probe the water interference from thermostat liquid infiltration. Temporal-concentration evolution of b) reagent $TMSCF_3$, c) reagent $TESCF_3$, d) side-product CF_3H, e) electrophile aldehyde, f) OTES-product, and g) OTMS-product.

Furthermore, a dominated turnover by $TMSCF_3$ was observed at the beginning stage of the competing reaction between 1:1 $TMSCF_3$ and $TESCF_3$. This was rationalised to be the less-hindered $TMSCF_3$ monopolising the anion from the initiator. On near-complete consumption of $TMSCF_3$, the sterically bulkier $TESCF_3$ started to engage in the reaction and underwent accelerated turnover. This dominant behaviour of $TMSCF_3$ over $TESCF_3$ was consistent under different conditions, Figure 55. However, the overall trifluoromethylation rates varied drastically between experiments conducted using different sources of reagents, Figure 55b-d. For example, entry b), Figure 55b) was performed using an aged bottle of $TESCF_3$, and a significantly higher loading of TBAT was added yet the reaction still proceeded slower than the other two entries. This irreproducibility by reagents from different batches or suppliers was also observed in earlier work[169], and is due to traces of unidentified exogenous inhibitors. Therefore, in the following investigation, unless otherwise stated, all reactions were conducted and compared using the same sources of reactants as entry d). All stock solutions were freshly prepared in the glovebox and measured on N_2-filled stopped-flow system immediately after.

a)

Reactants	entry b)	entry c)	entry d)
Aldehyde [M]	0.2	0.25	0.17
$TMSCF_3$ [M]	0.14	0.15	0.13
$TESCF_3$ [M]	0.15	0.15	0.13
TBAT [mM]	1.5	0.4	0.3

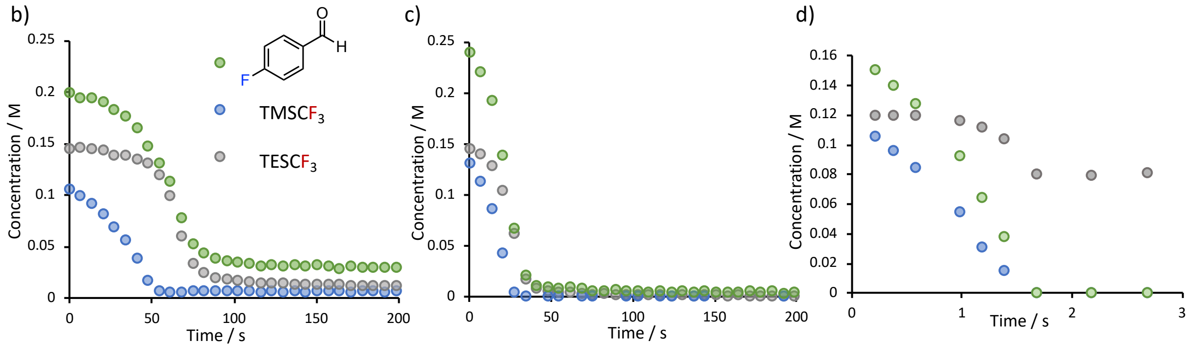

Figure 55. a) Conditions of the competing reaction between $TMSCF_3$ and $TESCF_3$ in THF at 300 K, experiments were conducted on different days using different sources of reagents. b) - d) Temporal-concentration profiles of the aldehyde, $TMSCF_3$ and $TESCF_3$, showing irreproducible results. Entry d) used a bottle of freshly ordered and distilled $TESCF_3$, which was utilised throughout following experiments.

The mechanism for the CF_3 transfer from $TMSCF_3$ to a carbonyl electrophile, in this case, 4-fluorobenzaldehyde, was proposed in Figure 56a.[169] The catalytic initiator reacts with $TMSCF_3$ to generate the silicon-free CF_3^- carbanion, which undergoes rapid equilibrium with $TMSCF_3$ again to afford the dominant bis(trifluoromethyl) siliconate anion. The CF_3^- then reacts with the carbonyl to proceed the trifluoromethylation, accompanied by the cation from the initiator. When $TESCF_3$ was added to the reaction, a competition between $TESCF_3$ and $TMSCF_3$ was observed, as shown in Figure 56. As discussed earlier, $TMSCF_3$ dominated the early turnover before $TESCF_3$ participated in. The reaction conditions used here were 0.18 M aldehyde, 0.13 M $TESCF_3$ and $TMSCF_3$, and 0.18 M PhF (IS) in THF at 300 K. TBAT concentration was increased from 0.24 mM, 0.30 mM, to 0.67 mM. At highest TBAT loading, the reactions completed within the deadtime of the stopped-flow experiment (0.22 s at 1 mL/s flow rate). Note the reduced production of OTMS-product, due to the extremely rapid water consumption of $TMSCF_3$ to form CF_3H. Two distinct trifluoromethylated products were generated (Figure 56b and 56c). However, whether the CF_3 on the two *O*-silylated products came exclusively from their parent reagents remained unknown. To probe this question, the non-pre-magnetised (*D*) channel (channel-*D*) was employed to serve as a '*magnetic-labelling*' tool for the CF_3 sources. If one reagent is delivered via channel-*D*, the CF_3^- anion from this reagent will not be polarised, hence '*magnetic-labelled*'. This distinct information will be carried with the CF_3 along its evolution.

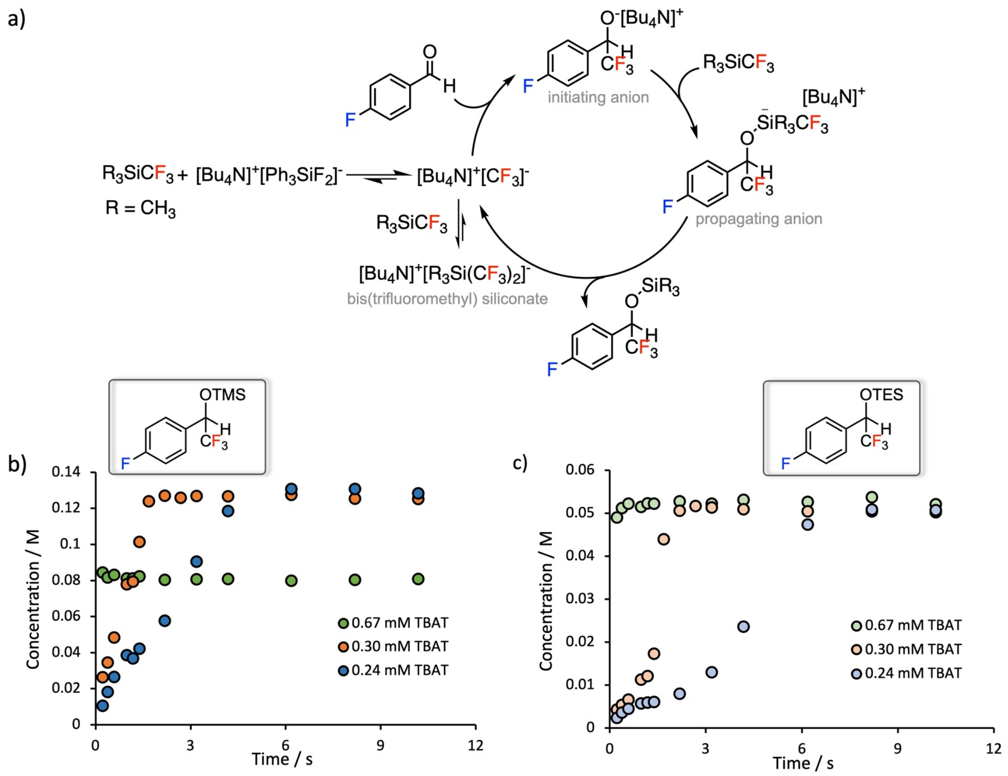

Figure 56. a) A proposed mechanism for the trifluoromethylation from $TMSCF_3$.[169] The concentration evolution focusing on the *O*-silylated products from b) $TMSCF_3$ and c) $TESCF_3$.

Firstly, temporal-concentration profiles of the products were monitored under standard conditions, where all solution were delivered via pre-magnetised channels (Figure 57a and 57b). The ^{19}F NMR analysis of the products have two different ^{19}F resonances, CF_3 from the reagent ($TMSCF_3$ or $TESCF_3$), and F from the aldehyde. The concentration of products was calculated using both ^{19}F respectively. When all species were pre-magnetised, the two ^{19}F atoms afforded well-agreed outcomes as expected. However, when only one reagent, for example $TMSCF_3$ was delivered via channel-*D*, while all other solutions via pre-magnetised channels, the non-polarised CF_3 carried this '*magnetic-label*' into the -OTMS product, in contrast to the pre-magnetised F originated from the aldehyde. The CF_3-derived product concentration consequently displayed a reduced profile comparing to its F-derived counterpart, as shown in Figure 57d and 57e. Intriguingly, since $TESCF_3$ was delivered via pre-magnetised channel as normal, without perturbation, both the CF_3 and F in the -OTES product should be pre-magnetised and display identical concentration evolution. However, this obviously contradicted the observation shown in Figure 57e. The CF_3-derived concentration of OTES-product (Figure 57e, green circles) was reduced from its F-derived counterpart. This is a straightforward indicator of chemical exchange between the CF_3^- anions from $TMSCF_3$ and $TESCF_3$. Correspondingly, the chemical exchange induced magnetisation transfer between the

CF_3 anions has raised the CF_3 of the -OTMS product (Figure 57e, yellow circles) to > 50%. This phenomenon was further proved by delivering TESCF_3 via channel-*D* (Figure 57f), displaying a reduction in the CF_3 concentration of the -OTMS product (Figure 57f, yellow circles).

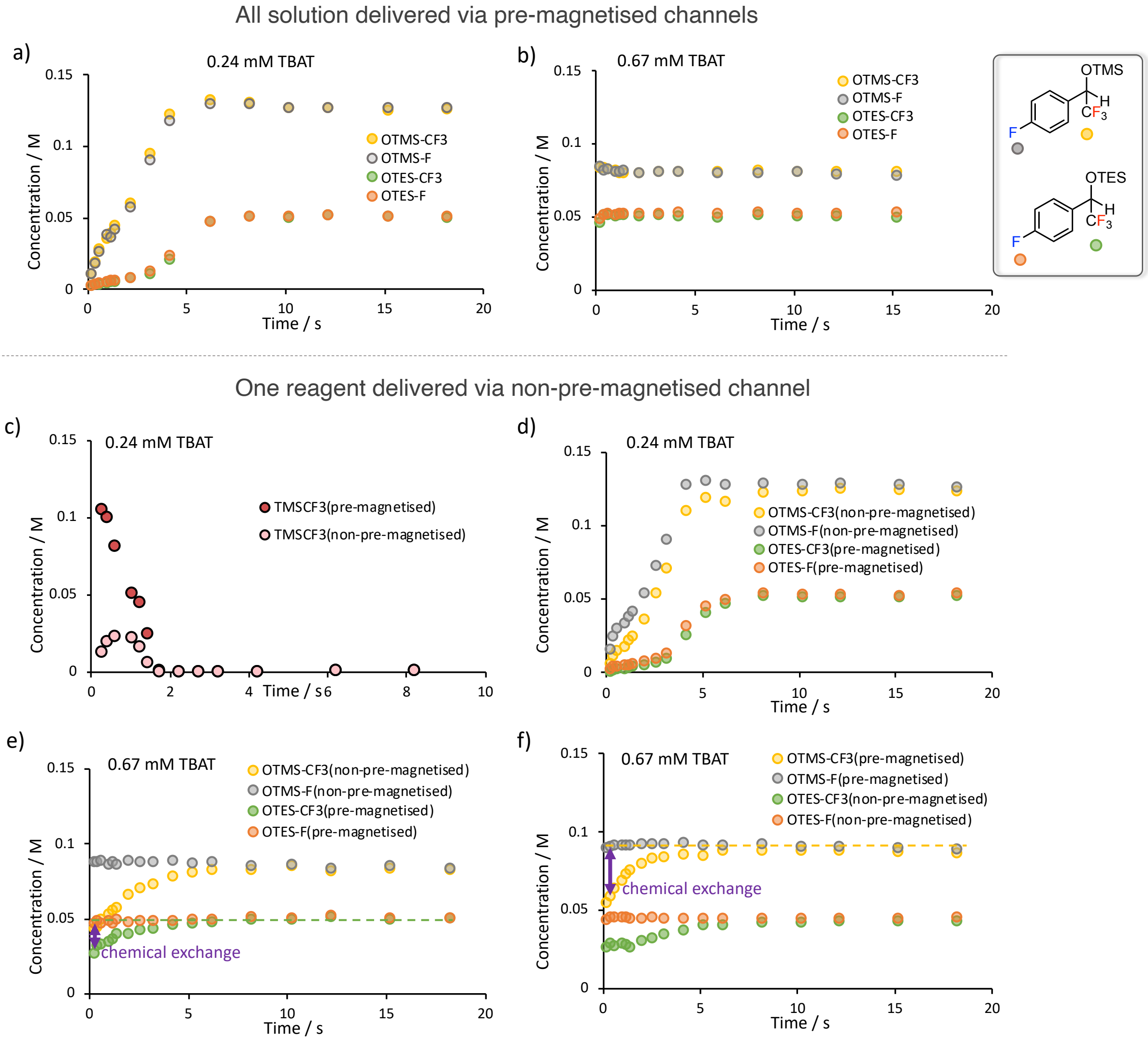

Figure 57. a) - b) The concentration evolution of *O*-silylated products, initiated by different TBAT loading. All solutions were delivered via pre-magnetised channels, the concentrations derived from -F and -CF_3 overlapped well with each other. c)-e) TMSCF_3 was delivered via channel-D. c) The different appearance of TMSCF_3 consumption due to non-pre-magnetisation. d) The slight deviation of *O*-silylated products profiles showing the chemical exchange, although not as obvious as e) and f) due to the lower TBAT concentration, i.e., slower reaction rate. e) A distinct disturbance in the OTES-CF_3 profile due to chemical exchange with non-pre-magnetised TMSCF_3. f) TESCF_3 was delivered via channel-D. A disturbance in the OTMS-CF_3 product was observed due to the chemical exchange, indicated by purple arrow.

Chapter 3 Longitudinal Relaxation Time Measurements

3.1 Importance of T_1 Measurements

T_1 measurements has been a long-standing topic since the early days of NMR spectroscopy. Section 1.2.1 introduced the variety of methods to measure T_1. Here the importance of T_1 measurements will be illustrated in the context of quantitative NMR (qNMR). The magnitude of T_1 for each of the nuclei being measured places limits on the acquisition rate of consecutive scans. That is, the entire spin ensemble needs to achieve complete relaxation (or equal relaxation for relative quantitation) before application of the next RF pulse. For example, for experiments using 90° pulses, the repetition time between consecutive excitation pulses, t_R, should be $\geq 5\times T_1$ to allow ≥99.3 % relaxation. When faster acquisitions are required, the pulse angle θ, can be reduced from 90° to allow shorter repetition time (t_R), at a penalty of sensitivity. Specifically, 99.3 % relaxation requires $t_R = 2.9\times T_1$ when $\theta = 30°$, affording a 50% sensitivity; and $t_R = 0.8\times T_1$ when $\theta = 10°$, affording a 17% sensitivity. Failure to adhere to this condition will lead to unevenly relaxed spins and inaccurate quantification. Therefore, T_1 measurements are recommended prior to any qNMR experiment to allow appropriate setup of NMR acquisition parameters. Noteworthily, in daily NMR experiments, the relaxation delays (RD) are sometimes set to an estimated value, particularly in automated experiments. This practice normally uses long RD to avoid signal suppression. However, it not only takes elongated experimental time and does not guarantee sufficient relaxation, therefore still posing risks to inaccurate quantitation.

Figure 58 shows the ^{31}P spectra of a mixture of 1:1 $O{=}PPh_3$ (T_1 = 3.5 sec) and PPh_3 (T_1 = 16 sec), demonstrating the impact of how incomplete relaxation leads to inaccurate quantitation. T_1 measurements of ^{31}P in standard 5mm NMR tube were performed on a mixture of 0.1021 M PPh_3 and 0.1008 M $O{=}PPh_3$ in solvent 9:1 THF/ H_2O. Inversion Recovery experiments for PPh_3 were acquired with a relaxation delay time of 80 s ($>5{*}T_1$), 0 dummy scan, 2 number scans, and an acquisition time of 0.05 s to allow optimal S/N and complete decay of FID. A variable delay list of 15 values/s {0, 0.05, 0.1, 0.5, 1, 3, 5, 9, 13, 18, 25, 40, 60, 80, 100} was used for T_1 measurement. Inversion Recovery experiments for $O{=}PPh_3$ were acquired with a relaxation delay time of 15 s, an acquisition time of 0.1 s, 0 dummy scan and 2 number scans. A variable delay list of 10 values/s {0, 0.01, 0.05, 0.1, 0.5, 1, 3, 5, 10, 15} was used for T_1 measurement. The spectrum in Figure 58a allows complete relaxation for $O{=}PPh_3$ but incomplete relaxation for PPh_3. This leads to suppression of the PPh_3 peak, thus an underestimated integral. In Figure 58b accurate quantitation is achieved by elongating t_R to ensure complete relaxation for both compounds.

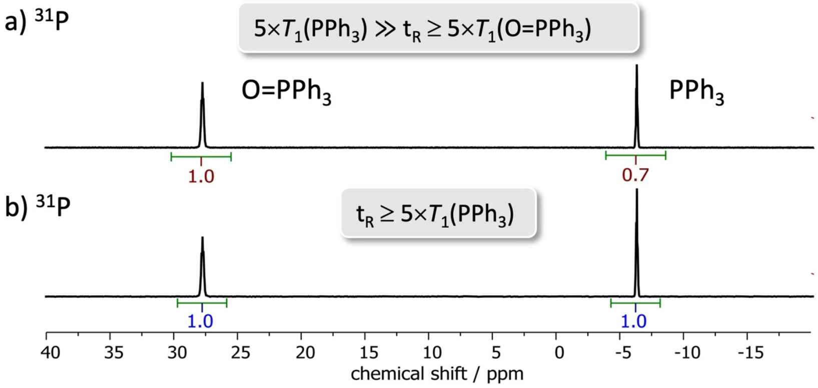

Figure 58. a) 1D ^{31}P NMR spectrum of 1:1 O=PPh$_3$ and Ph$_3$P. Incomplete relaxation of PPh$_3$ leads to reduced integral values for PPh$_3$ (maroon integrals). b) The same spectrum acquired with complete relaxation for both compounds, yielding accurate quantitation (blue integrals).

Another example is shown in Figure 59, highlighting the effect of an incorrectly parametrized ^{13}C{^{1}H} spectrum of 1,1-diphenyl-2-propyn-1-ol, where t_R<<5×T_1. In these inverse-gated proton-decoupled experiments, the proton decoupler is turned on only during the acquisition of free-induction-decay (FID) and turned off during RD to dissipate the Nuclear Overhauser Effects (NOEs). In general, the closer proximity to neighbouring protons, the greater the effect of the NOEs on the individual ^{13}C nuclei. Figure 59a shows the unequal NOEs at the different ^{13}C chemical sites lead to incorrect quantitation. When $t_R \geq 5\times T_1$ (Figure 59b), in this specific case, where only CH groups and quaternary carbons are present, the NOEs are dissipated, and accurate quantitation was retained. Commonly when CH$_2$ and CH$_3$ units are present, up to 10×T_1 is required to fully dissipate the greater NOEs.

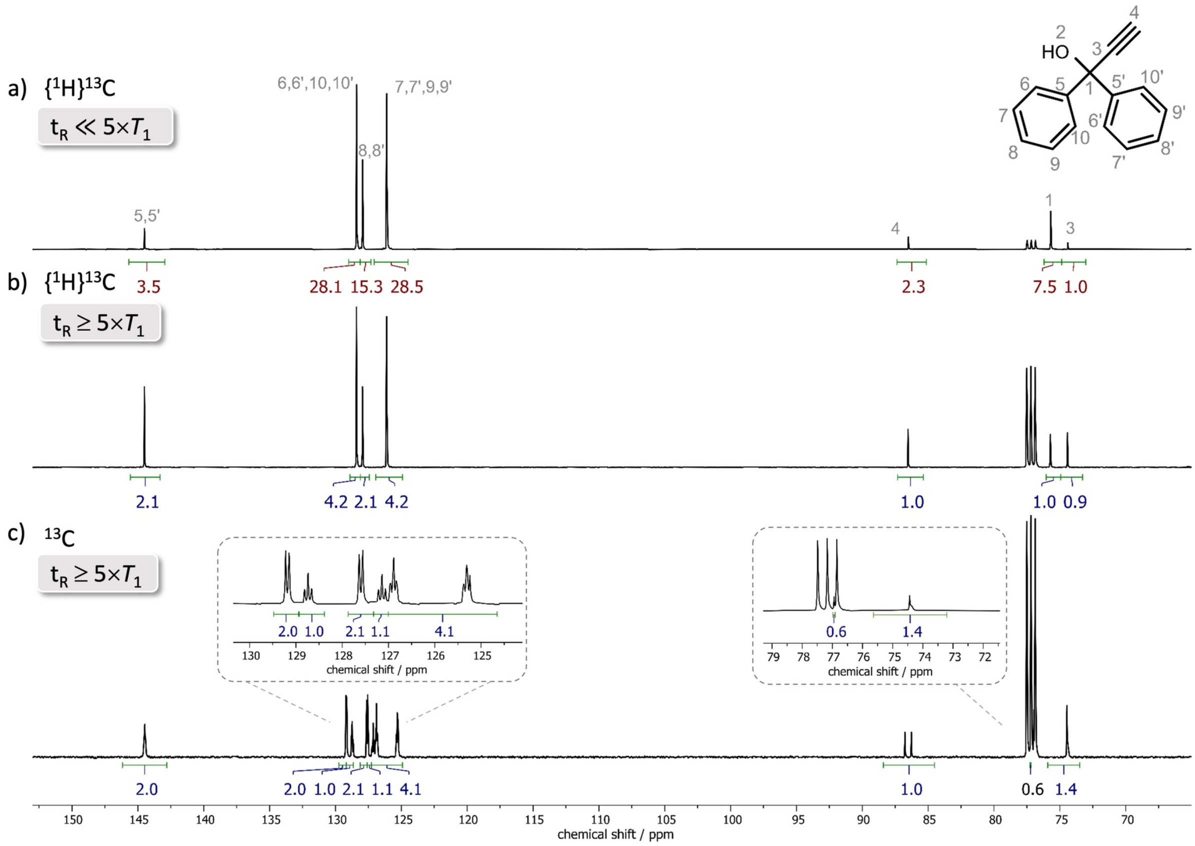

Figure 59. a) Inverse-gated $^{13}C\{^1H\}$ NMR spectrum of 1,1-diphenyl-2-propyn-1-ol acquired with $t_R \ll 5\times T_1$. The differential NOEs contributions at the seven ^{13}C sites result in incorrect quantitation (maroon integrals). b) The same spectrum acquired using $t_R \geq 5\times T_1$, so that NOEs are dissipated, and qNMR is established (blue integrals). c) ^1H-coupled ^{13}C spectrum acquired with $t_R \geq 5\times T_1$, both multiplicity and accurate quantitation retained.

Besides standard 1D experiments, T_1 measurements are also necessary before kinetic analysis. Similar to the investigation in pre-magnetisation effects, this can be demonstrated by a simulated first order reaction 'reactant A→product B' of reaction rate constant k. The concentrations of reactant A and product B at time t follow the equations:

$$[A]_t = [A]_0 \times e^{-kt}$$

$$[B]_t = [A]_0 \times [1 - e^{-kt}]$$

The recovered magnetisation during repetition time between scans, if under 90° pulses, follows the longitudinal relaxation recovery equation:

$$M_t = M_0 \times \left[1 - e^{-t_R/T_1}\right]$$

The observed NMR signals are governed by two processes, one from the reaction itself, the other from the relaxation recovery between consecutive scans. The overall results of the observed signals in an NMR experiment therefore follow the equation:

$$[A]_t = [A]_0 \times e^{-kt} \times \left[1 - e^{-t_R/T_{1A}}\right]$$

$$[B]_t = [A]_0 \times [1 - e^{-kt}] \times \left[1 - e^{-t_R/T_{1B}}\right]$$

This is a multiplication of two first-order processes. Figure 60 shows two examples of how the NMR acquisition parameters impact the observed reaction profiles. Figure 60a presents a scenario where the repetition time between scans is too short to afford sufficient relaxation, the signal saturation therefore directly leads to inaccurate kinetic analysis, a 50% error in the observed rate constant. Figure 60b shows an alternative approach to maintain the accurate quantitation as well as increasing the temporal resolution by using a smaller pulse angle. By reducing the pulse angle from 90° to 10°, the required repetition time t_R between scans is reduced from $5\times T_1$ to $0.8\times T_1$ for a 99.3% relaxation recovery, and correct kinetic analysis is obtained.

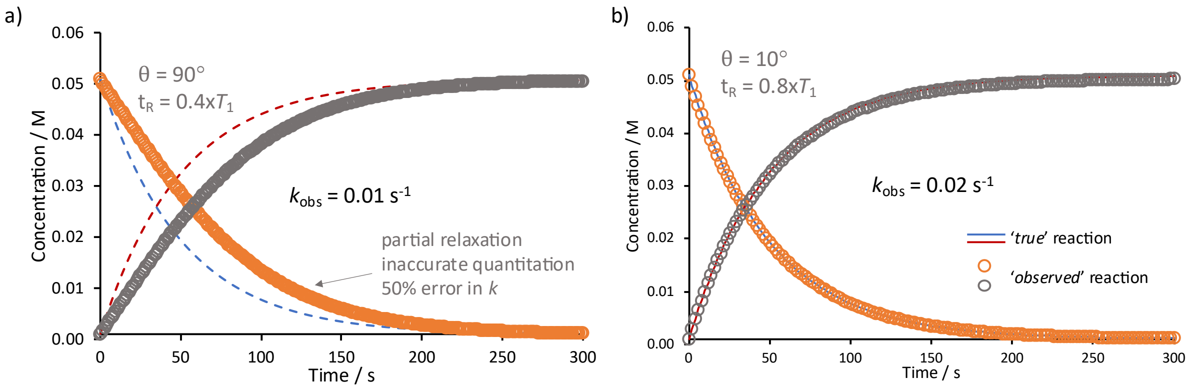

Figure 60. a) Simulated reactions profiles of a first order reaction 'reactant→product' (k=0.02 s^{-1}, $T_{1\text{reactant}}$=0.8 s, $T_{1\text{product}}$=2.5 s), monitored by NMR. a) when pulse angle θ=90°, interscan delay t_R (1.0 s) $\ll 5\times T_1$, the incomplete relaxation (circles) leads to significantly inaccurate kinetic analysis (lines). b) When θ=10°, which reduces the required t_R to $0.8\times T_1$ for a 99.3% relaxation recovery, accurate quantitation is retained. Reaction rates were derived by non-linear regression of the reactant concentration.

This simulation is further proved experimentally by an incorrectly parametrized ($t_R << 5\times T_1$; θ = 90°) experiment. Figure 61 shows the *in-situ* stopped-flow ^{19}F NMR analysis of the protodeboronation of 2,3,4,6-tetrafluorophenyl boronic acid as an experimental example. The repetition time t_R was set deliberately too short for adequate relaxation, resulting in experimental data (grey circles) that deviates considerably from the real temporal concentration profile (orange dashed line). The obtained NMR spectra (Figure 61c) and the non-linear first-order regression (Figure 61a, black line) both appeared to be reasonable, but giving a 36% error from the correct reaction rate. By proper adjustments of the repetition time t_R, and the pulse angle θ, reliable quantitation is achieved again, with the aid of interleaved approach when necessary (Figure 61b).

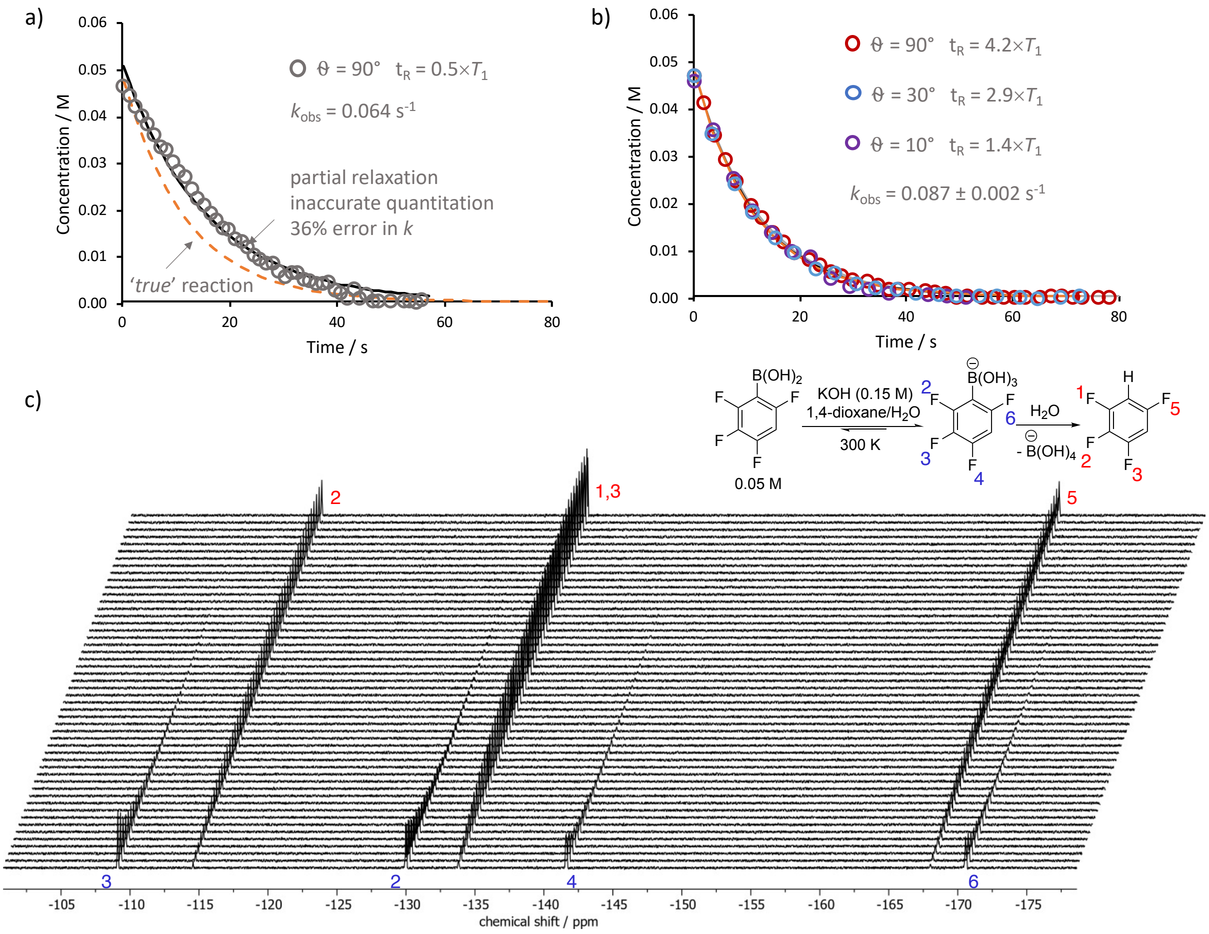

Figure 61. The protodeboronation of 2,3,4,6-tetrafluorophenyl boronate monitored by stopped-flow ^{19}F NMR spectroscopy. a) Repetition time t_R set too low, partially relaxed spins led to inaccurate kinetic analysis. b) Using variable pulse angle θ, repetition time t_R allowed sufficient relaxation in all cases, hence accurate quantitative analysis. c) Stacked stopped-flow ^{19}F spectra for the *in-situ* reaction monitoring in a), grey circles.

3.2 T_1 Measurements by FLIPS

The examples above reiterated the importance of prior determination of the longitudinal relaxation time constants T_1 for all of the nuclei being analysed in a qNMR experiment. As can be seen from previous sections, throughout the stopped-flow project, T_1 measurements have indeed been conducted extensively, either prior to reaction monitoring, or for pre-magnetisation investigation. The reason is straightforward, T_1 constants are important parameters for any quantitative NMR experiments, and the polarisation process is directly governed by the T_1 constants of studied spins as well. Among the range of T_1 methods introduced in Section 1.2.1, we used the most widely used method, the Inversion Recovery experiment for our routine T_1 measurements. However, during the investigation in the non-pre-magnetisation channel (section 2.3.1), an interesting phenomenon was observed. When inputting the analytes via the pre-magnetised channels and using the pulse sequence in Figure 48a, a trend of signal integrals against the pulse angle came to attention. Similar trends were observed consistently for all samples. An example of PPh_3 and $O=PPh_3$ is shown in Figure 62. It was noted that upon 90° pulses, signals were directly suppressed to a minimum intensity and remained unchanged, whereas at 60° and 30° pulses signal integrals went through a curved slide and eventually reached a '*steady-state*' at different intensities. All experimental parameters were kept identical except for the pulse angle. Furthermore, the '*steady-state*' of PPh_3 and $O=PPh_3$ varied, for instance, 30° pulses yielded the relatively highest integral for PPh_3 (Figure 62a) while the highest integrals for $O=PPh_3$ came from 60° pulses (Figure 62b). With the prior knowledge of T_1 values, it is sensible to extrapolate longitudinal relaxation must have played an important role here. Therefore, this unintentional observation triggers a question - 'how do the spins evolve under the application of the pulse sequence and lead to the different shapes of decline?'

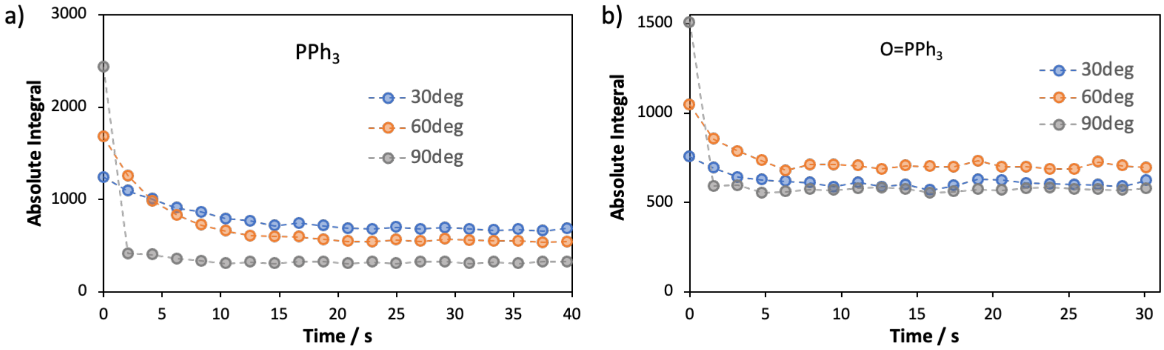

Figure 62. Experiments showing the decaying trend of absolute signal integrals obtained from experiments with variable pulse angle. a) PPh_3 (T_1=16.0s) experiment gives highest integral after reaching steady-state under 30° pulses; b) $O=PPh_3$ (T_1=3.6s) experiment gives highest integral under 60° pulses.

With this question in mind, a dissection of the magnetisation evolution under the pulse sequences was conducted. Figure 63a and 63b shows the pulse sequences for Inversion Recovery and FLIPS experiments respectively. The key difference between them is that rather than step-wise analysis of the exponential relaxation recovery, FLIPS acquires one scan after each excitation pulse, allowing collection of all data in a single experiment, hence greatly reduces spectrometer time. Figure 63c-e shows the magnetisation evolution under these sequences respectively. If the transverse magnetisation (M_{xy}) is completely dephased during the repetition time t_R between consecutive scans, the bulk magnetisation is aligned solely along the z-axis upon the application of the next excitation pulse. When $\theta = 90°$, Figure 63d, after the initial spectrum, the acquired signal directly reflects the longitudinal relaxation recovery during t_R. Alternatively, when $\theta \neq 90$, Figure 63e, there is residual z-magnetisation (blue arrow) after the pulse, and this eventually reaches a steady-state.

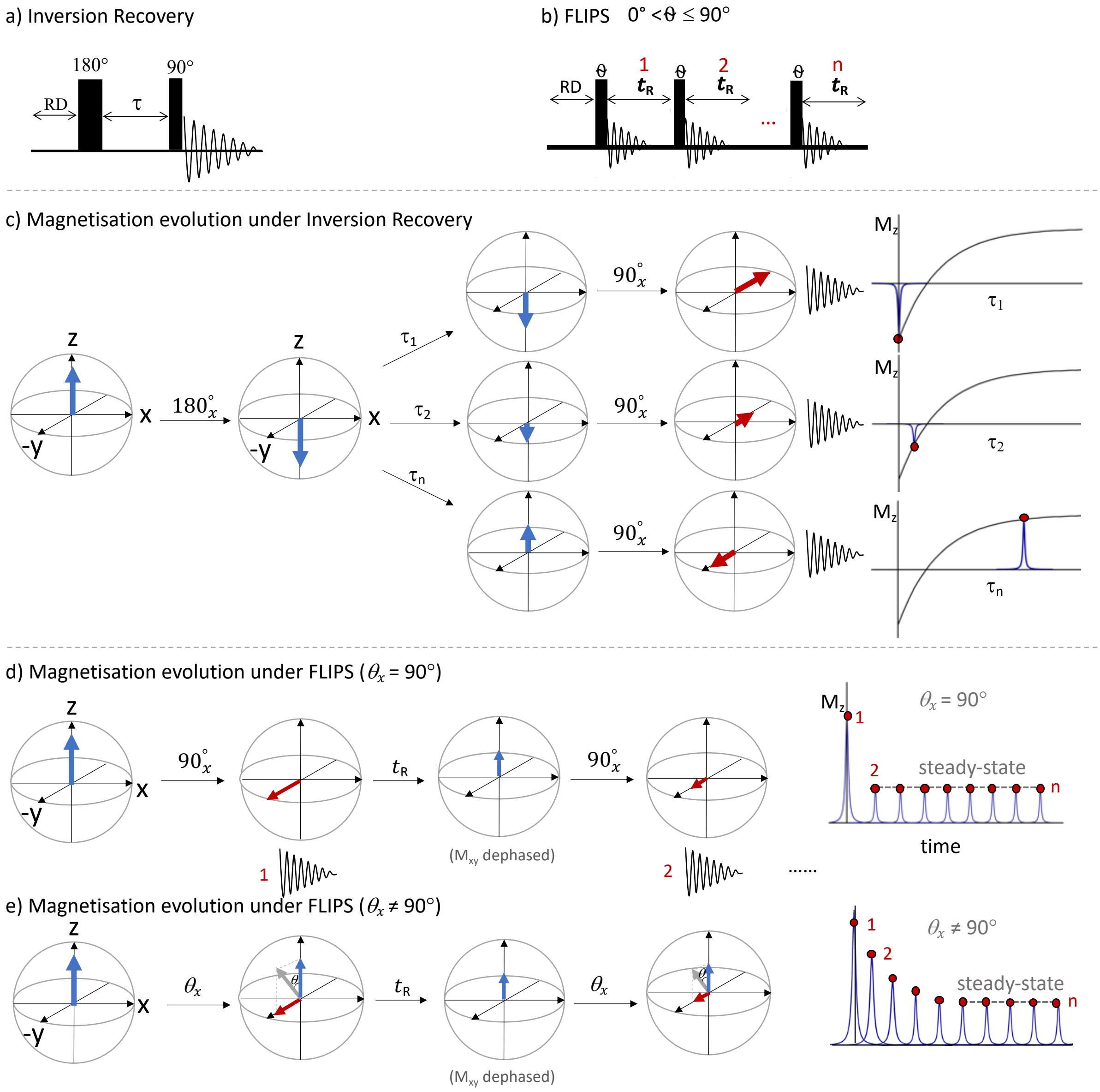

Figure 63. Pulse sequences of a) the Inversion Recovery experiment, and b) the FLIPS experiment. Graphic representation of the magnetisation evolution under c) the Inversion Recovery experiment, each signal is acquired after a variable delay time t_R, as shown on the right, these signals sample the recovery curve allowing calculation of T_1; and d) the FLIPS experiment, $\theta = 90°$ and e) the FLIPS experiment, $\theta \neq 90°$, all signals are simultaneously acquired in one experiment. Blue arrows are used for longitudinal (z-aligned) components of the bulk magnetisation and red arrows for transverse (x, y) components.

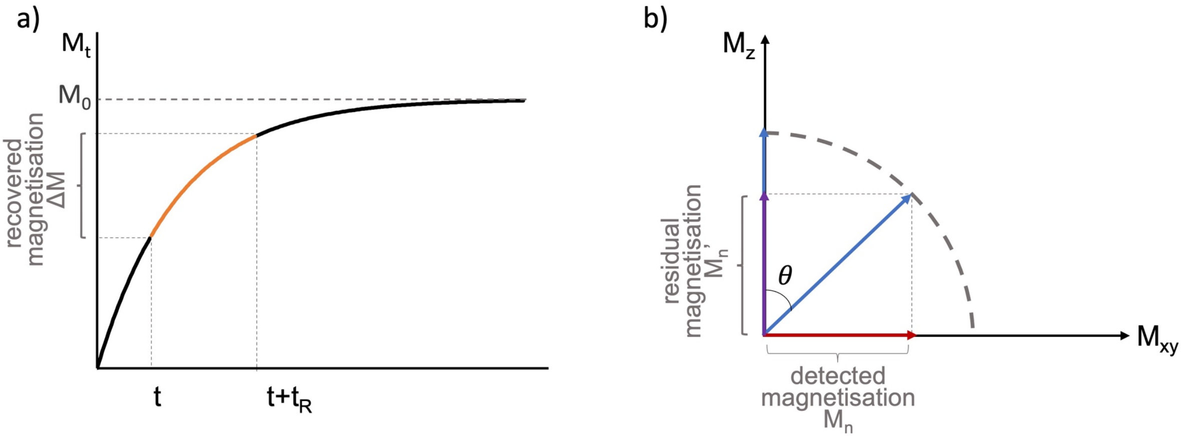

Figure 64. a) The pseudo-first order exponential longitudinal relaxation recovery is plotted to facilitate the equation derivation; orange line shows the recovered magnetisation during a repetition time tR. b) Upon the application of an excitation pulse of pulse angle θ, the magnetisation along the z-axis is flipped towards xy-plane. The detected magnetisation is the projection of this magnetisation vector on the xy-plane, leaving the projection on z-axis as the residual z-magnetisation which will continue to relax back to equilibrium before experiencing the next pulse.

The magnetisation evolution under the FLIPS pulse sequence can be described mathematically, as illustrated in Figure 64. The magnetisation vector starts from thermal equilibrium M_0. Upon the application of excitation pulses ($0° < \theta \leq 90°$), the magnetisation vector is rotated away from z-axis (the direction of B_0) towards the transverse plan. The magnetisation vector starts to relax upon the extinction of the pulse, and its relaxation recovery along the longitudinal axis follows the equation:

$$M_t = M_0 \cdot \left[1 - e^{-t/T_1}\right]$$

at time t:

$$M_t = M_0 \cdot \left[1 - e^{-t/T_1}\right]$$

at time t+t_R:

$$M_{t+tR} = M_0 \cdot \left[1 - e^{-(t+t_R)/T_1}\right]$$

Detected magnetisation on xy-plane:

$$M_n = M \times \sin\theta$$

Residual magnetisation on z-axis:

$$M_n' = M \times \cos\theta$$

Therefore, residual magnetisation on z-axis:

$$\mathrm{M}_\mathrm{n}' = \mathrm{M}_\mathrm{n} \times \cot\theta$$

The longitudinal relaxation recovery starting from xy-plane can be transformed to:

$$\mathrm{t} = T_1 \cdot \left[\ln \frac{\mathrm{M}_0}{\mathrm{M}_0 - \mathrm{M}_\mathrm{n}'}\right]$$

Recovered magnetisation during $\mathrm{t_R}$:

$$\mathrm{M}_{\mathrm{t+tR}} - \mathrm{M}_\mathrm{t} = \mathrm{M}_0 \cdot \left[e^{-t/T_1} - e^{-(t+t_R)/T_1}\right]$$

$$= \mathrm{M}_0 \cdot \left[e^{-T_1 \cdot \left[\ln\frac{\mathrm{M}_0}{\mathrm{M}_0 - \mathrm{M}_\mathrm{n} \times \cot\theta}\right] / T_1} - e^{-\left(T_1 \cdot \left[\ln\frac{\mathrm{M}_0}{\mathrm{M}_0 - \mathrm{M}_\mathrm{n} \times \cot\theta}\right] + t_R\right) / T_1}\right]$$

$$= \mathrm{M}_0 \cdot \left[\frac{\mathrm{M}_0 - \mathrm{M}_\mathrm{n} \times \cot\theta}{\mathrm{M}_0} - e^{-\ln\frac{\mathrm{M}_0}{\mathrm{M}_0 - \mathrm{M}_\mathrm{n} \times \cot\theta}} \times e^{-t_R/T_1}\right]$$

$$= (\mathrm{M}_0 - \mathrm{M}_\mathrm{n} \times \cot\theta)(1 - e^{-t_R/T_1})$$

As a result, detected signal by next excitation pulse is the projection of the bulk magnetisation vector on the xy-plane, and the bulk magnetisation vector comprises the residual magnetisation from previous excitation pulse and the recovered magnetisation during $\mathrm{t_R}$:

$$\mathrm{M}_\mathrm{n} = [\mathrm{M}_\mathrm{n} \times \cot\theta + (\mathrm{M}_0 - \mathrm{M}_{\mathrm{n}-1} \times \cot\theta)(1 - e^{-t_R/T_1})] \times sin\theta$$

$$= \mathrm{M}_0 \times sin\theta - (\mathrm{M}_0 \times sin\theta - \mathrm{M}_{\mathrm{n}-1} \times cos\theta) e^{-t_R/T_1}$$

M_0 is the thermal equilibrium, M_n and M_{n-1} are signal integrals obtained after respective pulses, θ is the pulse angle, and t_R is the repetition time between consecutive pulses. By extending this equation, an equation cluster is obtained as follows, the last term in the equation will continually decrease and eventually reach 0 when n→∞.

$$\mathrm{M}_1 = \mathrm{M}_0 \cdot \sin\theta$$

$$\mathrm{M}_2 = \mathrm{M}_0 \cdot \sin\theta \left[1 - (1 - \cos\theta)\mathrm{e}^{-t_R/T_1}\right]$$

$$\mathrm{M}_3 = \mathrm{M}_0 \cdot \sin\theta \left[1 - (1 - \cos\theta)\mathrm{e}^{-t_R/T_1} - \cos\theta\,(1 - \cos\theta)\mathrm{e}^{-2t_R/T_1}\right]$$

……

$$M_n = M_0 \cdot \sin\theta\left[1 - (1-\cos\theta)e^{-t_R/T_1} - \cos\theta\,(1-\cos\theta)e^{-2t_R/T_1} - \ldots\ldots - \cos\theta^{n-2}\,(1-\cos\theta)e^{-(n-1)t_R/T_1}\right]$$

$$M_n = M_0 \cdot \sin\theta\left[1 - \sum_{i=1}^{n-1}\cos\theta^{i-1}\,(1-\cos\theta)e^{-it_R/T_1}\right]$$ **Equation 13**

Consequently, by performing a FLIPS experiment and with known acquisition parameters θ, t_R, and acquired M_0 (thermal equilibrium), M_n and M_{n-1} (steady-state), the T_1 constant of the studied nuclei can be calculated following the Equation 14.

$$T_1 = \frac{t_R}{ln\left[\frac{M_0\cdot\sin\theta - M_{SS}\cdot\cos\theta}{M_0\cdot\sin\theta - M_{SS}}\right]}$$ **Equation 14**

3.2.1 Alternative Excitation Pulses for FLIPS

Since FLIPS experiment relies on the thermal equilibrium magnetisation to calculate T_1, it was found that it is more sensitive to pulse imperfections such as pulse miscalibration and off-resonance effects. Therefore, to improve its tolerance towards these pulse imperfections, specialised pulses such as Composite pulses[179,180] and BEBOP[181,182] (Broadband Excitation By Optimised Pulses) were employed. Composite pulses are a cluster of pulses with different pulse durations and phases to compensate for B_1 inhomogeneity or off-resonance effects, but often not simultaneously. The implementation of composite pulses is straightforward, Figure 65a shows an example of a series of composite pulses aiming at B_1 inhomogeneity compensation. Samples of 4-fluorophenyl boronic acid of variable concentrations were used. Inversion Recovery experiments were acquired with a 56818 Hz spectral window, 0 dummy scan, 2 number scans. Relaxation delay time was set to 10 s, acquisition time was 1 s. Variable delay list of 10 values/s {0.003, 0.05, 0.1, 0.5, 1, 2, 3, 5, 7, 10} was used for T_1 measurement. FLIPS experiments were acquired with a 56818 Hz spectral window, a repetition time of 1.56 s (0.70 s acquisition time and 0.80 s delay time), and 15 loops of 60° pulses. Using the T_1 constants obtained from Inversion Recovery as reference values, the improvements offered by composite pulses shows a trend $270^\circ_x 360^\circ_x 90^\circ_y > 90^\circ_x\ 110^\circ_y > 90^\circ_x 90^\circ_y > 90^\circ_x$, as is expected from literature.[112] For example, by replacing the hard 90°_x with a $270^\circ_x 360^\circ_{-x} 90^\circ_y$ composite pulse, the deviation of the T_1 constants from those measured by Inversion Recovery decreased from 6% to 3% (Figure 65b, red triangles to orange circles). Theoretically, the composite pulse sequences which offer the best compensation comes from those with the most complex sequences. This may not be necessary for implementation and may be particularly problematic for spins with short transverse relaxation time constants T_2.

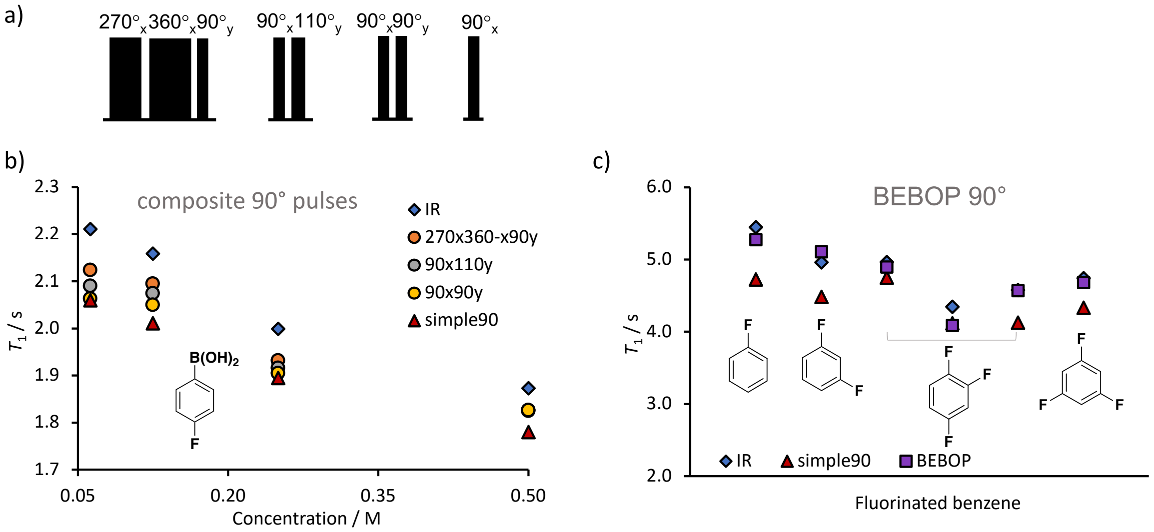

Figure 65. Application of a) a series of composite 90° pulses to the FLIPS experiments for the ^{19}F T_1 measurements of 4-fluorophenyl boronic acid of variable concentrations. Inversion Recovery (blue square) and FLIPS using normal hard 90° pulses (maroon triangle) were measured for comparison. b) The compensation for B_1 inhomogeneity performance shows an apparent trend $270°_x360°_x90°_y > 90°_x110°_y > 90°_x90°_y > 90°_x$, consistent with literature.[112] c) ^{19}F T_1 measurements of fluorinated benzene by BEBOP 90° pulses for off-resonance effect compensation (purple square) comparing to conventional hard 90° pulses (maroon triangle).

Based on this, BEBOP pulses (Broadband Excitation By Optimised Pulses) that provide uniform excitation tolerant towards B_1 inhomogeneity and of relatively shorter pulse durations were incorporated to the FLIPS experiment (Figure 65c) in place of the conventional hard pulses. In the experiments the transmitter offset was deliberately set (40-50 ppm) away from the studied signals. Comparing to Inversion Recovery, the conventional hard 90° pulses yielded T_1 constants of a difference of 9%, while BEBOP pulses alleviated the difference to 2%, showing a clear tolerance towards off-resonance effect. The application of BEBOP pulses requires parameter adjustments to fulfil desired excitation profile. Therefore, in practice, the FLIPS experiment of BEBOP pulses is advised when signals are dispersed on the spectrum, and the T_1 constants are generally long, such as ^{13}C experiments, so that one experiment is performed, and all signals are measured simultaneously. For ^{19}F spectra of wide chemical shift range, though, the T_1 constants are normally shorter, each FLIPS experiment takes tens of seconds, the T_1 measurements can therefore be performed from region to region, using simple hard pulses. Indeed, the specialised pulses have effectively improved the performance of FLIPS on measurement the T_1 constants. Nevertheless, since the relaxation recovery is an exponential process, small errors in the estimated T_1 make a marginal difference in the sense of quantitation

(4×T_1 achieves 98% relaxation, compared to 99.3% by 5×T_1), it is normally adequate to employ hard-pulse FLIPS as a simple and rapid method for T_1 estimation.

3.2.2 Validation of FLIPS in Comparison with Inversion Recovery

To further test the robustness of the method, the T_1 constants for a series of arbitrarily chosen compounds were systematically determined, containing ^{1}H, ^{13}C, ^{19}F, ^{29}Si, and ^{31}P nuclei, by Inversion Recovery, and by FLIPS respectively, shown in Table 6. Considering that Inversion Recovery is the most widely used method for T_1 measurement, it was used in this work as a reference to ascertain and evaluate the performance of other methodologies. The values estimated by FLIPS correlate satisfactorily ($T_1^{FLIPS} = 1.015\ T_1^{IR} – 0.05$; $R^2 = 0.989$) (Figure 66) with those by Inversion Recovery, while requiring about one tenth of the experimental time.

Table 6. T_1 constants of different nuclei measured by Inversion Recovery and FLIPS experiments respectively. Approximate experimental time needed for each measurement is shown in parentheses, signal averaging (number of scans) employed in Inversion Recovery and FLIPS experiments for each individual compound were kept consistent. For Inversion Recovery experiments, error was calculated from the least-square estimation of first-order exponential fitting; For FLIPS experiments, error was calculated by calculating the standard error from multiple measurements.

		T_1 [s]	
Sample[a]	**Nucleus**[b]	**Inversion Recovery**	**FLIPS**
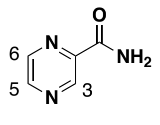	3-^{1}H:	2.91 ± 0.01	2.93 ± 0.01
	5-^{1}H:	3.16 ± 0.01	3.02 ± 0.01
	6-^{1}H:	1.71 ± 0.07	1.67 ± 0.01
0.05 M (methanol-d4)		(5min)	(30s)
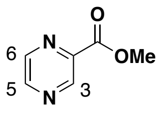	3-^{1}H:	6.09 ± 0.01	6.11 ± 0.02
	5-^{1}H:	5.91 ± 0.01	5.69 ± 0.01
	6-^{1}H:	6.05 ± 0.01	5.82 ± 0.02
0.06 M (methanol-d4)		(12min)	(50s)
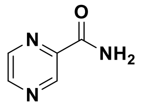	3-^{1}H:	32.38 ± 0.01	34.24 ± 0.39
	5-^{1}H:	16.18 ± 0.01	16.84 ± 0.16
	6-^{1}H:	16.62 ± 0.01	17.40 ± 0.18
0.08 M (degassed methanol-d4)		(45min)	(3min)
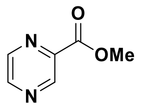	3-^{1}H:	31.20 ± 0.01	35.54 ± 0.37
	5-^{1}H:	17.86 ± 0.01	19.56 ± 0.09
	6-^{1}H:	18.29 ± 0.01	20.80 ± 0.27

0.06 M		(45min)	(3min)
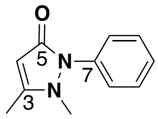	3-^{13}C:	15.76 ± 0.01	15.86 ± 0.66
	5-^{13}C:	14.99± 0.01	15.52 ± 0.44
	7-^{13}C:	18.45 ± 0.01	17.23 ± 0.18
0.5 M ($CDCl_3$)		(2h30min)	(25mins)
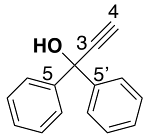	3-^{13}C:	19.24 ± 0.05	19.65 ± 1.36
	4-^{13}C:	14.11 ± 0.02	13.31 ± 0.96
	5,5'-^{13}C:	19.52 ± 0.01	17.75 ± 0.24
0.5 M ($CDCl_3$)		(2h30min)	(25mins)
	F_1 ^{19}F (0.05 M):	5.45 ± 0.01	5.14 ± 0.03
	1,3-F_2 ^{19}F (0.06 M):	4.96 ± 0.01	4.80 ± 0.01
	1,2,4-F_3 (0.06 M)		
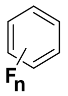	1-^{19}F:	4.58 ± 0.01	4.37 ± 0.02
	2-^{19}F:	4.35 ± 0.01	4.23 ± 0.02
($CDCl_3$)	4-^{19}F:	4.96 ± 0.01	4.80 ± 0.03
	1,3,5-F_3 ^{19}F (0.06 M):	4.74 ± 0.01	4.59 ± 0.01
		(8min)	(30s)
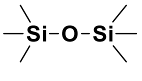	^{29}Si	38.31 ± 0.01	38.01 ± 0.81
0.1 M (toluene-d_8)		(5h47min)	(55min)
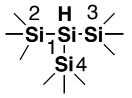	1-^{29}Si	38.99 ± 0.01	40.76 ± 0.45
	2,3,4-^{29}Si	47.73 ± 0.01	43.59 ± 0.92
0.1 M (DME)		(30h)	(4h)
Ph_3P	^{31}P	16.00 ± 0.01	15.49 ± 0.21
0.05 M (9:1 THF/H_2O)		(20min)	(2min)
$Ph_3P=O$	^{31}P	3.60 ± 0.01	3.40 ± 0.04
0.05 M (9:1 THF/H_2O)		(5min)	(20s)

[a] All samples contain natural abundance NMR active nuclei. The sample concentrations and solvent systems are detailed below the sample names. For degassed ^{1}H samples, freeze-pump-thaw method was repeated four times to degas the methanol-d_4 solvent, then samples were freshly prepared, transferred to septum capped NMR tube and measured on the same day. Each sample was prepared and measured separately, except for Ph_3P and $Ph_3P=O$ which were prepared as a mixture and measured in one NMR tube.

[b] The larger deviations for ^{1}H measurements of degassed samples are possibly due to the ingress of air during the 10-fold longer acquisitions required for Inversion Recovery.

[c] Compounds containing the more NMR sensitive nuclei, e.g., ^{1}H and ^{19}F, in sufficient concentration can afford a suitably high signal-to-noise ratio in a single scan, whereas those containing less sensitive nuclei, e.g. ^{13}C and ^{29}Si at natural abundance, normally require signal accumulation.

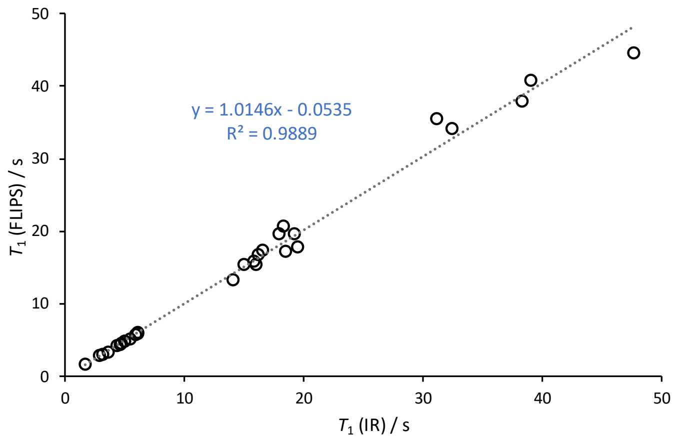

Figure 66. Correlation between the measured T_1 constants by FLIPS against those by Inversion Recovery experiments.

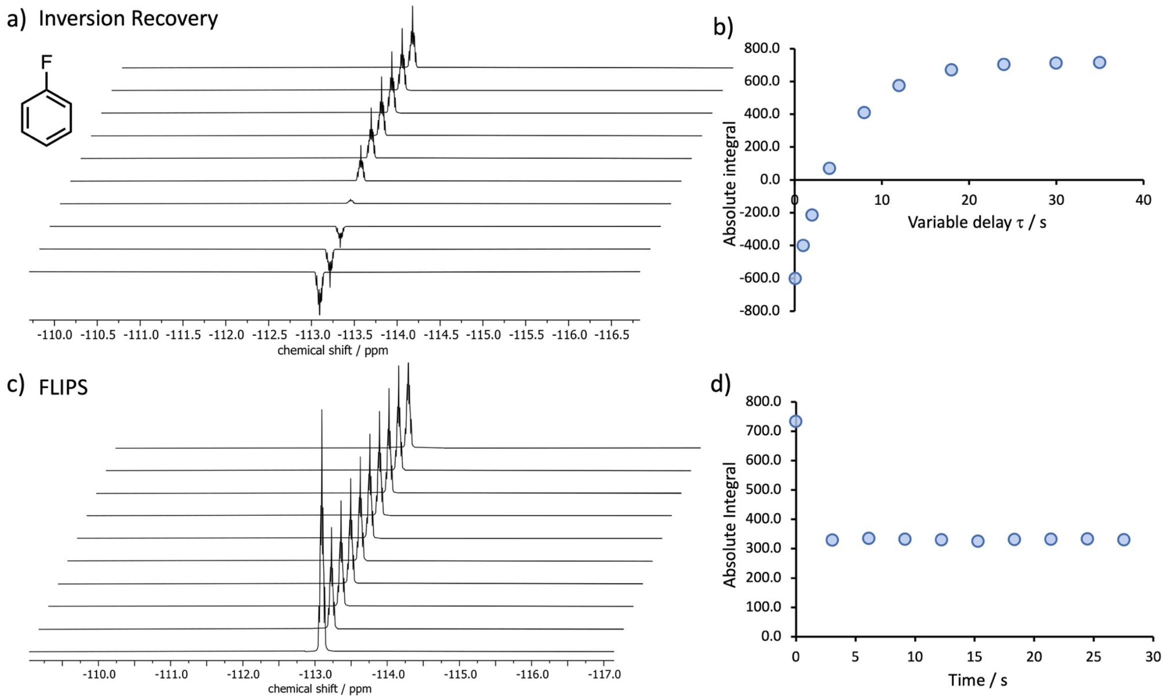

Figure 67. Stacked spectra to measure the T_1 constant of the ^{19}F in 0.05 M fluorobenzene in $CDCl_3$ by a) the Inversion Recovery experiment, and c) the FLIPS experiment. b) Plot of absolute integrals of the ^{19}F signals against variable delay τ by Inversion Recovery. d) plot of absolute integrals of the ^{19}F signals against time by FLIPS.

Two examples of the T_1 measurements in Table 6 were presented here, one ^{19}F and one ^{13}C. Figure 67 presents an example of the T_1 measurements of the ^{19}F in 0.05 M fluorobenzene in $CDCl_3$, by Inversion Recovery and FLIPS respectively. Figure 68 shows the proton-coupled ^{13}C spectrum of 0.5 M phenazone in $CDCl_3$, only the T_1 constants of the quaternary carbons are presented given their relatively longer T_1 constants (Figure 69).

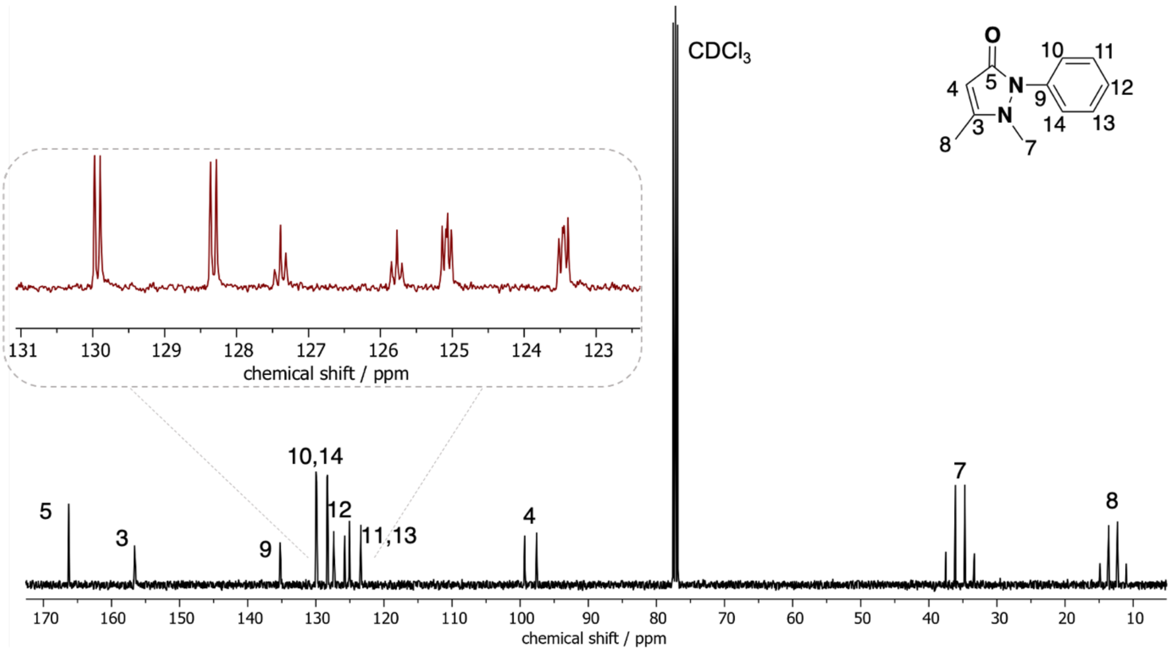

Figure 68. 1D proton-coupled ^{13}C spectrum of phenazone in CDCl$_3$.

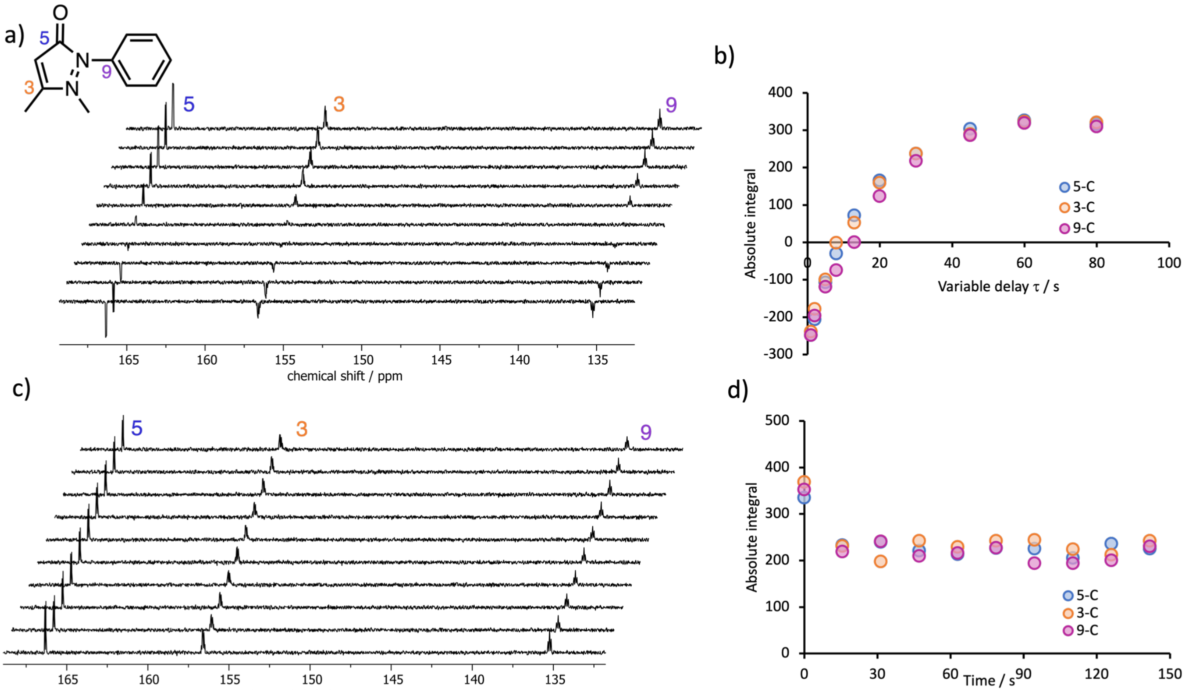

Figure 69. stacked spectra to measure the T_1 constants of the ^{13}C in 0.5 M phenazone in CDCl$_3$ by a) the Inversion Recovery experiment, and c) the FLIPS experiment. b) Plot of absolute integrals of the ^{13}C signals against variable delay τ by Inversion Recovery. d) plot of absolute integrals of the ^{13}C signals against time by FLIPS.

The results shown above proved FLIPS a rapid method for T_1 estimation. Overall, there are three key considerations prior to using the FLIPS method: i) The transverse magnetisation M_{xy} must be eliminated before the next excitation pulse. In practice this can be achieved by adjusting the acquisition time to avoid FID truncation, or by the employment of pulsed field gradients (PFGs); ii) FLIPS is more sensitive to pulse imperfections than the Inversion Recovery method. As discussed above, this can be alleviated by careful pulse calibrations, or by the application of composite pulses and optimised broadband excitation BEBOP pulses; iii) if signal averaging is needed for sensitivity enhancement, the relaxation delay (RD) needs to be $\geq 5\times T_1$. This last aspect inevitably leads to a dilemma, the choice of RD without a prior knowledge of T_1. Setting the RD too long seems a safer practice, but will elongate the experimental time, compromising the time-efficient feature of the method. More importantly, too short of an estimation will cause underestimation of M_0, which in turn yields underestimated T_1. In practice, the 'trial and error' approach can be adopted, the RD is generally set as 5 times the estimated T_1, if the measured T_1 is significantly larger than the estimated value, a new experiment can be performed with new acquisition parameters. While attempting to address this dilemma, we developed another method for T_1 measurements, which avoided the necessity of RD. This will be discussed in succeeding section.

In addition to the considerations stated above, we also noted that inverse-gated heteronuclear decoupling cannot be employed in FLIPS measurements because the transients are acquired repeatedly with an interval time normally much less than $5\times T_1$. Thus, any NOEs between the detected nuclei and the decoupled nuclei will enhance the relaxation, hence shortening the 'real' T_1. This effect can be sidestepped in Inversion Recovery method if the relaxation delay before each measurement is set to be long enough for the equilibrium to be re-established and for the NOEs to dissipate. On the contrary, the repetition time between consecutive acquisitions in the FLIPS method cannot be set long to re-establish the equilibrium, as for this technique the spins need to be saturated to the steady-state to calculate the T_1. An example on CH_3CH_2OH is given below to demonstrate this. The ^{13}C T_1 constants of CH_3CH_2OH were measured by Inversion Recovery and FLIPS methods, with no decoupling and with inverse-gated decoupling respectively. Table 7 presents a summary of the T_1 constants measured by these different experiments.

Table 7. T_1 constants of ^{13}C nuclei measured by Inversion Recovery with no decoupling and with inverse-gated decoupling, and by FLIPS experiment with no decoupling and with inverse-gated decoupling respectively.

T_1 [s]				
	^{13}C	CH_2	DMSO-d_6	CH_3
Inversion Recovery[a]	No decoupling	14.7	49.4	10.9
	Inverse-gated decoupling	14.6	49.8	11.1
FLIPS	No decoupling[b]	14.3	44.2	10.2
	Inverse-gated decoupling[c]	4.0	38.2	2.6

[a]: acquisition parameters, acquisition time t_{AQ}=1 s, relaxation delay =230 s, number of scans=2.

[b]: acquisition parameters, pulse angle θ=90°, acquisition time t_{AQ}=1 s, delay d30=13.94 s, number of scans=4.

[c]: acquisition parameters, pulse angle θ=90°, acquisition time t_{AQ}=1 s, delay d30=5 s, number of scans=4.

As evident from Table 7, since the relaxation delay in the Inversion Recovery experiments is set long, the NOEs from the cross relaxation between ^{1}H and ^{13}C have dissipated prior to the next measurement and therefore do not affect the measured T_1. However, the significantly shorter repetition time between consecutive measurements in the FLIPS experiment cannot dissipate the NOEs. Therefore the cross-relaxation enhances the signal intensities and results in '*shorter*' T_1. The NOEs will build up immediately even if the evolution time is set short. If the repetition time is set very long in the FLIPS experiment, relaxation will be complete, and no steady-state data is available to calculate T_1. When no decoupling is implemented in the FLIPS experiment, the T_1 constants can be measured correctly. It can also be noted that the relaxation of the ^{13}C of solvent DMSO-d_6 is enhanced in the inverse-gated decoupling FLIPS method, due to the residual ^{1}H in the solvent, but since there is only a small amount of residual ^{1}H, the enhancement is smaller. Despite the fact that inverse-gated decoupling renders the FLIPS experiments unsuccessful, the investigation of heteronuclear decoupling has inspired us to explore the NOE build-up process. This exploration has further led to a FLAPS method utilising the sensitivity enhancements afforded by NOEs and precluded the necessity of waiting very long delays to dissipate NOEs, a procedure that is commonly adopted.

3.3 T_1 Measurements by FLOPS

The FLIPS method accelerates the measurements of T_1 by an order of magnitude compared to conventional Inversion Recovery. Nevertheless, there commonly exists a question when setting up the experiment - 'how to correctly set the delays (τ and RD) that are applied within and between cycles?' This issue is also present in the Inversion Recovery method. Indeed, in both methods a value for T_1 needs to be estimated prior to conducting the experiment that then determines the '*real*' value. Another important issue, as mentioned earlier, is that FLIPS is more prone to pulse imperfections, such as mis-calibrated pulses and off-resonance effects, than Inversion Recovery. These issues can be alleviated by careful pulse calibration and by use of broadband specialised pulses, albeit requiring manual adjustment of experimental parameters, and thus taking additional time. In light of the above issues, the following method, which we termed 'FLOPS' (Faster Longitudinal relaxation measurement by Ordered Progressive Saturation) was developed. It essentially combines the advantages of the FLIPS experiment with the Progressive Saturation method (introduced in section 1.2.1) proposed by Freeman[77], as illustrated in Figure 70.

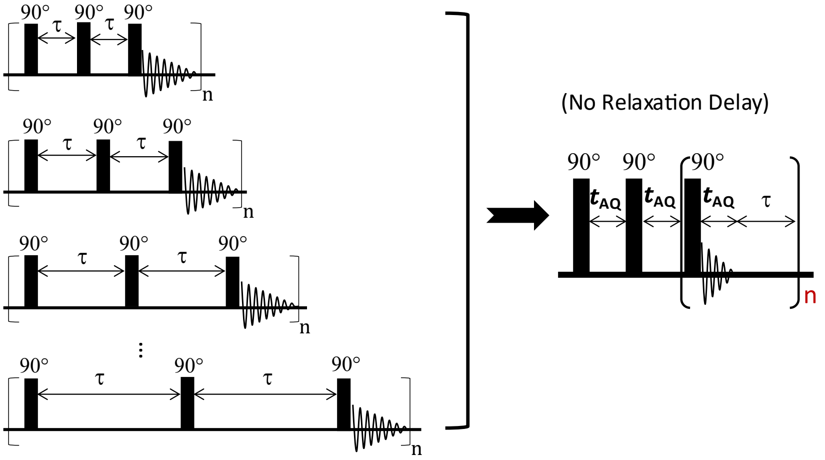

Figure 70. Graphical representation of the FLOPS (Faster Longitudinal relaxation by Ordered Progressive Saturation) method, inspired by the Progressive Saturation work from Freeman[77].

There is no initial relaxation delay (RD) present in the pulse sequence, and it adopts a simultaneous rather a stepwise acquisition mode, with variable delay times (τ) that are incremented between pulses. The FLOPS sequence measures the recovery curve (Figure 71), and pulse imperfections are compensated for by nonlinear least-square fitting to Equation 5. To compare and validate this method, a collection of 22 examples of ^{19}F internal standards that are commonly used in organic chemistry or biochemistry, was measured independently by FLIPS, FLOPS, and Inversion Recovery experiments. These fluorine-containing internal standards were prepared individually in four different deuterated solvents, DMSO-d_6, $CDCl_3$, CD_3OD, and CD_3CN. The results are shown in Table 8.

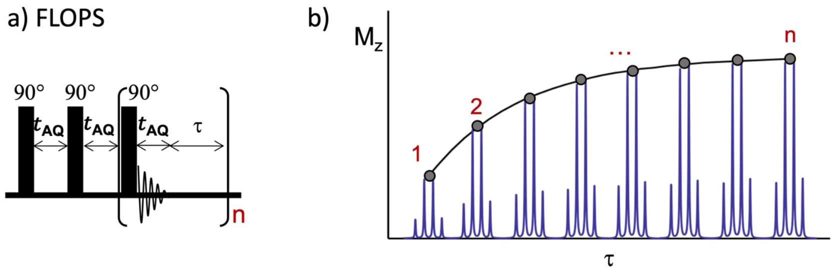

Figure 71. a) Pulse sequences of the FLOPS (Faster Longitudinal relaxation by Ordered Progressive Saturation) method. All excitation pulses are 90°, t_{AQ} is the acquisition time, no acquisition were performed between the first three pulses, the first delay τ_1 is set to 0; and b) data fitting for FLOPS experiments to derive T_1.

Figure 72 provides a visualised summary of the T_1 measurements in Table 8. It is straightforward to see that comparing to the Inversion Recovery results, the overall deviation of FLIPS at 10% (blue bars) was improved to 5% (orange bars) by FLOPS. Figure 72b also shows good correlation between the T_1 constants measured by different methods. In addition, Figure 73 offers a visual guide to the T_1 constants and the relative chemical shifts of these ^{19}F internal standards. Notably the absolute chemical shifts of ^{19}F compounds are sensitive to a range of factors including solvent system, temperature, concentration, magnetic field strength, *etc*. Therefore, Figure 73 is expected to provide a relative comparison between the listed ^{19}F compounds to facilitate the choice of internal standards.

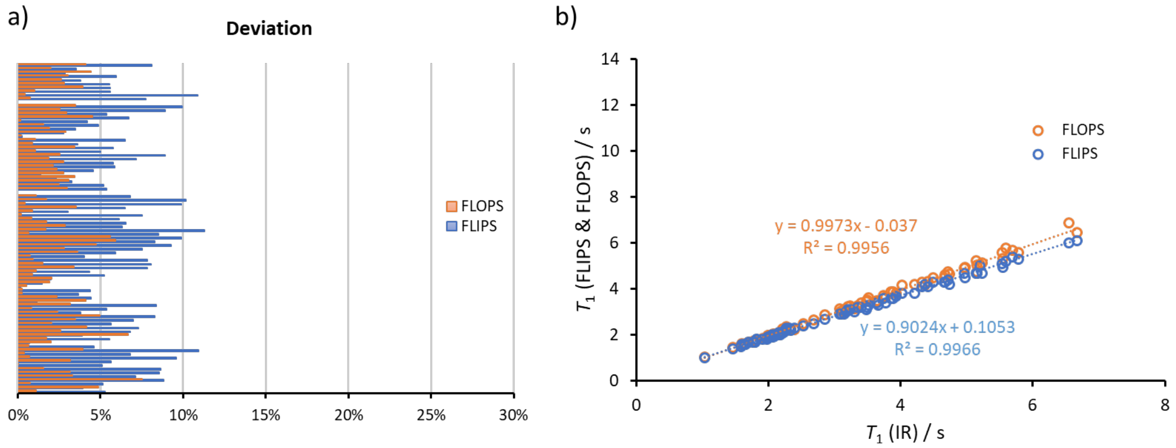

Figure 72. a) The deviation of T_1 constants measured by FLIPS and FLOPS, comparing to those measured by Inversion Recovery experiments. b) Correlation between the T_1 constants measured by FLIPS and FLOPS against those by Inversion Recovery respectively.

Table 8. T_1 constants of some ^{19}F internal standards (IS) measured by FLIPS, FLOPS, and Inversion Recovery experiments.

T_1 constants of ^{19}F internal standards [a]

IS name	solvent	δ / ppm	T_1 / s			
			Inversion Recovery	FLIPS	FLOPS	Avg.
1-fluoronaphthalene[183]	DMSO-d_6	-123.7	2.85	2.7	2.88	2.81
	$CDCl_3$	-123.4	4.37	4.2	4.16	4.24
	CD_3OD	-126.0	4.32	4.1	4.29	4.24
	CD_3CN	-125.2	5.15	4.7	4.77	4.87
para-difluorobenzene[184]	DMSO-d_6	-119.2	5.60	5.2	5.78	5.53
	$CDCl_3$	-119.7	6.67	6.1	6.46	6.41
	CD_3OD	-121.8	5.14	4.7	5.22	5.02
	CD_3CN	-121.2	5.69	5.4	5.69	5.59
1,3,5-trifluorobenzene[185]	DMSO-d_6	-107.5	4.03	3.8	4.15	3.99
	$CDCl_3$	-107.4	4.98	4.5	4.94	4.81
	CD_3OD	-109.4	4.72	4.4	4.74	4.62
	CD_3CN	-109.3	5.55	4.9	5.33	5.27
trifluoro acetic acid[64,168]	DMSO-d_6	-75.2	1.99	1.9	1.98	1.96
	$CDCl_3$	-75.6	2.32	2.3	2.27	2.30
	CD_3OD	-76.9	2.22	2.1	2.18	2.17
	CD_3CN	-76.9	2.39	2.3	2.23	2.31
1,3-bis(trifluoromethyl)benzene[186]	DMSO-d_6	-62.0	2.04	1.9	1.99	1.94
	$CDCl_3$	-63.0	2.16	2.0	2.07	2.04
	CD_3OD	-64.5	1.79	1.7	1.75	1.71
	CD_3CN	-63.5	2.10	2.0	2.02	1.99
fluorobenzene[171,187]	DMSO-d_6	-113.0	6.54	6.0	6.87	6.47
	$CDCl_3$	-113.1	5.20	5.0	5.07	5.09
	CD_3OD	-115.5	4.97	4.7	4.92	4.86
	CD_3CN	-114.9	5.78	5.3	5.60	5.56
4,4'-Difluorobenzophenone[188]	DMSO-d_6	-106.5	2.27	2.3	2.37	2.31
	$CDCl_3$	-105.8	3.35	3.2	3.27	3.27
	CD_3OD	-108.2	3.74	3.6	3.73	3.69
	CD_3CN	-108.3	4.50	4.3	4.49	4.43
3-Trifluoromethyl benzoic acid[189]	DMSO-d_6	-61.4	1.60	1.6	1.61	1.60
	$CDCl_3$	-62.9	1.83	1.8	1.79	1.81
	CD_3OD	-64.4	1.63	1.6	1.60	1.61
	CD_3CN	-63.4	2.01	1.9	1.99	1.96

4,4'-Difluorobiphenyl[168]	DMSO-d_6	-115.6	3.24	3.1	3.28	3.21
	$CDCl_3$	-115.8	4.67	4.3	4.51	4.49
	CD_3OD	-118.1	4.68	4.3	4.61	4.53
	CD_3CN	-117.5	5.53	5.1	5.59	5.41
octafluoronaphthalene[190]	DMSO-d_6	-155	1.04	1	1.03	1.03
	$CDCl_3$	-153.5	2.34	2.2	2.25	2.26
	CD_3OD	-157.6	2.16	2	2.10	2.09
	CD_3CN	-156.5	3.31	3	3.15	3.15
	DMSO-d_6	-147.3	0.99	1	0.96	0.98
	$CDCl_3$	-145	2.25	2.1	2.23	2.19
	CD_3OD	-148.3	2.07	2	2.04	2.04
	CD_3CN	-147.8	3.20	3	3.07	3.09
hexafluorobenzene[191,192]	DMSO-d_6	-162.6	2.18	2	2.05	2.08
	$CDCl_3$	-161.8	3.66	3.3	3.46	3.47
	CD_3OD	-165.4	3.50	3.2	3.52	3.41
	CD_3CN	-164.5	4.73	4.2	4.65	4.53
2,2,2-Trifluoroethanol[193]	DMSO-d_6	-75.2	3.52	3.3	3.62	3.48
	$CDCl_3$	-77.2	3.10	2.9	3.05	3.02
	CD_3OD	-78.8	3.41	3.2	3.38	3.33
	CD_3CN	-77.7	3.89	3.6	3.88	3.79
4-Fluorobenzoic acid[194]	DMSO-d_6	-106.9	3.20	3.1	3.23	3.17
	$CDCl_3$	-104.1	3.64	3.4	3.51	3.51
	CD_3OD	-108.6	4.22	3.8	4.20	4.07
	CD_3CN	-107.9	5.23	4.7	5.14	5.02
Sodium trifluoroacetate[172,195]	DMSO-d_6	-74.1	2.68	2.5	2.65	2.61
	$CDCl_3$	--[b]	--[b]	--[b]	--[b]	--[b]
	CD_3OD	-77	2.01	1.9	1.95	1.95
	CD_3CN	-76	2.21	2.1	2.27	2.19
Benzotrifluoride[170,196]	DMSO-d_6	-61.1	2.27	2.2	2.20	2.23
	$CDCl_3$	-62.7	2.25	2.2	2.17	2.21
	CD_3OD	-64.3	1.82	1.8	1.77	1.80
	CD_3CN	-63.2	2.10	2	2.05	2.05
o-Fluoroacetophenone[197]	DMSO-d_6	-110.6	3.08	2.9	3.15	3.04
	$CDCl_3$	-109.4	3.93	3.7	3.82	3.82
	CD_3OD	-111.8	4.42	4.1	4.33	4.28
	CD_3CN	-111.7	5.16	4.7	5.03	4.96
222-trifluoroacetophenone[198]	DMSO-d_6	-70.6	2.53	2.4	2.50	2.60
	$CDCl_3$	-71.4	3.18	3	3.07	3.26

	CD_3OD	-84.5	2.07	2	2.06	2.72
	CD_3CN	-72.3	3.85	3.6	3.89	4.06
4-(Trifluoromethyl)benzyl alcohol[199]	DMSO-d_6	-60.7	1.70	1.7	1.69	1.70
	$CDCl_3$	-62.5	2.06	2	2.00	2.02
	CD_3OD	-63.9	1.66	1.6	1.63	1.63
	CD_3CN	-62.9	2.00	1.9	1.97	1.95
3,5-bis(trifluoromethyl)phenol[200]	DMSO-d_6	-61.7	1.46	1.4	1.46	1.44
	$CDCl_3$	-63.1	2.04	1.9	1.94	1.96
	CD_3OD	-64.7	1.59	1.5	1.54	1.54
	CD_3CN	-63.7	1.98	1.8	1.93	1.90
Potassium hexafluorophosphate[201]	DMSO-d_6	-70.2	3.78	3.4	3.64	3.61
	$CDCl_3$	--[b]	--[b]	--[b]	--[b]	--[b]
	CD_3OD	-74.8	3.14	2.9	3.12	3.05
	CD_3CN	-73.0	3.48	3.1	3.46	3.35
4-chlorobenzotrifluoride[202]	DMSO-d_6	-61.1	2.01	1.9	1.99	1.97
	$CDCl_3$	-62.6	2.22	2.1	2.14	2.15
	CD_3OD	-64.1	1.80	1.7	1.75	1.75
	CD_3CN	-63.1	2.08	2	2.02	2.03
4-bromobenzotrifluoride[203]	DMSO-d_6	-61.2	1.91	1.8	1.86	1.86
	$CDCl_3$	-62.8	2.16	2.1	2.07	2.11
	CD_3OD	-64.3	1.76	1.7	1.73	1.73
	CD_3CN	-63.3	2.07	1.9	1.98	1.98

[a]: all samples were prepared at a concentration of 0.05 M, measured at 300 K; all measurements were acquired in an automated manner, i.e., no pulse calibration was performed.

[b]: no data available due to insolubility.

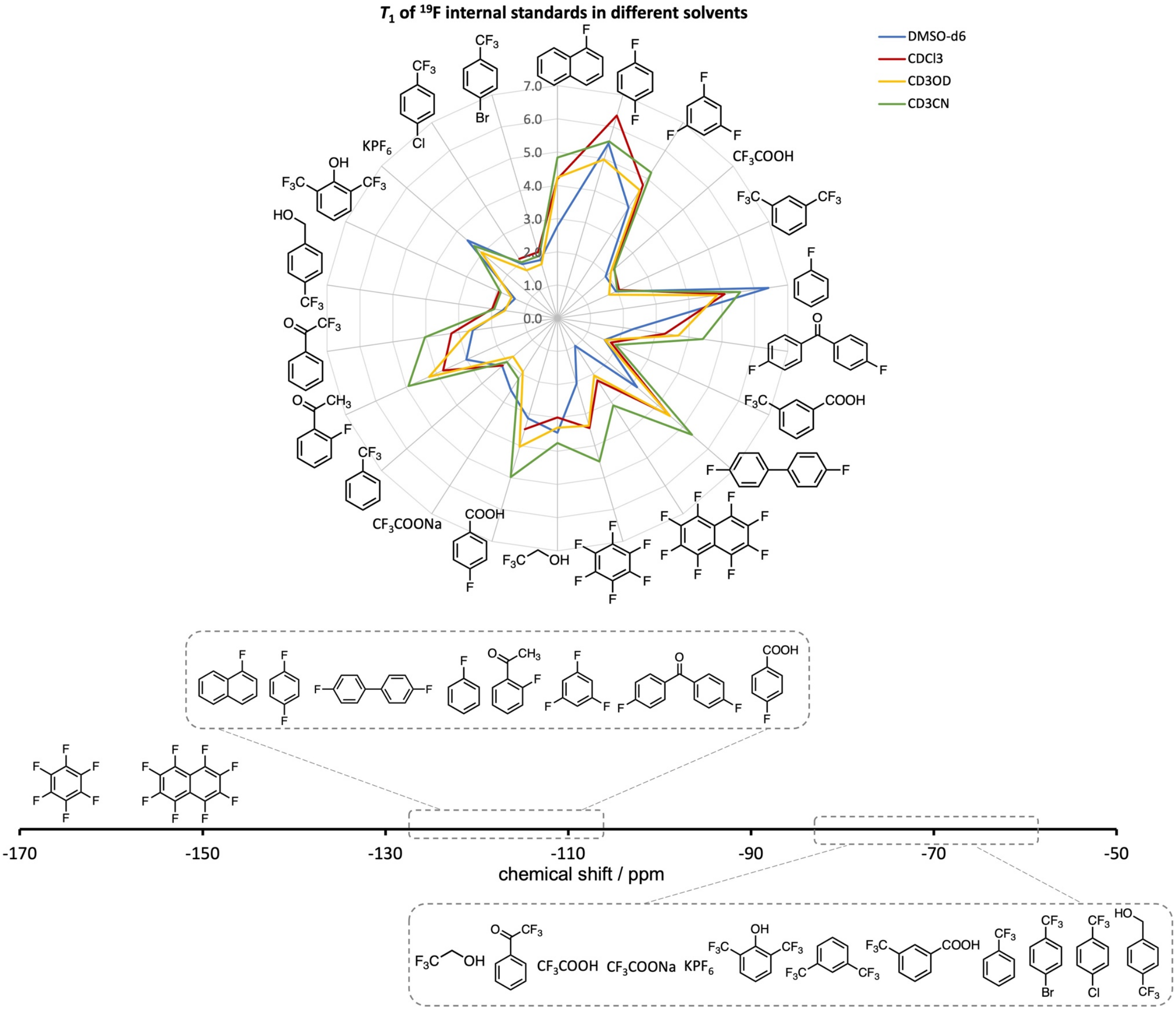

Figure 73. A map of the T_1 constants of ^{19}F internal standards in different solvent systems, with T_1 constants ranging from 1-7 seconds; and their approximate chemical shift range. Note that octafluoronaphthalene has two sets of ^{19}F signals with similar T_1, only one of them is presented in the map.

3.4 T_1 Measurements by FLAPS

3.4.1 Longitudinal Relaxation with Heteronuclear Decoupling

The previous section discussed the application of inverse-gated heteronuclear decoupling will inherently corrupt FLIPS for T_1 measurements. This is due to the NOEs between consecutive acquisitions, which lead to artificially enhanced relaxation. This idea, albeit proved disadvantageous for relaxation measurements, intrigued us to monitor the NOEs build-up and dissipation using the FLIPS sequence. Figure 74a shows the FLIPS pulse sequences with continuous decoupling to monitor the NOEs. In contrast to inverse-gated decoupling, the decoupler was turned on throughout the experiment apart from the RD. RD was kept >>10×T_1 to make sure the thermal equilibrium M_0 acquired after the first pulse is not affected by NOEs. The signals at steady-state were measured under the influence of NOEs, as M_{NOE}. Each individual experiment therefore gives an NOE effect M_{NOE}/M_0. The experiment was repeated with incremented τ to monitor the effects of NOEs as a function of decoupling time (Table 9).

For all $^{13}C\{^1H\}$ experiments, continuous decoupling utilises an acquisition time t_{AQ}=1 s, pulse angle θ=90°, 4 scans, a relaxation delay RD=230 s (>>10*T_1). Figure 74b clearly shows the enhancement (M_{NOE}/M_0) grows smoothly towards an asymptote as the decoupling time τ between pulses is increased. Fitting the enhancement, M_{NOE}/M_0, to an exponential function gives growth rates that are almost identical to the longitudinal relaxation rates (1/T_1) measured independently. These results indicated to us the potential to utilise NOEs in relaxation measurements.

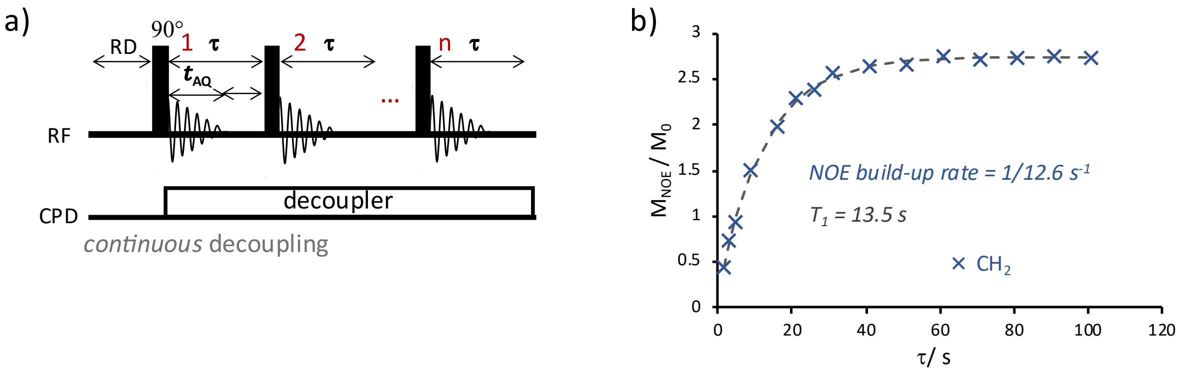

Figure 74. a) FLIPS pulse sequences with composite pulse decoupling (CPD) to investigate the build-up of NOEs. The decoupler was kept on throughout the experiment apart from the relaxation delay (RD), RD was set >>10*T_1 to measure the '*true*' equilibrium magnetisation (M_0). WALTZ16[109] was used as the decoupling scheme for $^{13}C\{^1H\}$ experiments. b) CH_3CH_2OH in DMSO-d_6. A plot of measured $^{13}C\{^1H\}$ with NOEs (M_{NOE}) over M_0 as a function of τ for CH_2. NOE build-up rate was obtained from a three-parameter mono-exponential fit. T_1 constant was measured independently.

Table 9. T_1 constants of ^{13}C in CH_3CH_2OH, and M_{NOE}/M_0 values acquired from each $^{13}C\{^1H\}$ FLIPS experiment with variable decoupling time.

	CH_2	DMSO-d6	CH_3
T_1 / s	13.5	42.5	10.8
	continuous decoupling		
decoupling time τ / s		M_{NOE}/M_0	
1.5	0.446	0.042	0.518
3	0.736	0.091	0.888
5	0.946	0.133	1.146
9	1.508	0.232	1.777
16	1.986	0.369	2.302
21	2.300	0.455	2.561
26	2.391	0.516	2.579
31	2.569	0.578	2.665
41	2.640	0.646	2.724
51	2.669	0.760	2.767
61	2.757	0.825	2.954
71	2.713	0.871	2.871
81	2.744	0.909	2.940
91	2.766	0.941	2.900
101	2.748	0.965	2.849

Indeed, the build-up of NOEs follows a pseudo exponential growth as a function of decoupling time.[100,204]

$$M_\infty - M_t = (M_\infty - M_0) \times e^{-t/T_1} \qquad \textbf{Equation 15}$$

M_∞ is the signal integral measured with continuous irradiation of the decoupled nucleus, M_0 is the integral measured without decoupling, and $M_\infty/M_0 = \eta + 1$, η is the NOE factor. By rearrangement we obtain equation, which shows how a series of signals observed with NOEs as a function of decoupling time, embed the information required for determining the relaxation time T_1.

$$M_t = (\eta + 1)M_0 - (\eta M_0 \times e^{-t/T_1}) \qquad \textbf{Equation 16}$$

3.4.2 Impact of Heteronuclear Decoupling on Sample Temperature

Since continuous heteronuclear decoupling was implemented throughout the experiments, it is sensible to investigate the impact of this on sample temperature. Sample heating has a few potential hazards. The first is that temperature variations within a sample will deteriorate the spectral quality and degrade samples that are intolerant towards temperature fluctuations. Moreover, prolonged high decoupling power may even damage precious cryogenic probes, particularly at ultra-high magnetic field strength[122]. The most used broadband decoupling methods today are composite pulse decoupling[205] (CPD) and adiabatic decoupling[111]. Considering for the 9.4 Tesla spectrometer utilised throughout this work, CPD is considered the most convenient method, sample heating upon the application of CPD was therefore examined. Nevertheless, it is worthwhile to note that adiabatic decoupling pulses provide a good alternative to achieve uniform broadband decoupling and minimise the power dissipation to the sample. Therefore, it is advised to use adiabatic decoupling when the required decoupling bandwidth is very broad, or/and the continuous high power poses risks to the probe.

The NMR methanol thermometer method[206] was used to monitor the real-time temperature of the sample upon continuous irradiation of the heteronuclei, in this case, ^{13}C. The N_2 gas flow rate was set to 450 L/h, the temperature of the N_2 gas flow was set to 300 K. Pure methanol was added to a 5mm NMR tube. The chemical shift difference between the two ^{1}H signals in the methanol was used to calculate the temperature of the sample, using the following equation:[206]

$$T(K) = 409.0 - 36.54 \times \Delta\delta - 21.85 * \Delta\delta^2 \qquad \textbf{Equation 17}$$

Repetitive $^{1}H\{^{13}C\}$ spectra were acquired with Bruker default sequence 'zgdc', with 30° flip angle, relaxation delay of 20s, acquisition time of 3s, one scan, and monitored over 11 minutes (30 spectra). The ^{13}C power level was set to 33W, GARP[207] decoupling method was used, and the CPD power level was elevated from 1.03 W to 8 W, Figure 75a upper CPD method. Table 10 presents an example of this experiment acquired with CPD power level at 1.03 W.

Table 10. Temperature monitoring of the sample upon continuous CPD application.

time / s	δ (OH) / ppm	δ (CH_3) / ppm	Δδ / ppm	T / K
23	5.654	4.120	1.534	301.535
46	5.654	4.120	1.533	301.585
69	5.654	4.120	1.533	301.586
92	5.654	4.120	1.533	301.586
115	5.654	4.121	1.534	301.553
138	5.654	4.121	1.533	301.588
161	5.655	4.121	1.534	301.571
184	5.655	4.121	1.534	301.574
207	5.655	4.121	1.534	301.561
230	5.655	4.121	1.533	301.588
253	5.655	4.121	1.534	301.552
276	5.655	4.121	1.534	301.561
299	5.656	4.122	1.534	301.547
322	5.655	4.121	1.534	301.576
345	5.655	4.121	1.534	301.564
368	5.655	4.121	1.534	301.541
391	5.655	4.121	1.534	301.570
414	5.655	4.121	1.534	301.542
437	5.655	4.121	1.534	301.575
460	5.655	4.121	1.534	301.566
483	5.655	4.121	1.534	301.544
506	5.655	4.121	1.534	301.566
529	5.655	4.122	1.533	301.603
552	5.655	4.122	1.533	301.589
575	5.655	4.121	1.534	301.583
598	5.655	4.121	1.534	301.546
621	5.655	4.122	1.534	301.572
644	5.655	4.121	1.534	301.567
667	5.655	4.122	1.534	301.562
690	5.655	4.122	1.534	301.580

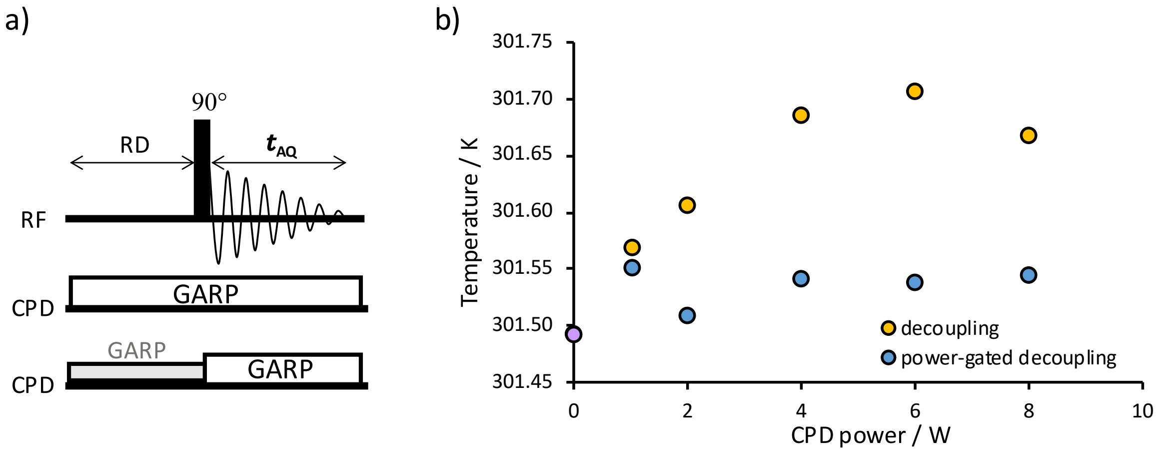

Figure 75. a) The NMR experiments to monitor sample temperature upon application of continuous CPD. Upper CPD method: GARP decoupling at a constant power level; lower CPD method: power-gated GARP decoupling. b) Temperature of the sample upon continuous CPD application at variable power levels. Yellow circles represent temperature of sample acquired with consistent CPD power throughout the experiment; Blue circles represent that acquired with power-gated decoupling method; purple circle represent sample temperature without CPD as reference.

A common alleviation to the sample heating is to utilise power-gated decoupling method, Figure 75a, lower CPD method. A relatively lower power is applied during the relaxation delay period to build up the NOEs, while a higher power for decoupling is used during acquisition. For comparison, the power-gated decoupling experiments were implemented with Bruker default sequence ‘zgpg’. Identical acquisition parameters were used as the previous ‘zgdc’ experiments, with the only difference being a lower power at 0.26 W during relaxation delay. Figure 75b shows the temperature change against CPD power level from these two different decoupling methods, the purple circle denotes the sample temperature when no CPD was applied as a reference value. A temperature fluctuation of ± 0.2 K was observed, and power-gated decoupling method further reduced the fluctuation to ± 0.05 K. This negligible sample heating proved that on a 9.4 T magnet, traditional CPD methods are well suited for broadband decoupling. Nevertheless, when ultra-high magnetic field strength is involved, care needs to be taken and adiabatic decoupling schemes would be recommended alternatives.

3.4.3 Choice of Heteronuclear Decoupling Schemes

As discussed in section 1.3.2, two categories of decoupling schemes are mostly use today on high resolution spectrometers, the composite pulse decoupling and the adiabatic decoupling. For high field spectrometers, typically from 9.4 Tesla to 14.1 Tesla, CPD are in general the ‘*default*’ schemes for heteronuclear decoupling. For ultrahigh field spectrometers above 16.5

to 28 Tesla, adiabatic decoupling is mostly or even exclusively employed to avoid excessive power usage[122]. Throughout this work, a 9.4 Tesla spectrometer was utilised. The CPD scheme for ^{1}H decoupling was WALTZ16[109], and that for X-nuclei was GARP[110]. However, it is worth bearing in mind that these recommended decoupling methods are sometimes not suitable or sufficient for challenging samples.

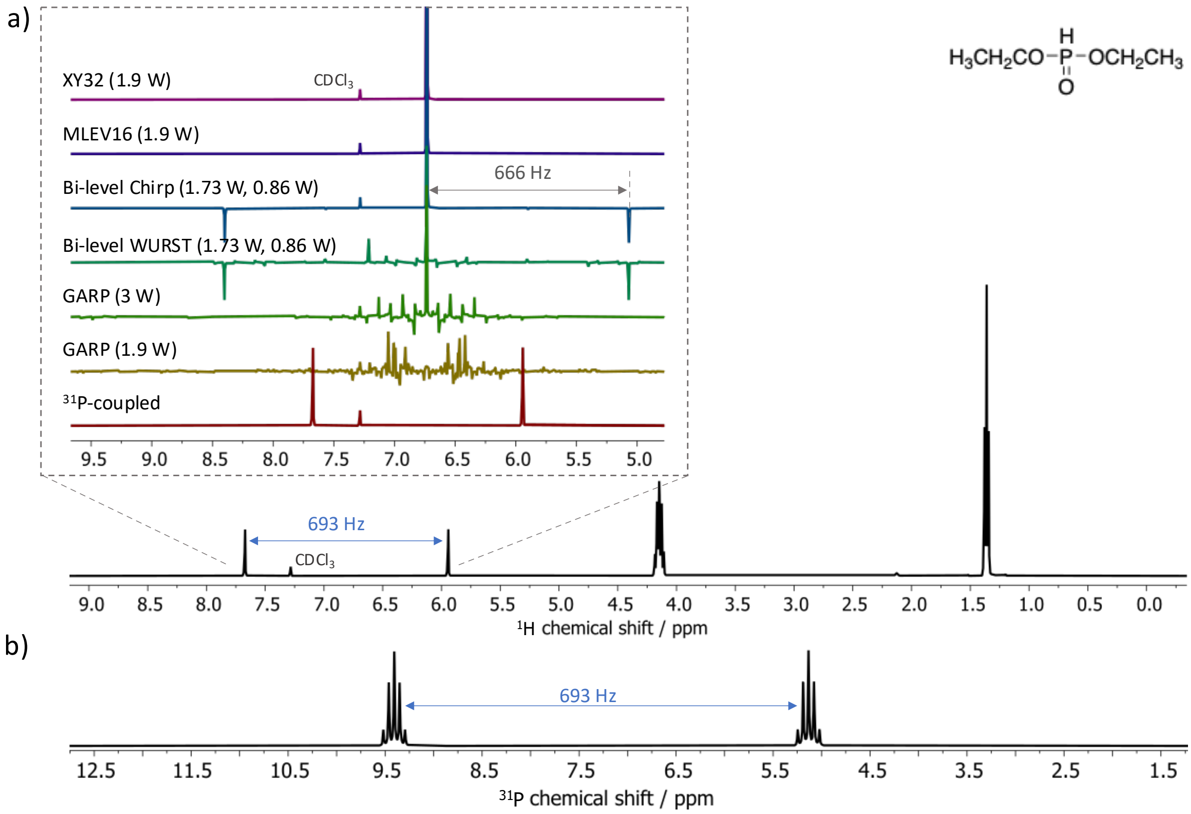

Figure 76. a) A full ^{1}H spectrum with ^{31}P-coupled of diethyl phosphate in $CDCl_3$. Inset: {^{31}P}^{1}H spectra focusing on the PH signal to compare the performance of different decoupling schemes. b) ^{1}H-coupled ^{31}P spectrum of diethyl phosphate in $CDCl_3$, showing the one bond coupling constant $^{1}J_{PH}$.

Figure 76 presents a sample of diethyl phosphite which has a large one-bond ^{31}P-^{1}H coupling constant $^{1}J_{PH}$ of 693 Hz. The offset frequency of decoupling radiofrequency was set at the centre of the ^{31}P doublet (Figure 76b). Using the GARP sequence at a ‘default’ power level of 1.9 W could not resolve this large $^{1}J_{PH}$, rendering the resultant spectrum useless (Figure 76a, inset, mustard spectrum). Increasing the power level to 3 W started to generate the ^{1}H signal but with severe decoupling artefacts. After careful parameter adjustments, a bi-level Chirp decoupling scheme was able to decouple the ^{31}P effectively (inset, blue spectrum), at a main power level less than half of the CPD. Two negative decoupling sidebands appeared symmetrically at 666 Hz away from the parent peak, which was a consequence of the periodic 1500 us Chirp pulses. For the studies of complex systems, these sidebands could be problematic if they obscure or overlap with other signals. The location and intensity of these sidebands are dependent on the magnitude of the *J*-coupling constants and the duration of the adiabatic pulse[111]. Therefore, one method to reduce the sidebands is to shorten the pulse length. However, this will inevitably lead to increased decoupling power level. For this particular sample, it was found that alternative CPD schemes MLEV16[108] and XY32 were able to generate a sharp and clean $\{^{31}P\}^1H$ singlet free of decoupling sidebands (inset, top two spectra). WALTZ16 was tested as well but did not yield satisfactory decoupling result. One possible explanation for this improvement could be that although MLEV16 provides a smaller decoupling bandwidth (Table 2), it offers a moderately higher decoupling efficiency at the resonant frequency than WALTZ16 and is more tolerant toward B_2 inhomogeneity. Note that only one ^{31}P signal was present in this sample that requires decoupling. In the case of multiple ^{31}P resonances distributing across a wide chemical shift range, MLEV16 might not perform well enough considering its relatively narrow decoupling bandwidth and bi-level adiabatic decoupling are expected to be more robust under such circumstances. Figure 77 proved the quantification was retained for both bi-level Chirp decoupling and MLEV16.

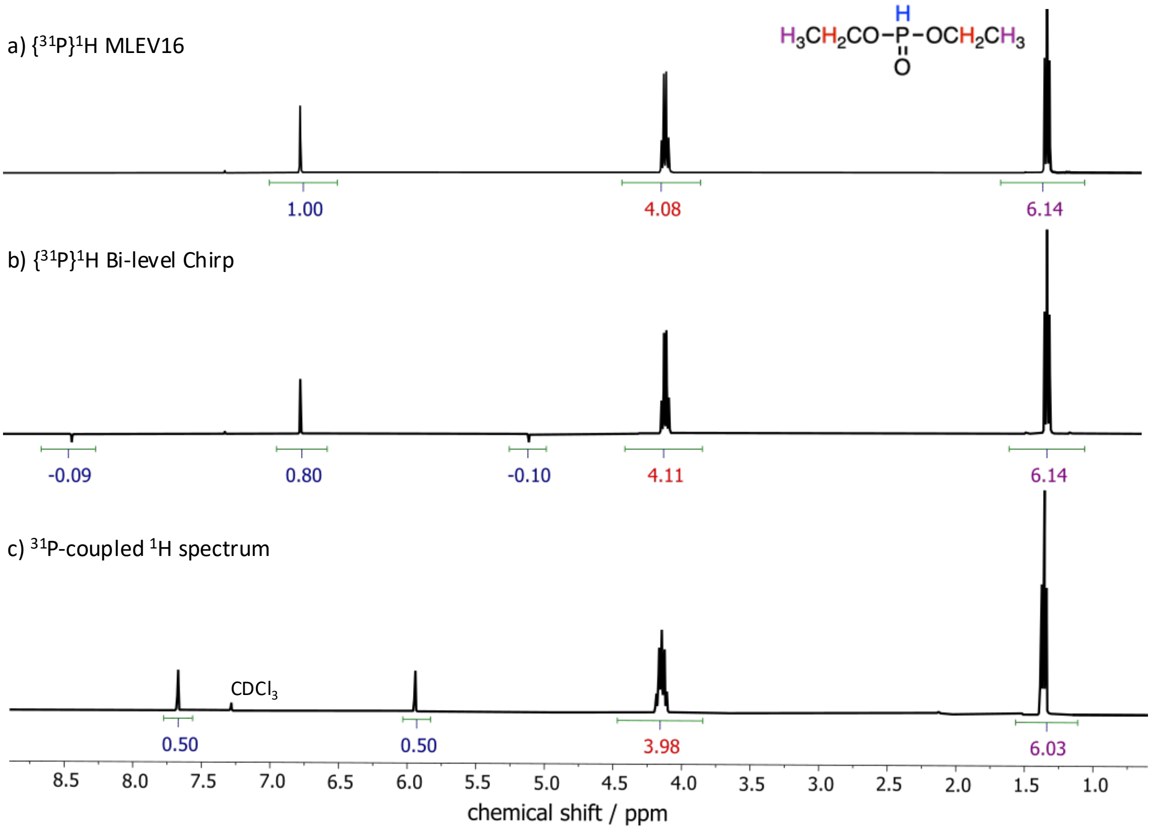

Figure 77. Quantitative ^1H spectrum of diethyl phosphate in $CDCl_3$, different ^1H sites were labelled with different colours. a) $\{^{31}P\}^1H$ spectrum acquired with composite pulse decoupling method MLEV16. b) $\{^{31}P\}^1H$ spectrum acquired with Bi-level adiabatic Chirp pulses, note the decoupling sidebands need to be accounted for the total integral. c) ^{31}P-coupled ^1H spectrum.

3.4.4 FLAPS Method

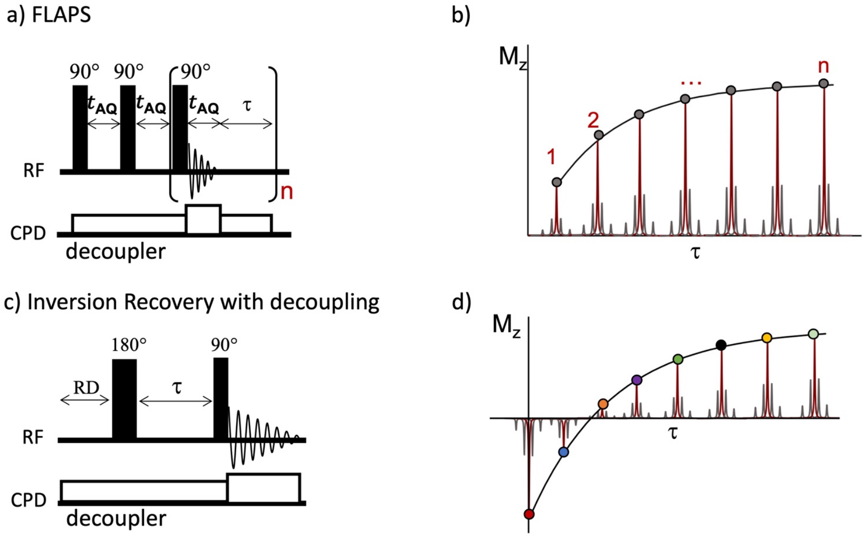

Figure 78. Pulse sequences and their data fitting for T_1 derivation. a) The FLAPS (Faster Longitudinal relaxation by Amplified Progressive Saturation) method, with power-gated heteronuclear decoupling. b) Data fitting for FLAPS experiments to derive T_1, note the decoupled resonances that afford sensitivity enhancement from coalescing the intensity of multiplet into a singlet and from the Nuclear Overhauser Enhancements (NOEs)[93]. c) The Inversion Recovery experiment with power-gated heteronuclear decoupling, and d) its data fitting.

After examining the impacts of continuous heteronuclear decoupling on relaxation and temperature variation, a method termed 'FLAPS' (Faster Longitudinal relaxation by Amplified Progressive Saturation) was developed. The pulse sequence of FLAPS was shown in Figure 78a. The only difference between FLAPS and FLOPS is the implementation of CPD, to benefit from sensitivity enhancements. This sensitivity boost arises from two factors, i) the collapse of the multiplet into a narrow singlet, and ii) the NOEs enhancement, with a maximum factor $\eta = {}^{\gamma_I}/_{2\gamma_S}$ (where γ_I and γ_S are the gyromagnetic ratios of the decoupled and detected nuclei, respectively). Both effects lead to enhanced signal-to-noise ratios (S/N), particularly when the detected nucleus, e.g., ^{13}C, ^{15}N, ^{29}Si, is scalar and/or dipolar coupled to abundant and high-γ nucleus ^{1}H. In Figure 79 the advantages of FLAPS were demonstrated using an arbitrarily chosen sample acetophenone. The FLAPS and FLOPS spectra were acquired using identical parameters. Improvements in S/N, ranging from ×6 at C(6) to ×29 at C(2,4) were obtained simply by the implementation of continuous ^{1}H-decoupling. The methyl carbon, C(8), of acetophenone exemplifies how the longitudinal relaxation rates, T_1, are unaffected (Figure 79b) by the simultaneous enhancement in resolution and sensitivity (Figure 79c).

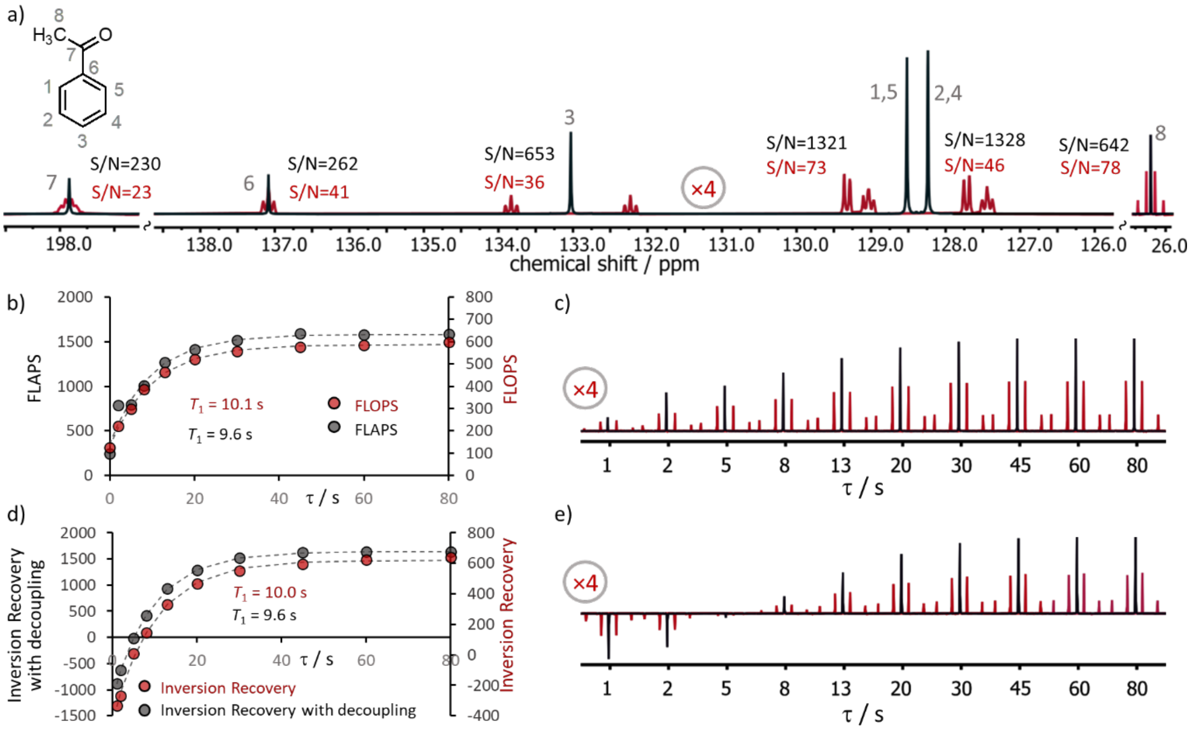

Figure 79. a) Overlaid ^{13}C (maroon) from FLOPS, and ^{13}C{^{1}H} spectra (black) from FLAPS, of 2 M acetophenone in CDCl$_3$, showing the S/N improvements across the spectrum from proton decoupling and NOE enhancement. ^{13}C spectrum was sized up ×4 times for visual guidance. b) An example of the CH$_3$ carbon (C$_8$) measured by FLOPS and FLAPS experiments; and c) the corresponding overlaid ^{13}C (maroon) and ^{13}C{^{1}H} spectra (black) obtained by FLOPS and FLAPS, respectively. d) The CH$_3$ carbon (C$_8$) measured by Inversion Recovery with power-gated decoupling and without decoupling; and e) overlayed ^{13}C (maroon) and ^{13}C{^{1}H} spectra (black). Secondary axes were used for measurements without decoupling.

The successful application of FLAPS sparked another inspiration. Conventional ^{13}C T_1 measurements, for example prior to determining kinetic isotope effects,[208–210] employ Inversion Recovery methods with inverse-gated proton-decoupling[100]. These experiments apply a relaxation delay between individual scans of up to 10-12×T_1 of the slowest relaxing nuclei to dissipate the NOEs generated during the FID acquisition[209] and are thus very time-consuming. However, while the acquisition of 1D quantitative inverse gated ^{13}C{^{1}H} requires the unequal NOE enhancements at *different* ^{13}C environments to be eliminated,[100] or corrected,[211] it is the *same* ^{13}C signal in a series of spectra that is measured and compared when determining relaxation rates at a specific site. Therefore, when measuring ^{13}C T_1 values, the application of a very long delay at the beginning of each cycle not only leads to a prolonged experiment time, but also sacrifices the NOE enhancement (η_{max} = 2 in the case of ^{13}C{^{1}H}). Following the FLAPS method, an Inversion Recovery experiment with continuous power-gated heteronuclear decoupling was implemented (Figure 78c). The outcome is illustrated in

Figures 78d and 78e, where continuous-decoupling Inversion Recovery results in an 8-fold enhancement at C(8), meaning that the T_1 value can be determined with the same S/N about an order of magnitude faster than with the inverse-gated $^{13}\text{C}\{^{1}\text{H}\}$ Inversion Recovery sequence, and the Inversion Recovery without any ^{1}H decoupling.

Table 11. T_1 constants of different nuclei measured by Inversion Recovery, Inversion Recovery with decoupling, FLOPS, FLAPS and FLIPS experiments respectively. Signal-to-noise ratios are shown in parentheses for comparison. Experimental times for each experiment are shown in square brackets.

		T_1 / s (S/N)				
Sample [a]	nucleus	Inversion Recovery without decoupling	Inversion Recovery with decoupling	FLOPS	FLAPS	FLIPS [b]
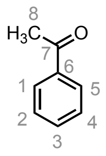	1,5-^{13}C	7.6 *(74)*	6.8 *(1276)*	7.6 *(73)*	7.8 *(1321)*	7.4 *(32)*
	2,4-^{13}C	7.7 *(47)*	6.9 *(1276)*	7.9 *(46)*	7.9 *(1328)*	7.2 *(18)*
	3-^{13}C	5.8 *(37)*	5.1 *(633)*	6.2 *(36)*	4.9 *(653)*	6.2 *(20)*
	6-^{13}C	37.9 *(31)*	37.5 *(187)*	34.7 *(41)*	37.0 *(262)*	34.5 *(21)*
	7-^{13}C	39.3 *(17)*	41.8 *(173)*	38.1 *(23)*	41.4 *(230)*	36.4 *(11)*
	8-^{13}C	10.0 *(82)*	9.6 *(613)*	10.1 *(78)*	9.6 *(642)*	9.2 *(45)*
		[47min]	[47min]	[13min]	[13min]	[9min]
$HC(=O)OCH_2CH_3$	1-^{13}C	18.1 *(51)*	18.6 *(440)*	18.8 *(52)*	19.7 *(438)*	17.1 *(31)*
	2-^{13}C	20.3 *(33)*	19.5 *(420)*	18.0 *(35)*	19.6 *(418)*	20.2 *(16)*
	3-^{13}C	14.7 *(38)*	14.5 *(494)*	13.6 *(40)*	13.2 *(485)*	13.0 *(28)*
		[1h 12min]	[1h 15min]	[20min]	[20min]]	[13min]
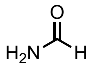	^{15}N[c]	14.6 *(33)* [38h 40min]	14.2 *(818)* [9h 38min]	13.5 *(281)* [19h 55min]	14.3 *(1023)* [2h 34min]	13.3 *(20)* [8h 31min]
$Si(CH_3)_4$	^{29}Si	32.6 *(52)*	31.7 *(184)*	33.4 *(69)*	33.8 *(231)*	30.1 *(46)*
		[6h 2min]	[6h 8min]	[1h 38min]	[1h 38min]	[2h 18min]
$O=PH(OCH_2CH_3)_2$	^{31}P	6.6 *(567)*	6.5 *(4433)*	6.6 *(604)*	6.5 *(4529)*	5.9 *(229)*
		[27min]	[27min]	[9min]	[9min]	[5min]
PPh_3	^{31}P	17.8 *(312)*	16.4 *(5069)*	18.1 *(316)*	18.2 *(5237)*	17.5 *(65)*
		[1h 25min]	[1h 25min]	[20min]	[20min]	[15min]

[a]all samples contain natural abundance NMR active nuclei. [b]the S/N of FLIPS are dependent on the arbitrary choice of repetition time between the pulse train and the flip angle. [c]due to the low sensitivity of ^{15}N, experiments without ^{1}H decoupling were acquired with more scans. All experiments were acquired in automated manner, i.e., no pulse calibrations were conducted.

The benefits of continuous decoupling in T_1 measurements can be exploited in a range of low-sensitivity nuclei (X = ^{13}C, ^{15}N, ^{29}Si, ^{31}P), to utilise the high natural abundance and high gyromagnetic ratio of ^{1}H (γ=26.7×10^{7} rad·s^{-1}·T^{-1}), shown in Table 11. Figure 80 presents the stacked NMR spectra from FLOPS and FLAPS experiments of formamide, their corresponding data fitting for deriving T_1, and sensitivity comparison between ^{1}H-coupled and ^{1}H-decoupled experiments. It is also interesting to note that, for NMR spectra of nuclei with negative gyromagnetic ratios, such as ^{15}N ($\gamma = -2.7\times10^{7}$ rad·s^{-1}·T^{-1}) and ^{29}Si ($\gamma = -5.3\times10^{7}$ rad·s^{-1}·T^{-1}), it is conventionally recommended to avoid {^{1}H}-NOEs as signal attenuation or even cancellation can occur. However, by fully exploiting the negative NOE, significant enhancements can still be achieved. For example, T_1 measurements on formamide using continuous decoupling-$^{15}N\{^{1}H\}$ FLAPS and Inversion Recovery gave $\eta = -4.97$, close to the negative maximum achievable for $^{15}N\{^{1}H\}$, and thus providing a substantial increase in S/N over the ^{1}H-coupled experiments. This negative η can be seen in Figure 81. Two 1D ^{15}N and $\{^{1}H\}^{15}N$ experiments were acquired and processed with identical parameters. The $\{^{1}H\}^{15}N$ spectrum was 180° out of phase compared to the ^{1}H-coupled spectrum. An NOE factor of (–1585-399)/399 = –4.97 was detected, owing to the two directly attached ^{1}H on the ^{15}N. This translated into a 4-fold S/N enhancement from NOEs. For tetramethylsilane (TMS), however, the ^{29}Si signal experienced a moderately negative NOEs of -0.17, which would lead to signal attenuation. Nevertheless, the removal of *J*-couplings offers a dominant contribution to the sensitivity gain, $\{^{1}H\}^{29}Si$ experiments therefore still proved beneficial (Figure 82).

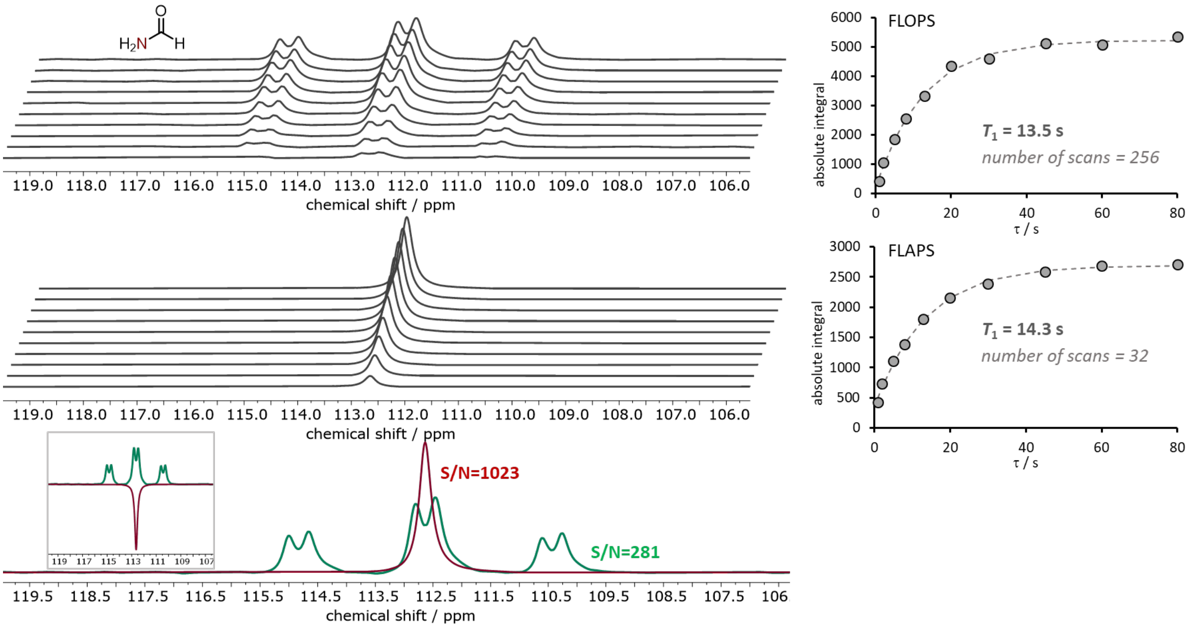

Figure 80. (top) stacked spectra of ^{15}N FLOPS experiment, and data fitting to generate T_1 constants of formamide; (middle) stacked spectra of $\{^{1}H\}^{15}N$ FLAPS experiment, and data fitting; (bottom) superimposed spectra of the last spectrum taken from FLOPS and FLAPS respectively to compare the sensitivity. (inset) FLOPS and FLAPS spectra are 180° out of phase under the same processing parameters, due to a negative NOEs factor of –5.

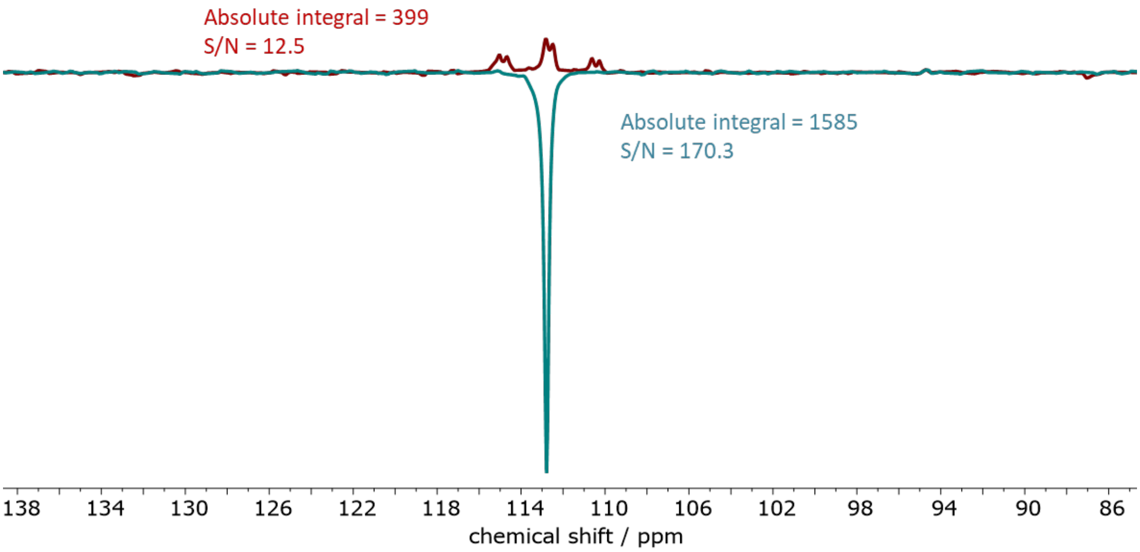

Figure 81. Overlaid 1D spectra of ^{15}N and $\{^1H\}^{15}N$ experiments, showing a negative NOEs of -5. Two experiments were acquired and processed with identical parameters for back-to-back comparison.

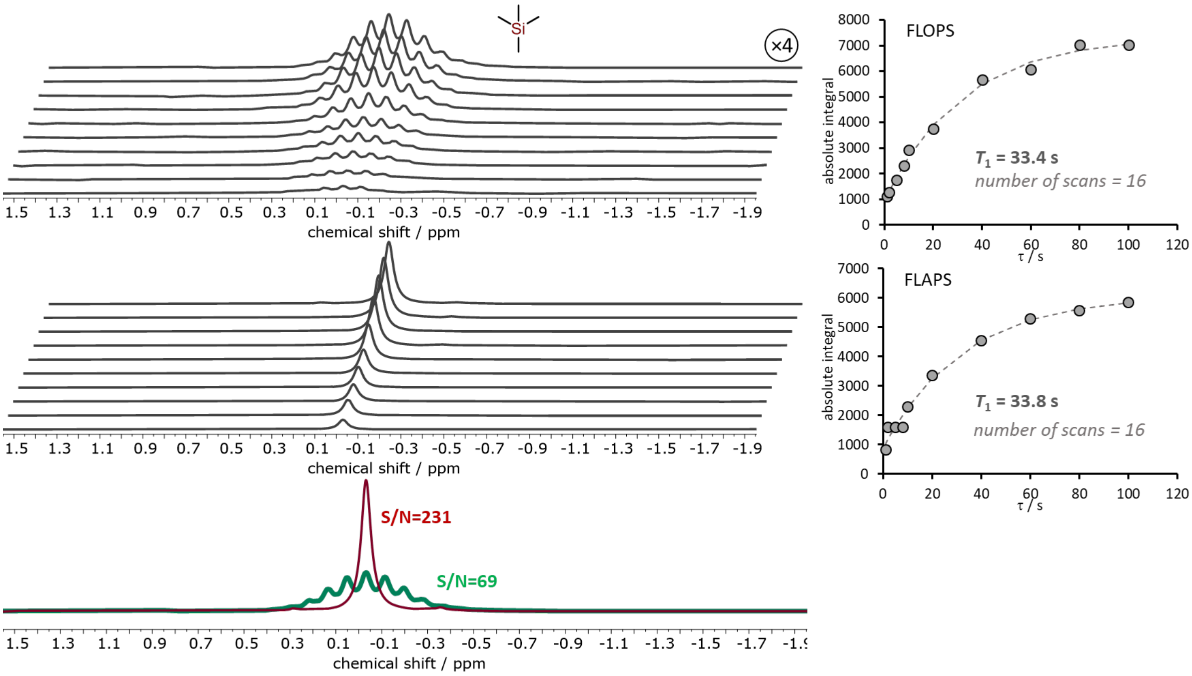

Figure 82. (top) stacked spectra of ^{29}Si FLOPS experiment, and data fitting to generate T_1 constant of TMS; (middle) stacked spectra of $\{^1H\}^{29}Si$ FLAPS experiment, and data fitting; (bottom) superimposed spectra of the last spectrum taken from FLOPS and FLAPS respectively for sensitivity comparison.

3.4.5 Using Pulsed Field Gradients in FLOPS and FLAPS

In FLOPS and FLAPS experiments, the fitting parameter α (Equation 5) remains in the range $0 < \alpha < 1$. The value of α depends on the longitudinal relaxation recovery occurred during the acquisition time. To sample more of the recovery curve, α needs to be as close as possible to 1. Otherwise, if only the latter part of the curve is measured, the fitted results could deviate significantly. For all the samples used in this work, the α values were among the range $0.6 < \alpha < 1$, Table 12. Therefore, the measured T_1 were in good agreements with those from Inversion Recovery experiments. However, in the extreme narrowing limit, where $T_2 = T_1$, a considerable amount of longitudinal relaxation might have been achieved during acquisition time. To alleviate this issue, two solutions would be helpful in manually shortening the acquisition time. The first is to apply a weighting exponential function upon data processing; the second is by the implementation of pulsed field gradients (PFGs) immediately after data acquisition (Figure 83), to speed up the dephase of transverse magnetisation. Noteworthy, both approaches are at a price of line broadening effects.

Table 12. The α values of FLOPS and FLAPS experiments from the fitting to Equation 5.

α values from the fitting									
Nuclei	^{13}C								
	acetophenone						$HCOOCH_2CH_3$		
FLOPS	0.92	0.93	0.65	0.72	0.71	0.78	0.89	0.89	0.90
FLAPS	0.90	0.90	0.61	0.60	0.59	0.76	0.83	0.90	0.92

Nuclei	^{15}N	^{29}Si	^{31}P	
	H_2NCHO	$Si(CH_3)_4$	$O{=}PH(OCH_2CH_3)_2$	$P(Ph)_3$
FLOPS	0.93	0.86	0.75	0.89
FLAPS	0.88	0.85	0.74	0.86

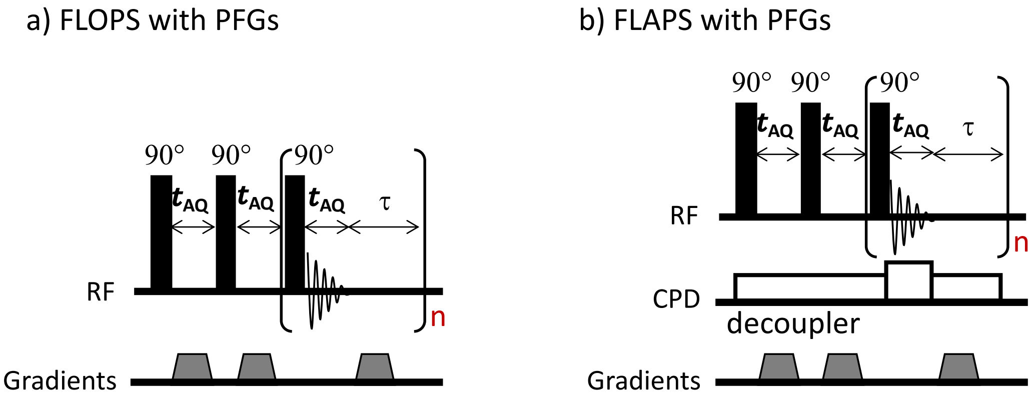

Figure 83. Pulse sequences of a) the FLOPS method with pulsed field gradients; and b) the FLAPS method with pulsed field gradients.

Figure 84 shows the comparison of T_1 measurements with and without PFGs using an example of ^{13}C in CH_3OH. It is evident that by employing proton-decoupling, FLAPS (Figure 84a, red circles) showed an approximately 180% enhancement comparing to FLOPS (grey circles). With the further application of PFGs to FLAPS (blue circles), the recovery curve was able to be measured closer from the origin, with an improved α value at 0.91 from 0.81 of FLAPS. Another benefit of the PFGs can be seen in Figure 84b and 83c. Due to the signal amplification, the original acquisition time of 2.5 s for FLOPS experiment was not sufficient for the transverse magnetisation to fully dephase in the FLAPS experiment, hence residual transverse magnetisation before the next excitation pulse led to phase distortions (Figure 84b). By employing PFGs immediately after FIDs acquisition this distortion effect was effectively alleviated (Figure 84c).

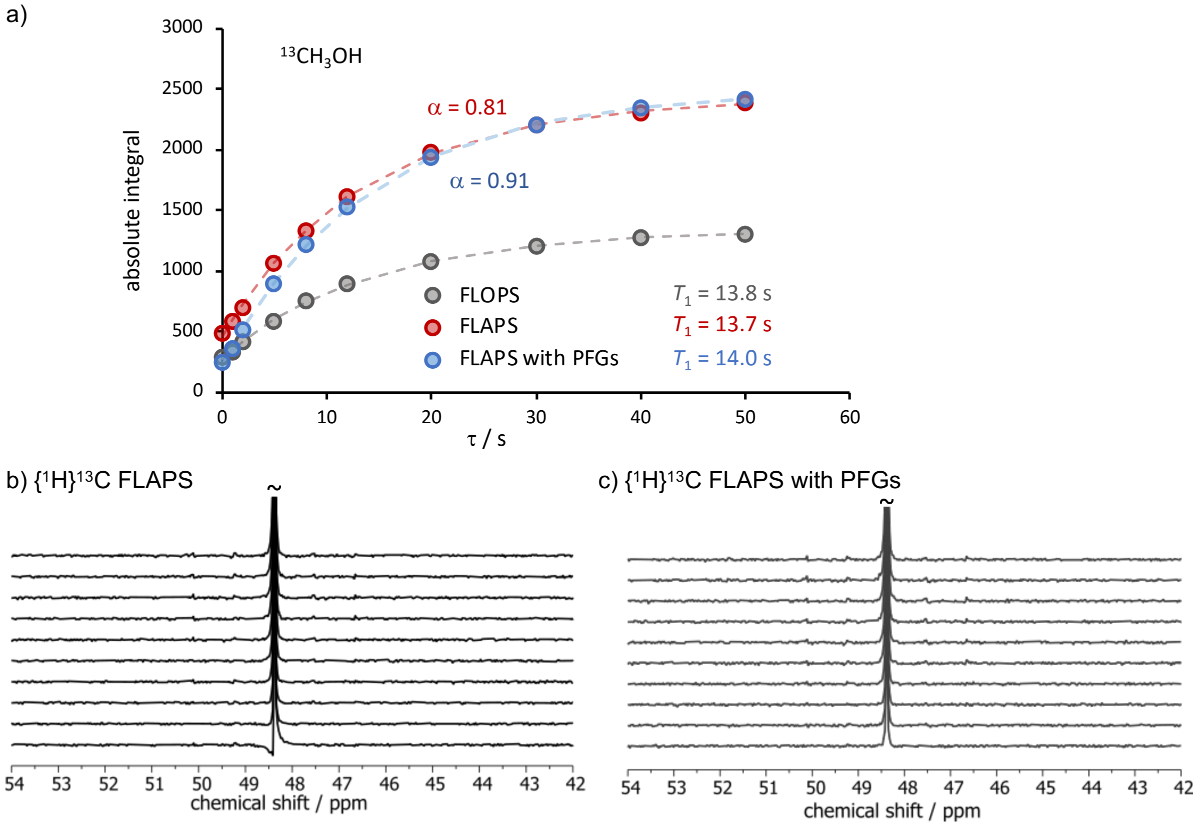

Figure 84. a) ^{13}C T_1 measurements of CH_3OH in $CDCl_3$, using FLOPS, FLAPS, and FLAPS with pulse field gradients respectively. b) Stacked ^{13}C spectra of FLAPS experiment, showing the phase distortion of the 1st spectrum. c) Stacked ^{13}C spectra of FLAPS experiment with PFGs, the phase distortion was removed.

Chapter 4 Conclusion

In summary, the work herein has covered two aspects of NMR spectroscopy, a state-of-the-art stopped-flow NMR technique for the interrogation of rapid irreversible chemical reactions, and an NMR parameter called the longitudinal relaxation (T_1) constant. The stopped-flow insert is compatible with standard NMR spectrometers, its results thus far could be summarised into four categories, i) evaluation of the physical parameters of the stopped-flow apparatus, ii) investigation in the key NMR parameters to ensure qualitative and quantitative analysis, iii) successful implementation of the stopped-flow NMR technique for *in-situ* real-time monitoring of irreversible chemical reactions in the timescale of milliseconds, and iv) utilisation of the non-pre-magnetised delivery channel to probe chemical exchanges in challenging systems.

The evaluation of stopped-flow parameters began with the pre-magnetisation profiles of four delivery syringes, including three 'pre-magnetised' syringes and one 'non-pre-magnetised' syringe. Their different characteristics originate from the assembly of the stopped-flow apparatus. The pre-magnetisation level depends on factors such as the delivery volume from different syringes, the flow rate, and the T_1 constants of analytes. These factors need to be taken into consideration when quantitative information is desired. A systematic profile for the three pre-magnetised syringes was constructed to provide a guideline on the pre-magnetisation level with respect to delivery volume at a commonly employed flow rate of 1 mL/s. In practice, an appropriate choice of internal standards that have similar T_1 constants as the analytes could be helpful. Key NMR parameters to afford qualitative and quantitative kinetic information was also evaluated. Optimisation of the pulse angle and interscan delay allows the optimal balance between sensitivity and data density to be achieved. For very fast reactions, where the reaction rate *k* is larger than the relaxation rate $1/T_1$, 90° pulses can be used for maximum sensitivity with only the first data point retained to construct the reaction profile. Multiple interleaved stopped-flow experiments with different time offsets need to be performed for manually enhanced data density. After establishing the above-mentioned procedures, this stopped-flow NMR technique was able to monitor irreversible reactions, such as the protodeboronation of pentafluorophenyl boronic acid which has a half-life time of 45 milliseconds at 313 K.

In addition to the conventional pre-magnetised syringes, the non-pre-magnetised syringe, which serves as the solvent syringe in conventional stopped-flow experiments, was utilised for magnetisation transfer studies. The pre-magnetisation level of this channel was investigated, posing a limit of its application. That is, the T_1 constants of analytes cannot be shorter than 1/5 of the deadtime (0.15 - 0.22 s). Otherwise, the spins would achieve complete pre-magnetisation before measurements take place. Trifluoromethylation of aldehydes by competing $TMSCF_3$ and $TESCF_3$ was conducted for the magnetisation transfer studies. Since the CF_3 anions were short-living intermediates, traditional magnetisation transfer NMR experiments were not applicable under such circumstances. Instead, by '*magnetic-labelling*' the CF_3 source from the non-pre-magnetised channel, the chemical exchange between CF_3 anions from $TMSCF_3$ and $TESCF_3$ was confirmed without the necessity of isotopic labelling.

As restated above, T_1 has played a significant role throughout this work. It defines the pre-magnetisation level of analytes delivered via the stopped-flow syringes. It also governs the repetition rates of consecutive pulses in an NMR experiment to ensure sufficient relaxation. Consequently, T_1 measurement has become an essential procedure prior to any quantitative NMR experiments. To facilitate these routine measurements, a set of 'FLIPS', 'FLOPS', 'FLAPS' experiments were developed. The primary advantage of these methods over the traditional Inversion Recovery experiment lies in the time-saving feature. Different from Inversion Recovery method sampling the relaxation recovery curve in a step-wise manner, these proposed methods acquire the data points simultaneously in a single cycle. Therefore, FLIPS offers a 10-fold time-efficiency comparing to the Inversion Recovery approach, and a deviation of measured T_1 constants within 10%, accurate enough for the purpose of quantitative analysis. The FLIPS pulse sequence retains the relaxation delay parameter, which needs to be $> 5\times T_1$ when multiple transients are accumulated for sensitivity. Without a prior estimation of T_1, the setup of RD normally involves trial-and-error, a process that could be time-consuming. To avert this, FLOPS was further developed, removing the RD and less sensitive to pulse imperfections. Consequently, FLOPS improves the deviation of measured T_1 constants to within 5%. Nevertheless, it takes twice the experimental time comparing to FLIPS. Therefore, for abundant and high-γ nuclei such as ^1H and ^{19}F, when a single transient is sufficient to afford high S/N, FLIPS provides a fast method for T_1 measurements. For less sensitive nuclei, particularly in the absence of a prior estimation of T_1, FLOPS offers a good alternative to minimise the risk of improper parameter setup. Based on the FLOPS method, it was found that continuous heteronuclear decoupling could be implemented without affecting the T_1 constants. This discovery led to significant sensitivity enhancement, or equivalently time-efficiency, for ^1H-attached insensitive nuclei such as ^{13}C, ^{15}N, ^{29}Si, or ^{31}P, when proton-decoupling was utilised throughout the T_1 measurements. This method was term FLAPS, to highlight the amplified signals from *J*-coupling removal and NOEs.

Chapter 5 Future Work

The work presented here provides new possibilities for the studies of chemical reactions. The stopped-flow NMR technique has pushed the limits of *in-situ* irreversible reaction monitoring to the millisecond timescale, a task impossible with traditional methods. Nonetheless, there are a range of improvements that can be envisioned to offer a more powerful technique.

The first pursuit, unsurprisingly, lies in even faster reaction monitoring. The fastest reaction that can be measured by a stopped-flow system is primarily limited by its phenomenological deadtime. The main contributor to the deadtime of the current stopped-flow is the transport time to deliver the analytes from the mixer to the NMR flow cell. Current work is ongoing within the group, to significantly reduce the transport time by shortening the distance between the mixer and the flow cell, and by simultaneously increasing the flow rate.

A second ambition focuses on a wider compatibility of chemical reactions. At this stage the stopped-flow insert can operate over a temperature range of +5 to 60 °C, the good temperature control proved to be valuable for the study of reactions at variable temperature. However, the pressure range is currently restricted to ambient pressure. The incorporation of a pressure vessel to the stopped-flow NMR apparatus is a challenging task, particularly considering the limited space within the spectrometer probe. Thus far, high-pressure stopped-flow systems coupling to UV-Vis have been commercially available, their adaption to NMR spectrometers without modifying the spectrometer probe is yet to be realised. By integrating high-pressure tolerance to the stopped-flow NMR technique, it undoubtedly would be of great value for the study of pressure-dependent reactions. Another foreseen improvement could be the chemical compatibility, which is primarily determined by the materials involved in the flow path. For example, hydrofluoric acid is incompatible with silica.

Chemical exchange studies by the non-pre-magnetisation channel have been validated by the competing trifluoromethylation of aldehydes. This functionality can be lent to other chemical systems where the lifetime of exchanging species is shorter than the traditional magnetisation transfer experiments. Moreover, the implementation of methods such as selective inversion recovery would encounter a challenge when the exchanging spins are too close to neighbouring resonances in a spectrum. The selective pulse needs to achieve an extremely narrow excitation bandwidth, or equivalently has a very long pulse length, to satisfy the required selection. Under such circumstances, the non-pre-magnetisation channel could provide a good alternative as no complex pulse manipulation is needed. Throughout the project, ^{19}F NMR analysis is almost exclusively utilised owing to its favourable NMR properties and its firm foundation within the Lloyd-Jones group. The applications of the stopped-flow instrument, including the traditional syringes and the non-pre-magnetisation syringe, can be easily extended for the use of other NMR-active nuclei.

Regarding the collection of the T_1 methods, it is rather important to raise the awareness of T_1 measurement amongst wider NMR users, particularly when the majority of NMR experiments acquired in chemistry laboratories today are in an automated manner. Taking advantage of NOEs in T_1 measurement seemed to have transiently emerged, nonetheless, its existence appeared to be quickly overlooked or forgotten. The time-saving benefits afforded by these '*lost*' techniques could be significant in an accumulative manner. Potential future work on the FLOPS and FLAPS method is mainly stimulated by curiosity, rather than practicalities. One possibility is to improve the recovery curve, by partially inverting the z-magnetisation rather than suppressing it. This could be useful for rapidly relaxing species in the extreme narrowing regime, alleviating the need for pulsed field gradients. Thus far, the commonly-used organic compounds in this work have not posed great challenges to the methods developed herein. It would be interesting to see how other compounds, for example, with strong couplings or complex macromolecules would behave.

Chapter 6 Pulse Programmes

All NMR experiments reported in this thesis were recorded on a 400 MHz Bruker Ascend spectrometer equipped with a 5mm BBFO cryoprobe. The pulse sequences below are coded for Bruker TopSpin® 3.6.2.

6.1 FLIPS Pulse Programmes

6.1.1 Hard Pulse FLIPS

```
;FLIPS_hard pulse - rapid T1 estimation for quantitative NMR
;Ran Wei, Claire L. Dickson, Dušan Uhrín, Guy C. Lloyd-Jones*
;doi: 10.1021/acs.joc.1c01007
;pseudo 2D sequence, generates a 'ser' file
;This sequence has not been widely tested, use at your own risk
;
;$CLASS=HighRes
;$DIM=2D
;$TYPE=
;$SUBTYPE=
;$COMMENT=


#include <Avance.incl>
#include <De.incl>

"acqt0=-p1*2/3.1416"
"d11=30m"
"d2=d1-d11"
"d30=d10-aq-de-2*d11-p1"

1 ze
2 d2
3 d11
 p1 ph1
 ACQ_START(ph30,ph31)
 aq DWELL_GEN:f1
 d30
 d11 mc #0 to 3 F1QF()
 rcyc=2
```

```
exit

ph1=0
ph30=0
ph31=0


;pl1 : f1 channel - power level for pulse (default)
;p1 : f1 channel -  90 degree high power pulse
;d1 : relaxation delay; 1-5 * T1
;d2: d1 - d30
;d10 : repetition time between pulses for relaxation recovery; d10=aq+de+d30+2*d11+p1
;d11 : delay for disk I/O [30 msec]
;d30: interval time between acquisition and next pulse; d30>=0
;NS: 1 * n, total number of scans: NS * TD0

;F1MODE : QF
;td1 : number of repetitive pulses (recommended 8)
```

6.1.2 Composite Pulse FLIPS

```
;FLIPS_composite90 - rapid T1 estimation for quantitative NMR
;Ran Wei, Claire L. Dickson, Dušan Uhrín, Guy C. Lloyd-Jones*
;doi: 10.1021/acs.joc.1c01007
;pseudo 2D sequence, generates a 'ser' file
;This sequence has not been widely tested, use at your own risk
;
;$CLASS=HighRes
;$DIM=2D
;$TYPE=
;$SUBTYPE=
;$COMMENT=

#include <Avance.incl>
#include <De.incl>

"acqt0=-p1*2/3.1416"
"d11=30m"
"d2=d1-d11"
"d30=d10-aq-de-2*d11-p3-p4-p1-4u"
"p3=(270/90)*p1"
"p4=(360/90)*p1"

1 ze
2 d2
3 d11
  p3 ph1
  2u
  p4 ph2
  2u
  p1 ph3
  ACQ_START(ph30,ph31)
  aq DWELL_GEN:f1
  d30
  d11 mc #0 to 3 F1QF()
  rcyc=2
exit

ph1=0
```

```
ph2=2
ph3=1
ph30=0
ph31=0

;pl1 : f1 channel - power level for pulse (default)
;p1 : f1 channel -  90 degree high power pulse
;p3 : f1 channel -  270 degree high power pulse
;p4 : f1 channel -  360 degree high power pulse
;d1 : relaxation delay; 1-5 * T1
;d2: d1 - d11
;d10 : repetition time between pulses for relaxation recovery; d10= aq+de+d30+2*d11+p3+p4+p1+4u
;d11 : delay for disk I/O [30 msec]
;d30: interval time between acquisition and next pulse; d30>= 0
;NS: 1 * n, total number of scans: NS * TD0

;F1MODE : QF
;td1 : number of repetitive pulses (recommended 8)
```

6.1.3 BEBOP Pulse FLIPS

```
;FLIPS_BEBOP90 - rapid T1 estimation for quantitative NMR
;BEBOP 90deg pulse (Broadband Excitation By Optimised Pulses)
;Ran Wei, Claire L. Dickson, Dušan Uhrín, Guy C. Lloyd-Jones*
;doi: 10.1021/acs.joc.1c01007
;pseudo 2D sequence, generates a 'ser' file
;
;This sequence has not been widely tested, use at your own risk
;
;$CLASS=HighRes
;$DIM=2D
;$TYPE=
;$SUBTYPE=
;$COMMENT=


#include <Avance.incl>
#include <De.incl>

"p30 = 1000000.0/ (cnst50*4)"
"cnst30 = (p30/p1)*(p30/p1)"
"spw40 = plw1/cnst30"
"acqt0=-p1*2/3.1416"
"d11=30m"
"d2=d1-d11"
"d30=d10-aq-de-2*d11-p40"

1 ze
2 d2
3 d11
  (p40:sp40 ph1):f1
  ACQ_START(ph30,ph31)
  aq DWELL_GEN:f1
  d30
  d11 mc #0 to 3 F1QF()
  rcyc=2
exit

ph1=0
```

```
ph30=0
ph31=0


;pl1 : f1 channel - power level for pulse (default)
;p1 : f1 channel -  90 degree high power pulse
;p40: duration of 1st 90-degree swept-frequency pulse
;d1 : relaxation delay; 1-5 * T1
;d2: d1 - d11
;d10 : repetition time between pulses for relaxation recovery; d10=aq+de+d30+2*d11+p40
;d11 : delay for disk I/O [30 msec]
;d30: interval time between acquisition and next pulse; d30 > = 0
;spw40: RF power of 1st 90-degree swept-frequency pulse
;spnam40: filename for 1st 90-degree swept-frequency pulse
;cnst50: maximum RF power of 1st 90-degree swept-frequency pulse
;NS: 1 * n, total number of scans: NS * TD0

;F1MODE : QF
;td1 : number of repetitive pulses (recommended 8)
```

6.1.4 Conventional/hard pulse (alternative)

```
;FLIPS_hard pulse(alternative) - rapid T1 estimation for quantitative NMR
;Ran Wei, Claire L. Dickson, Dušan Uhrín, Guy C. Lloyd-Jones*
;doi: 10.1021/acs.joc.1c01007
;pseudo 2D sequence, generates a 'ser' file
;This sequence has not been widely tested, use at your own risk
;
;$CLASS=HighRes
;$DIM=2D
;$TYPE=
;$SUBTYPE=
;$COMMENT=


#include <Avance.incl>
#include <De.incl>

"p0=p1*cnst18/90.0"
"acqt0=-tan((p0/p1)*(3.14159/4))*p1*(2/3.14159)" ;corrected acqt0 for arbitrary flip angle
"d11=30m"
"d2=d1-d11"
"d30=d10-aq-de-2*d11-p0"

1 ze
2 d2
3 d11
  p0 ph1
  ACQ_START(ph30,ph31)
  aq DWELL_GEN:f1
  d30
  d11 mc #0 to 3 F1QF()
  rcyc=2
exit

ph1=0
ph30=0
ph31=0
```

```
;pl1 : f1 channel - power level for pulse (default)
;p1 : f1 channel -  90 degree high power pulse
;p0 : pulse of flip angle define by CNST18
;cnst18: flip angle for excitation pulse; X for X degree flip angle
;d1 : relaxation delay; 1-5 * T1
;d2: d1 - d30
;d10 : repetition time between pulses for relaxation recovery; d10=aq+de+d30+2*d11+p0
;d11 : delay for disk I/O [30 msec]
;d30: interval time between acquisition and next pulse; d30>=0
;NS: 1 * n, total number of scans: NS * TD0

;F1MODE : QF
;td1 : number of repetitive pulses (recommended 8)
```

6.2 FLOPS Pulse Programmes

6.2.1 Standard FLOPS

```
;FLOPS for T1 measurements
;Ran Wei, Claire L. Dickson, Dušan Uhrín, Guy C. Lloyd-Jones*
;pseudo 2D sequence, generates a 'ser' file
;no relaxation delay (d1)
;
;$CLASS=HighRes
;$DIM=2D
;$TYPE=
;$SUBTYPE=
;$COMMENT=



#include <Avance.incl>
#include <De.incl>

"acqt0=-p1*2/3.1416"
"d2=aq"
"d3=aq-30m-0.2u"
"d11=30m"
"l3=0"
"l4=0"



1 ze
2 p1 ph1
  d2
  p1 ph1
  d3
  0.1u iu3               ;increment scan counter
  if "l3 == 1"
  {
  0.1u ivd               ;increment vdlist pointer in first scan, to skip first delay in vd list (should be set to 0)
  }
  "l4=0"
3 d11
  "d4=vd"                ;correct time calculation
```

```
  0.1u iu4                  ;increment td1 counter
  p1 ph1
  ACQ_START(ph30,ph31)
  aq DWELL_GEN:f1
  if "l4 == td1"
  {
  d11                       ;for last pseudo-2d increment use d11 not delay from vdlist
  }
  else
  {
  d4                        ;for all but last pseudo-2d increment use delay from vdlist (d4=vd)
  }
  d11 mc #0 to 3 F1QF(ivd)
  rcyc=2
exit

ph1=0
ph30=0
ph31=0


;pl1 : f1 channel - power level for pulse (default)
;p1 : f1 channel -  90 degree high power pulse
;l3: scan counter - to allow the delay list pointer to be incremented in the first scan
;l4: td1 counter -
;d2: aq - the minimum delay between the first three 90 pulses
;d3: d2 with 30m removed
;d11 : delay for disk I/O [30 msec]
;NS: 1 * n, total number of scans: NS * TD0
;td1 : number of FIDs = number of delays in vd-list
;define VDLIST - first value should be 0 in FLOPS and FLAPS experiment
```

6.2.2 FLOPS with Pulsed Field Gradients

```
;FLOPS for T1 measurements with pulsed field gradients
;Ran Wei, Claire L. Dickson, Dušan Uhrín,, Guy C. Lloyd-Jones*
;pseudo 2D sequence, generates a 'ser' file
;no relaxation delay (d1)
;
;$CLASS=HighRes
;$DIM=2D
;$TYPE=
;$SUBTYPE=
;$COMMENT=


#include <Avance.incl>
#include <Grad.incl>
#include <De.incl>

"acqt0=-p1*2/3.1416"
"d2=aq"
"d3=aq+30m-0.2u"
"d11=30m"
"l3=0"
"l4=0"
"d4=vd"


1 ze
2 p1 ph1
  50u UNBLKGRAD
  p16:gp1
  d16
  d2
  50u BLKGRAD
  p1 ph1
  50u UNBLKGRAD
  p16:gp1
  d16
  d3
  0.1u iu3            ;increment scan counter
```

```
  if "l3 == 1"
  {
  0.1u ivd                 ;increment vdlist pointer in first scan, to skip first delay in vd list
  }
  50u BLKGRAD
  "l4=0"
3 d11
  50u BLKGRAD
  "d4=vd"
  0.1u iu4                 ;increment td1 counter
  p1 ph1
  ACQ_START(ph30,ph31)
  aq DWELL_GEN:f1
  50u UNBLKGRAD
  p16:gp1
  d16
  if "l4 == td1"
  {
  d11                     ;for last pseudo-2d increment use d11 not delay from vdlist
  }
  else
  {
  d4                      ;for all but last pseudo-2d increment use delay from vdlist (d4=vd)
  }
  50u BLKGRAD
  d11 mc #0 to 3 F1QF(ivd)
  rcyc=2
exit

ph1=0
ph30=0
ph31=0


;pl1 : f1 channel - power level for pulse (default)
;p1 : f1 channel -  90 degree high power pulse
;l3: scan counter - to allow the delay list pointer to be incremented in the first scan
;l4: td1 counter
;d2: aq - the minimum delay between the first three 90 pulses
;d3: aq with extra d11
```

```
;d4: delays from vdlist
;d11 : delay for disk I/O [30 msec]
;gpz1: CTP gradient 50-90%
;gpnam1: SINE.100
;NS: 1 * n, total number of scans: NS * TD0
;td1 : number of FIDs = number of delays in vd-list (first vd value should set to 0)

;define VDLIST
```

6.3 FLAPS Pulse Programme

6.3.1 Standard FLAPS

```
;FLAPS for T1 measurements
;Ran Wei, Claire L. Dickson, Dušan Uhrín, Guy C. Lloyd-Jones*
;pseudo 2D sequence, generates a 'ser' file
;no relaxation delay (d1)
;with power-gated decoupling
;
;$CLASS=HighRes
;$DIM=2D
;$TYPE=
;$SUBTYPE=
;$COMMENT=

#include <Avance.incl>
#include <De.incl>

"acqt0=-p1*2/3.1416"
"d2=aq"
"d3=aq+30m-0.2u"
"d11=30m"
"d12=20u"
"l3=0"
"l4=0"
"d4=vd"

1 ze
2 d12 pl13:f2             ;set lower power level for decoupler
  d12 cpd2:f2             ;decoupler on
  p1 ph1
  d2
  p1 ph1
  d3
  0.1u iu3                ;increment scan counter
  if "l3 == 1"
  {
  0.1u ivd                ;increment vdlist pointer in first scan, to skip first delay in vd list (should be set to 0)
  }
```

```
  "l4=0"
3 d11 cpd2:f2              ;decoupler on
  "d4=vd"
  0.1u iu4                  ;increment td1 counter
  4u do:f2                  ;decoupler off
  d12 pl12:f2              ;set higher power level for decoupler
  d12 cpd2:f2              ;decoupler on
  p1 ph1
  ACQ_START(ph30,ph31)
  aq DWELL_GEN:f1
  4u do:f2
  d12 pl13:f2                ;set lower power level for decoupler
  d12 cpd2:f2               ;decoupler on
  if "l4 == td1"
  {
  d11                          ;for last pseudo-2d increment use d11 not delay from vdlist
  }
  else
  {
  d4                       ;for all but last pseudo-2d increment use delay from vdlist (d4=vd)
  }
  d11 do:f2 mc #0 to 3 F1QF(ivd)
  rcyc=2
exit

ph1=0
ph30=0
ph31=0

;pl1 : f1 channel - power level for pulse (default)
;pl12: f2 channel - power level for CPD/BB decoupling
;pl13: f2 channel - power level for second CPD/BB decoupling
;p1 : f1 channel -  90 degree high power pulse
;l3: scan counter - to allow the delay list pointer to be incremented in the first scan
;l4: td1 counter -
;d2: aq - the minimum delay between the first three 90 pulses
;d3: aq with extra d11
;d4: delays from vdlist
;d11 : delay for disk I/O                    [30 msec]
;d12: delay for power switching              [20 usec]
```

```
;NS: 1 * n, total number of scans: NS * TD0
;cpd2: decoupling according to sequence defined by cpdprg2
;pcpd2: f2 channel - 90 degree pulse for decoupling sequence
;td1 : number of FIDs = number of delays in vd-list

;define VDLIST - first value should be 0 in FLOPS and FLAPS experiment
```

6.3.2 FLAPS with Pulsed Field Gradients

```
;FLAPS for T1 measurements with pulsed field gradients
;Ran Wei, Claire L. Dickson, Dušan Uhrín, Guy C. Lloyd-Jones*
;pseudo 2D sequence, generates a 'ser' file
;no relaxation delay (d1)
;with power gated decoupling
;
;$CLASS=HighRes
;$DIM=2D
;$TYPE=
;$SUBTYPE=
;$COMMENT=


#include <Avance.incl>
#include <Grad.incl>
#include <De.incl>

"acqt0=-p1*2/3.1416"
"d2=aq"
"d3=aq+30m-0.2u"
"d11=30m"
"d12=20u"
"l3=0"
"l4=0"
"d4=vd"

1 ze
2 d12 pl13:f2               ;set lower power level for decoupler
  d12 cpd2:f2               ;turn on decoupler
  p1 ph1
  50u UNBLKGRAD
  p16:gp1
  d16
  50u BLKGRAD
  d2
  p1 ph1
  50u UNBLKGRAD
  p16:gp1
```

```
  d16
  d3
  0.1u iu3                          ;increment scan counter
  if "l3 == 1"
  {
  0.1u ivd                          ;increment vdlist pointer in first scan, to skip first delay in vd list
  }
  50u BLKGRAD
  "l4=0"
3 d11 cpd2:f2                       ;turn on decoupler
  50u BLKGRAD
  "d4=vd"
  0.1u iu4                          ;increment td1 counter
  4u do:f2
  d12 pl12:f2                       ;set higher power level for decoupler
  d12 cpd2:f2                       ;turn on decoupler
  p1 ph1
  ACQ_START(ph30,ph31)
  aq DWELL_GEN:f1
  4u do:f2
  50u UNBLKGRAD
  p16:gp1
  d16
  d12 pl13:f2                        ;set lower power level for decoupler
  d12 cpd2:f2                        ;turn on decoupler
  if "l4 == td1"
  {
  d11                                ;for last pseudo-2d increment use d11 not delay from vdlist
  }
  else
  {
  d4                                 ;for all but last pseudo-2d increment use delay from vdlist (d4=vd)
  }
  50u BLKGRAD
  d11 do:f2 mc #0 to 3 F1QF(ivd)
  rcyc=2
exit
```

```
ph1=0
ph30=0
ph31=0


;pl1 : f1 channel - power level for pulse (default)
;pl12: f2 channel - power level for CPD/BB decoupling
;pl13: f2 channel - power level for second CPD/BB decoupling
;p1 : f1 channel -  90 degree high power pulse
;l3: scan counter - to allow the delay list pointer to be incremented in the first scan
;l4: td1 counter -
;d2: aq - the minimum delay between the first three 90 pulses
;d3: aq with extra d11
;d4: delays from vdlist
;d11 : delay for disk I/O                              [30 msec]
;d12: delay for power switching                        [20 usec]
;NS: 1 * n, total number of scans: NS * TD0
;cpd2: decoupling according to sequence defined by cpdprg2
;pcpd2: f2 channel - 90 degree pulse for decoupling sequence
;gpz1: CTP gradient 50-90%
;gpnam1: SINE.100
;td1 : number of FIDs = number of delays in vd-list (first vd value should set to 0)

;define VDLIST
```

7 References

1 Y. Ben-Tal, P. J. Boaler, H. J. A. Dale, R. E. Dooley, N. A. Fohn, Y. Gao, A. García-Domínguez, K. M. Grant, A. M. R. Hall, H. L. D. Hayes, M. M. Kucharski, R. Wei and G. C. Lloyd-Jones, *Prog. Nucl. Magn. Reson. Spectrosc.*, 2022, **129**, 28–106.

2 H. S. Gutowsky and A. Saika, *J. Chem. Phys.*, 1953, **21**, 1688–1694.

3 H. M. McConnell, *J. Chem. Phys.*, 1958, **28**, 430–431.

4 J. Kaplan, P. P. Yang and G. Fraenkel, *J. Chem. Phys.*, 1974, **60**, 4840–4845.

5 S. Forsén and R. A. Hoffman, *J. Chem. Phys.*, 1963, **39**, 2892–2901.

6 Z. Luz and S. Meiboom, *J. Chem. Phys.*, 1963, **39**, 366–370.

7 A. Allerhand and H. S. Gutowsky, *J. Chem. Phys.*, 1964, **41**, 2115–2126.

8 H. S. Gutowsky, R. L. Vold and E. J. Wells, *J. Chem. Phys.*, 1965, **43**, 4107–4125.

9 F. Bloch, *Phys. Rev.*, 1946, **70**, 460–474.

10 A. B. Jones, G. C. Lloyd-Jones and D. Uhrín, *Anal. Chem.*, 2017, **89**, 10013–10021.

11 M. Davy, C. L. Dickson, R. Wei, D. Uhrín and C. P. Butts, *Analyst*, 2022, **147**, 1702–1708.

12 F. A. L. Anet and A. J. R. Bourn, *J. Am. Chem. Soc.*, 1967, **89**, 760–768.

13 A. Kumar, R. R. Ernst and K. Wüthrich, *Biochem. Biophys. Res. Commun.*, 1980, **95**, 1–6.

14 J. Jeener, B. H. Meier, P. Bachmann and R. R. Ernst, *J. Chem. Phys.*, 1979, **71**, 4546–4553.

15 J. Fejzo, W. M. Westler, S. Macura and J. L. Markley, *J. Magn. Reson.*, 1991, **92**, 20–29.

16 A. Caprihan and E. Fukushima, *Phys. Rep.*, 1990, **198**, 195–235.

17 M. V. Gomez and A. de la Hoz, *Beilstein J. Org. Chem.*, 2017, **13**, 285–300.

18 J. F. McGarrity, J. Prodolliet and T. Smyth, *Org. Magn. Reson.*, 1981, **17**, 59–65.

19 J. F. McGarrity and J. Prodolliet, *J. Org. Chem.*, 1984, **49**, 4465–4470.

20 J. F. McGarrity, C. A. Ogle, Z. Brich and H. R. Loosli, *J. Am. Chem. Soc.*, 1985, **107**, 1810–1815.

21 J. Grimaldi, J. Baldo, C. McMurray and B. D. Sykes, *J. Am. Chem. Soc.*, 1972, **94**, 7641–7645.

22 R. O. Kühne, T. Schaffhauser, A. Wokaun and R. R. Ernst, *J. Magn. Reson.*, 1979, **35**, 39–67.

23 J. L. Sudmeier and J. J. Pesek, *Inorg. Chem.*, 1971, **10**, 860–863.

24 S. Funahashi, K. Ishihara, S. I. Aizawa, T. Sugata, M. Ishii, Y. Inada and M. Tanaka, *Rev. Sci. Instrum.*, 1993, **64**, 130–134.

25 S. Akoka, L. Barantin and M. Trierweiler, *Anal. Chem.*, 1999, **71**, 2554–2557.

26 S. Kobayashi, *Chem. – An Asian J.*, 2016, **11**, 425–436.

27 V. Sans and L. Cronin, *Chem. Soc. Rev.*, 2016, **45**, 2032–2043.

28 K. A. Farley, U. Reilly, D. P. Anderson, B. P. Boscoe, M. W. Bundesmann, D. A. Foley, M. S. Lall, C. Li, M. R. Reese and J. Yan, *Magn. Reson. Chem.*, 2017, **55**, 348–354.

29 G. Suryan, *Proc. Indian Acad. Sci. - Sect. A*, 1951, **33**, 107.

30 R. R. Ernst and W. A. Anderson, *Rev. Sci. Instrum.*, 1966, **37**, 93–102.

31 R. L. Haner and P. A. Keifer, *Encyclopedia of Magnetic Resonance*, John Wiley & Sons, Ltd: Chichester, U.K., 2009, pp 1– 11.

32 S. K. Küster, E. Danieli, B. Blümich and F. Casanova, *Phys. Chem. Chem. Phys.*, 2011, **13**, 13172–13176.

33 D. A. Foley, E. Bez, A. Codina, K. L. Colson, M. Fey, R. Krull, D. Piroli, M. T. Zell and B. L. Marquez, *Anal. Chem.*, 2014, **86**, 12008–12013.

34 J. A. Iggo, D. Shirley and N. C. Tong, *New J. Chem.*, 1998, **22**, 1043–1045.

35 D. L. Olson, T. L. Peck, A. G. Webb, R. L. Magin and J. V Sweedler, *Science (80-.).*, 1995, **270**, 1967–1970.

36 A. M. R. Hall, R. Broomfield-Tagg, M. Camilleri, D. R. Carbery, A. Codina, D. T. E. Whittaker, S. Coombes, J. P. Lowe and U. Hintermair, *Chem. Commun.*, 2018, **54**, 30–33.

37 J. Bart, A. J. Kolkman, A. J. Oosthoek-de Vries, K. Koch, P. J. Nieuwland, H. (J. W. G. . Janssen, J. (P. J. M. . van Bentum, K. A. M. Ampt, F. P. J. T. Rutjes, S. S. Wijmenga, H. (J. G. E. . Gardeniers and A. P. M. Kentgens, *J. Am. Chem. Soc.*, 2009, **131**, 5014–5015.

38 G. Finch, A. Yilmaz and M. Utz, *J. Magn. Reson.*, 2016, **262**, 73–80.

39 P. Giraudeau and F.-X. Felpin, *React. Chem. Eng.*, 2018, **3**, 399–413.

40 F. Dalitz, M. Cudaj, M. Maiwald and G. Guthausen, *Prog. Nucl. Magn. Reson. Spectrosc.*, 2012, **60**, 52–70.

41 S. T. Knox, S. Parkinson, R. Stone and N. J. Warren, *Polym. Chem.*, 2019, **10**, 4774–4778.

42 T. Maschmeyer, P. L. Prieto, S. Grunert and J. E. Hein, *Magn. Reson. Chem.*, 2020, **58**, 1234–1248.

43 A. M. R. Hall, J. C. Chouler, A. Codina, P. T. Gierth, J. P. Lowe and U. Hintermair,

Catal. Sci. Technol., 2016, **6**, 8406–8417.

44 M. T. Drexler, D. A. Foley, H. W. Ward and H. J. Clarke, *Org. Process Res. Dev.*, 2015, **19**, 1119–1127.

45 D. A. Foley, C. W. Doecke, J. Y. Buser, J. M. Merritt, L. Murphy, M. Kissane, S. G. Collins, A. R. Maguire and A. Kaerner, *J. Org. Chem.*, 2011, **76**, 9630–9640.

46 S. H. Smallcombe, S. L. Patt and P. A. Keifer, *J. Magn. Reson. Ser. A*, 1995, **117**, 295–303.

47 D. W. Jones and T. F. Child, ed. J. S. B. T.-A. in M. and O. R. Waugh, Academic Press, 1976, vol. 8, pp. 123–148.

48 G. C. Fu and R. H. Grubbs, *J. Am. Chem. Soc.*, 1992, **114**, 5426–5427.

49 X. Chen, E. R. Hortelano, E. L. Eliel and S. V. Frye, *J. Am. Chem. Soc.*, 1992, **114**, 1778–1784.

50 C. Geletneky, F. Försterling, W. Bock and S. Berger, *Chem. Ber.*, 1993, **126**, 2397–2401.

51 S. H. Bertz, C. M. Carlin, D. A. Deadwyler, M. D. Murphy, C. A. Ogle and P. H. Seagle, *J. Am. Chem. Soc.*, 2002, **124**, 13650–13651.

52 K. H. Mok, T. Nagashima, I. J. Day, J. A. Jones, C. J. V. Jones, C. M. Dobson and P. J. Hore, *J. Am. Chem. Soc.*, 2003, **125**, 12484–12492.

53 R. Franco, A. Favier, P. Schanda and B. Brutscher, *J. Magn. Reson.*, 2017, **281**, 125–129.

54 A. C. Jones, A. W. Sanders, M. J. Bevan and H. J. Reich, *J. Am. Chem. Soc.*, 2007, **129**, 3492–3493.

55 S. E. Denmark, B. J. Williams, B. M. Eklov, S. M. Pham and G. L. Beutner, *J. Org. Chem.*, 2010, **75**, 5558–5572.

56 B. Chance, *J. Franklin Inst.*, 1940, **229**, 737–766.

57 J. T. Arnold, S. S. Dharmatti and M. E. Packard, *J. Chem. Phys.*, 1951, **19**, 507.

58 Q. H. Gibson and L. Milnes, *Biochem. J.*, 1964, **91**, 161–171.

59 A. J. White, K. Drabble and C. W. Wharton, *Biochem. J.*, 1995, **306**, 843–849.

60 H. Fabian and D. Naumann, *Methods*, 2004, **34**, 28–40.

61 J. Lew, S. S. Taylor and J. A. Adams, *Biochemistry*, 1997, **36**, 6717–6724.

62 M. Weitzer, M. Schatz, F. Hampel, F. W. Heinemann and S. Schindler, *J. Chem. Soc. Dalt. Trans.*, 2002, 686–694.

63 E. A. Nalefsk and A. C. Newton, ed. A. C. Newton, Humana Press, Totowa, NJ, 2003, pp. 115–128.

64 R. Wei, A. M. R. Hall, R. Behrens, M. S. Pritchard, E. J. King and G. C. Lloyd-Jones,

European J. Org. Chem., 2021, **2021**, 2331.

65 J. J. Grimaldi and B. D. Sykes, *Rev. Sci. Instrum.*, 1975, **46**, 1201–1205.

66 A. L. Dunn and C. R. Landis, *Magn. Reson. Chem.*, 2017, **55**, 329–336.

67 E. von Harbou, R. Behrens, J. Berje, A. Brächer and H. Hasse, *Chemie Ing. Tech.*, 2017, **89**, 369–378.

68 M. D. Christianson and C. R. Landis, *Concepts Magn. Reson. Part A*, 2007, **30A**, 165–183.

69 H. Y. Carr and E. M. Purcell, *Phys. Rev.*, 1954, **94**, 630–638.

70 D. D. Boehr, H. J. Dyson and P. E. Wright, *Chem. Rev.*, 2006, **106**, 3055–3079.

71 I. R. Kleckner and M. P. Foster, *Biochim. Biophys. Acta*, 2011, **1814**, 942–968.

72 P. B. Kingsley, *Concepts Magn. Reson.*, 1999, **11**, 243–276.

73 R. L. Vold, J. S. Waugh, M. P. Klein and D. E. Phelps, *J. Chem. Phys.*, 1968, **48**, 3831–3832.

74 R. Freeman and H. D. W. Hill, *J. Chem. Phys.*, 1969, 51, 3140–3141.

75 M. Huisjen and J. S. Hyde, *J. Chem. Phys.*, 1974, **60**, 1682–1683.

76 P. W. Percival and J. S. Hyde, *J. Magn. Reson.*, 1976, **23**, 249–257.

77 R. Freeman and H. D. W. Hill, *J. Chem. Phys.*, 1971, **54**, 3367–3377.

78 R. Kaptein, K. Dijkstra and C. E. Tarr, *J. Magn. Reson.*, 1976, **24**, 295–300.

79 A. Haase, *Magn. Reson. Med.*, 1990, **13**, 77–89.

80 I. V Mastikhin, *J. Magn. Reson.*, 2005, **172**, 231–237.

81 I. J. Day, J. C. Mitchell, M. J. Snowden and A. L. Davis, *J. Magn. Reson.*, 2007, **187**, 216–224.

82 D. Canet, G. C. Levy and I. R. Peat, *J. Magn. Reson.*, 1975, **18**, 199–204.

83 R. K. Gupta, J. A. ferretti, E. D. Becker and G. H. Weiss, *J. Magn. Reson.*, 1980, **38**, 447–452.

84 R. L. Streever and H. Y. Carr, *Phys. Rev.*, 1961, **121**, 20–25.

85 R. J. Kurland and R. G. Parrish, *J. Magn. Reson.*, 1975, **17**, 295–300.

86 N. M. Loening, M. J. Thrippleton, J. Keeler and R. G. Griffin, *J. Magn. Reson.*, 2003, **164**, 321–328.

87 D. C. Look and D. R. Locker, *Phys. Rev. Lett.*, 1968, **20**, 987–989.

88 D. C. Look and D. R. Locker, *Rev. Sci. Instrum.*, 1970, **41**, 250–251.

89 D. R. Messroghli, A. Radjenovic, S. Kozerke, D. M. Higgins, M. U. Sivananthan and J. P. Ridgway, *Magn. Reson. Med.*, 2004, **52**, 141–146.

90 G. A. Morris, *J. Magn. Reson.*, 1980, **41**, 185–188.

91 J. Kowalewski and G. A. Morris, *J. Magn. Reson.*, 1982, **47**, 331–338.

92 V. Sklenář, D. Torchia and A. Bax, *J. Magn. Reson.*, 1987, **73**, 375–379.

93 A. W. Overhauser, *Phys. Rev.*, 1953, **92**, 411–415.

94 T. R. Carver and C. P. Slichter, *Phys. Rev.*, 1953, **92**, 212–213.

95 U. L. Günther, eds. H. Heise and S. Matthews, Springer Berlin Heidelberg, Berlin, Heidelberg, 2013, pp. 23–69.

96 A. Lesage, M. Lelli, D. Gajan, M. A. Caporini, V. Vitzthum, P. Miéville, J. Alauzun, A. Roussey, C. Thieuleux, A. Mehdi, G. Bodenhausen, C. Coperet and L. Emsley, *J. Am. Chem. Soc.*, 2010, **132**, 15459–15461.

97 A. J. Rossini, C. M. Widdifield, A. Zagdoun, M. Lelli, M. Schwarzwälder, C. Copéret, A. Lesage and L. Emsley, *J. Am. Chem. Soc.*, 2014, **136**, 2324–2334.

98 T. D. W. Claridge, in *High-Resolution NMR Techniques in Organic Chemistry*, Elsevier, Boston, 3rd edn., 2016, pp. 315–380.

99 D. Canet, S. Bouguet-Bonnet, S. Leclerc and M. Yemloul, ed. G. Webb, Academic Press, 2011, vol. 74, pp. 89–123.

100 R. Freeman, H. D. W. Hill and R. Kaptein, *J. Magn. Reson.*, 1972, **7**, 327–329.

101 P. Moutzouri, P. Kiraly, A. R. Phillips, S. R. Coombes, M. Nilsson and G. A. Morris, *Anal. Chem.*, 2017, **89**, 11898–11901.

102 W. A. Anderson and R. Freeman, *J. Chem. Phys.*, 1962, **37**, 85–103.

103 R. R. Ernst, *J. Chem. Phys.*, 1966, **45**, 3845–3861.

104 R. Freeman, S. P. Kempsell and M. H. Levitt, *J. Magn. Reson.*, 1979, **35**, 447–450.

105 J. S. Waugh, *J. Magn. Reson.*, 1982, **50**, 30–49.

106 M. H. Levitt and R. Freeman, *J. Magn. Reson.*, 1981, **43**, 502–507.

107 M. H. Levitt, R. Freeman and T. Frenkiel, *J. Magn. Reson.*, 1982, **50**, 157–160.

108 M. H. Levitt, R. Freeman and T. Frenkiel, *J. Magn. Reson.*, 1982, **47**, 328–330.

109 A. . Shaka, J. Keeler, T. Frenkiel and R. Freeman, *J. Magn. Reson.*, 1983, **52**, 335–338.

110 A. J. Shaka and P. B. Barker, *J. Magn. Reson.*, 1985, **64**, 541–552.

111 Ē. Kupče, *J. Magn. Reson.*, 2020, **318**, 106799.

112 T. D. W. Claridge, in *High-Resolution NMR Techniques in Organic Chemistry*, ed. T. Claridge, Elsevier, Boston, 3rd edn., 2016, pp. 457–498.

113 A. J. Shaka, C. J. Lee and A. Pines, *J. Magn. Reson.*, 1988, **77**, 274–293.

114 Z. Starcuk, K. Bartusek and Z. Starcuk, *J. Magn. Reson. Ser. A*, 1994, **107**, 24–31.

115 R. Fu and G. Bodenhausen, *J. Magn. Reson. Ser. A*, 1995, **117**, 324–325.

116 R. Fu and G. Bodenhausen, *J. Magn. Reson. Ser. A*, 1996, **119**, 129–133.

117 V. J. Basus, P. D. Ellis, H. D. W. Hill and J. S. Waugh, *J. Magn. Reson.*, 1979, **35**, 19–37.

118 E. Kupce and R. Freeman, *J. Magn. Reson. Ser. A*, 1995, **115**, 273–276.

119 J. M. Bohlen and G. Bodenhausen, *J. Magn. Reson. Ser. A*, 1993, **102**, 293–301.

120 Ē. Kupce, R. Freeman, G. Wider and K. Wüthrich, *J. Magn. Reson. Ser. A*, 1996, **122**, 81–84.

121 E. Tenailleau and S. Akoka, *J. Magn. Reson.*, 2007, **185**, 50–58.

122 A. Bahadoor, A. Brinkmann and J. E. Melanson, *Anal. Chem.*, 2021, **93**, 851–858.

123 G. A. Morris and R. Freeman, *J. Am. Chem. Soc.*, 1979, **101**, 760–762.

124 K. Müller, in *Progress in Fluorine Science*, ed. G. Haufe, Academic Press, 2019, pp. 91–139.

125 M. Morgenthaler, E. Schweizer, A. Hoffmann-Röder, F. Benini, R. E. Martin, G. Jaeschke, B. Wagner, H. Fischer, S. Bendels, D. Zimmerli, J. Schneider, F. Diederich, M. Kansy and K. Müller, *ChemMedChem*, 2007, **2**, 1100–1115.

126 M. B. van Niel, I. Collins, M. S. Beer, H. B. Broughton, S. K. F. Cheng, S. C. Goodacre, A. Heald, K. L. Locker, A. M. MacLeod, D. Morrison, C. R. Moyes, D. O'Connor, A. Pike, M. Rowley, M. G. N. Russell, B. Sohal, J. A. Stanton, S. Thomas, H. Verrier, A. P. Watt and J. L. Castro, *J. Med. Chem.*, 1999, **42**, 2087–2104.

127 B. E. Smart, *J. Fluor. Chem.*, 2001, **109**, 3–11.

128 K. L. Kirk, *J. Fluor. Chem.*, 2006, **127**, 1013–1029.

129 W. K. Hagmann, *J. Med. Chem.*, 2008, **51**, 4359–4369.

130 J. Wang, M. Sánchez-Roselló, J. L. Aceña, C. del Pozo, A. E. Sorochinsky, S. Fustero, V. A. Soloshonok and H. Liu, *Chem. Rev.*, 2014, **114**, 2432–2506.

131 D. Cartwright, in *Organofluorine Chemistry*, 1994, pp. 237–262.

132 T. Fujiwara and D. O'Hagan, *J. Fluor. Chem.*, 2014, **167**, 16–29.

133 Y. Zhou, J. Wang, Z. Gu, S. Wang, W. Zhu, J. L. Aceña, V. A. Soloshonok, K. Izawa and H. Liu, *Chem. Rev.*, 2016, **116**, 422–518.

134 Y. Ogawa, E. Tokunaga, O. Kobayashi, K. Hirai and N. Shibata, *iScience*, 2020, **23**, 101467.

135 A. Borodine, *Justus Liebigs Ann. Chem.*, 1863, **126**, 58–62.

136 W. J. Middleton, *J. Org. Chem.*, 1975, **40**, 574–578.

137 R. E. Banks, S. N. Mohialdin-Khaffaf, G. S. Lal, I. Sharif and R. G. Syvret, *J. Chem. Soc. Chem. Commun.*, 1992, 595–596.

138 G. Resnati and D. D. DesMarteau, *J. Org. Chem.*, 1991, **56**, 4925–4929.

139 H. F. Hodson, D. J. Madge, A. N. Z. Slawin, D. A. Widdowson and D. J. Williams, *Tetrahedron*, 1994, **50**, 1899–1906.

140 G. S. Lal, G. P. Pez and R. G. Syvret, *Chem. Rev.*, 1996, **96**, 1737–1756.

141 R. P. Singh and J. M. Shreeve, *Acc. Chem. Res.*, 2004, **37**, 31–44.

142 F. Camps, E. Chamorro, V. Gasol and A. Guerrero, *J. Org. Chem.*, 1989, **54**, 4294–4298.

143 S. Furuta, M. Kuroboshi and T. Hiyama, *Bull. Chem. Soc. Jpn.*, 1999, **72**, 805–819.

144 M. Shimizu and T. Hiyama, *Angew. Chemie Int. Ed.*, 2005, **44**, 214–231.

145 S. Rozen, *Acc. Chem. Res.*, 2005, **38**, 803–812.

146 F. A. Davis and W. Han, *Tetrahedron Lett.*, 1992, **33**, 1153–1156.

147 N. Shibata, E. Suzuki and Y. Takeuchi, *J. Am. Chem. Soc.*, 2000, **122**, 10728–10729.

148 A. Togni, A. Mezzetti, P. Barthazy, C. Becker, I. Devillers, R. Frantz, L. Hintermann, M. Perseghini and M. Sanna, *Chimia (Aarau).*, 2001, **55**, 801–805.

149 J.-A. Ma and D. Cahard, *Chem. Rev.*, 2004, **104**, 6119–6146.

150 T. D. Beeson and D. W. C. MacMillan, *J. Am. Chem. Soc.*, 2005, **127**, 8826–8828.

151 J. C. Edwards, *Magn. Reson. Chem.*, 2016, **54**, 492–493.

152 J. Battiste and R. A. Newmark, *Prog. Nucl. Magn. Reson. Spectrosc.*, 2006, **48**, 1–23.

153 Y.-B. Wan and X.-H. Li, *Chinese J. Anal. Chem.*, 2015, **43**, 1203–1209.

154 H. Kovacs and Ē. Kupče, *Magn. Reson. Chem.*, 2016, **54**, 544–560.

155 M. C. Loewen, J. Klein-Seetharaman, E. V Getmanova, P. J. Reeves, H. Schwalbe and H. G. Khorana, *Proc. Natl. Acad. Sci. U. S. A.*, 2001, **98**, 4888–4892.

156 R. Kaptein, eds. L. J. Berliner and J. Reuben, Springer US, Boston, MA, 1982, pp. 145–191.

157 I. Kuprov and P. J. Hore, *J. Magn. Reson.*, 2004, **168**, 1–7.

158 C. L. Dickson, G. Peat, M. Rossetto, M. E. Halse and D. Uhrín, *Chem. Commun.*, 2022, **58**, 5534–5537.

159 J. L. Kitevski-LeBlanc and R. S. Prosser, *Prog. Nucl. Magn. Reson. Spectrosc.*, 2012, **62**, 1–33.

160 L. Castañar, P. Moutzouri, T. M. Barbosa, C. F. Tormena, R. Rittner, A. R. Phillips, S. R. Coombes, M. Nilsson and G. A. Morris, *Anal. Chem.*, 2018, **90**, 5445–5450.

161 F. Malz and H. Jancke, *J. Pharm. Biomed. Anal.*, 2005, **38**, 813–823.

162 S. K. Bharti and R. Roy, *TrAC - Trends Anal. Chem.*, 2012, **35**, 5–26.

163 J. E. Power, M. Foroozandeh, R. W. Adams, M. Nilsson, S. R. Coombes, A. R. Phillips and G. A. Morris, *Chem. Commun.*, 2016, **52**, 2916–2919.

164 J. B. Verstraete and M. Foroozandeh, *J. Magn. Reson.*, 2022, **336**, 107146.

165 M. Foroozandeh, M. Nilsson and G. A. Morris, *J. Magn. Reson.*, 2019, **302**, 28–33.

166 J.-B. Verstraete and M. Foroozandeh, *J. Magn. Reson.*, 2022, **336**, 107146.

167 P. A. Cox, A. G. Leach, A. D. Campbell and G. C. Lloyd-Jones, *J. Am. Chem. Soc.*, 2016, **138**, 9145–9157.

168 P. A. Cox, M. Reid, A. G. Leach, A. D. Campbell, E. J. King and G. C. Lloyd-Jones, *J. Am. Chem. Soc.*, 2017, **139**, 13156–13165.

169 C. P. Johnston, T. H. West, R. E. Dooley, M. Reid, A. B. Jones, E. J. King, A. G. Leach and G. C. Lloyd-Jones, *J. Am. Chem. Soc.*, 2018, **140**, 11112–11124.

170 A. García-Domínguez, T. H. West, J. J. Primozic, K. M. Grant, C. P. Johnston, G. G. Cumming, A. G. Leach and G. C. Lloyd-Jones, *J. Am. Chem. Soc.*, 2020, **142**, 14649–14663.

171 A. García-Domínguez, P. H. Helou de Oliveira, G. T. Thomas, A. R. Sugranyes and G. C. Lloyd-Jones, *ACS Catal.*, 2021, **11**, 3017–3025.

172 H. L. D. Hayes, R. Wei, M. Assante, K. J. Geogheghan, N. Jin, S. Tomasi, G. Noonan, A. G. Leach and G. C. Lloyd-Jones, *J. Am. Chem. Soc.*, 2021, **143**, 14814–14826.

173 I. Ruppert, K. Schlich and W. Volbach, *Tetrahedron Lett.*, 1984, **25**, 2195–2198.

174 R. P. Singh and J. M. Shreeve, *Tetrahedron*, 2000, **56**, 7613–7632.

175 G. K. S. Prakash, C. Panja, H. Vaghoo, V. Surampudi, R. Kultyshev, M. Mandal, G. Rasul, T. Mathew and G. A. Olah, *J. Org. Chem.*, 2006, **71**, 6806–6813.

176 V. V Levin, A. D. Dilman, P. A. Belyakov, M. I. Struchkova and V. A. Tartakovsky, *European J. Org. Chem.*, 2008, **2008**, 5226–5230.

177 G. Jin, X. Zhang, D. Fu, W. Dai and S. Cao, *Tetrahedron*, 2015, **71**, 7892–7899.

178 A. García-Domínguez, A. G. Leach and G. C. Lloyd-Jones, *Acc. Chem. Res.*, 2022, **55**, 1324–1336.

179 R. Freeman, S. P. Kempsell and M. H. Levitt, *J. Magn. Reson.*, 1980, **38**, 453–479.

180 M. H. Levitt, *Prog. Nucl. Magn. Reson. Spectrosc.*, 1986, **18**, 61–122.

181 T. E. Skinner, K. Kobzar, B. Luy, M. R. Bendall, W. Bermel, N. Khaneja and S. J. Glaser, *J. Magn. Reson.*, 2006, **179**, 241–249.

182 K. Kobzar, S. Ehni, T. E. Skinner, S. J. Glaser and B. Luy, *J. Magn. Reson.*, 2012, **225**, 142–160.

183 F. A. Franchina, M. E. Machado, P. Q. Tranchida, C. A. Zini, E. B. Caramão and L. Mondello, *J. Chromatogr. A*, 2015, **1387**, 86–94.

184 X. Zhao and D. W. C. MacMillan, *J. Am. Chem. Soc.*, 2020, **142**, 19480–19486.

185 J.-J. Dai, C. Fang, B. Xiao, J. Yi, J. Xu, Z.-J. Liu, X. Lu, L. Liu and Y. Fu, *J. Am. Chem.*

Soc., 2013, **135**, 8436–8439.

186 L. Ruyet and T. Besset, *Beilstein J. Org. Chem.*, 2020, **16**, 1051–1065.

187 J. B. Geri, M. M. Wade Wolfe and N. K. Szymczak, *Angew. Chemie Int. Ed.*, 2018, **57**, 1381–1385.

188 R. Rigger, A. Rück, C. Hellriegel, R. Sauermoser, F. Morf, K. Breitruck and M. Obkircher, *J. AOAC Int.*, 2017, **100**, 1365–1375.

189 F. Huang, S. Pan, Y. Pu, H. Ben and A. J. Ragauskas, *RSC Adv.*, 2014, **4**, 17743–17747.

190 I. Pravst, M. P. Iskra, M. Jereb, M. Zupan and S. Stavber, *Tetrahedron*, 2006, **62**, 4474–4481.

191 I. Djordjevic, G. Wicaksono, I. Solic and T. W. J. Steele, *Results Chem.*, 2020, **2**, 100066.

192 C. Pezzetta, A. Folli, O. Matuszewska, D. Murphy, R. W. M. Davidson and D. Bonifazi, *Adv. Synth. Catal.*, 2021, **363**, 4740–4753.

193 A. J. Plaunt, K. J. Clear and B. D. Smith, *Chem. Commun.*, 2014, **50**, 10499–10501.

194 Z. Talebpour and H. R. Bijanzadeh, *Food Chem.*, 2007, **105**, 1682–1687.

195 J. Yu, W. Cui, D. Zhao and R. P. Mason, ed. A. B. T.-F. and H. Tressaud, Elsevier, Amsterdam, 2008, pp. 197–276.

196 P. J. Foth, F. Gu, T. G. Bolduc, S. S. Kanani and G. M. Sammis, *Chem. Sci.*, 2019, **10**, 10331–10335.

197 E. S. Esakkimuthu, N. Marlin, M.-C. Brochier-Salon and G. Mortha, *AppliedChem*, 2022, 2.

198 J.-J. Ma and W.-B. Yi, *Org. Biomol. Chem.*, 2017, **15**, 4295–4299.

199 P. Buist, D. Marecak, B. Dawson and B. Black, *Can. J. Chem.*, 1996, **74**, 453–456.

200 A. D. James, C. Marvalin, A. Luneau, A. Meissner and G. Camenisch, *Drug Metab. Dispos.*, 2017, **45**, 900 LP – 907.

201 G. Ochoa, C. D. Pilgrim, J. Kerr, M. P. Augustine and W. H. Casey, *Geochim. Cosmochim. Acta*, 2019, **244**, 173–181.

202 X.-Q. Chu, L.-W. Sun, Y.-L. Chen, J.-W. Chen, X. Ying, M. Ma and Z.-L. Shen, *Green Chem.*, 2022, **24**, 2777–2782.

203 M.-T. Chen, X.-Y. Tang and M. Shi, *Org. Chem. Front.*, 2017, **4**, 86–90.

204 J. H. Noggle and R. E. Schirmer, eds. J. H. Noggle and R. E. Schirmer, Academic Press, New York, 1971, pp. 113–124.

205 R. Freeman and E. Kupče, *NMR Biomed.*, 1997, **10**, 372–380.

206 C. Ammann, P. Meier and A. Merbach, *J. Magn. Reson.*, 1982, **46**, 319–321.

207 A. J. Shaka, P. B. Barker and R. Freeman, *J. Magn. Reson.*, 1985, **64**, 547–552.

208 D. A. Singleton and A. A. Thomas, *J. Am. Chem. Soc.*, 1995, **117**, 9357–9358.

209 E. E. Kwan, Y. Park, H. A. Besser, T. L. Anderson and E. N. Jacobsen, *J. Am. Chem. Soc.*, 2017, **139**, 43–46.

210 H. J. A. Dale, A. G. Leach and G. C. Lloyd-Jones, *J. Am. Chem. Soc.*, 2021, **143**, 21079–21099.

211 P. Giraudeau and E. Baguet, *J. Magn. Reson.*, 2006, **180**, 110–117.